MEASUREMENT OF THE SPIN STRUCTURE FUNCTION $g_1(x, Q^2)$ OF THE PROTON IN THE RESONANCE REGION

Yelena Alexandrovna Prok
Richmond, VA

B.A., University of Virginia, 1997

A Dissertation Presented to the Graduate
Faculty of the University of Virginia
in Candidacy for the Degree of Doctor of Philosophy

Department of Physics

University of Virginia
May, 2004

Abstract

Inclusive double spin electron asymmetries have been measured by scattering polarized electrons off the solid polarized $^{15}NH_3$ target in Hall B of Jefferson Lab in 2000-2001. The virtual photon asymmetry $A_1(x)$, the longitudinal spin structure function, $g_1(x, Q^2)$, and the first moment, Γ_1^p, have been evaluated for a kinematic range of $0.05 \geq Q^2 \leq 4.5\ GeV^2$. The extracted results complement the existing data in the resonance region, and extend it to lower and higher Q^2 regions. The results are important in the study of Q^2 evolution of nucleon structure from the hadronic to partonic degrees of freedom.

Acknowledgements

I thank my advisors Don Crabb and Ralph Minehart for their help and guidance. I thank all the past and present members of the Polarized Target Group at the University of Virginia. I thank Chris Keith and Mike Seely of the Target Group at Jefferson Lab for their help and patience while maintaining the Hall B target for seven months. I thank Paul McKee and Cole Smith for helping me with computer and programming problems. I thank Harut Avakian, Elton Smith and Stepan Stepanyan for helping me with Hall B software and calibrations problems. I thank Peter Bosted, Sebastian Kuhn and Gail Dodge for their advice with analysis projects. Finally, I thank Renee Fatemi for being a true friend and an inspiration.

Contents

List of Figures

List of Tables

Chapter 1

Introduction

In the 1960s high energy electron beams were used at the Stanford Linear Accelerator Center(SLAC) to probe the hadronic structure of the proton and deuterium targets. It was found that the electrons were scattered with large values of momentum transfer more often than was expected. This observation suggested that the proton consisted of discrete scattering centers . The distribution of electrons in energy and angle indicated that the scattering centers had no internal structure of their own. Later experiments at SLAC and CERN confirmed these observation, and it was established that the proton and neutron are not elementary but are made out of 'partons' [1]. The partons were classified in two types: electrically neutral massless vector particles with spin 1 called gluons, and spin $\frac{1}{2}$ fractionally charged fermions called quarks. There are six known flavors of quarks, which are listed in Table 1.1, with their electrical charges Q, strangeness quantum number S and isospin (T, T_3) [1].

The three light quarks u,d,s are identified with the three states in the fundamental representation of the flavor SU(3). Hadrons are constructed as flavor SU(3) states;

Table 1.1: Quark Quantum Numbers

	Q	T	T_3	S
u	2/3	1/2	1/2	0
d	-1/3	1/2	-1/2	0
s	-1/3	0	0	-1
c	2/3	0	0	0
t	2/3	0	0	0
b	-1/3	0	0	0

when the spin of the quarks is taken into account, the total symmetry group becomes SU(3)×SU(2). The static properties of hadrons, such as charge of the proton, do not reveal the parton structure, however, the magnetic moment of the proton is different from the one expected for a point-like particle. Experiments using beams of muons with momenta up to 280 GeV have shown that quarks have an apparent substructure of their own when resolved to very small distances. What appeared to be a quark at some momentum scale showed an additional quark-antiquark pair at a higher momentum. Such evolution with momentum transfer squared Q^2 is predicted by the theory of strong interactions, Quantum Chromodynamics (QCD).Transitions such as $q \to q + g, g \to q + \bar{q}, g \to g + g$ can occur, and as nucleon structure is resolved to smaller and smaller distances, more partons are revealed, each with a progressively smaller fraction of initial quark momentum. Therefore, a conclusion was made that a nucleon consists of 'valence' quarks carrying the quantum numbers and a 'sea' of $q\bar{q}$ pairs [2].

The interactions between quarks and antiquarks are mediated by the gluons. Analogous to the electric charge in QED, the quarks and antiquarks carry a 'strong charge', called 'color'. An important difference between QED and QCD is that, while the photon has no charge, the gluons carry a color charge. This makes QCD a non-Abelian field theory, i.e. the theory in which the field quanta themselves are a field source [2]. The fact the the gluons can interact with themselves gives rise to additional vertex couplings, such as three or four gluon couplings, which do not exist in QED. The three types of color charge are called red R, blue B and green G, with the corresponding anticolors $\bar{R}, \bar{B}, \bar{G}$. The colors carried by the eight gluons are the following: $R\bar{B}, R\bar{G}, B\bar{R}, G\bar{R}, B\bar{G}, G\bar{B}, (R\bar{R}-G\bar{G})/\sqrt{2}, (R\bar{R}+G\bar{G}-2B\bar{B})/\sqrt{6}$. The underlying QCD symmetry is color SU(3), which is believed to be exact as opposed to the flavor symmetry which is known to be broken. The color is not observable, and all colors appear with equal probability. Only 'colorless' quark systems are observed in nature. The simplest color singlets are $q\bar{q}$, qqq,$\bar{q}\bar{q}\bar{q}$ which correspond to mesons, baryons and antibaryons respectively. The confinement of 'colored' objects can be explained by the color force increasing with the increasing separation. As the separation decreases, the force becomes weaker, so that at very small distances (very large momenta), the quarks no longer interact, a phenomenon called asymptotic freedom. The strong coupling is defined as a perturbation series; to first order it is:

$$\alpha_s(Q^2) = \frac{12\pi}{33-2n_f}\frac{1}{\ln(Q^2)/\Lambda^2)}, \tag{1.1}$$

where n_f is the number of active quark flavors, Q^2 is the absolute value of the four-momentum squared, and the parameter Λ is determined experimentally. The value of Λ has a large range (50 MeV to 500 MeV), that results from the uncertainty in the minimum value of Q^2 for which the assumption of asymptotic freedom is justified. Each process has additional contributions from the higher order terms and non-asymptotic (higher twist) terms falling off as $1/Q^2$. A proper extraction of Λ from various experimental processes requires the inclusion of higher order terms in the expansion of α_s, and higher terms in the matrix element of the process. Both of these must be calculated using the same renormalization scheme. The decrease of the strong coupling constant with increasing momentum can be explained qualitatively as the color charge being spread out by gluon branching processes that grow in number with increasing Q^2. At $Q^2 \sim \Lambda$, α_s becomes very large, suggesting that the quark confinement takes place at $r_c \sim 1/\Lambda$, which results in r_c roughly the size of a hadron.

In the high energy limit of non-interacting partons, the Quark Parton Model (QPM) has been a successful tool in understanding many hadronic processes. However, the model fails to describe the Q^2 dependence of the measured quantities, such as cross sections and structure functions of a nucleon. For example, in QPM the spin structure function of a proton is related to the quark spin distributions:

$$g_1(x) = \frac{1}{2}\sum_i e_i^2 \Delta q_i(x). \tag{1.2}$$

The sensitivity to quark spin polarization results from the fact that the quark's spin must be anti-parallel to the virtual photon's spin in order for the quark to absorb the virtual photon. This stems from the conservation of angular momentum in the limit of massless collinear quarks. The QPM, however, does not take into account internal parton interactions. A model with a more rigorous approach is QCD, which introduces a momentum scale dependence into the structure functions due to the gluon radiation and the transverse momentum of the partons [3]. This Q^2 dependence is calculated using the method called Operator Product Expansion (OPE) together with the renormalization group equations. The expansion is given in terms of 'twist', which is the difference between the mass dimension and the spin of the operators that participate in the expansion. The matrix elements of these operators are not calculable, and have to be measured, but the Q^2 dependent coefficients are calculable. The lowest order twist-two coefficients are finite as $Q^2 \to \infty$, and the higher twist terms fall off as $1/Q^2$, making them more important at the low Q^2 scale. The full Q^2 dependence is complicated and consists of two main sources: Q^2 dependence of the higher twist terms and the Q^2 dependence caused by QCD radiative corrections.

In the framework of QCD, the total helicity of the nucleon can be evaluated as:

$$\frac{1}{2} = \frac{1}{2}\Delta\Sigma(\mu) + L_q(\mu) + J_q(\mu), \tag{1.3}$$

where $\Delta\Sigma$ corresponds to the intrinsic quark spin, L_q is the quark angular momentum, J_q is the gluon contribution, and the scheme dependence is indicated by μ. In the QPM model, the spin of a nucleon was assumed to be made out of the spins of quarks, so that:

$$\Delta\Sigma = \int_o^1 dx \sum_i (\Delta q_i(x) + \Delta\bar{q}_i(x)) = 1. \tag{1.4}$$

The surprise came from the 1970s experiments at SLAC and CERN, which measured this number to be far from one. The EMC experiment [4] at CERN found the value of $\Delta\Sigma$ at Q^2=10.7 GeV^2: $\Delta\Sigma = 0.17 \pm 0.12 \pm 0.17$. Obviously, some part of a nucleon spin is carried by the angular momentum of quarks and gluons, however it is not easy to separate the two. It is important to note that in QCD neither the quark nor gluon spin operators are conserved separately, only their sum is. For this reason, the spin fraction carried by quarks or gluons depends on the renormalization scheme. Measurements over a large range of Q^2 are necessary to separate the individual components of nucleon spin.

As Q^2 gets smaller, another factor enters into the Q^2 evolution of the structure functions, namely, the excitation of nucleon resonances in the regime where the invariant mass of the final state $W \leq 2$ GeV. The resonance behavior is not well described by any of the existing models, and is usually parametrized in terms of the measured processes, and interpolation between two fundamental predictions: the Bjorken Sum Rule in the high energy limit, and the Gerasimov-Drell-Hearn Sum Rule valid for the real photon point of $Q^2 = 0$.

The lack of data in the low Q^2 region ($Q^2 \leq 1$) GeV was the motivation for the EG1b (also known as EG2000) experiment that took place in Hall B of Jefferson Lab in 2000-2001. In this thesis I present an analysis of the data and an extraction of the spin structure function $g_1(x)$.

Chapter 2

Theory of structure functions

2.1 Inelastic Inclusive Scattering

Inelastic scattering plays an important role in our understanding of quarks and gluons and how their interactions are governed by QCD. An example of such scattering is shown in Fig. 2.1

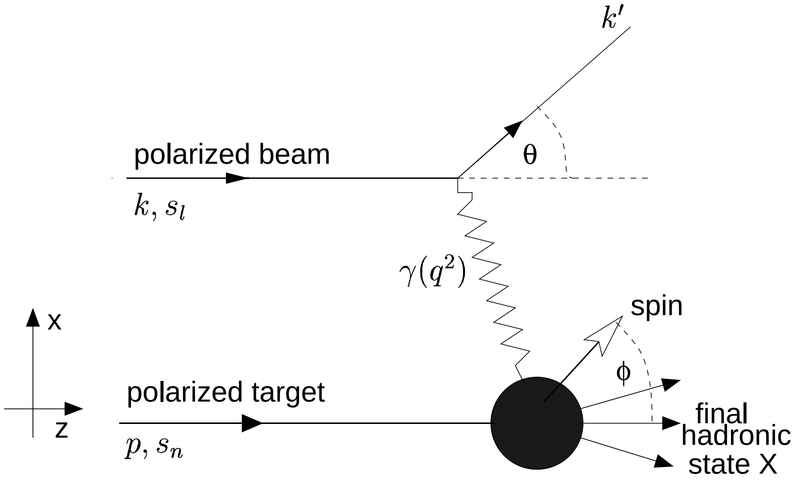

Figure 2.1: Inclusive Inelastic Scattering

Consider the process shown in fig. 2.1, in which an incident lepton (e^-, in this case) is incident on a nucleon (proton, in this case) target, and scatters off the target inelastically. e is the incident electron, p is the target proton, and X is the system of hadrons produced through the inelastic scattering. Experimentally, the produced hadrons X are not observed, and only the electron momentum is measured in the final state. Such experiments are called inclusive experiments. The kinematic variables of the scattering process are defined in Table 2.1 The scattering process takes place mainly through the electromagnetic interaction. In the lowest order, the scattering is approximated by an exchange of a virtual photon γ^*. The process can be separated into two parts:

Table 2.1: Kinematic Variables

Variable	expression	definition
M	M_p	mass of the proton
m	m_e	mass of the electron
k	(E, k_x, k_y, k_z)	incoming e 4-momentum
k'	(E', k'_x, k'_y, k'_x)	outgoing e 4-momentum
p	(M,0,0,0)	nucleon 4-momentum
q	(ν, q_x, q_y, q_z)	virtual photon 4-momentum
$Q^2 = -q^2$	$2EE'(1 - cos\theta) = 4EE'sin^2(\frac{\theta}{2})$	
ν	$E - E' = \frac{p \cdot q}{M}$	energy of the virtual photon
s_l	$\frac{1}{m}(\mathbf{k},0,0,E)$	spin of the incident e^-
s_n	$\frac{1}{M}(\mathbf{p},0,0,E)$	spin of the target nucleon
θ		scattering angle of e^- in the LAB frame
W^2	$(p+q)^2 = M^2 + 2p \cdot q + q^2$	Mass of the final hadronic state
x	$\frac{Q^2}{2M\nu}$	Bjorken dimensionless variable
y	$\frac{\nu}{E}$	Bjorken dimensionless variable

1) The leptonic part which consists of the emission of a virtual photon of energy, ν, and 4-momentum, q, by an electron of 4-momentum k.

2) The hadronic part which consists of the absorption of the emitted virtual photon by a nucleon of momentum p. Diagrammatically, this is shown in Fig.2.2

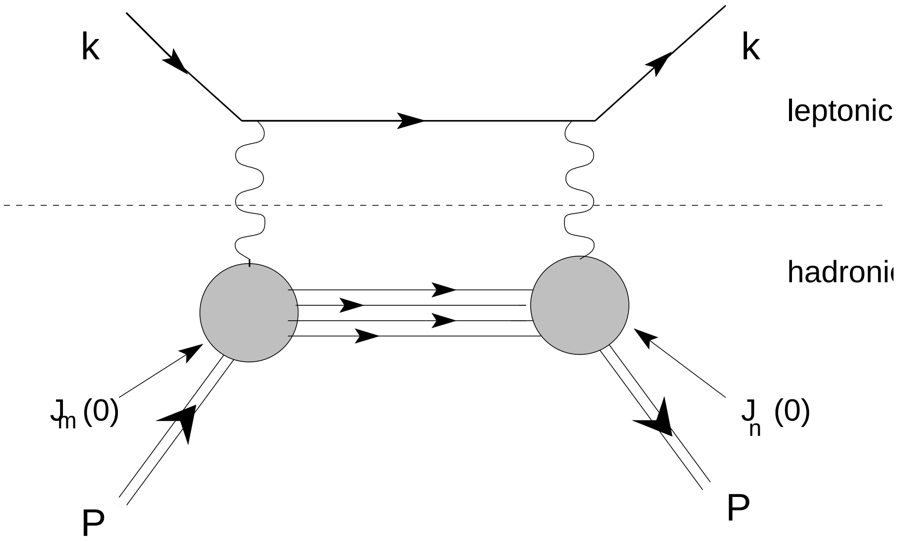

Figure 2.2: Separation into a leptonic tensor $L^{\mu\nu}$ and a hadronic tensor $W^{\mu\nu}$

The scattering amplitude $\mathcal{M}$ for a given X state is defined by

$$\mathrm{i}\mathcal{M} = (-ie)^2 \left(\frac{-ig_{\mu\nu}}{q^2}\right) < k' s'_l | j_l^\mu(0) | k, s_l >< X s'_X | j_h^\nu(0) | p, s_n > \quad , \tag{2.1}$$

where

- $s_l (s'_l)$ is the polarization of the incoming (outgoing) electron
- $s_n (s'_X)$ is the polarization of the initial (final) proton (hadrons) and can be choosen to be the value of the spin along an arbitrary quantization axis, usually the electron

axis, so that $s_n = \pm\frac{1}{2}$

- j_l^μ , j_h^ν are the leptonic and hadronic electromagnetic currents. The differential cross section is obtained from $\mathcal{M}$ by squaring the amplitude and multiplying it by the phase space factor. The polarization of the final lepton is not measured. Final state hadrons are not detected and all possible final states need to be summed over. This gives the following differential cross section:

$$\begin{aligned} d\sigma &= \frac{(2\pi)^4}{(2E)(2M)} \cdot \frac{d^3k'}{(2\pi)^3(2E')} \cdot \sum_X \sum_{s',\lambda'} \int \Pi_{n=1}^X \frac{d^3p_n}{(2\pi)^3(2E_n)} \cdot \frac{e^4}{Q^4} \cdot \delta^4(p+q-\sum_{n=1}^X p_n) \\ &\times < k, s_l | j_l^\mu(0) | k' s_l' >< k' s_l' | j_l^\nu(0) | k, s_l > \qquad (2.2) \\ &\times < p, s_n | j_{\mu h}(0) | X, s_X' >< X, s_X' | j_{\nu h}(0) | p, s_n > . \end{aligned}$$

In the equation above the definition of a leptonic tensor is used:

$$L^{\mu\nu} = \sum_{s_l'} < k' s_l' | j_e^\nu(0) | k, s_l >< k, s_l | j_e^\mu(0) | k' s_l' > . \qquad (2.3)$$

For a point-like fermion, it could be written explicitly:

$$< k, s_l | j_e^\nu(0) | k, s_l >= \bar{u}(k, s_l) \gamma^\nu u(k, s_l). \qquad (2.4)$$

Using several properties of the γ matrices, the leptonic tensor can be written as:

$$L^{\mu\nu} = 2[(k'^\mu k^\nu + k'^\nu k^\mu) - (k \cdot k') g^{\mu\nu} - i\epsilon^{\mu\nu\rho\sigma} q_\rho s_l^\sigma], \qquad (2.5)$$

where $g^{\mu\nu}$ is the metric tensor, $\epsilon^{\mu\nu\rho\sigma}$ is the Levi-Civita's antisymmetric tensor and s_l^σ is the spin four-vector of an incident electron. It can be seen that this tensor can be separated in symmetric and antisymmetric parts. This antisymmetric tensor is the only one to contain information about the incoming electron spin. The hadronic tensor can be defined from the hadronic current j^h_ν by the following relation:

$$W_{\mu\nu}(p,q) = \frac{1}{4\pi}\sum_{X,s'_X}[(2\pi)^4\delta^4(p+q-p_X) < p, s_n|j^h_\mu(0)|X, s'_X >< X, s'_X|j^h_\nu(0)|p, s_n >], \tag{2.6}$$

where the sum contains all hadronic states X of spin s'_X that are not measured. The proton is not a point-like particle, so an explicit expression for its tensor does not exist. The most general form of the hadronic tensor is derived using the requirements of the Lorentz invariance, translation and time reversal invariance, hermiticity and parity conservation. The hadronic tensor has to be defined as a function of all available Lorentz vectors which are present in the absorption process of a virtual photon by a polarized nucleon. These vectors are p_μ, q_μ and s^σ_n . The general form of this tensor is a linear combination of all the tensors built from these Lorentz vectors, from the metric tensor $g_{\mu\nu}$ and from Levi Civita $\epsilon_{\mu\nu\alpha\beta}$. The coefficients of this combination are also Lorentz invariants, i.e. functions of ν and Q^2. Moreover, all spins are summed up, and all momenta are integrated over except p, q and p_X.

$$W_{\mu\nu} = W_1(-g_{\mu\nu} + \frac{q_\mu q_\nu}{q^2}) + \frac{W_2}{M^2}(p_\mu - \frac{p\cdot qq_\mu}{q^2})(p_\nu - \frac{p\cdot qq_\nu}{q^2}) \tag{2.7}$$

$$+iMG_1\epsilon_{\mu\nu\lambda\sigma}q^\lambda s^\sigma_n + \frac{i}{M}G_2\epsilon_{\mu\nu\lambda\sigma}q^\lambda(p\cdot qs^\sigma_n - s\cdot qp^\sigma), \tag{2.8}$$

where the coefficients W_1, W_2, G_1 and G_2 are called the structure functions. They depend on ν and Q^2 and summarize everything that is not known about the nucleon structure. Like a leptonic tensor, the hadronic tensor can also be divided in a symmetric part and an antisymmetric part. The unpolarized structure functions W_1 and W_2 parameterize the spin-averaged part of the hadronic tensor, while G_1 and G_2 describe polarization effects. The contraction of both tensors allows one to compute the cross section by introducing the nucleon structure functions. Knowing that the contraction of a symmetric tensor with the antisymmetric tensor gives zero and that the information on the nucleon spin is contained in the antisymmetric part of the hadronic tensor, both the electron beam and the nucleon target need to be polarized in order to extract the information about the spin of the target. The contraction of the symmetric parts of $L^{\mu\nu}$ and $W_{\mu\nu}$ gives the spin independent cross section which in its most general form is written as:

$$\frac{d^2\sigma}{d\Omega dE'} = \frac{4\alpha^2 E'^2}{Q^4}\left[\cos^2\frac{\theta}{2}W_2 + 2\sin^2\frac{\theta}{2}W_1\right]. \tag{2.9}$$

The contraction of the antisymmetric parts and the difference of both cross sections where leptons and hadrons are polarized parallel ($\sigma^{\uparrow\uparrow}$) or anti-parallel ($\sigma^{\uparrow\downarrow}$), gives the spin dependent cross section:

$$\frac{d^2\Delta\sigma}{d\Omega dE'} = \frac{d^2\sigma^{\uparrow\downarrow}}{d\Omega dE'} - \frac{d^2\sigma^{\uparrow\uparrow}}{d\Omega dE'}, \tag{2.10}$$

$$\frac{d^2\Delta\sigma}{d\Omega dE'} = \frac{4\alpha^2}{Q^2}\frac{E'}{E}[MG_1(E + E'cos\theta) - Q^2G_2]. \tag{2.11}$$

Bjorken proposed in 1969, that in the deep inelastic limit defined by large ν and Q^2 but $\frac{Q^2}{\nu}$ finite, the structure functions would depend only on the ratio $\frac{Q^2}{\nu}$ or, equivalently on the variable x, defined as $\frac{Q^2}{2M\nu}$. In the Bjorken limit, the structure functions can be redefined as functions of x alone:

$$\begin{aligned} F_1(x) &= MW_1(\nu,Q^2), \\ F_2(x) &= \nu W_2(\nu,Q^2), \\ g_1(x) &= M^2\nu G_1(\nu,Q^2), \\ g_2(x) &= M\nu^2 G_2(\nu,Q^2). \end{aligned} \tag{2.12}$$

The hadronic tensor can be rewritten in terms of the kinematic variables x and Q^2:

$$W_{\mu\nu} = F_1(-g_{\mu\nu} + \frac{q_\mu q_\nu}{q^2}) + \frac{F_2}{(p\cdot q)}(p_\mu - \frac{(p\cdot q)q_\mu}{q^2})(p_\nu - \frac{(p\cdot q)q_\nu}{q^2}) \tag{2.13}$$

$$+g_1\frac{i}{p\cdot q}\epsilon_{\mu\nu\lambda\sigma}q^\lambda s_n^\sigma + g_2\frac{i}{(p\cdot q)^2}\epsilon_{\mu\nu\lambda\sigma}q^\lambda((p\cdot q)s_n^\sigma - (s\cdot q)p^\sigma) \tag{2.14}$$

and the spin independent and spin dependent deep inelastic cross sections:

$$\frac{d^2\sigma}{dxdQ^2} = \frac{4\pi\alpha^2}{Q^4x}[(1 - \frac{Q^2}{2MEx} - \frac{Q^2}{4E^2})F_2(x,Q^2) + \frac{Q^4}{4M^2E^2x}F_1(x,Q^2)], \tag{2.15}$$

$$\frac{d^2\Delta\sigma}{dxdQ^2} = \frac{4\pi\alpha^2}{MExQ^2}[(2 - \frac{Q^2}{2MEx} - \frac{Q^2}{2E^2})g_1(x,Q^2) - \frac{2Mx}{E}g_2(x,Q^2)]. \tag{2.16}$$

The relation between the kinematic variables in DIS is shown in Fig 2.3. The energy of the virtual photon is in the range $0 < \nu < E$. The maximum value of Q^2 is $2ME$, and corresponds to $x = 1$ (elastic scattering).

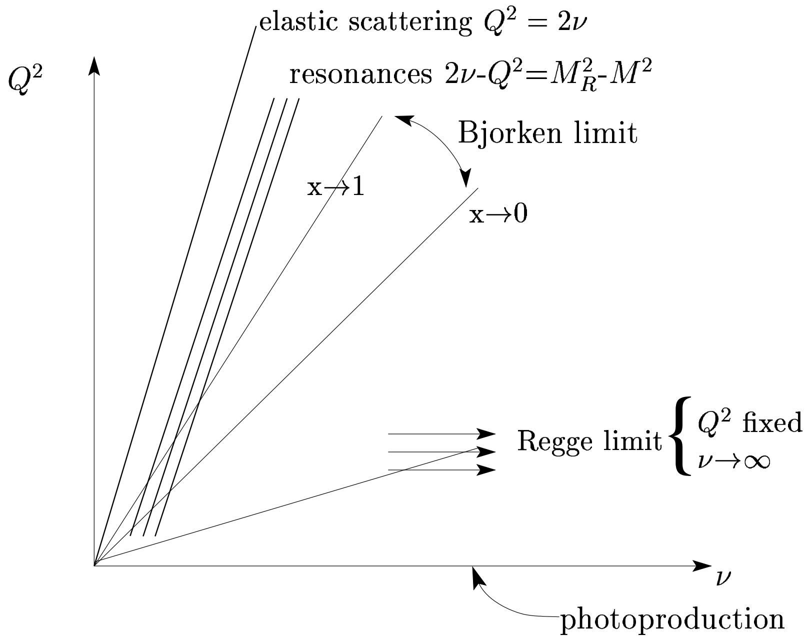

Figure 2.3: Kinematic domains in electron-nucleon scattering

2.2 Structure functions in QCD

2.2.1 Asymptotic Freedom

Within the Standard Model, the strong interactions are described by QCD, which is a gauge invariant, non-Abelian theory based on the internal color symmetry $SU(3)_c$. QCD describes the interaction of an octet of massless vector gluons and a triplet of massless quarks with spin $\frac{1}{2}$. Formally, the interaction involves the generalized field tensors [5]:

$$G^a_{\mu\nu} = \partial_\mu A^a_\nu - \partial_\nu A^a_\mu + g f_{abc} A^b_\mu A^c_\nu, \tag{2.17}$$

where A^a_μ is the gluon vector potential, $a = 1...8$ are the octet color labels, g is the strong interaction coupling constant, and f_{abc} are the structure constants for $SU(3)_c$. The term $f_{abc}A^b_\mu A^c_\nu$ is characteristic for a non-Abelian gauge theory, and results from the fact that the generators of the gauge transformations do not commute with each other:

$$[T_a, T_b] = i f_{abc} T_c. \tag{2.18}$$

It is generally believed that this fact is responsible for the unique properties of the strong interaction, in particular, asymptotic freedom and confinement. The interaction also involves quark spinor fields ψ_j, where $j = 1, 2, 3$ labels the quark color. There are two covariant derivatives, $(D_\mu)_{ij}$ acting on the quark fields, and D_μ^{bc} acting on gluon fields:

$$\begin{aligned} (D_\mu)_{ij} &= \delta_{ij}\partial_\mu - igL^a_{ij}A^a_\mu, \\ D^{bc}_\mu &= \delta_{bc}\partial_\mu + gf_{abc}A^a_\mu, \end{aligned} \tag{2.19}$$

where L_a are 3×3 matrices representing the eight generators T_a. The Lagrangian density for the strong interaction is given by:

$$\mathcal{L} = -\frac{1}{4} G^a_{\mu\nu} G^{a\mu\nu} + i\bar{\psi}_i \gamma_\mu (D^\mu)_{ij} \psi_j. \tag{2.20}$$

The last term in this equation is an implied sum of identical terms, one for each flavor. Using the Lagrangian above, Feynman Rules can be derived for diagrams involved in the interaction. It has been found that if the parameters of a theory such as g are treated as constant numbers, the integrals involved in certain Feynman diagrams diverge. A mechanism to remedy this situation is called a renormalization scheme, and is based on the idea of allowing parameters to depend on a parameter λ. In this process, new fields, such as $\psi \to Z_\psi(\lambda)\psi$, are introduced and the λ dependence is adjusted to cancel divergencies as $\lambda \to \infty$. Both ψ and A_μ are renormalized:

$$\begin{aligned} \psi_B &= Z_\psi^{1/2}(\lambda)\psi, \\ (A_B^a)_\mu &= Z_A^{1/2}(\lambda)A_\mu^a, \end{aligned} \tag{2.21}$$

where B stands for 'bare' quantities. The functions $Z(\lambda)$ are adjusted by choosing an arbitrary mass parameter μ and demanding a certain result for the complete propagator and complete vertex at point $p^2 = -\mu^2$. The mass parameter μ is not related to the mass of physical particles but is a point where the infinities are subtracted. This is called the renormalization point. For a massless theory like QCD the renormalization point is the only mass parameter of the theory. The truncated one-particle Green's function $\Gamma(p_i, g, \mu)$ is related to the corresponding bare Green's function:

$$\Gamma = Z\Gamma_B. \tag{2.22}$$

All bare quantities are independent of the renormalization scale, therefore:

$$\mu\frac{\partial \Gamma_B}{\partial \mu} = \mu\frac{\partial}{\partial \mu}(Z^{-1}\Gamma) = 0. \tag{2.23}$$

Green's functions in QCD have two labels (n_A, n_ψ) to specify the number of gluon fields n_A and the number n_ψ of the quark fields. Utilizing the appropriate QCD fields and equation 2.23 results in the Renormalization Group Equation (RGE) for QCD:

$$\left(\mu\frac{\partial}{\partial \mu} + \beta\frac{\partial}{\partial g} - n_A\gamma_A - n_\psi\gamma_\psi\right)\Gamma^{(n_A,n_\psi)}(p_i, g, \mu) = 0, \tag{2.24}$$

where $\gamma_A = \frac{\mu}{2}\frac{d}{d\mu}(\ln Z_A)$ and $\gamma_\psi = \frac{\mu}{2}\frac{d}{d\mu}(\ln Z_\psi)$. The RGE equation is an exact consequence of the theory, and generally is not satisfied by a calculation to a given order in perturbation theory. In order to calculate the functions $\beta, \gamma_A, \gamma_\psi$, the relevant self energy and vertex diagrams need to be evaluated. It is important to note that the lowest order calculation of $\beta, \gamma_A, \gamma_\psi$ is independent of the chosen renormalization scheme, however, the gauge still needs to be fixed. Working in the Landau gauge, and after some formidable calculations, the results are obtained:

$$\begin{aligned}
\gamma_\psi &= 0 + \mathcal{O}(g^4), \\
\gamma_A &= -\frac{g^2}{16\pi^2}\left[\frac{13}{6}C_2(G) - \frac{4}{3}T(R)\right] + \mathcal{O}(g^4), \\
\beta &= -\frac{g^3}{16\pi^2}\left[\frac{11}{3}C_2(G) - \frac{4}{3}T(R)\right] + \mathcal{O}(g^5),
\end{aligned} \tag{2.25}$$

where $C_2(G)$ is a constant that depends on the group: $\delta_{ab}C_2(G) = f_{acd}f_{bcd}$, and for $SU(3)$ it gives $C_2(SU(3)) = 3$. $T(R)$ is a constant that depends on the representation that the gluons belong to and the number n_f of quark flavors: $\delta_{ab}T(R) = n_f Tr(L^a L^b)$. For $SU(3)$ and the octet representation $T(SU(3)octet) = \frac{1}{2}n_f$. The final expressions for β and γ are:

$$\begin{aligned}
\beta(g) &= -\beta_0\frac{g^3}{16\pi^2} - \beta_1\frac{g^5}{(16\pi^2)^2} + \mathcal{O}(g^7), \\
\gamma(g) &= \gamma_1\frac{g^2}{16\pi^2} + \mathcal{O}(g^4), \\
\beta_0 &= 11 - \frac{2}{3}n_f, \\
\gamma_1 &= -(\frac{13}{2} - \frac{2}{3}n_f).
\end{aligned} \tag{2.26}$$

$\beta(g)$ is negative for $n_F < 17$, so that g decreases with the increasing energy scale, leading to the asymptotic freedom. An interesting fact to note is that β is negative due to the presence of gluons in QCD. The gluons 'anti-screen' the color charge, so that the coupling constant increases as the distance between quarks increases.

In order to understand the high momentum ($p'_j = \eta p_j, \eta \rightarrow \infty$) behavior of the theory, it is informative to look at the mass dimension of the truncated Green's functions in QCD. It is [5]:

$$[\Gamma^{(n_A,n_\psi)}] = [M]^{4-n_A-\frac{3}{2}n_\psi}. \tag{2.27}$$

This equation and the fact that the coupling constant g_μ is dimensionless lead to the modified renormalization group equation:

$$\left((\eta\frac{\partial}{\partial\eta} - \beta\frac{\partial}{\partial g_\mu} + (4 - n_A - \frac{3}{2}n_\psi) + n_A\gamma_A + n_\psi\gamma_\psi\right)\Gamma^{(n_A,n_\psi)}(\eta p_j; g, \mu) = 0. \tag{2.28}$$

A solution to this equation is found by introducing an effective coupling constant $\bar{g}(g,\eta)$:

$$\ln\eta = \int_g^{\bar{g}(g,\eta)} \frac{dx}{\beta(x)}. \tag{2.29}$$

Using the leading order expressions for γ_A, γ_ψ, a solution to RGE is obtained:

$$\Gamma^{(n_A,n_\psi)}(\eta p_j; g, \mu) = \eta^{4-n_A-\frac{3}{2}n_\psi}\left[\frac{\bar{g}(g,\eta)}{g^2}\right]^{n_A\gamma_1/2\beta_0} \times \Gamma^{(n_A,n_\psi)}(p_j; \bar{g}(g,\eta), \mu). \tag{2.30}$$

This result is important as it tells us that $\Gamma^{(n_A,n_\psi)}$ at momentum ηp_j is related to $\Gamma^{(n_A,n_\psi)}$ at lower momentum p_j, but evaluated with the effective coupling constant $\bar{g}(g,\eta)$. In the high momentum limit, this result essentially gives an expression for asymptotic freedom. Taking an arbitrary p_j and using the fact that $\bar{g}^2 \to 0$ as $\eta \to \infty$ results in:

$$\Gamma(\eta p_j; g, \mu) \overset{\eta\to\infty}{\to} \eta^{4-n_A-\frac{3}{2}n_\psi} \left[\frac{\bar{g}(g,\eta)}{g^2}\right]^{n_A\gamma_1/2\beta_0} \times \Gamma_{Free}(p_j; \bar{g}(g,\eta)), \tag{2.31}$$

where $Free$ means evaluated in a free field theory. The effective coupling constant is evaluated by substituting the lowest order result for β into equation 2.29:

$$\bar{g}^2(g,\eta) = \frac{g^2}{1 + \frac{g^2\beta_0}{8\pi^2}\ln\eta}. \tag{2.32}$$

This result predicts the logarithmic decrease of the coupling constant at large momentum scales or short distances. The scale of the logarithmic momentum dependence is unknown, and has to be determined. A certain combination of μ and g defines the behavior of the coupling constant:

$$\begin{aligned} \bar{g} &= \frac{g^2}{1 + \frac{g^2\beta_0}{8\pi^2} ln(\frac{Q^2}{\mu^2})} \qquad (2.33) \\ &= \frac{16\pi^2}{\beta_0}\left[ln(\frac{Q^2}{\mu^2}) + ln(e^{16\pi^2/g^2\beta_0})\right]^{-1} \\ &= \frac{16\pi^2}{\beta_0 \ln(\frac{Q^2}{\Lambda^2_{QCD}})}, \end{aligned}$$

where $\Lambda^2_{QCD} = \mu^2 e^{-16\pi^2/\beta_0 g}$ is the only parameter in massless QCD that has to be measured experimentally. It is found by fitting the calculation of the cross section of a given process to the experimental value [6]. After that, other physical quantities need to be calculated in terms of this scale parameter.

In analogy with the fine structure constant in QED, a strong coupling constant is defined

$$\alpha_\mu = \frac{\bar{g}^2(\mu)}{4\pi}. \tag{2.34}$$

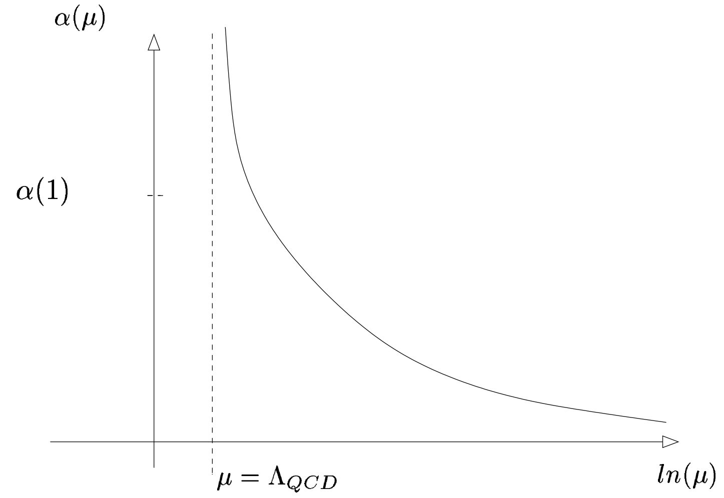

Figure 2.4: Energy dependence of the QCD coupling constant

As shown in Figure 2.4, the value of α_μ goes to infinity at a mass scale of Λ_{QCD}. At a sufficiently large Q^2, quarks become asymptotically free, and their interactions can be neglected. Λ_{QCD} defines a region where the partons in a nucleon can be viewed as a collection of non-interacting particles. This treatment of a nucleon can be described by the Quark-Parton Model.

2.2.2 Structure functions in the Quark-Parton Model

The time scale for the virtual photon to interact with the target nucleon is $x_0 \sim (\frac{1}{Q^2})^{\frac{1}{2}}$ and in the Bjorken limit ($Q^2 \rightarrow \infty, x_0 \rightarrow \infty$) it is much shorter than the time scale which characterizes the strong interactions. Hence, the partons 'seen' by a photon with large Q^2 appear to be quasi-free, and this allows us to use the impulse approximation. In the impulse approximation, DIS is described by the sum of the incoherent elastic scatterings of the virtual photon off the quarks. The struck parton has a large momentum relative to the one of the non-interacting partons, and can be regarded as asymptotically free. This parton and the remnant target partons 'fragment' into hadrons which can be experimentally detected. The time scale of a hadronisation process is longer than that of the collision process, and can be neglected in determining the scattering cross-section. A deep inelastic scattering process as seen in the parton model is shown in Figure 2.5. In the frame in which the nucleon momentum is very large (the Breit frame) the parton mass and any momentum transverse to the nucleon direction can be neglected. Therefore, the four-momentum of the parton i is $p_i = xp$, where p is the nucleon four-momentum and x is the fraction of this momentum carried by the parton.

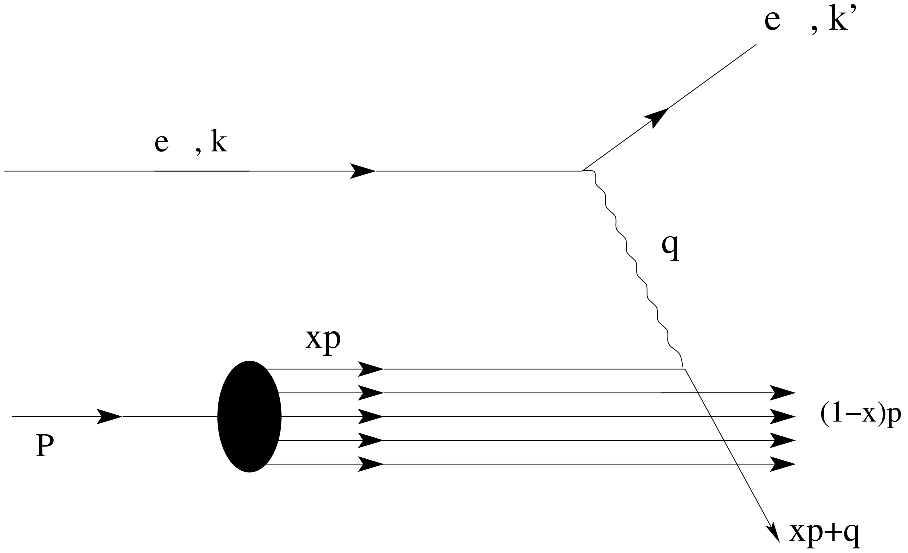

Figure 2.5: DIS in the parton model

In the impulse approximation, the proton matrix element in the hadronic tensor $W_{\mu\nu}$ can be replaced by a sum of quark matrix elements, weighted with the parton distribution functions.

$$W^{\mu\nu} = i \int d^4x e^{iq\cdot x} \int_0^1 d\xi \sum_f f_f(\xi) \frac{1}{\xi} < q_f(p)|J^\mu(x)J^\nu(0)|q_f(p) > |_{p=\xi P}, \tag{2.35}$$

where p is a momentum of a quark $= \xi P$, $\frac{1}{\xi}$ in front of the matrix element gives the proper normalization of the proton state in terms of the quark states, and $f_f(\xi)$ is a parton distribution function interpreted as a probability of finding a quark of type f with fraction ξ of the proton momentum. The matrix element of $W^{\mu\nu}$ can be evaluated explicitly using the Feynman Rules for the noninteracting fermions. The two leading diagrams for this process are shown in Figure 2.6. The matrix element for the first diagram can be evaluated as:

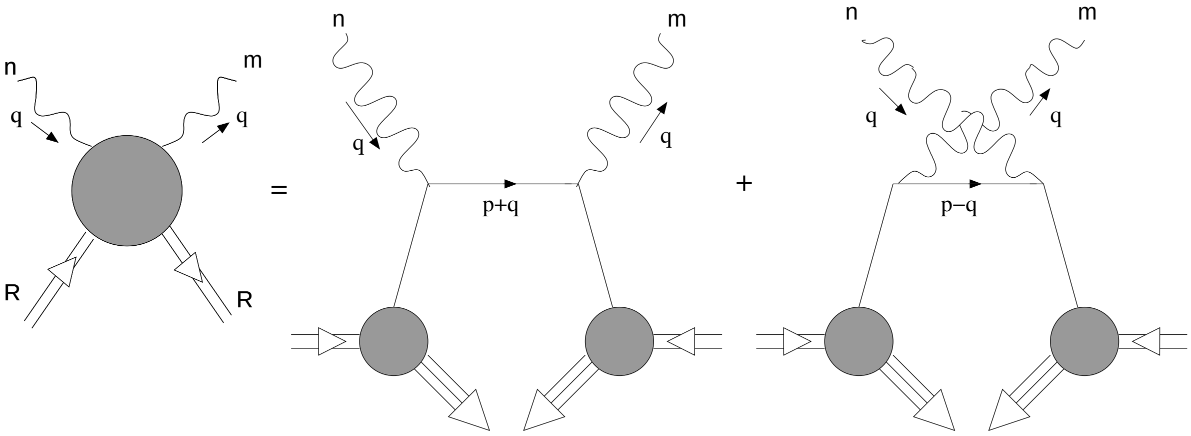

Figure 2.6: Evaluation of $W_{\mu\nu}$ in the parton model

$$< q_f(p)|J_\mu(x)J_\nu(0)|q_f(p) >= \tag{2.36}$$

$$iQ_f\gamma^\mu\bar{u}(p)\frac{i(p+q)}{(p+q)^2+i\varepsilon}iQ_f\gamma^\nu u(p) \tag{2.37}$$

$$= Q_f^2 tr[p\gamma^\mu(p+q)\gamma^\nu]\delta((p+q)^2) \tag{2.38}$$

$$= 4Q_f^2[p_\mu(p+q)_\nu + p_\nu(p+q)_\mu - g^{\mu\nu}(p\cdot q)]\delta((p+q)^2) \tag{2.39}$$

$$= 4Q_f^2[p_\mu(p+q)_\nu + p_\nu(p+q)_\mu - g^{\mu\nu}(p\cdot q)]\frac{\xi}{Q^2}\delta(\xi - \frac{Q^2}{2P\cdot q}). \tag{2.40}$$

The second diagram gives a similar contribution after the interchange of q, μ with $(-q), \nu$, however, the contribution vanishes in the physical region relevant for deep inelastic scattering. Therefore, the hadronic tensor is

$$\begin{aligned} W_{\mu\nu} &= \int_0^1 d\xi \sum_f f_f(\xi)\frac{1}{\xi}\frac{\xi}{Q^2}4Q_f^2[p_\mu(p+q)_\nu + p_\nu(p+q)_\mu - g^{\mu\nu}(p\cdot q)]\delta(\xi - \frac{Q^2}{2P\cdot q}) \\ &= \int_0^1 d\xi \sum_f f_f(\xi)\frac{4Q_f^2}{Q^2}(p\cdot q)[-g_{\mu\nu} + \frac{2p_\mu p_\nu}{p\cdot q} + \frac{p_\mu p_\nu + p_\nu p_\mu}{p\cdot q}]\delta(\xi - \frac{Q^2}{2P\cdot q}) \end{aligned} \tag{2.41}$$

By adding and subtracting terms proportional to $q^\mu q^\nu$ it can be seen that this expression is of the form of the general hadronic tensor

$$\begin{aligned} W_{\mu\nu} &= (-g^{\mu\nu} + \frac{q^\mu q^0}{q^2})W_1 + \frac{1}{M^2}(p^\mu - q^\mu\frac{p\cdot q}{q^2})(p^\nu - q^\nu\frac{p\cdot q}{q^2})W_2, \\ & W_1(\nu, Q^2) \to F_1(\xi), \\ & \frac{\nu W_2}{2M}(\nu, Q^2) \to F_2(\xi). \end{aligned} \tag{2.42}$$

Matching the corresponding terms gives:

$$\begin{aligned} F_1(\xi) &= \sum_f \int_0^1 \frac{1}{2}d\xi f_f(\xi)Q_f^2\delta(\xi - \frac{Q^2}{2p\cdot q}) = \frac{1}{2}\sum_f Q_f^2 f_f(\xi), \\ F_2(\xi) &= \sum_f \int_0^1 d\xi f_f(\xi)\xi Q_f^2\delta(\xi - \frac{Q^2}{2p\cdot q}) = \sum_f Q_f^2 f_f(\xi)\xi. \end{aligned} \tag{2.43}$$

$F_1(\xi)$ at a given ξ can be interpreted as the likelihood of finding a quark with longitudinal momentum fraction ξ, summed over all quark flavors weighted with the corresponding quark charges squared. $F_2(\xi)$ corresponds to the total momentum fraction carried by all the quarks and antiquarks in the nucleon, weighted by the squares of the quark charges. Expressions for F_1 and F_2 can be written explicitly for a particular nucleon. In the case of a proton:

$$\begin{aligned} F_1(\xi) &= \frac{1}{2}[\frac{4}{9}(u(\xi)+\bar{u}(\xi))+\frac{1}{9}(d(\xi)+\bar{d}(\xi)+s(\xi)+\bar{s}(\xi)], \\ F_2(\xi) &= \xi[\frac{4}{9}(u(\xi)+\bar{u}(\xi))+\frac{1}{9}(d(\xi)+\bar{d}(\xi)+s(\xi)+\bar{s}(\xi))]. \end{aligned} \tag{2.44}$$

In the equations above, the assumption was used that the proton is made out of two up and one down valence quarks, and more massive flavors (c,b,t) were neglected.

In analogy with the unpolarized structure functions, the spin dependent structure functions are interpreted in the parton model. They were defined in the Bjorken limit as

$$\begin{aligned} g_1(x,Q^2) &= M^2\nu G_1(\nu,Q^2), \\ g_2(x,Q^2) &= M\nu^2 G_2(\nu,Q^2). \end{aligned} \tag{2.45}$$

In order to interpret these in the parton model, the polarization states of the virtual photon and the proton need to be considered. Their spins can be aligned or anti-aligned, giving rise to two polarized cross sections $\sigma_{\frac{3}{2}}$ and $\sigma_{\frac{1}{2}}$ respectively:

$$\sigma_{\frac{3}{2}} \propto W_1 - M\nu G_1 - q^2 G_2 \propto F_1(\xi,Q^2) - g_1(\xi,Q^2) = \sum_i e_i^2 q_i^{\downarrow}(\xi,Q^2),$$

$$\sigma_{\frac{1}{2}} \propto W_1 + M\nu G_1 + q^2 G_2 \propto F_1(\xi, Q^2) + g_1(\xi, Q^2) \;=\; \sum_i e_i^2 q_i^{\uparrow}(\xi, Q^2). \quad (2.46)$$

The function g_2 is dependent on the transverse momentum of the constituent quarks, since quarks with opposite spins and longitudinal momentum enter the formula with the opposite sign and cancel out. Since initially it was assumed that quarks have zero transverse momentum, g_2 should be zero. This approximation holds in the scaling limit, but a nonzero value can be obtained by allowing the quarks to have intrinsic fermi motion inside the nucleon. Here, g_2 is neglected and g_1 is rewritten as

$$g_1(\xi, Q^2) = \frac{1}{2} \sum_i e_i^2 [q_i^{\uparrow}(\xi, Q^2) - q_i^{\downarrow}(\xi, Q^2)]. \quad (2.47)$$

The functions $q_i^{\uparrow}(\xi, Q^2)$, $q_i^{\downarrow}(\xi, Q^2)$) are the quark distribution functions representing the probability of finding a quark of flavor i with the spin parallel(anti-parallel) to the nucleon spin.

2.2.3 Q^2-evolution of the distribution functions

There are several sources of Q^2-evolution of the distribution functions. Different kinematic regions are affected more by some of them than by the others. In the region of high Q^2, there are two main factors that cause this dependence: perturbative QCD corrections to the cross section for point-like quarks, and the dependence on the resolving power of the lepton probe [7]. The correction terms due to both effects are logarithmic, depending on $\ln(Q^2)$. The pQCD corrections are caused by the quarks radiating extra gluons during the reaction processes, similar to the QED radiative corrections. The coupling constant that governs pQCD corrections is also Q^2 dependent, and becomes so large in the low Q^2 region that the perturbation theory can no longer be applied. The second source of Q^2-evolution is the dependence of resolution on the energy of the exchanged virtual photon. This means that probing the nucleon with the photons of various energy results in different 'pictures' of the nucleon, in particular, the probability of finding a quark of flavor i and momentum fraction ξ varies with Q^2. The distance down to which the nucleon is probed is called the 'resolution' of the virtual photon, and is roughly given by the uncertainty principle:

$$\Delta x = \frac{0.2}{Q(GeV)}. \tag{2.48}$$

For values of $Q^2 \sim 0.5\ GeV^2$, the distance resolved is compatible with the nucleon size, so that scattering occurs on the nucleon as a whole. For values of $Q^2 \sim$ few GeV^2, the internal structure of the nucleon is resolved, and the virtual photon will scatter off the valence quarks. At even higher values of Q^2 more structure is resolved, and the gluon and sea quark interactions start affecting the scattering cross section. This phenomenon is shown in Figure 2.7.

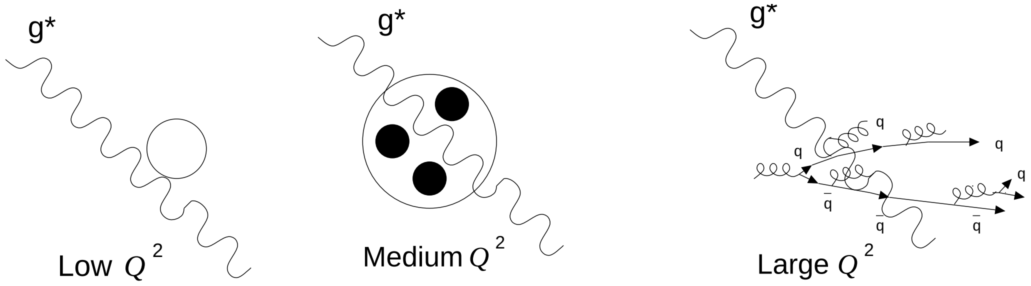

Figure 2.7: Resolution of the virtual photon

The gluons participate in the following transitions:

$$\begin{aligned} q &\rightarrow q+g, \\ g &\rightarrow q+\bar{q}, \\ \bar{q} &\rightarrow \bar{q}+g, \\ g &\rightarrow g+g. \end{aligned} \tag{2.49}$$

These interactions effectively reduce the observed momentum of the valence quarks because the total nucleon momentum is now shared between many partons. This results in decreasing valence quark distribution functions q_i as Q^2 increases, and a corresponding increase in the sea $q-\bar{q}$ pairs. What at low Q^2 looks like a valence quark of momentum fraction ξ, at high Q^2 looks like a combination of a valence quark, a sea of quark-antiquark pairs, and additional gluons. Each of these partons carries a momentum fraction ξ' smaller than the momentum of the original quark ξ. The result of this process is that at high Q^2, there is an increase of the quark distribution functions at low ξ and a decrease at higher ξ. The evolution of the distribution functions can be formally described by the Altarelli-Parisi equations, which are discussed in Appendix C. The resulting equations show a logarithmic Q^2 dependence of the quark distribution functions due to the gluon emission:

$$\begin{aligned} \frac{dq_i(x,Q^2)}{d\ln Q^2} &= \frac{\alpha_s(Q^2)}{2\pi}\int_z^1 \frac{dy}{y}\left[P_{qq}(\frac{x}{y})q_i(y,Q^2)+P_{qg}(\frac{x}{y})g(y,Q^2)\right], \\ \frac{dg(x,Q^2)}{d\ln Q^2} &= \frac{\alpha_s(Q^2)}{2\pi}\int_z^1 \frac{dy}{y}\left[\sum_j P_{gq}(\frac{x}{y})q_j(y,Q^2)+P_{gg}(\frac{x}{y})g(y,Q^2)\right]. \end{aligned} \tag{2.50}$$

A splitting function $P_{qq}(\frac{x}{y})$ may be interpreted as the probability for a quark with momentum fraction y to radiate a gluon, leaving the quark with momentum fraction x. Once the parton distributions are known at some scale Q_0^2, they can be calculated at any other scale where perturbative QCD applies. There are additional sources of Q^2-dependence which become important in the low Q^2 region. These additional corrections are often called the 'higher twist effects', and arise from the fact that the quarks are bound inside of a nucleon and possess a momentum component perpendicular to the virtual photon momentum. These corrections produce a term proportional to $1/Q^2$ [7], and can be calculated using a method called Operator Product Expansion.

2.3 Structure functions in perturbative QCD

2.3.1 Operator Product Expansion

The behavior of the deep inelastic structure functions can be derived from the perturbative QCD. In principle, the theory cannot be applied to the hadronic states since they are fundamentally non-perturbative entities. However, information on the Q^2 dependence of the hadronic tensor can be obtained. This information is derived by using the renormalization group equations. The result contains non-calculable constants which have to be experimentally measured. A method applied in the QCD analysis of the deep inelastic scattering is called the Operator Product Expansion (OPE), and is discussed in Appendix B. This method succeeds in expressing the moments of structure functions in terms of hadronic matrix elements of the various operators, which depend upon the reaction and are generally not calculable, and the calculable coefficient functions, whose Q^2 dependence is specified by the renormalization group equations:

$$\begin{aligned}
\int_0^1 d\xi\xi^{n-2}F_L(\xi,Q^2) &= \sum_i A_{L,n}^{(i)}\tilde{C}_{L,n}^{(i)}(Q^2), \\
\int_0^1 d\xi\xi^{n-2}F_2(\xi,Q^2) &= \sum_i A_{2,n}^{(i)}\tilde{C}_{2,n}^{(i)}(Q^2). \qquad (2.51)
\end{aligned}$$

The structure functions F_2 and F_L are related to the previously discussed functions W_1 and W_2

$$\begin{aligned}
F_L(\xi,Q^2) &= -W_1(\nu,Q^2)+(1+\frac{\nu^2}{Q^2})W_2(\nu,Q^2), \\
F_2(\xi,Q^2) &= \frac{\nu W_2(\nu,Q^2)}{2M}. \qquad (2.52)
\end{aligned}$$

The so-called longitudinal structure function F_L corresponds to the total cross section for the longitudinal photon scattering off protons. Equations 2.52 are called the moment sum rules for the structure functions. They do not directly predict the values of the structure function, but their evolution with Q^2. If a structure function is measured at a given Q_0^2, its value can be predicted for other values of Q^2. This is possible because the coefficient functions $\tilde{C}_{L,n}^{(i)}$ and $\tilde{C}_{2,n}^{(i)}$ are of short distance nature and can be calculated in perturbative QCD. The constants $A_{L,n}^{(i)}$ and $A_{2,n}^{(i)}$ are related to the hadronic matrix elements and are not calculable in perturbative QCD. They need to be measured experimentally. In the free field approximation, the operator product expansion reproduces the predictions of the parton model, but at finite Q^2, the renormalization group equations produce a logarithmic Q^2 dependence which breaks the Bjorken scaling. To summarize this argument we can define the nth moment of the structure function $F(x, Q^2)$ [8]:

$$M^n(Q^2) = \int_0^1 x^{n-2} F(x, Q^2) dx, \tag{2.53}$$

where the integration includes the elastic contribution. According to the OPE discussed in this section, the moment can be expanded in powers of $1/Q^2$:

$$M_n(Q^2) = \sum_{\tau=2,even}^{\infty} E_{n\tau}(Q^2/\mu^2) O_{n\tau}(\mu) (\frac{1}{Q^2})^{1/2(\tau-2)}, \tag{2.54}$$

where $O_{n\tau}(\mu)$ are the nucleon matrix elements of operators of twist τ and spin n, composed of quark and gluon fields. The dimensionless coefficient function $E_{n\tau}(Q^2/\mu^2)$ can be expressed perturbatively as a power series in the strong coupling constant $\alpha_s(\mu^2)$:

$$E_{n\tau}(Q^2/\mu^2) = \sum_{i=0}^{\infty} \alpha_s^i(\mu^2) e_{n\tau}^i (Q^2/\mu^2). \tag{2.55}$$

The renormalization scale μ^2 dependence cancels in the product of $E_{n\tau}$ and $O_{n\tau}$, but when they are treated separately, it is chosen at the hadron mass scale. In case of the leading twist ($\tau = 2$), there is a flavor non-singlet quark operator $O_{\tau=2}^{NS}$ with corresponding matrix element a_n^{NS} and coefficients E_{n2}^{NS}, and with a singlet quark $O_{\tau=2}^{S}$ and gluon $O_{\tau=2}^{G}$ operators. The singlet operators mix under renormalization group equations, with the corresponding matrix elements $a_n^{\pm}$ and coefficients $E_{n2}^{\pm}$ [9]. The terms beyond the first in equation 2.54 are called the higher twist corrections, and contain two types of corrections. One type of correction is due to the fact that when the target mass is non-vanishing, operators with spin other than n can contribute to the expansion, which contains the target mass terms. This correction is of kinematic origin, as opposed to the other type of correction terms which physically represent interactions between the struck quark and remnants of the target. An additional source of Q^2 dependence comes from the QCD radiative corrections, such as gluon radiation. This dependence is implicitly contained in the expansion of coefficient functions.

The success of the operator product expansion lies in the fact that it provides a clear separation of the short distance calculable effects from the long distance effects. Also, the results of OPE in the leading order can be shown to be completely equivalent to the Altarelli-Parisi equation 2.50. Applying the renormalization group equation to the expansion, or integrating the Altarelli-Parisi equation results in the same prediction for the non-singlet case:

$$M^N(Q^2) = \left[\frac{\ln(\frac{Q^2}{\Lambda^2})}{\ln(\frac{Q_0^2}{\Lambda^2})}\right]^{-d^N} M^N(Q_0^2). \tag{2.56}$$

In the equation above, Q_0^2 is a large value of Q^2 from which the evolution of the moments is predicted, and constant d^N is called the anomalous dimension. This equation demonstrates how a measurement of a structure function at a given value of Q^2 can be used to predict its value at a different Q^2. Translated into distribution functions, equation 2.56 predicts that the fraction of momentum carried by valence quarks decreases with increasing Q^2, which implies that the fraction of momentum carried by sea quarks and gluons must increase with Q^2. The average value of x decreases with Q^2, which implies that the distribution functions grow with Q^2 at small x.

2.4 $g_1(x, Q^2)$ and its first moment

2.4.1 Sum Rules

Using the theoretical foundation from previous sections, the spin structure function g_1 can be discussed in detail. In particular, g_1^p of the proton will be the focus of this thesis. In the Quark Parton Model, g_1 is defined as

$$\begin{aligned} g_1(x, Q^2) &= \frac{1}{2}\sum_i e_i^2 \left[q_i^{\uparrow}(x, Q^2) - q_i^{\downarrow}(x, Q^2)\right] \\ &= \frac{1}{2}\sum_i e_i^2 \left[\Delta q_i(x) + \Delta \bar{q}_i(x)\right]. \end{aligned} \tag{2.57}$$

g_1 can be interpreted as the weighted sum of the quark momentum distributions times their helicity. The individual quark contribution Δq is related to the matrix element of the axial current $\bar{\Psi}\gamma_\mu\gamma_5\Psi$, and is called the axial charge. Formally g_1 measures the axial charge, which is different from helicity due to the relativistic effects. The first moment of g_1 is generally given by the Operator Product Expansion, in terms of hadronic matrix elements of certain operators multiplied by calculable coefficient functions. The result simplifies in the case of free quark fields

$$\Gamma_1^p = \int_0^1 dx g_1^p(x) = \frac{1}{2}\int_0^1 \sum_i e_i^2 \Delta q_i(x) dx. \tag{2.58}$$

It is convenient to express the first moment in terms of the $SU(3)_f$ nucleon axial charges a_j, which are defined as hadronic matrix elements of the octet of quark $SU(3)_f$ axial-vector currents $J_{5\mu}^j$ and the flavor singlet axial current $J_{5\mu}^0$ taken between the proton states

$$\begin{aligned} Ma_j S_\mu &= \langle P,S|J^j_{5\mu}|P,S\rangle; \quad J^j_{5\mu} = \bar{\Psi}\gamma_\mu\gamma_5\frac{\lambda_j}{2}\Psi, \\ Ma_0 S_\mu &= \langle P,S|J^0_{5\mu}|P,S\rangle; \quad J^0_{5\mu} = \bar{\Psi}\gamma_\mu\gamma_5\Psi. \end{aligned} \tag{2.59}$$

Here, λ_j are the Gell-Mann matrices, and $S^\mu(\lambda)$ is a proton's spin vector corresponding to a helicity state λ. On the other hand, in the parton model, the forward protonic matrix element of the axial vector current of a quark field of certain flavor can be expressed in terms of the spin dependent parton distributions

$$\langle P,S|\bar{\Psi}_f(0)\gamma_\mu\gamma_5\Psi_f(0)|P,S\rangle = 2MS_\mu\int_0^1 dx\,[\Delta q_f(x)+\Delta\bar{q}_f(x)]\,. \tag{2.60}$$

Using the above equations, we can rewrite the nucleon axial charges in terms of the polarized quark distributions. Neglecting the heavier quark flavors gives

$$\begin{aligned} a_0 &= \int_0^1 dx\left[\Delta u(x)+\Delta\bar{u}(x)+\Delta d(x)+\Delta\bar{d}(x)+\Delta s(x)+\Delta\bar{s}(x)\right], \\ a_3 &= \int_0^1 dx\left[\Delta u(x)+\Delta\bar{u}(x)-\Delta d(x)-\Delta\bar{d}(x)\right], \\ a_8 &= \int_0^1 dx\left[\Delta u(x)+\Delta\bar{u}(x)+\Delta d(x)+\Delta\bar{d}(x)-2\Delta s(x)-2\Delta\bar{s}(x)\right]. \end{aligned} \tag{2.61}$$

The two flavor non-singlet components a_3 and a_8 and the singlet a_0 are independent of Q^2 in the Leading Order (one loop corrections included) . The non-singlet combinations remain independent of Q^2 and conserved to any order in α_s, while the singlet component a_0 becomes Q^2 dependent beyond the leading order. Finally, in the Leading Order QCD, using the SU(3) flavor decomposition, Γ_1^p is expressed as

$$\Gamma_1^p = \int_0^1 dx g_1^p(x) = \frac{1}{12}\left[a_3 + \frac{1}{3}a_8 + \frac{4}{3}a_0\right]. \tag{2.62}$$

Several sum rules predict the value of this integral, in particular, the Ellis-Jaffe sum rule. The sum rule uses the known measurements of the axial nucleon charges from neutron and hyperon-beta decays, and relates them to the integrals over the structure functions. The Ellis-Jaffe sum rule assumes that the strange and sea quarks are not polarized ($\Delta s = 0, \Delta\bar{u} = \Delta\bar{d} = 0$), which results in $a_0 = a_8$. The value of a_3 relies on the fundamental SU(2) isospin symmetry, and is known from the ratio of axial-vector to vector coupling constants in neutron decay $a_3 = -\frac{g_A}{g_V} = 1.2670 \pm 0.0035$. Using the $SU(3)$ flavor symmetry allows to express $\frac{g_A}{g_V}$ in terms of a_3 and a_8, giving $a_8 = 0.58 \pm 0.03$. Consequently, the Ellis-Jaffe sum rule gives the following numeric prediction for the value of the proton and neutron integrals:

$$\begin{aligned} \Gamma_1^p &= \int_0^1 dx g_1^p(x) = \frac{3}{36}a_3 + \frac{1}{36}a_8 + \frac{4}{36}a_0 = 0.186 \pm 0.004, \\ \Gamma_1^n &= \int_0^1 dx g_1^n(x) = -\frac{3}{36}a_3 + \frac{1}{36}a_8 + \frac{4}{36}a_0 = -0.025 \pm 0.004. \end{aligned} \tag{2.63}$$

The assumptions that were made in the Ellis-Jaffe sum rule are SU(3) flavor symmetry and the approximation of massless quarks, which are both reasonable but not very precise [3]. The Bjorken sum rule does not make any of these assumptions, and is based only on current algebra and the isospin symmetry between the proton and neutron quark distribution functions. For that reason, this sum rule is considered to be a fundamental sum rule, and a crucial test of QCD. The rule relates the difference between the integrals Γ_1^p and Γ_1^n to the ratio $\frac{g_A}{g_V}$.

$$\Gamma_1^p - \Gamma_1^n = \frac{1}{6}\left[\Delta u - \Delta d\right] = \frac{1}{6}\frac{g_A}{g_V}. \tag{2.64}$$

Both the Bjorken and the Ellis-Jaffe sum rules are valid in the scaling limit, and need to be corrected for the QCD radiative corrections. Experiments dedicated to measurements of g_1 have been carried out for more than 3 decades. The first data were obtained at SLAC in 1978. Since then, more measurements have been taken at various accelerators around the world: SLAC, CERN, Fermilab, DESY, and more recently, at Jefferson Lab. The Bjorken sum rule has been confirmed by every experiment conducted over the years, however, the Ellis-Jaffe sum rule has been shown to be strongly violated. The first surprising results were obtained by the European Muon Collaboration (EMC) in 1988. The unexpectedly low value of Γ_1 obtained by the EMC was termed the 'spin crisis' and raised many questions about the parton model. This low value was confirmed by the later experiments. Here, Γ_1^p is quoted for the mean value of $Q^2 = 10.7$ GeV^2 for the EMC experiment.

$$\Gamma_1^p\left[\langle Q^2\rangle\right] = 0.128 \pm 0.013 \pm 0.019. \tag{2.65}$$

This result is considerably smaller than the value predicted by the Ellis-Jaffe sum rule, and has interesting implications for the composition of the proton spin. From the value of Γ_1^p, the matrix element of the flavor singlet axial current can be obtained:

$$a_0 = \frac{3}{4}\left[12\Gamma_1^p - a_3 - \frac{1}{3}a_8\right] = 0.06 \pm 0.12 \pm 0.17. \tag{2.66}$$

In the framework of the parton model, a_0 is expected to be close to 1, as follows from the argument below. From the earlier discussion:

$$a_0 = \Delta\Sigma = \int_0^1 dx \Delta\Sigma(x),$$

$$\Delta\Sigma = \Delta u(x) + \Delta\bar{u}(x) + \Delta d(x) + \Delta\bar{d}(x) + \Delta s(x) + \Delta\bar{s}(x).$$

The distribution functions $\Delta q(x)$ represent the difference between the number of quarks with momentum fraction x with spin component $\pm\frac{1}{2}$ along the direction of motion of the proton, so the total contribution coming from a given flavor quark is

$$S = \frac{1}{2}\int_0^1 dx \Delta q(x) = \frac{1}{2}a_0. \tag{2.67}$$

In the parton model, all quarks move parallel to the proton, so that each quark has momentum that is a fraction x of the proton momentum ($p = xP$), and there is no orbital angular momentum contribution. Assuming that the gluons are not polarized, $S^{quarks} = \frac{1}{2}$ and a_0=1. Relativistic corrections bring these numbers down, but there is still a large discrepancy between the experiment and the parton model predictions. This discrepancy led to the questions of the validity of the experimental results, as well as the validity of the naive parton model.

The question of the validity of the experimental results reduces to the uncertainty of the low x extrapolation. Obtaining the experimental value of Γ_1 requires integrating the measured structure function $g_1(x, Q^2)$ over the entire x range from $x = 0$ to $x = 1$ for a given fixed value of Q^2. Generally, there are experimental acceptance limitations which prevent a single experiment from measuring the full range of x at a fixed Q^2, so that extrapolations are necessary in order to include the unmeasured regions in x. The large x region is considered to be fairly well understood; since $g_1(x)$ measures the difference of quark distributions, it must approach zero as x approaches 1. This idea is supported by the observed behavior of the unpolarized structure functions. There is no clear dependence expected in the low x region, and extrapolation at low x is more problematic. The traditional approach to this problem has been to use the Regge parametrization. The Regge parametrization predicts $g_1(x) \sim x^{-\alpha_{a_1}}$, where α_{a_1} is the intercept of Regge trajectory of the a_1 meson. In this approach, $g_1(x)$ is nearly constant at $x = 0$. More recently, the Next-to-Leading-Order (NLO) QCD calculations showed that the Regge parametrization is likely to underestimate the low x contribution. However, the extrapolation methods used by the EMC are generally accepted, and are not thought to be the cause of the unexpected result. The next question that arises, is how much we can trust the theoretical predictions based on the naive parton model, which treats the partons as non-interacting free fields.

2.4.2 Q^2 evolution of $g_1(x, Q^2)$ and its first moment

In the naive parton model, the quark distribution functions depend on the momentum fraction x the quarks carry. In QCD, there are two sources of Q^2 dependence. The QCD radiative corrections take into account the effects of hard gluons in the hard process, and the higher twist corrections take into account interactions between the active quark and the rest of the target [10]. The evolution of g_1 follows the same ideas that were discussed in the case of the unpolarized structure functions. In the perturbative QCD the Q^2-evolution of g_1 is given by [11]:

$$g_1(x, Q^2) = \frac{1}{2}\sum_i e_i^2 C_q(x, \alpha_s) \otimes \Delta q_i(x, Q^2) + \frac{1}{N_f} C_g(x, \alpha_s) \otimes \Delta g(x, Q^2). \tag{2.68}$$

$N_f(= 3)$ is the number of active quark flavors, $C_q(x, \alpha_s)$ and $C_g(x, \alpha_s)$ are the coefficient functions directly related to the polarized photon-quark and photon-gluon hard scattering sections, respectively. The convolution function used in the equation is defined as:

$$C(x, \alpha_s) \otimes q(x, Q^2) = \int_x^1 \frac{dy}{y} C(\frac{x}{y}, \alpha_s) q(x, Q^2).$$

Equation 2.68 demonstrates explicit dependence of the nucleon spin structure function on the gluon spin distribution $\Delta g(x, Q^2)$. In the naive parton model, $C_q = \delta(1-x)$ and $C_q = 0$, so that gluons decouple, and the resulting equation is the familiar equation 2.58. Beyond the leading order, the quark and gluon distribution functions and the coefficient functions depend on the mass factorization scale. The so called factorization scheme dependence results from the ambiguity in how the perturbative physics is divided between the definition of quark/gluon spin distributions and coefficient functions [11, 12]. There are several factorization schemes used in the literature, and they are characterized by their treatment of the higher order terms in the expansion of the coefficient functions. In the Modified-Minimal-Subtraction ($\bar{M}S$) scheme, the first moment of the NLO correction to C_g vanishes, so that ΔG does not contribute to Γ_1 [11]. In the Adler-Bardeen (AB) scheme, the first moment of C_g is not zero, leading to the dependence of Γ_1 on the integral $\int \Delta g dx$, which leads to a difference in the singlet quark distribution $\Delta\Sigma$ in these 2 schemes. Once a choice of factorization scale is made, the Q^2-evolution of g_1 can be written using the Altarelli-Parisi equations[1,4]. The evolution equations are given in terms of 3 components: nonsinglet quark distribution $\Delta q_{NS}(x, Q^2)$, singlet quark distribution $\Delta\Sigma(x, Q^2)$, and gluon distribution $\Delta g(x, Q^2)$. The evolution is characterized in terms of the splitting functions $P_{ij}(x, \alpha)$ which can be computed perturbatively in terms of the hard cross sections. The nonsinglet quark distribution evolves independently:

$$\frac{d}{d\ln Q^2}\Delta q_{NS}(x, Q^2) = \frac{\alpha_s(Q^2)}{2\pi} P_{qq}^{NS} \otimes \Delta q_{NS}. \tag{2.69}$$

The singlet quark and gluon distributions mix:

$$\frac{d}{d\ln Q^2}\left[\begin{pmatrix}\Delta\Sigma \\ \Delta G\end{pmatrix} = \frac{\alpha_s(Q^2)}{2\pi}\begin{pmatrix}P_{qq} & P_{qg} \\ P_{gp} & P_{gg}\end{pmatrix} \otimes \begin{pmatrix}\Delta\Sigma \\ \Delta G\end{pmatrix}\right]. \tag{2.70}$$

The Q^2-evolution of Γ_1 is given by the Operator Product Expansion, in complete analogy with the unpolarized case discussed earlier. The hadronic matrix is expanded near the light cone in powers of $1/Q^2$, as described in Appendix B. The result is given by the product of the hadronic matrix elements of local operators and the coefficient functions, calculable in perturbative QCD. The antisymmetric part of the operator product appearing in the hadronic matrix is given in momentum space [3]:

$$T^A_{\mu\nu} = i\varepsilon_{\mu\nu\lambda\sigma}q^\lambda \sum_{n=1,odd}(\frac{2}{Q^2})^n q_{\mu_1}...q_{\mu_{n-1}} \sum_{i=0}^{9} R_i^{\sigma\mu_1...\mu_{n-1}} E_i^n(Q^2/\mu^2, \alpha_s), \tag{2.71}$$

where the operators R_i transform as the SU(3) flavor octet with $i = 1, ...8$, and as flavor singlets with $i = 0, 9$. For the first moment case (n=1) there are 8 non-singlet operators and one singlet operator. The proton matrix elements of the two leading twist operators $R_{1,i}$ and $R_{2,i}$ are:

$$\begin{aligned}\langle P,S|R_{1,i}^{\sigma\mu_1..\mu_{n-1}}|P,S\rangle &= \frac{-2Ma_n^i}{n}\left[S^\sigma P^{\mu_1}...P^{\mu_{n-1}}\right],\\ \langle P,S|R_{2,i}^{\sigma\mu_1..\mu_{n-2}}|P,S\rangle &= Md_n^i(S^\sigma P^\lambda - S^\lambda P^\sigma)P^{\mu_1}...P^{\mu_{n-2}},\end{aligned} \tag{2.72}$$

where S is the spin vector of the proton, and matrix elements a_n^i and d_n^i contain the incalculable, non-perturbative part of the dynamics. Applying Cauchy integration to both sides of equation 2.71, and expressing the antisymmetric part of the hadronic tensor in terms of the structure functions g_1 and g_2 results in the following equations:

$$\int_0^1 dx x^{n-1} g_1(x,Q^2) = \frac{1}{2}\sum_i \delta_i a_n^i E_{1,i}^n(Q^2,g) \quad n=1,3,5.., \tag{2.73}$$

$$\int_0^1 dx x^{n-1} g_2(x,Q^2) = \frac{1-n}{2n}\sum_i \delta_i \left[a_n^i E_{1,i}^n(Q^2,g) - d_n^i E_{2,i}^n(Q^2,g)\right] \quad n=3,5,7...$$

The coefficient functions $E_{1,i}^n(Q^2,g)$ and $E_{1,i}^n(Q^2,g)$ are the Fourier transforms of the singular functions that emerged from the OPE. They are calculated in the framework of perturbative QCD, as the power series expansion in the coupling constant g. They satisfy the Renormalization Group Equations and become also functions of the renormalization mass scale μ^2. Beyond the leading order, calculation of the coefficient functions becomes scheme-dependent. In the modified Minimal Subtraction scheme, the functions are calculated for the 3 flavors of massless quarks [13]:

$$\begin{aligned}E_{NS}(Q^2) &= 1-(\frac{\alpha_s}{\pi}) - 3.58(\frac{\alpha_s}{\pi})^2 - 20.22(\frac{\alpha_s}{\pi})^3,\\ E_S(Q^2) &= 1-0.333(\frac{\alpha_s}{\pi}) - 1.10(\frac{\alpha_s}{\pi})^2.\end{aligned} \tag{2.74}$$

Using these results, equation 2.62 can now be modified:

$$\Gamma_1^p(Q^2) = \frac{1}{12}\left[E_{NS}(Q^2)[a_3 + \frac{1}{3}a_8] + E_S(Q^2)\frac{4}{3}a_0\right]. \tag{2.75}$$

These perturbative corrections turn out to be small for the EMC data [14], and do not significantly change the value of a_0 which was expected to be ~ 1 in the non-interacting theory, but was measured to be much smaller. The corrected value becomes [14]: $a_0 = 0.17 \pm 0.12 \pm 0.17$. The conclusion is that the QCD-improved corrections do not resolve the question why the value of a_0 is much smaller than expected.

2.4.3 $\Gamma_1(Q^2)$ and the axial anomaly

An explanation of $a_0 \sim 0$ is provided by the phenomenon known as the axial anomaly. In the Naive Parton Model the axial coupling a_0 describes the contribution of the quark spins to the proton spin by treating the flavor singlet axial current $J^0_{5\mu}$ as the quark spin-density operator. In this treatment, $J^0_{5\mu}$ is the spin-density operator for free fields, and therefore it describes the spin state of a quark in a free parton state. Experimentally, quarks are accessed in the nucleon state where they interact strongly. It follows that $J^0_{5\mu}$ can only describe the experimental data if it is a conserved current.

The axial current is given:

$$J^0_{5\mu} = \bar{\psi}_f(x)\gamma_\mu\gamma_5\psi_f(x), \tag{2.76}$$

where $\psi_f(x)$ is a free quark field. The application of the free Dirac equation of motion to this current results in the following expression:

$$\partial_\mu J^0_{5\mu} = 2im_q\psi_f(x)\gamma_5\psi_f(x), \tag{2.77}$$

where m_q is the mass of a quark. In the limit of massless quarks, the axial current appears to be conserved. However, this argument is incorrect, as was shown first by Adler, Bell and Jackiw [14, 15] in the context of QED. They showed that there is an anomalous contribution to the axial current, and as a result of that, the current is not conserved. In QCD the anomaly induces a point-like interaction between the axial current and gluons [14]. The anomaly causes a gluon contribution to a_0, and makes the contribution of the quark spin to the nucleon spin $\Delta\Sigma$ dependent on the factorization scheme. Consequently, the axial current is scheme dependent and is not conserved when $m_q = 0$. In the Adler-Bardeen scheme, a_0 is decomposed into the quark ($\Delta\Sigma$) and gluon (Δg) contributions [12]:

$$a_0(Q^2) = \Delta\Sigma - n_f\frac{\alpha_s(Q^2)}{2\pi}\Delta g(Q^2). \tag{2.78}$$

This equation suggests that $\Delta\Sigma$ cannot be obtained by measuring a_0 without knowing the value of Δg. In some other factorization schemes, $\Delta\Sigma = a_0(Q^2)$ but it becomes dependent on Q^2. The important conclusion that can be drawn here is that the small value of a_0 does not necessarily mean that $\Delta\Sigma$ is small. Another implication of the anomaly is that the gluon contribution to the nucleon spin does not decouple as $Q^2 \to \infty$, and needs to be taken into account even in the scaling limit.

2.5 The Resonance Region

2.5.1 GDH Sum Rule

An interesting and still largely experimentally unexplored kinematic region is the one of low and moderate Q^2 ($Q^2 \leq 1$). Scattering experiments performed in this region probe the hadronic as well as partonic degrees of freedom. As the transition between hadronic and partonic scales occurs, the nucleon resonances and multi-pion states become important. For this reason this kinematic region is known as the resonance region.

The nucleon resonances are usually described in terms of the photon helicity amplitudes [6]. The virtual photon can be polarized transversely or longitudinally. Transverse photons have helicity $\lambda = \pm 1$, and correspond to right or left-handed circular polarization, while longitudinal photons have $\lambda = 0$. The polarization vectors are $\varepsilon^{\mu}_{\pm}$ for the transverse photons and ε^{μ}_{0} for the longitudinal ones.

$$\begin{aligned} \varepsilon^{\mu}_{\pm} &= \frac{1}{\sqrt{2}}(0, \mp 1, -i, 0), \\ \varepsilon^{\mu}_{0} &= \frac{1}{Q}(|q|, 0, 0, \nu). \end{aligned} \tag{2.79}$$

The corresponding components of the electromagnetic current $J_{\mu\nu}$ are

$$\begin{aligned} J_{\pm} &= \varepsilon^{\mu}_{\pm} J_{\mu\nu} = \pm\frac{1}{\sqrt{2}}(J_x + iJ_y), \\ J_0 &= \varepsilon^{\mu}_{0} J_{\mu\nu} = \frac{Q}{\nu} J_z. \end{aligned} \tag{2.80}$$

The helicity amplitudes can now be constructed. The amplitudes connect a nucleon

$N_{\frac{1}{2},m_S}$ with a spin projection m_S, with any nucleon resonance N^*_{j,m_j}, of spin j and projection m_j. For a nucleon of mass M and spin $\frac{1}{2}$, it is common to define three basic amplitudes [6]:

$$\begin{aligned} A_{\frac{1}{2}} &= \frac{e}{2M}\sqrt{\frac{M}{W^2-M^2}}\langle N^*_{j,+\frac{1}{2}}|J_+|N_{\frac{1}{2},-\frac{1}{2}}\rangle, \\ A_{\frac{3}{2}} &= \frac{e}{2M}\sqrt{\frac{M}{W^2-M^2}}\langle N^*_{j,+\frac{3}{2}}|J_+|N_{\frac{1}{2},+\frac{1}{2}}\rangle, \\ S_{\frac{1}{2}} &= \frac{e}{2M}\sqrt{\frac{M}{W^2-M^2}}\langle N^*_{j,\frac{1}{2}}|J_0|N_{\frac{1}{2},\frac{1}{2}}\rangle. \end{aligned} \tag{2.81}$$

The total cross sections at a given resonance can be written in terms of the helicity amplitudes. The transverse, longitudinal and interference cross sections are respectively:

$$\begin{aligned} \sigma_T(\nu_R, Q^2) &= \frac{2M}{\Gamma_R M_R}\left[|A_{\frac{1}{2}}|^2 + |A_{\frac{3}{2}}|^2\right], \\ \sigma_L(\nu_R, Q^2) &= \frac{4M}{\Gamma_R M_R}\left[|S_{\frac{1}{2}}|^2\right], \\ \sigma_{LT}(\nu_R, Q^2) &= \frac{2M}{\Gamma_R M_R}\left[|A_{\frac{1}{2}}|^2 + |S_{\frac{3}{2}}|^2\right], \end{aligned} \tag{2.82}$$

$$\tag{2.83}$$

where $\nu_R = \frac{M_R^2 - M^2 + Q^2}{2M}$, M_R is the invariant mass of the resonance and Γ_R is its decay width. The same cross sections can be written in terms of the structure functions g_1 and F_1. In particular, the transverse and interference cross sections are:

$$\begin{aligned} \sigma_T^{1/2}(\nu_R, Q^2) &= \frac{4\pi^2\alpha}{MK}(F_1 + g_1 - \frac{2Mx}{\nu}g_2), \\ \sigma_T^{3/2}(\nu_R, Q^2) &= \frac{4\pi^2\alpha}{MK}(F_1 - g_1 + \frac{2Mx}{\nu}g_2), \end{aligned}$$

$$\sigma_{LT}(\nu_R, Q^2) \qquad = \frac{4\pi^2\alpha}{MK}\frac{Q}{\nu}(g_1 + g_2), \tag{2.84}$$

where K is the photon flux. Combining the above equations, it is possible to write down the individual resonance contribution to g_1:

$$g_1 = \frac{MK}{8\pi^2\alpha(1 + Q^2/\nu^2)}\left[\sigma_T^{1/2} - \sigma_T^{3/2} + \frac{2Q}{\nu}\sigma_{LT}\right]. \tag{2.85}$$

In the real photon limit, the GDH (Gerasimov-Drell-Hearn) Sum Rule relates the difference of the two photoabsorption cross-sections to the anomalous magnetic moment of the nucleon κ [16, 17]:

$$-\frac{\kappa^2}{4} = \frac{M}{8\pi^2\alpha}\int_{\nu_{th}}^{\infty}\frac{\sigma_T^{1/2} - \sigma_T^{3/2}}{\nu}d\nu, \tag{2.86}$$

where ν_{th} is the one pion photoproduction threshold. The GDH sum rule is derived using general principles of physics such as the Lorentz and gauge invariance, causality and unitarity [18], and an assumption that the unsubtracted dispersion relation could be used for the spin dependent part of the forward Compton amplitude. The right side of this equation is clearly related to the first moment Γ_1. Strictly speaking, the GDH sum rule is derived in the real photon limit ($Q^2 = 0$), but assuming that the real photon cross sections connect smoothly to the virtual photon ones, the sum rule can be generalized for the case of the virtual photons. Expressing the cross sections in terms of the spin structure functions and using $K = \nu - \frac{Q^2}{2M}$ gives the generalized Q^2-dependent GDH sum rule:

$$I_{GDH}(Q^2) \qquad = \frac{2M}{Q^2}\int_0^{x_0}\left[g_1(x, Q^2) - \frac{Q^2}{\nu^2}g_2(x, Q^2)\right]dx$$

$$= \frac{M^2}{8\pi^2\alpha}\int_{\nu_{th}}^{\infty}(1-\frac{Q^2}{2M\nu}(\sigma_{1/2}(\nu,Q^2)-\sigma_{3/2}(\nu,Q^2))\frac{d\nu}{\nu}. \quad (2.87)$$

It is interesting to see what the generalized GDH sum rule predicts for Γ_1. For convenience, the quantity $I_1(Q^2)$ is defined:

$$\begin{aligned} I_1(Q^2) &= \frac{2M^2}{Q^2}\int_0^{x_0} g1(x,Q^2)dx \quad (2.88)\\ &= \frac{M^2}{8\pi^2\alpha}\int_{\nu_{th}}^{\infty}\frac{1-Q^2/2m\nu}{1+Q^2/\nu^2}(\sigma_{1/2}(\nu,Q^2)-\sigma_{3/2}(\nu,Q^2)+\frac{2Q}{\nu}\sigma_{LT}(\nu,Q^2))\frac{d\nu}{\nu}. \end{aligned}$$

As $Q^2 \rightarrow 0$:

$$\lim_{Q^2\rightarrow 0} I_1(Q^2) \Longrightarrow \frac{M^2}{8\pi^2\alpha}\int_{\nu_{th}}^{\infty}(\sigma_{1/2}(\nu,Q^2)-\sigma_{3/2}(\nu,Q^2))\frac{d\nu}{\nu}, \quad (2.89)$$

$$\Gamma_1 = \frac{Q^2}{2M^2}I_1(Q^2) \Longrightarrow \frac{Q^2}{16\pi^2\alpha}(-\frac{2\pi^2\alpha\kappa^2}{M^2}) \Longrightarrow -\frac{Q^2\kappa^2}{8M^2}. \quad (2.90)$$

The conclusion that can be drawn here is that Γ_1 approaches 0 with a negative slope, and since it is positive in the high Q^2 region, it should rapidly change its sign somewhere in the resonance region $0 < Q^2 < 1$ GeV.

The GDH equation 2.86 depends on the $1/\nu$ term, therefore the low-energy resonances are expected to play a more important role in the sum rule [18]. Some of these resonances are $P_{33}(1232)$, $P_{11}(1440)$, $D_{13}(1520)$ and $S_{11}(1535)$. The lowest-lying resonce $P_{33}(1232)$ is particularly important. It is believed that approximately 80% of the GDH sum rule is contributed by $P_{33}(1232)$ [18]. These facts provide the basis of some phenomenological models that try to connect the sum rule of g_1 in the resonance region to the Ellis-Jaffe sum rule in the DIS region.

2.5.2 Phenomenological Models

The strong variation of Γ_1^p with Q^2 in the resonance region is caused by the transition from the resonance-driven coherent scattering to the incoherent scattering off the constituent quarks. The evolution of the sum rule was originally described by Anselmino et al [19] through the parameterization based on the vector meson dominance model. The model was later refined by Burkert and Ioffe [20] by treating explicitly the contributions of individual resonances.They suggested that the contribution from resonance production has a strong Q^2-dependence for small Q^2, and then decreases rapidly with increasing Q^2. At $Q^2 = 0$, approximately 80% of the GDH sum rule is given by the contribution of the Δ resonance $P_{33}(1232)$. The $\Delta(1232)$ resonance is a spin $\frac{3}{2}$ isobar of the nucleon, and is given by the strength of the $A_{\frac{3}{2}}$ amplitude. The $A_{\frac{3}{2}}$ amplitude requires a change of helicity, and a flip of the quark spin. At large Q^2 the quark mass can be neglected. If quarks are massless Dirac particles, the photon coupling to the quark vector current conserves helicity, and the helicity changing amplitude $A_{\frac{3}{2}}$ should be suppressed with respect to the helicity conserving amplitude $A_{\frac{1}{2}}$ [6]. However, at small Q^2, the magnetic dipole transition is of spin-flip type, and it dominates the Δ photoproduction, so that $\sigma_{3/2}/\sigma_{1/2} \sim 3$. Other resonances should be treated likewise, but they are neglected in the Burkert-Ioffe model since their contributions to the GDH sum rule are relatively small. [20]. Therefore, the model needs to be modified, and the resonant and non-resonant contributions are considered separately. The quantity $I_1(Q^2)$ is split into the resonant and non-resonant parts, and the non-resonant part of $I_1(Q^2)$ is parameterized by a smooth function which is a sum of a monopole and a dipole term [21]:

$$I_1^p(Q^2) = I^{res}(Q^2) + 2m_p^2\Gamma_p^{as}\left[\frac{1}{Q^2+\mu^2} - \frac{c\mu^2}{(Q^2+\mu^2)^2}\right], \tag{2.91}$$

where $I^{res}(Q^2)$ is the contribution of $\Delta(1232)$, Γ_p^{as} is the asymptotic value of $\Gamma_p(Q^2)$ at large Q^2, μ is the mass parameter characterizing the model, which is set to $\mu = m_p$ here. The constant c is chosen from the boundary condition that the GDH sum rule must be fulfilled at the real photon point $Q^2 = 0$:

$$c = 1 + \frac{1}{2}\frac{\mu^2}{m_p^2}\frac{1}{\Gamma_p^{as}}\left[\frac{1}{4}\kappa_p^2 + I^{res}(0)\right]. \tag{2.92}$$

Using the experimental data on $\Delta(1232)$ photoproduction, the model predicts a change of sign for $\Gamma_1^p(Q^2)$ at $Q^2 \sim 0.8$ Gev^2. The sign change is generated by the contribution of the $\Delta(1232)$ resonance, which gives a large negative value at small Q^2.

In another model, Soffer and Teryaev [22] suggested that the strong Q^2-dependence of the Γ_1 integral should be analyzed together with Γ_2, the first moment of the second spin structure function. The authors decompose $I_1(Q^2)$ into two contributions [22]:

$$I_1 = I_{1+2} - I_2, \tag{2.93}$$

where

$$\begin{aligned} I_{1+2}(Q^2) &= \frac{2M^2}{Q^2}\int_0^1 (g_1(x,Q^2) + g_2(x,Q^2))dx, \\ I_2(Q^2) &= \frac{2M^2}{Q^2}\int_0^1 g_2(x,Q^2)dx. \end{aligned} \tag{2.94}$$

The behavior of I_2 is constrained by the Burkhardt-Cottingham sum rule which predicts:

$$\int_0^1 g_2(x)dx = 0. \tag{2.95}$$

The elastic contribution to the above integral generates the strong Q^2-dependence of I_2. At $Q^2 = 0$:

$$I_2(0) = \frac{\kappa_p^2 + e\kappa_p}{4}, \tag{2.96}$$

where e is the nucleon charge in elementary units. Since the GDH sum rule predicts $I_1(0) = -\frac{\kappa_p^2}{4}$, one should have $I_{1+2}(0) = \frac{e\kappa_p}{4}$. For large Q^2, I_{1+2} is not different from I_1 due to the Burkhardt-Cottingham sum rule, and since I_{1+2} is known for both large Q^2 and $Q^2 = 0$, it is possible to interpolate smoothly between the two limiting cases. The fluctuation of Γ_1 follows the subtraction of Burkhardt-Cottingham value from I_{1+2}. For the proton case, the authors use the simplest parametrization to interpolate I_{1+2} between $Q^2 = 0$ and large Q^2 [22]:

$$I_{1+2}(Q^2) = \theta(Q_0^2 - Q^2)\left[\frac{e\kappa_p}{4} - \frac{2m_p^2 Q^2}{(Q_0^2)^2}\int_0^1 g_1(x)dx\right] + \theta(Q^2 - Q_0^2)\frac{2m_p^2}{Q^2}\int_0^1 g_1(x)dx. \tag{2.97}$$

The resulting crossing point for Γ_1^p is at $Q^2 \sim 0.2\ GeV^2$, which is below the resonance region.

The evolution of $\Gamma_1^p(Q^2)$ as described by the Soffer-Teryaev and Burkert-Ioffe models is shown in Fig. 2.8, along with the GDH sum rule prediction and the perturbative QCD region behaviour.

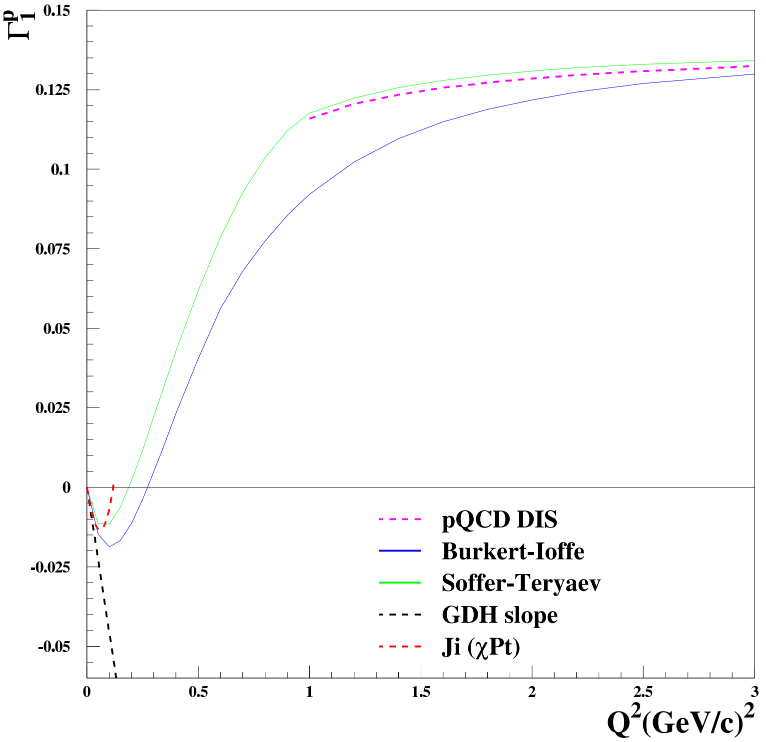

Figure 2.8: The Q^2-evolution of Γ_1^p integral

2.6 Experimental Observables

Spin structure functions are measured in the inclusive inelastic processes such as the one shown in Figure 2.1. It is actually the virtual photon that probes the nucleon but it is the electron that is detected in the experiment, so the electron observables need to be translated into the photon quantities of interest. The virtual photon-nucleon cross sections are given in terms of the helicity amplitudes $A_{\frac{1}{2}}$, $A_{\frac{3}{2}}$, and $S_{\frac{1}{2}}$ mentioned previously. The optical theorem relates the cross sections to the helicity amplitudes, and, as previously discussed, the cross sections are also related to the structure functions, and give rise to the following expressions:

$$\begin{aligned}
\sigma^T_{\frac{1}{2}} &= \frac{4\pi^2\alpha}{K}A_{\frac{1}{2}} = \frac{4\pi^2\alpha}{Km_p}(F_1 + g_1 - \frac{2m_px}{\nu}g2), \\
\sigma^T_{\frac{3}{2}} &= \frac{4\pi^2\alpha}{K}A_{\frac{3}{2}} = \frac{4\pi^2\alpha}{Km_p}(F_1 - g_1 + \frac{2m_px}{\nu}g2), \\
\sigma^L_{\frac{1}{2}} &= \frac{4\pi^2\alpha}{K}S_{\frac{1}{2}} = \frac{4\pi^2\alpha}{Km_p}(\frac{F_2}{\nu}(1 + \frac{\nu^2}{Q^2}) - \frac{1}{m_p}F_1), \\
\sigma^{LT}_{\frac{1}{2}} &= \frac{4\pi^2\alpha}{K}[A^2_{\frac{1}{2}} + S^2_{\frac{1}{2}}]^{1/2}\frac{Q}{M\nu}(g_1 + g_2),
\end{aligned} \tag{2.98}$$

where $K = \nu - \frac{Q^2}{2M}$ is the equivalent photon energy.

For a longitudinally polarized nucleon and the transversely polarized virtual photon, the scattering asymmetry is given by

$$A_1 = \frac{\sigma^T_{\frac{1}{2}} - \sigma^T_{\frac{3}{2}}}{\sigma^T_{\frac{1}{2}} + \sigma^T_{\frac{3}{2}}}. \tag{2.99}$$

The interference between the longitudunal and transverse virtual photon-nucleon amplitudes gives rise to the second virtual photon asymmetry :

$$A_2 = \frac{2\sigma_{LT}}{\sigma^T_{\frac{1}{2}} + \sigma^T_{\frac{3}{2}}}. \tag{2.100}$$

The spin structure functions can now be expressed through virtual photon asymmetries, as discussed in Appendix A:

$$\begin{aligned}
A_1(x, Q^2) &= \frac{g_1(x, Q^2) - \gamma^2 g_2(x, Q^2)}{F_1(x, Q^2)}, \\
A_2(x, Q^2) &= \frac{\gamma^2\,[g_1(x, Q^2) + g_2(x, Q^2)]}{F_1(x, Q^2)},
\end{aligned} \tag{2.101}$$

where $\gamma = \frac{2mx}{Q}$. The measured lepton asymmetries are defined through the lepton-nucleon asymmetries:

$$\begin{aligned} A_{\|} &= \frac{\sigma^{\uparrow\downarrow} - \sigma^{\uparrow\uparrow}}{\sigma^{\uparrow\downarrow} + \sigma^{\uparrow\uparrow}}, \\ A_{\perp} &= \frac{\sigma^{\downarrow\leftarrow} - \sigma^{\uparrow\leftarrow}}{\sigma^{\downarrow\leftarrow} + \sigma^{\uparrow\leftarrow}}, \end{aligned} \tag{2.102}$$

where ↑↑ (↑↓) is the spin configuration with the nucleon and lepton spins aligned, while ↑← (↓←) is the configuration with the transversely polarized nucleon and longitudinally polarized lepton. The measured lepton asymmetries can be related to the desired virtual photon asymmetries:

$$A_{\|} = D(A_1 + \eta A_2), \tag{2.103}$$

$$\begin{aligned} A_{\perp} &= d(A_2 - \zeta A_1), \\ D &= [1-(1-y)\epsilon]/(1+\epsilon R), \\ y &= \frac{\nu}{E}, \\ R &= \frac{\sigma_L}{\sigma_T}, \\ \epsilon &= [4(1-y) - \gamma^2 y^2]/[2y^2 + 4(1-y) + \gamma^2 y^2], \\ d &= D\sqrt{\frac{2\epsilon}{1+\epsilon}}, \\ \eta &= \epsilon\gamma y/[1-\epsilon(1-y)], \\ \zeta &= \eta\frac{1+\epsilon}{2\epsilon}. \end{aligned} \tag{2.104}$$

The spin structure function g_1 can be determined from measurements of $A_{||}$:

$$g_1 = \frac{F_1}{1+\gamma^2}\left[A_{||}/D + (\gamma - \eta)A_2\right], \tag{2.105}$$

where the unpolarized structure function F_1 is known from previous measurements, and A_2 is either measured separately or estimated. $A_{||}$ is obtained from the measured experimental asymmetry A_{exp}:

$$A_{||} = \frac{A_{exp}}{P_B P_T F} + \Delta_{RC}, \tag{2.106}$$

where $P_B P_T$ is the product of beam and target polarizations, F is the dilution factor which accounts for scattering from the unpolarized components of the target, and Δ_{RC} account for the QED radiative effects. The experimental electron asymmetry is expressed in terms of measured scattering rates, N, normalized to the number of incident electrons N_e:

$$A_{exp} = \frac{N^{\uparrow\downarrow}/N_e^{\uparrow\downarrow} - N^{\uparrow\uparrow}/N_e^{\uparrow\uparrow}}{N^{\uparrow\downarrow}/N_e^{\uparrow\downarrow} + N^{\uparrow\uparrow}/N_e^{\uparrow\uparrow}}. \tag{2.107}$$

2.7 Experimental Objectives

A series of experiments was performed in Hall B of Jefferson Lab with the objective of measuring the double spin asymmetry A_{exp}, and extracting from it the spin structure functions and their integrals. The subject of this thesis is the analysis of experiment EG1b, which was a continuation of an earlier experiment EG1. The emphasis of the experiment was to explore the little known resonance region, $W \leq 2$ GeV. The kinematic range of the experiment is shown in Figure 2.9.

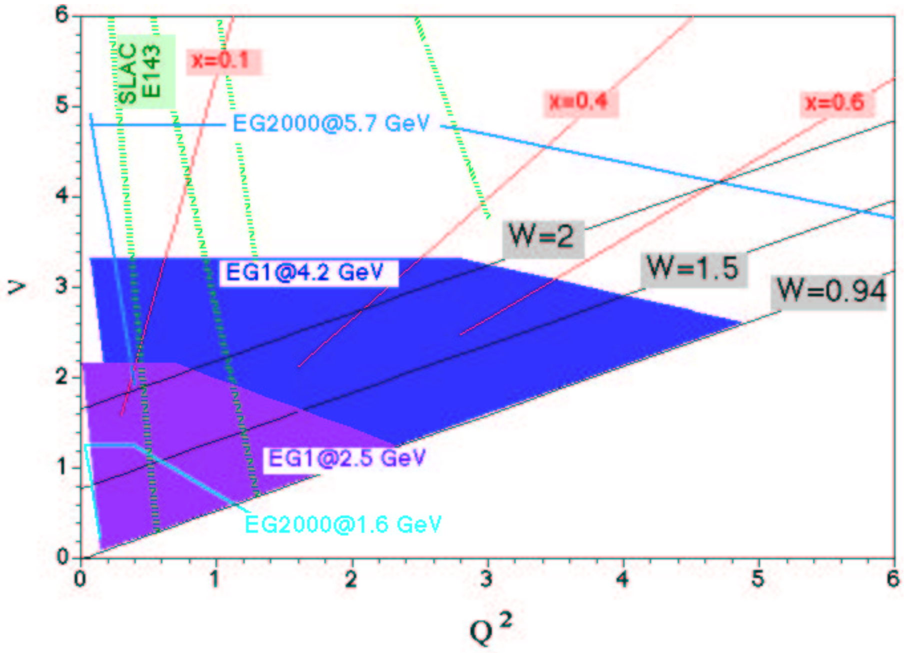

Figure 2.9: Kinematics of the EG1b experiment compared to the ones from previous experiments

A_{exp} was measured by scattering polarized electrons off polarized protons and deuterons using a cryogenic polarized target, a source of polarized electrons and the CLAS detector in Hall B. The experiment was completed in April of 2000 after accumulating over 23 billion triggers. An analysis of some of that data obtained with the polarized protons is presented in this thesis.

Chapter 3

The Electron Beam at TJNAF

3.1 RF accelerating structure

The Thomas Jefferson National Accelerator Facility operates a continuous wave polarized electron accelerator producing a high current beam of electrons up to an energy of about 5.7 GeV. Electrons are accelerated by microwave electric fields generated in klystrons and are propagated through wave guides to RF accelerating cavities. A klystron is a powerful type of microwave amplifier, in which a low energy microwave signal breaks a continuous electron beam into 'bunches'. The pulsed beam passes through a resonant waveguide, where it induces a high energy microwave signal. The transmitted microwave radiation is transported to a superconducting RF cavity where it accelerates electrons. The electric field induced in the RF cavity is roughly parallel to the beam axis, with its maximum value on the axis, and decaying to zero, radially, at the walls. The electromagnetic field induces charge on the interior surfaces of the cavities such that the electrons moving through the cavity 'see' a positive charge in front of them and accelerate toward that charge.

The TJNAF accelerator consists of a 45 MeV injector capable of producing three beams, two anti-parallel superconducting linac segments connected by nine recirculation arcs, a beam switch yard and three experimental halls: A,B, and C. The electron beam originates in the injector, which generates a beam with a nominal energy of 45 MeV and a nominal 1500 MHz bunch structure. The injector can modulate the beam intensity with a bunch periodicity of three, allowing the three end stations to receive beams of different intensity [23]. The injector consists of a room temperature section providing beam of 100 KeV, followed by a superconducting linac section with eight RF cavities contained in three separate cryogenic modules. The room temperature section houses a 100 KeV electron gun with a control electrode capable of providing a 10mA DC beam [24]. Two superconducting RF cavities and an adjustable 3-slit aperture system are used to control the intensity and chopping of the beam. The 100 KeV beam is captured by a room temperature RF cavity where the electrons are accelerated to 0.54 MeV. The 0.54 MeV electron beam is accelerated in superconducting RF cavities to an energy of 50 MeV for injection into the linac. The diagram of the accelerator is shown below.

The main accelerating structure consists of the two superconducting linacs approximately 240 meters long, which are connected by the recirculating arcs. Each linac segment contains 25 cryomodules, each with 8 superconducting RF cavities. The accelerating cavities are 5-cell, 1497 MHz, elliptical niobium cavities that were developed at Cornell University. A separate klystron drives each individual cavity, so that each can be run at its optimal level with precise control over the phase and gradient. The cryomodules are separated from each other by a room temperature

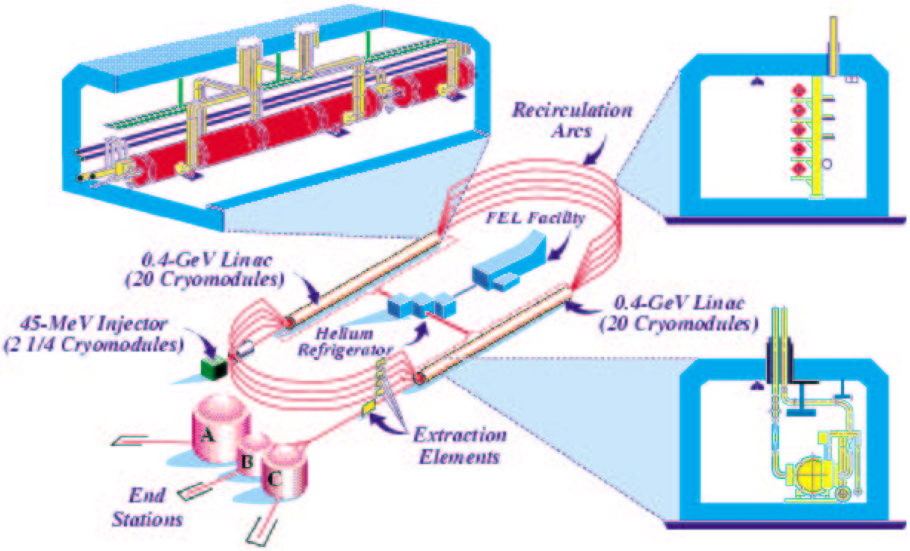

Figure 3.1: CEBAF Accelerator Diagram.

section containing focusing quadrupole magnets, dipole steering magnets, beam diagnostics and vacuum equipment. In the original design, the electron beam received a boost of approximately 800 Mev after each circulation through the linacs, resulting in the maximum energy of 4 GeV after 4 passes. The performance of the RF cavities has recently surpassed the original specifications, so that a maximum energy of 5.7 GeV has been obtained. The beam transport system composed of steering magnets and focusing quadrupole magnets serves to confine and guide the beam through the accelerator. The linacs are connected by transport lines, consisting of sections called 'spreaders', recirculation arcs , and 'recombiners'. [23]. Spreaders bend the beam vertically in a dipole through an angle α inversely proportional to the beam energy, recombiners are magnets that bend each individual beam by $-\alpha$. The recirculation arc regions were designed to minimize the synchrotron radiation effects, by incorporating sufficiently large bending radii and strong focusing. The energy spread in the beam is $\sim \Delta E/E \sim 10^{-4}$, with the beam current ranging from 100 pA to 100 μA.

The three beams are separated at the switch yard, and delivered to the experimental halls with the separation between bunches of 2.04 ns. The three experimental halls are equipped with spectrometers designed for a variety of research programs. Hall A is designed for high-resolution experiments, and houses two high resolution spectrometers with $\Delta p/p \sim 10^{-4}$, and solid angle (10 msr) and large momentum acceptance $(10 - 15\%)$. The spectrometer arrangement allows measurements involving non-coplanar kinematics. Hall B is equipped with the CEBAF Large Acceptance Spectrometer (CLAS) which was designed for photonuclear and electronuclear studies with low luminosity ($\sim 10^{34}$ cm^{-2}sec^{-1}). CLAS allows multi-particle detection and identification within $\sim 80\%$ of 4π and 0.1 to 6 GeV/c in momentum. Hall C contains two magnetic spectrometers of medium momentum resolution ($\sim$ 10 MeV). They are the High Momentum Spectrometer(HMS) with a maximum momentum of 7 GeV/c the Short Orbit Spectrometer (SOS) with a maximum momentum of 1.8 GeV/c.

3.2 Polarized electrons and polarimetry

The accelerator has been able to deliver polarized electron beams since 1998, when the original thermionic gun was replaced by a polarized gun. The polarized electrons are produced by inducing bandgap photoemission from a strained GaAs cathode. The cathode is made by growing layers of various GaAs substrates with different lattice spacing. Pure GaAs is grown on top of GaAs$_{0.72}P_{0.28}$. The smaller lattice spacing of GaAs$_{0.72}P_{0.28}$ creates strain on the spacing of GaAs, shifting electron energy levels slightly, and breaking the degeneracy [25], as shown in Figure 3.2. The result of this process is a gap in the sublevels of the $P_{3/2}$ electrons in the valence band of GaAs, which allows a polarization of theoretical 50% limit from pure GaAs. When the cathode is illuminated by a circularly polarized laser light, polarized electrons are produced in the conduction band of the material. By using light of appropriate frequency, electrons from the valence $P_{3/2}$ m=3/2 state are excited to the conduction $S_{1/2}$ m=1/2 state. Because of the sufficiently wide gap between the $P_{3/2}$ sublevels, electrons from the m=1/2 level do not reach the conduction band. Electrons excited to the conduction band are bound to the surface of the material by $\sim$ 4 eV, so they cannot escape. For this reason the surface of GaAs is treated with the monolayer of cesium and fluorine to lower the work function so that electrons can escape. The additional monolayer creates a surface dipole moment such that the vacuum energy level outside the crystal lies below the energy minimum of the conduction band in the rest of the material [26]. The sign of electron polarization is flipped at frequency of 1 Hz by reversing the laser polarization with a pseudo-random sequence.

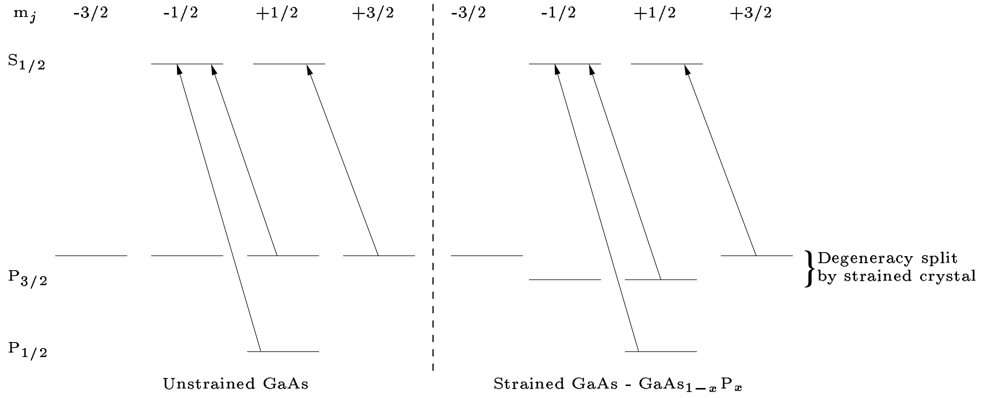

Figure 3.2: Energy levels for GaAs and strained GaAs.

The accelerator provides polarized electron beam simultaneously to the three experimental halls by selecting the appropriate orientation of electron spin at the injector. This is done with a Wien filter [27] which consists of perpendicular magnetic and electric fields transverse to the electron momentum. The Wien filter can rotate the polarization of the beam passing through it without changing the momentum itself. This is achieved by selecting the electric field for the desired spin rotation and adjusting the magnetic field so that the net Lorentz force on the electrons is zero. The electron spins undergo precession when the beam is recirculated in the linac and electrons interact with the bending magnetic field. The total precession angle depends on the number of passes and beam energy in the injector and linac. A precession angle which is a multiple of π results in the maximum final polarization, but since this condition is not always obtainable, the beam polarization can have a small transverse component.

The polarization of the beam is measured initially at the injector using a 5 MeV Mott polarimeter[28]. The beam polarization is measured again in Hall B by a Møller polarimeter located upstream of the polarized target. In a Møller polarimeter, beam electrons scatter from a target also containing polarized electrons. The Hall B Møller polarimeter target is a 25-μm thick magnetized iron foil where a fraction of electrons are polarized. Two scattered electrons are guided by two sets of quadrupole magnets to the two fiber scintillators where they are detected in coincidence. The kinematics of Møller scattering provides a strong correlation between the electron energy and the scattering angle [29]. The scattering cross section depends on the scattering angle, and the polarization of the beam and target electrons. By measuring the asymmetry in the number of electrons scattered with the beam polarized parallel and anti-parallel to its momentum, and knowing the Møller target polarization, the beam polarization can be extracted. The typical beam polarization during the EG1b run was $\sim 70\%$.

The position of the electron beam is monitored by three beam-position monitors (BPMs), located at 36.0 m, 24.6 m, and 8.2 m upstream of the CLAS target. The monitors measure (x,y) coordinates of the beam as well as its intensity. Every 20 seconds this information enters the data stream. The (x,y) profile of the beam is determined in a dedicated measurement with a harp scan. A harp is a device that moves thin iron wires through the beam. The scattered electrons are then detected with the use of a Cerenkov detector. The wires are oriented at 45° with respect to the horizontal axis. There are 3 harps in Hall B, located at 36.7, 22.1 and 15.5 m upstream of the CLAS target. The motion of a harp is controlled by a stepper motor that is synchronized with a VME scaler readout of the PMT signals. The acquired count rate plotted as a function of (x,y) is fit to a Gaussian with a constant background term. As a result, the beam position, the spread of the beam, and the signal-to-halo ratio are obtained.

The electron beam is stopped in a Faraday cup, which provides an accurate measurement of the integrated beam current. The Faraday cup is a 4000 kg block of lead located 29 m downstream of the CLAS target. The block of lead is supported by the ceramic platform inside a vacuum chamber. The Faraday cup is connected to a capacitor which accumulates charge and discharges it after 10^{-10} Coulomb of charge has accumulated. The frequency with which the discharge takes place is recorded in the data acquisition system.

Some typical CLAS electron beam parameters are displayed in Table 3.1

Table 3.1: Beam Parameters.

Quantity	Range	Precision	Monitor
Energy	0.8-6.0 GeV	$\delta E/E < 0.1\%$	Beam Orbit Stability
Polarization	$40 - 80\%$	$\delta P/P < 3\%$	Møller Polarimeter
Position	± 3 mm	100 μ m	BPMs
Width	$\sigma < 250$ μ m	10 μ m	Wire scans
Beam halo	1:100000		Wire scans
Current	1-30 nA	1 %	Faraday cup

Chapter 4

Polarized Target

4.1 Introduction

Targets containing polarized nucleons are an essential part of the scattering experiments which investigate the spin structure of the nucleons. Solid polarized targets consist of solid diamagnetic materials doped with paramagnetic radicals, which are essential for the polarization enhancement. The theory and technology of producing such targets have been developed over the past 40 years, and the work in this field continues. Solid polarized targets offer some advantages over their gaseous and liquid counterparts, such as high density, high construction flexibility and continuous mode of operation [30]. A solid target polarized via the method of Dynamic Nuclear Polarization was used in the EG1b experiment. This chapter will describe the theory behind the DNP method, and its application to the experimental target. It will also describe the design of the EG1b target in view of the constraints imposed by the geometry of the CLAS detector, the choice of target materials and the method of

Table 4.1: DNP Parameters.

Name	Symbol	Value
External Magnetic field	B	≤ 5.1 T
Temperature	T	~ 1 K
Bohr Magneton	μ_B	$5.788 \times 10^{-11} MeV \cdot T^{-1}$
Spin	J	
z-comp. of e^- spin	S_z	$\pm 1/2$
z-comp. of nucleon spin	I_z	varies
number of nuclei	N_I	varies
number of unpaired electrons	N_S	varies
g-factor	g_J	varies
magnetic moment	μ_J	varies
proton gyromagnetic ratio	$\gamma_p = g_p \mu_p$	$2.67 \times 10^8 s^{-1} T^{-1}$

detection and measurement of the resulting polarization.

4.2 Dynamic Nuclear Polarization

4.2.1 Thermal Equilibrium Polarization

The basic idea behind various methods of achieving high nuclear polarization in polarized targets is to produce high atomic polarization in the sample and then transfer that polarization to the nuclear spins. The reason why this is preferred lies in the fact that a nucleus has a much smaller magnetic moment than an electron, so that it is easier to reach high electron polarization than to polarize the nuclear spins directly. After a high electron polarization is achieved, the dipole-dipole interaction between the electron and nuclear spin transfers polarization to the nucleus. Important parameters for polarization are listed in Table 4.1. For atoms in states with magnetic moment μ_J in a magnetic field B, the Boltzmann factor $e^{\frac{\mu_J B}{kT}}$, determines the population at temperature T. Low temperature at high magnetic field maximizes the population in the state of lowest magnetic energy. At high temperature the magnetic Zeeman energy $E_Z = \mu B$ of a state with spin J is much lower than its thermal energy $E_T = kT$, and the polarization of the spins is given by the Brillouin function $B_J(x)$[31]:

$$P_J = B_J(x) = B_J(\frac{g_J \mu_J J B}{kT}). \tag{4.1}$$

For particles of spin 1/2 the Brillouin function is reduced to the hyperbolic tangent:

$$P_{1/2} = \tanh(\frac{\mu B}{kT}). \tag{4.2}$$

As can be seen from this formula, the polarization depends on the product of the g-factor g_J and magnetic moment of the particle μ_J (called the gyromagnetic ratio) which is fixed for a given particle, and the ratio of the magnetic field to temperature, B/T. Given the small value of the proton's gyromagnetic ratio, the value of B/T must be at least on the order of $\sim 10^3$ Tesla/Kelvin in order to create a significant nuclear thermal equilibrium polarization. On the other hand, a field of 1 T at the temperature of 1 K is sufficient to polarize free electrons to a value over 90%[30]. Dynamic nuclear polarization is then used to transfer the high electron polarization to the nuclear spins.

4.2.2 The Solid State Effect

The method of DNP is based on the Solid State Effect which was discovered in 1958, and is observed at low temperature and high magnetic field in a solid that contains atomic nuclei with non-zero spin and unpaired atomic electrons [31]. The unpaired

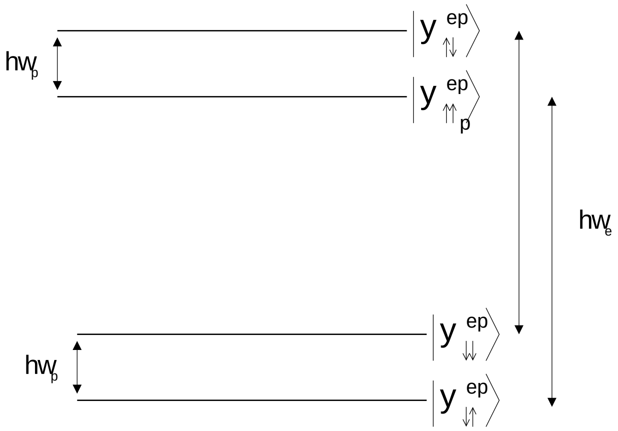

Figure 4.1: Energy levels of e-p spin system placed in a magnetic field. Without a perturbing Hamiltonian the system is described by four 'pure' eigenstates

electrons are introduced into the material by irradiation or chemical doping. The state of lower Zeeman energy has the electron spin anti-aligned with the magnetic field, while the opposite is true for the proton. The resulting energy diagram in the case of non-interacting particles is shown in Figure 4.1. While the spins are not interacting with each other, when the system is irradiated by an rf-field with frequency ω the only allowed transitions are the ones with $\Delta S_z = \pm 1$ or $\Delta I_z = \pm 1$. The component of the rf field B_1 which is perpendicular to the direction of the external static field B perturbs the Hamiltonian by [32]:

$$H_1 = -g_x \mu_B B_1 S_x \cos\omega t - (\mu_p / I) B_1 I_x \cos\omega t. \tag{4.3}$$

When the frequency ω is near the electron Larmor frequency $\omega_s = \frac{g_s \mu_s}{B\hbar}$, the corresponding transitions will have $\Delta S_z = \pm 1$ and the transition probability can be labelled W. Moreover, there is a dipole-dipole interaction between the proton and electron magnetic moments, given by the following Hamiltonian[32]:

$$H_{dip} = \frac{1}{r^3}\left[\mu_1 \cdot \mu_2 - \frac{3}{r^2}(\mu_1 \cdot r)(\mu_2 \cdot r)\right] = \frac{g\mu_B(\mu_p/I)}{r^3}\left[I \cdot S - 3r^{-2}(I \cdot r)(S \cdot r)\right], \tag{4.4}$$

where r is the vector joining the positions of the nucleus and the free electron. This interaction arises from a magnetic field B_S at the nucleus due to the dipole moment of the electron:

$$B_S = \frac{g\mu_B}{r^3}. \tag{4.5}$$

The field B_S is much smaller than the Zeeman field, but it results in mixing of the 'pure' electron states. Now these states will have a small admixture from the nuclear spin state with the opposite spin orientation. The amplitude of mixing is given by the coupling ε[30]:

$$\varepsilon = \frac{3}{2}\frac{\hbar\gamma_I\gamma_S}{\omega_I r^3}\sin\theta\cos\theta \sim \frac{B_S}{B_0} \sim 10^{-4}, \tag{4.6}$$

where the gyromagnetic ratios are $\gamma_I = \frac{\mu_I}{\hbar}$ and $\gamma_S = \frac{g_S\mu_B}{\hbar}$. The dipole-dipole interaction induces simultaneous spin flips of an electron and a nucleus, which is otherwise forbidden. The probability of such transitions is labeled V. A modified diagram of the energy levels of the electron-proton system is shown in Figure 4.2. The perturbation hamiltonian H_1 has non-zero matrix elements between the states $\Psi_{\uparrow\uparrow}$ and $\Psi_{\downarrow\downarrow}$, and states $\Psi_{\uparrow\downarrow}$ and $\Psi_{\downarrow\uparrow}$, therefore, the rf field can induce transitions between these pairs of states. The transition probability V is ε^2 times smaller than that for the allowed transitions, but it is nonzero, and gives rise to the 'solid state effect'.

Another process that takes place in the system of spins is the thermal interaction of spins with the lattice. Due to their spin-orbit coupling, free electrons have a strong

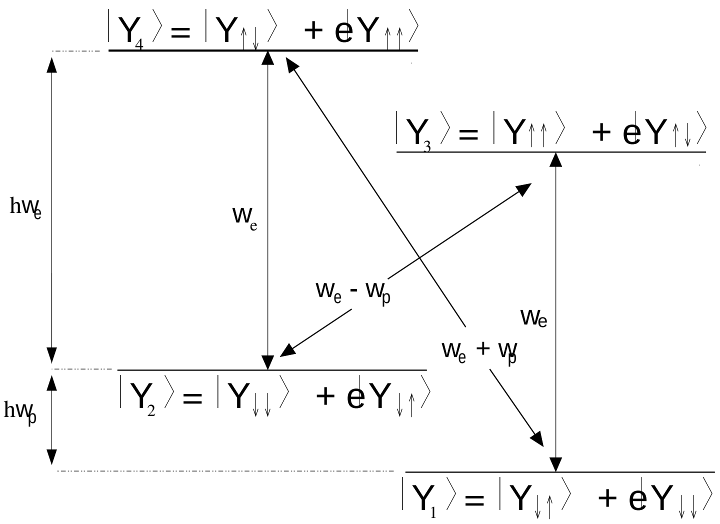

Figure 4.2: Allowed transitions in e-p spin system. The dipole interaction mixes eigenstates, and the transitions where both particles change their state are possible.

interaction with the thermal vibrations of the solid [32]. This interaction produces energy exchanges between the electron spins and the lattice, so that the electron spin lattice relaxation is fast. Nuclear spins, on the other hand, are weakly coupled to the lattice. Nuclear spin-lattice relaxation is slow because it takes place through the forbidden transitions induced by the electron spin-lattice coupling [32]. With these facts in mind, the solid state effect can be summarized as the following process. When an rf field with the appropriate frequency $(\omega_e \pm \omega_p)$ is applied to the e-p spin system, it can produce a change in a nuclear and electron spin orientation, after which, the electron spin goes quickly back to its lower magnetic energy position, while the nuclear spin remains in its present state due to its slow relaxation time.

The polarization of both spin species (electrons and protons) can be defined as follows [30]:

$$P_S = \frac{n_- - n_+}{n_- + n_+} = \frac{n_- - n_+}{N_S}, \qquad P_I = \frac{N_- - N_+}{N_I}. \tag{4.7}$$

Labeling the relaxation times for the electrons as T_S and for the protons as T_I, the evolution equations for the spin system can be written[30]:

$$\begin{aligned} \frac{dP_S}{dt} &= -V(P_S - P_I) + \frac{1}{T_S}(P_S^L - P_S), \\ \frac{dP_I}{dt} &= \frac{N_S}{N_I}V(P_S - P_I) - \frac{1}{T_I}(P_I^L - P_I), \end{aligned} \tag{4.8}$$

where $'L'$ indicates the thermal equilibrium (lattice) values. The stationary values of polarization are obtained from the condition: $\frac{dP_{S,I}}{dt} = 0$:

$$\begin{aligned} P_S &= \frac{P_I^L \frac{N_I T_S}{N_S T_I} + P_S^L(\frac{N_I}{N_S T_I V} + 1)}{\frac{N_I}{N_S T_I V} + \frac{N_I T_S}{N_S T_I} + 1}, \\ P_I &= \frac{P_I^L(\frac{N_I}{N_S T_I V} + \frac{N_I T_S}{N_S T_I}) + P_S^L}{\frac{N_I}{N_S T_I V} + \frac{N_I T_S}{N_S T_I} + 1}. \end{aligned} \tag{4.9}$$

From the equation 4.8, it can be seen that the nuclear polarization will grow faster with high electron concentration N_S/N_I, short electron relaxation time T_S and long nuclear relaxation time T_I. These conditions can be summarized in the following way:

$$\frac{N_I T_S}{N_S T_I} \ll 1. \tag{4.10}$$

If this condition holds, the evolution equations 4.9 can be simplified [30]:

$$\begin{aligned} P_S &= \frac{P_S^L(\frac{N_I}{N_S T_I V} + 1)}{\frac{N_I}{N_S T_I V} + \frac{N_I T_S}{N_S T_I} + 1} \simeq P_S^L, \\ P_I &= \frac{P_I^L(\frac{N_I}{N_S T_I V}) + P_S^L}{\frac{N_I}{N_S T_I V} + 1}. \end{aligned} \tag{4.11}$$

In addition, if the electron spin transitions are taking place at a rate $N_S V$ that is much faster than the relaxation times of the protons, the thermal equilibrium electron polarization can be completely transferred to the protons. In this scheme, the protons can reach a polarization as high as the electron equilibrium value:

$$P_I^{max} = P_S^L. \tag{4.12}$$

In principle, this mechanism works only for the protons relatively close to the paramagnetic centers, however, the remote protons also become polarized through the phenomenon called 'spin diffusion'. The 'spin diffusion' is produced by the nuclear dipole-dipole interaction, which induces mutual spin flips of two neighboring nuclear spins, providing a method for the transport of the nuclear polarization throughout the target material. Therefore, the nuclear polarization is created in the vicinity of the free electrons, and then is transmitted to the remote nucleons [32].

4.2.3 Equal Spin Temperature Theory

In the ideal solid state effect only one of the forbidden transitions is excited. This is true if the electron paramagnetic resonance (EPR) line width (D) is much less than the nuclear Larmor frequency ω_I. The condition holds in target materials where the electron concentration is small enough that the electron spin-spin interactions do not enter the picture. However, modern polarized target materials contain a high concentration of unpaired electrons, on the order of $10^{19} e/cm^3$. The high electron concentration leads to an additional static magnetic field seen by the electrons. The electron-electron dipole interaction is weak compared to the Zeeman interaction, and introduces a perturbation of the electron energy levels, so that the energy levels are not discrete anymore, but become bands of quasi-continuous states, called the 'spin packets' [33] [30]. The distributions of the occupation numbers within the broadened resonance line reach a state of internal equilibrium at a temperature different from the lattice temperature. This spin temperature influences the nuclear polarization. Spin temperature models describe the DNP process in polarized target materials more accurately than does the ideal solid state effect.

Spin temperature models introduce the electron Zeeman reservoir temperature T_{Ze} and the electron dipole interaction reservoir temperature T_{SS}. These temperatures define the populations of spin packets and the distribution within each packet. T_{SS} is introduced as it describes the additional energy reservoir independent from the Zeeman and lattice reservoir. Generally, two temperatures are needed for a description of a spin system. The electron Zeeman temperature defines the population distribution of the spin packets. For a spin 1/2 system the distribution becomes [30]:

$$n_- - n_+ \sim \exp(-\frac{\hbar\omega_s}{2kT_{Ze}}). \tag{4.13}$$

The spin-spin temperature T_{SS} describes the distribution within the spin packets according to the dipole interaction:

$$n_\pm(\omega - \omega_S) \sim \exp(-\frac{\hbar(\omega - \omega_s)}{2kT_{SS}}), \tag{4.14}$$

where ω is the running variable. Combining the two equations, the population difference between the Zeeman levels is obtained:

$$(n_- - n_+)(\omega - \omega_S) \sim \exp\left[-\frac{\hbar}{2k}(\frac{\omega_S}{T_{Ze}} - \frac{\omega_S - \omega}{T_{SS}})\right]. \tag{4.15}$$

At thermal equilibrium and in the absence of the rf field, T_{Ze} and T_{SS} become equal to the lattice temperature, so that after a period of thermal relaxation:

$$(n_{-} - n_{+})(\omega - \omega_S)^{TE} = \exp(-\frac{\hbar\omega}{2kT_L}). \tag{4.16}$$

The spin temperature of the diluted electron system in a solid can be changed by rf irradiation with frequency close to ω_S. At the same time, the nuclear Zeeman and electron spin reservoirs exchange energy since they usually are of a similar size. As a result of these processes, the nuclear Zeeman reservoir comes to thermal equilibrium with the combined electron Zeeman and dipolar reservoirs. This leads to the transfer of the electron polarization to the nucleons.

In this scheme, the DNP process can be described in two main steps [33]. In the first step, an rf field with frequency $\omega_s - \delta\omega$ 'cools' the electron spin-spin energy reservoir. As the energy from the field is absorbed by the spin system, $E = \hbar\omega_s$ is responsible for changing the electron Zeeman energy and flipping the electron spin, while the rest of the energy $E = \hbar\delta\omega$ is absorbed by the electron spin-spin interaction reservoir. In the second step, called 'thermal mixing', the Zeeman nuclear and electron spin-spin reservoirs exchange energy as they come to a thermal equilibrium. This is achieved through the forbidden transitions in which a nucleon spin flips along with the flip-flop of two electrons. In such transitions, the nuclear Zeeman energy changes by $\hbar\omega_I$ while the electron Zeeman energy remains constant. Since the lattice is not participating in the transition, the spin-spin reservoir is responsible for the energy conservation, so the energy $E = \hbar\omega_I$ is exchanged between the electron spin-spin and nuclear Zeeman reservoirs. Finally, due to this exchange, both reservoirs acquire a common temperature. In the case of the equal spin temperatures, the nuclear polarization is given by the common spin temperature T_{SS}:

$$P_{1/2} = \tanh(\frac{\mu B}{kT_{SS}}). \tag{4.17}$$

An interesting consequence of this model, is that the optimum frequency for the DNP process is given by the temperature of the spin-spin reservoir, so that nuclei with different magnetic moments can be simultaneously polarized at the same microwave frequency [33].

4.3 Target Materials

Target materials suitable for scattering experiments need to satisfy several conditions, such as a high ratio of free to bound nucleons, sufficient resistance to radiation damage and the possibility of repairing the radiation damage. The obvious choices such as H_2 for the protons and D_2 for the deuterons are in their para-state with spin zero at low temperatures, and are not polarizable. The materials currently used in polarized targets have been chosen as a result of many experiments testing various host and dopant materials. Typical materials are butanol, propandiol, LiH, NH_3 and deuterated versions of these [33]. A paramagnetic dopant needs to be embedded in these target materials to provide the unpaired electrons, either chemically or by irradiation.

The target material used in the EG1b experiment was $^{15}NH_3$ for the polarized protons and $^{15}ND_3$ for the polarized deuterons. Ammonia targets produce high polarizations and are resistant to radiation damage. Also, this damage is relatively easy to repair by a heating process, called annealing. Another advantage of ammonia targets is a high ratio of free nucleons (3/18). One disadvantage of this material is the polarizability of ^{15}N. However, the polarization is carried by the unpaired proton in the ^{15}N nucleus, so the small correction to the data can be estimated adequately.

The target material is prepared by slowly freezing the ammonia gas at 77 K, and then crushing it into small pieces, approximately $1-3$ mm in diameter. The small sizes of the granules help to keep them efficiently cooled by the liquid helium during the experiment, and reduce potential damage from the beam heating. After this procedure, paramagnetic centers are introduced into the material to make it suitable for the DNP. Free electrons, lattice 'holes', or free radicals can generally serve as paramagnetic centers in the target material. Paramagnetic centers in the form of free radicals are introduced into ammonia targets by irradiating the beads with an electron beam. Electron spin resonance measurements showed that the free radicals $\mathrm{N}\dot{H}_2$ and $\mathrm{N}\dot{D}_2$ created by irradiation serve as paramagnetic centers in the solid $^{15}\mathrm{NH}_3$ and $^{15}\mathrm{ND}_3$ targets respectively [33]. In order to keep the ESR line width D relatively narrow, the number of centers needs to be optimized, as an excess is harmful to the polarization process.

During a scattering experiment, the target material continues to accumulate paramagnetic centers. While the pre-experimental radiation doping takes place at relatively high temperatures of $80-90$ K, the centers are created and will be stable at 1 K. These low temperature stable atoms can have a g-factor different from 2, which would cause their Larmor frequency to be different from the frequency of the polarizing microwave field. As a result of this, the newly created centers do not participate in the DNP process, but they still contribute to the relaxation process, via dipolar

Figure 4.3: A photo of target cell after beam exposure.The beads in the center turn purple from the beam exposure, while the edges do not receive much beam.

coupling to the nuclear spins [30]. As the number of new centers increases, the nuclear polarization deteriorates. The damage can be repaired by heating the target material to the temperature $\sim 80-90$ K for $^{15}NH_3$ and higher for $^{15}ND_3$. During this process, the free radicals created at low temperature are recombined and the number of paramagnetic centers decreases. In the case of the $^{15}NH_3$ targets, the maximum polarization is reduced after each annealing cycle, which shows that there is a second mechanism of radiation damage [30]. After several cycles, the target material has to be replaced.

The target material for EG1b experiment was frozen and granulated at the Polarized Target Lab of the Physics Department of University of Virginia. This material was irradiated in the summer of 1998 at the FEL facility of TJNAF. The polarization values for the $^{15}NH_3$ material varied from 60 to 90% during the run. The target had to be annealed approximately every $2-3$ weeks. A picture of the ammonia granules recovered after the experiment is shown in Fig. 4.3. The beads change their color from white and grey to purple after exposure to the electron beam. The edges of the target cell received little beam, and the material retained its white color, while beads in the center of the cell turned purple.

4.4 EG1b Polarized Target

The EG1b polarized target was designed and built by a collaboration of the Italian Istituto Nazionale di Fisica Nucleare, TJNAF, Oxford Instruments and the University of Virginia. The design of the target cryostat was constrained by the unique geometry of the Hall B detector. The cryostat had to fit inside a small magnetic field-free region in the center of the detector, it had to be accessible for the insertion of the target material, and it had to include apertures for the scattered particles in the forward and side directions. The target system consists of a superconducting 5 T magnet, a helium evaporation refrigerator, microwave and NMR systems and an insert housing the target material. Each of these components is described in the following subsections. A diagram of the target inside the Hall B detector is shown in Figure 4.4.

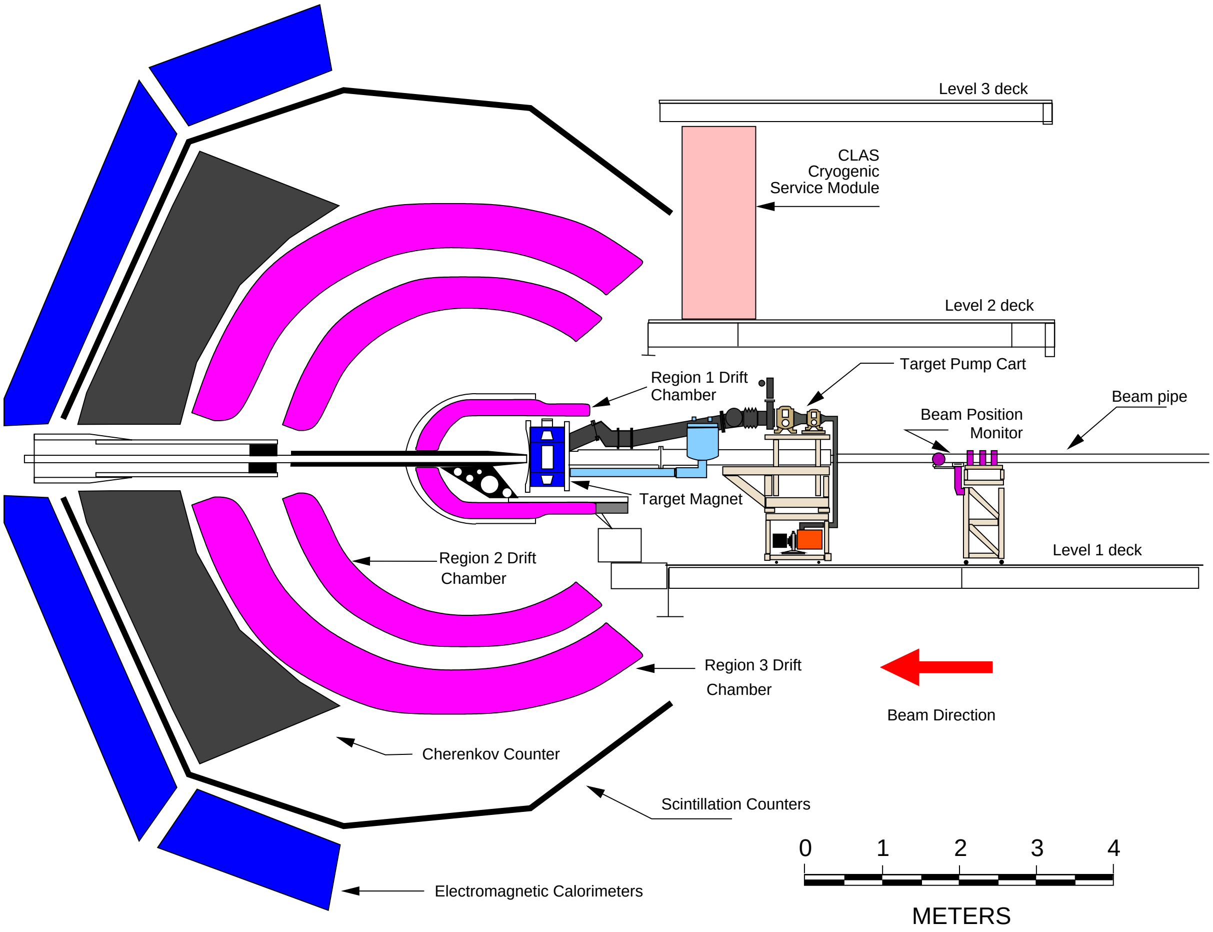

Figure 4.4: Polarized target inside the CLAS detector.

4.4.1 The Magnet

The 5 T magnetic field is produced by a superconducting pair of Helmholtz coils, made out of Niobium-Titanium alloy with critical temperature $\sim 9K$. Below the critical temperature, the magnet becomes superconducting. A schematic diagram of the magnet is shown in Figure 4.5. When the superconducting switch is heated above its critical temperature its resistance is much higher than that of the rest of the magnet, so that the current circulates between the magnet and the leads. After

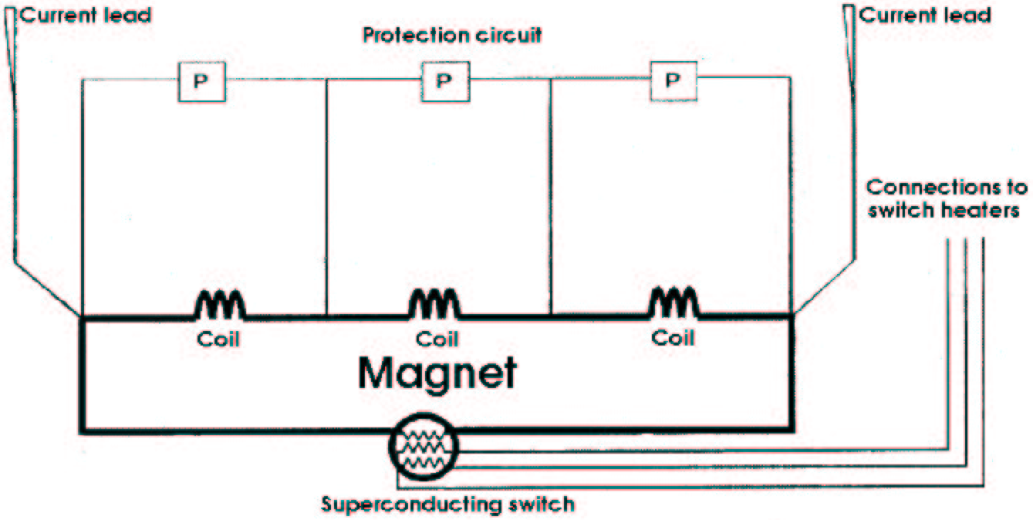

Figure 4.5: Electric circuit diagram of the magnet. Superconducting switch is used to put the magnet into 'persistent' mode.

the magnet is energized, the switch is cooled to make it superconducting, and forces current to circulate through the magnet coils and switch, bypassing the leads. Then, the current in the leads is ramped down. At this point, the current is circulating through the superconducting magnet coils alone and the energy loss is very small. In this 'persistent' mode, the field decays very slowly, at a rate of 1 part in 10^6 per hour.

The magnet produces a uniform field, varying less than 10^{-4} over a cylindrical volume of 20 mm in length and diameter [34]. The bore of the magnet is 20 cm in diameter, with the $\pm 50^\circ$ aperture for particles scattered in the forward direction. The 8 cm gap between the Helmholtz coils provides additional apertures for particles scattered at large angles of $70 - 105^\circ$. The axis of the magnet is parallel to the beam direction; this configuration is necessary to produce longitudinal electron polarization. In addition, the target magnetic field does not interact with the electron beam, but it is effective in shielding the drift chambers from the low energy Møller electrons. The scattered particles are bent by the target field in the azimuthal direction. The field falls off rapidly with distance ($\sim 1/r^3$), and is negligible at the drift chambers. The influence of the target field is taken into account during the particle reconstruction.

The magnet is cooled by the liquid helium bath at 4.2 K. Helium is supplied by a connecting 2 m tube from the reservoir which is filled from a 500 l buffer dewar. In turn, the dewar is filled by the TJNAF End Station Refrigerator. Due to the space limitation, only the magnet chamber is located inside the detector while the reservoir and connecting piping is located outside CLAS. The total volume of LHe in the magnet chamber and reservoir is 25 l. The connecting pipe from the reservoir to the magnet chamber is the only opening into the magnet space. The target cryostat containing the magnet and other parts of the target system is surrounded by a vacuum region to isolate it from its surroundings. The outer vacuum chamber (OVC) has a valve to relieve the pressure in case of a cryogenic leak into the vacuum space. The magnet reservoir has four mechanical pressure relief valves to vent helium gas in case of a magnet quench.

The boil-off from the magnet chamber is guided through a heat exchanger that cools the aluminum radiation shield surrounding the magnet. Multi-layers of aluminized mylar superinsulation surround the magnet as well. Six apertures are cut from the aluminum heat shield, corresponding to the six sectors of CLAS. These apertures minimize the energy losses experienced by the particles scattered at large angles [34].

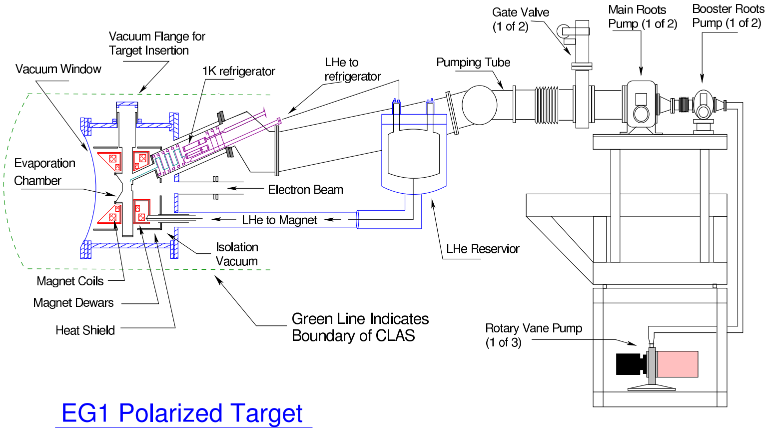

Figure 4.6: Diagram of the polarized target system. The cryostat contains a superconducting 5 T magnet which is cooled by LHe supplied from a LHe reservoir.

4.4.2 The Evaporation Refrigerator

The helium in the target chamber is supplied from a ^{4}He evaporation refrigerator that cools it to ~ 1 K. A cooling power of approximately 0.8 W is provided by a system of Roots and rotary-vane vacuum pumps that reach a pumping speed for helium gas of 3300 m^3/h [34]. The refrigerator is inserted through a 200 mm diameter pumping tube that connects the banjo and the pumping system. Due to the space restrictions imposed by CLAS, the tube is at an angle of 30° from the horizontal. LHe is supplied to the refrigerator from the same reservoir as the magnet through a vacuum-insulated and vapor cooled transfer line. The refrigerator consists of the copper separator pot, two sets of heat exchangers, and two lines that deliver helium to the banjo. LHe enters the separator pot, where the rotary pump connected to the separator induces the flow. The purpose of the separator is to separate liquid from helium vapor. LHe passes through the sintered filter with liquid accumulating at the bottom of the pot, while vapor is blocked by the sinter, and then pumped away. The exiting vapor is used to cool the heat exchangers. The liquid accumulated in the separator is guided into the target chamber through either of the two lines controlled by needle valves. The 'bypass' tube is straight while the 'run' tube is a spiral in thermal contact with the lower heat exchanger, so that LHe is cooled by the pumped vapor while passing through the 'run' tube. The 'bypass' line is used during the initial cooldown of the system, while the 'run' line is used during the normal running. Various sensors are used to monitor the temperature, pressure and flow rates of LHe. A diagram of the refrigerator is shown in Figure 4.7.

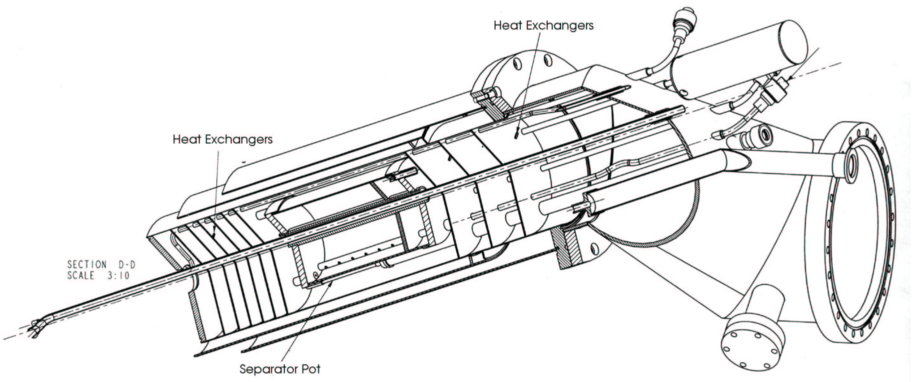

Figure 4.7: Helium Evaporation Refrigerator.

4.4.3 The target chamber and the minicup

The target chamber (called the 'banjo') is located at the bore of the magnet coils. It is suspended from the top of the cryostat, and thermally insulated by the outer vacuum can. Both the banjo and the suspension tube are made of the stainless steel. The tube, used for target insertion, is thermally connected to the 75 K heat shield of the magnet. The banjo contains the LHe bath for the target material.The banjo has six 0.05 mm windows parallel to the magnet apertures through which the scattered particles can exit. The back plane of the banjo has an aluminum window of thickness 0.071 mm and diameter of 21 mm for the entering electron beam. The closing window has a conical shape to minimize the distance the beam has to travel between the entrance and exit windows. The exit window is located at the center of the cone, with a thickness of 0.071 mm and a diameter of 42 mm [34].

An additional container, called the 'minicup', was added to the banjo to reduce the pumping volume of liquid helium, and potentially to reduce the temperature of the target beads. The minicup consists of a rectangular column made from Kapton foil, attached to a base made of Torlon. It is 19.56 cm tall, 3.81 cm wide and 0.13 mm thick. It is wide enough to allow the target insert to be placed inside the cup without touching the walls. Torlon was chosen for the base because it has poor thermal conductivity, minimizing heat exchange between the minicup and the banjo. In addition, the base has a hexagonal shape, so that it fits in the cylindrical tail of the banjo, but only touches at its six vertices. The minicup was equipped with a superconducting helium level probe, a resistor thermometer, and a 100 Ω heater on the bottom. The heater was used to evaporate LHe before annealing the target. The minicup and the banjo are shown in Figure 4.8.

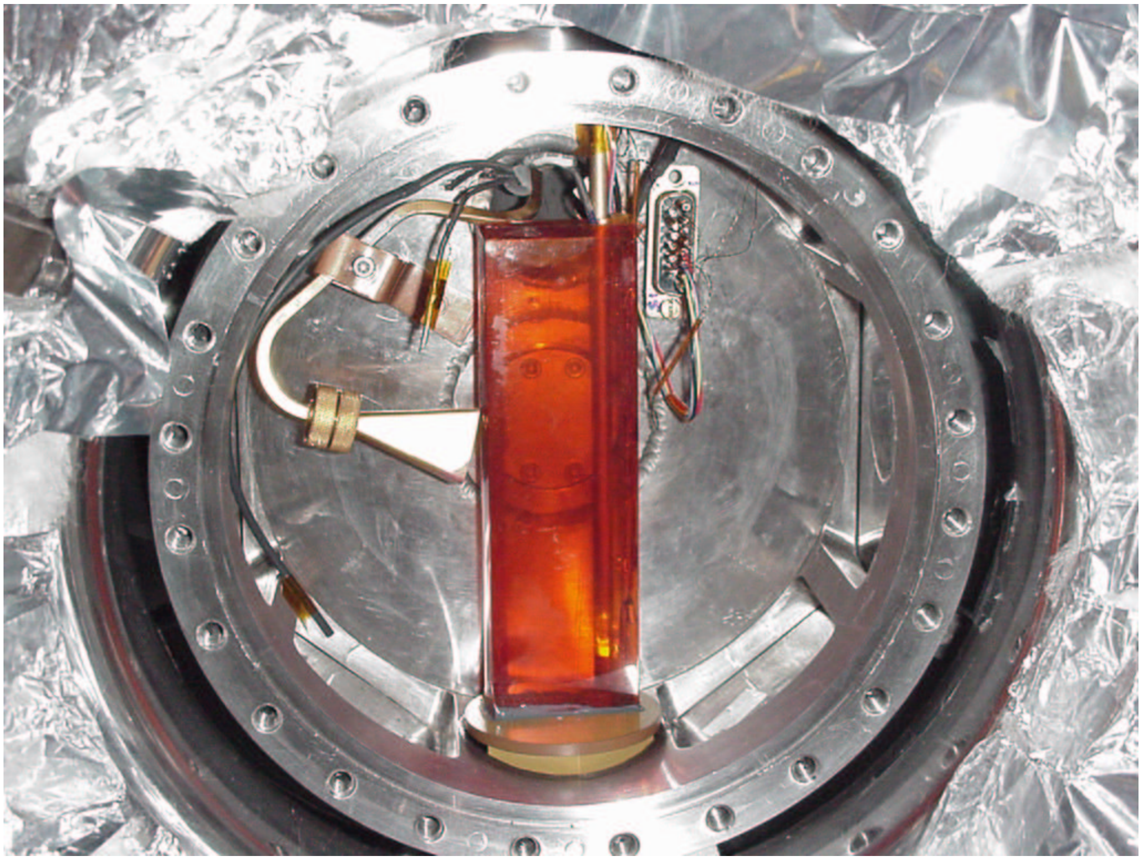

Figure 4.8: Banjo with the minicup.

4.4.4 The Target Inserts

The target material and various instrumentation such as temperature sensors, NMR cables and radiation waveguides are attached to the target insert. It was designed and built by the INFN of Genova. As shown in Fig 4.9, it consists of an aluminum structure with four plastic cells for the target material. The target cells were made out of polychlorotrifluoroethylene (PCTFE) with a thickness of 0.2 mm. This material was chosen because it is hydrogen-free and would not produce an NMR background at the proton Larmor frequency, and it has better resistance to radiation damage than other materials. The cells are 15 mm in diameter and 10 mm in length with 0.025 mm aluminum entrance windows and 0.05 mm kapton exit windows. Tiny holes in the exit windows allow LHe to enter and cool the ammonia beads. The aluminum structure is attached to a brass disk which is connected to the 75 K magnet shield, minimizing the heat load on the insert. The brass disk is also used as a heat sink for the NMR and microwave instrumentation. A block of teflon is inserted between the aluminum structure and the brass disk to reduce thermal conductivity along the insert. The brass disk is connected to the top flange by a threaded rod, which is attached through a vacuum tight seal to a stepping motor. The remotely controlled stepping motor is used to move the desired cell into the beam. With this design it was possible to make measurements with different targets without opening the cryostat.

Two of the cells were filled with ammonia beads: one with $^{15}NH_3$ and the other with $^{15}ND_3$. Another cell contained a 2.3 mm thick carbon disk while the fourth cell was left empty. The carbon and the empty cells were used for background measurements and systematic checks.

In order to maximize the amount of ammonia in the cells, and to reduce background the NMR coils used to monitor the polarization were wrapped around the outside surface of the cells . The geometry of the coils was optimized to make them maximally sensitive to the target polarization. The coils were made out of 0.15 mm thick CuNi tubing, and bent into rectangular loops. One loop was used to measure the polarization of the $^{15}NH_3$ beads, while the $^{15}ND_3$ coil requires higher inductance, and four superimposed loops had to be used. The NMR coils were connected to the top flange by the cryogenic coaxial coils.

Temperature sensors, such as thermocouples and RuO resistors, were located at

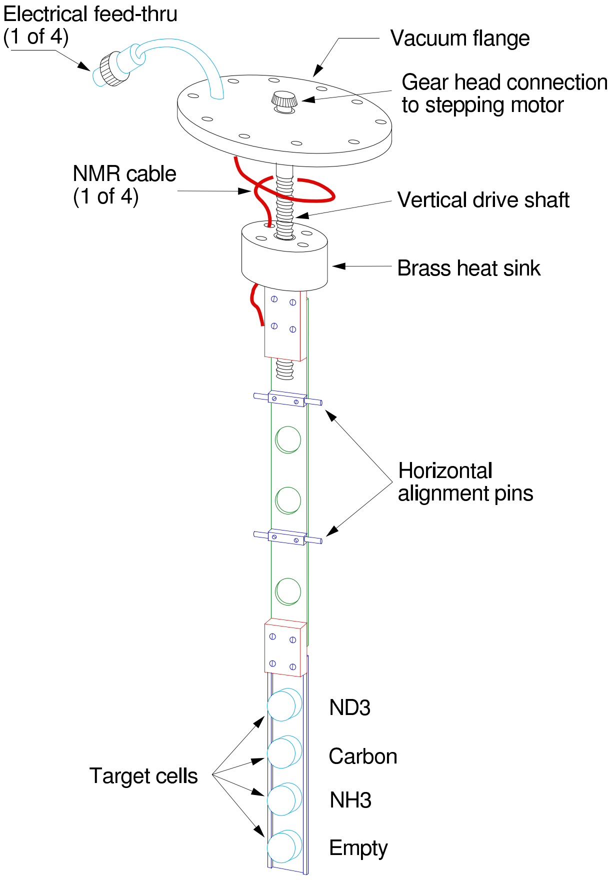

Figure 4.9: Target Insert.

various points in the insert. Heater coils were placed below each ammonia target cell for annealing.

A second target insert was designed and built by the Jefferson Lab Polarized Target Group for the purpose of background studies using solid ^{15}N. This allowed the first measurements of electron scattering from solid ^{15}N, providing data needed to subtract the ^{15}N contribution from the ^{15}NH$_3$ scattering data. The insert consisted of a Torlon cell of 15.7 mm in diameter and 12.7 mm in length, covered by kapton windows on both sides. Isotopically enriched ^{15}N gas at room temperature is fed into the cell. The insert was placed then into the target chamber where it was cooled by LHe, causing the gas inside the cell to condense. A heater wire was wrapped around the filling tubes to prevent the ^{15}N from freezing and plugging the tubes before the cell was full. A carbon disk identical to the one on the polarized target insert was placed on the ^{15}N insert for additional checks [34]. A picture of the ^{15}N insert stick is shown in Fig 4.10.

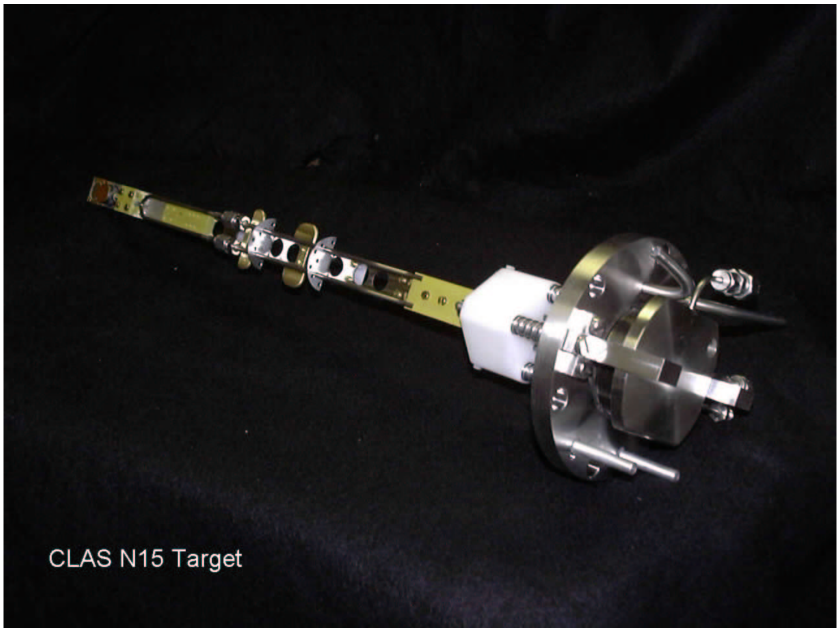

Figure 4.10: ^{15}N insert stick.

4.4.5 The Microwave system

During the experiment, the ammonia beads were irradiated by the microwave field used for the DNP process. Microwaves were generated by an Extended Interaction Oscillator (EIO), located at the top of the refrigerator. The EIO generator consists of a klystron in which electrons are emitted from a cathode filament and accelerated through a resonant cavity towards a collector. While passing through the resonant cavity electrons emit coherent radiation at a fixed frequency. This frequency can be changed by mechanically adjusting the size of the cavity. The allowed adjustment is ±2% of the central value, which was 140 GHz during the experiment. This value corresponds to the electron Larmor frequency at the 5 T magnetic field. The negative and positive nuclear spin states are separated by approximately 400 MHz, so that either polarization state can be achieved by varying the microwave frequency, and without reversing the magnetic field.

Microwaves are delivered to the target material through a system of wave guides, consisting of rectangular WR-6 waveguides outside the cryostat and a 5 mm CuNi tube inside. The connection between the tube and the waveguide is made through a rectangular-to-round adaptor, and is thermally isolated through a vacuum-tight seal made by a 0.1 mm thick piece of FEP film. The CuNi tube is inserted into the cryostat through an opening in the refrigerator pumping tube, and is connected to a gold-plated rectangular horn that is oriented to transmit microwaves to whichever target cell is in the electron beam. The frequency of the microwaves is measured by an EIP model 599C frequency counter, while the generated power is measured by an HP model 432 power meter.

4.4.6 The NMR system

The principle of the Nuclear Magnetic Resonance

The target polarization during the experiment was monitored by a Nuclear Magnetic Resonance (NMR) System. As implied by its name, the method lies in inducing and detecting nuclear magnetic transitions, where the rate of transitions is proportional to the population difference between the energy levels, therefore indicating the original polarization value. The magnetization of the material $\vec{M}$ is related to its polarization P. For a sample of volume, V, with N spins, each with the spin value I, the macroscopic magnetization is defined as [30]:

$$\vec{M} = Ng\mu_N IP_I = \sum_i^N \frac{\vec{\mu_i}}{V}, \tag{4.18}$$

where $\vec{\mu_i}$ is the magnetic moment of the individual spins.

If a rotating rf-field with amplitude, $\vec{B_1}$, and frequency, ω, is applied perpendicularly to the external field, $\vec{B_0}$, nuclear Zeeman transitions are induced with the probability depending on $\Delta\omega = \omega_0 - \omega$, where ω_0 is the Larmor frequency. The rate of these transitions will indicate the polarization of the target nucleons. An oscillating rf-field of frequency ω_1 is generated by a current in the coil that surrounds the material, and which is a part of the rf-resonance circuit. Depending on the sign of the target polarization, the coil either absorbs or emits energy with a corresponding energy gain or loss in the resonance circuit. In other words, the transverse magnetization sweeps through the coil with frequency ω and induces a voltage in the rf circuit, which is measured and translated into the corresponding polarization of the sample.

In order not to reduce the polarization by the measurement process, the amplitude of B_1 is taken to be relatively small: [30]

$$\omega_1^2 = \gamma^2 B_1^2 \ll \frac{1}{T_1 T_2}, \tag{4.19}$$

where T_1 and T_2 are the spin-lattice and spin-spin relaxation times respectively. The sweeping transverse magnetization can be pictured in a frame of reference which rotates around the static field B_0 with the frequency ω. The angle α between the transverse magnetization and the rf-field direction is [30]:

$$\tan\alpha = M_{y'}/M_{x'} = \frac{1}{T_2(\omega_0 - \omega)}. \tag{4.20}$$

The transverse magnetization is:

$$\vec{M_\perp} = M_\perp \begin{pmatrix} cos(\alpha) \\ sin(\alpha) \\ 0 \end{pmatrix}, \quad M_\perp = \sqrt{M_{x'}^2 + M_{y'}^2}. \tag{4.21}$$

As the rf-frequency is slowly swept through the Larmor frequency, the transverse magnetization completes a circle in the x', y' plane as shown in Fig.4.11. The magnetization consists of the absorptive part $M_{y'}$ and the dispersive part $M_{x'}$. At resonance the dispersive part of the magnetization is zero, while the absorptive part is at maximum. This absorptive component is used for the NMR measurements.

Detection method

During the experiment, the target polarization was measured using the Q-meter technique. The Q-meter measures the voltage and corresponding power loss or gain due to the induced nuclear spin transitions. The technique makes use of the change in magnetic susceptibility of the material. The susceptibility of a system is defined as [30]:

$$M_z = \chi_0 H_0 = \chi_0 \frac{1}{\mu_0} B_0, \tag{4.22}$$

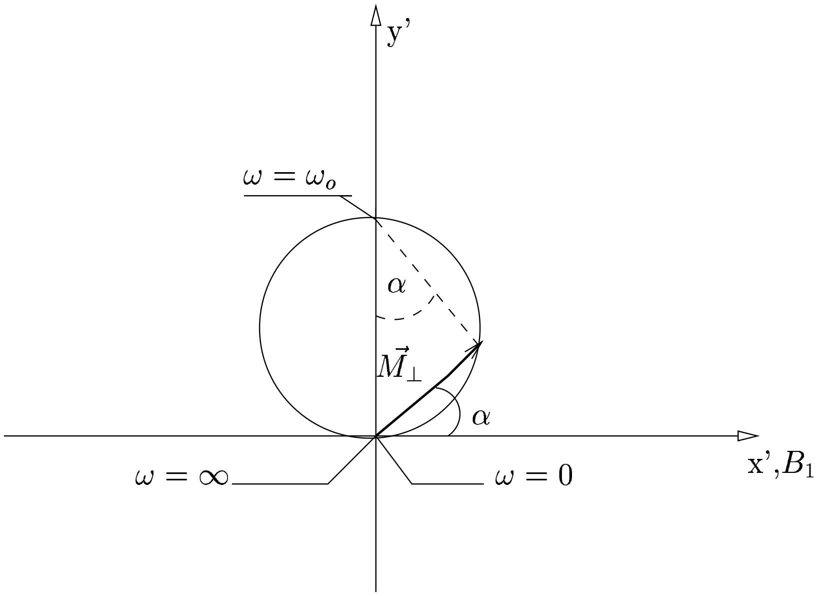

Figure 4.11: The transverse magnetization in the rotating frame. As the rf-frequency is slowly swept through the Larmor frequency, the transverse magnetization completes a circle in the x', y'.

where μ_0 is the permeability of the material. Similar to magnetization, the susceptibility can be written as a sum of real (dispersive) and imaginary (absorptive) parts.

$$\chi = \chi' - i\chi'' = \frac{\mu_0}{2B_1}(M_{x'} + iM_{y'}). \tag{4.23}$$

The voltage across the circuit is proportional to the impedance of the coil, which in turn is proportional to the susceptibility of the material filling the coil. The impedance of the circuit is:

$$\begin{aligned} Z(\omega) &= R_c + i\omega L_c(1 + 4\pi\eta\chi(\omega)), \qquad (4.24) \\ Z(\omega) &= R_c + \omega L_c \cdot 4\pi\eta\chi''(\omega) + i\omega L_c(1 + 4\pi\eta\chi'(\omega)), \end{aligned}$$

where R_c is a coil resistance, η is the filling factor of the coil and L_c is the inductance of the empty coil. In the vicinity of the resonant frequency the dispersive part χ' becomes small compared to the absorptive part χ''. Therefore, the change in energy due to the nuclear Zeeman transitions is reflected in the absorptive part of the impedance. The power gained or dissipated is proportional to χ'' [30]:

$$P_c = \frac{1}{2} T_c^2 \omega L_c \cdot 4\pi\eta\chi''(\omega), \tag{4.25}$$

with I_c being the current circulating in the coil. The energy and power change of the system is defined by the difference in Zeeman populations. Therefore the absorptive part of the susceptibility measures the polarization P of the sample [33]:

$$P = C \cdot \int_{\Delta\omega} \chi''(\omega) d(\omega). \tag{4.26}$$

Since the Zeeman levels are broadened, χ'' has to be integrated over the entire sweeping frequency region. The constant of proportionality is determined by a calibration measurement in thermal equilibrium.

Fig. 4.12 shows the diagram of the Q-meter circuit. The coil surrounding the target material inside the cryogenic target chamber is connected by a coaxial cable to the electronics of a Q-meter at room temperature. In order to reduce the effects of capacitance and resistance of the connecting cable on the LCR circuit, the length of the cable is chosen to be an integer number of half wavelengths at the Larmor frequency. The Q-meter is designed to measure the voltage change across the circuit as a function of the input frequency. The circuit is powered by a generator which sweeps the rf-frequency through the Larmor frequency of the target. A Rohde and

Swartz RF generator was used during the experiment, with an input voltage of 100mV rms. As the target material absorbs or emits energy, the inductance of the coil changes, causing the impedance change of the circuit. The change in impedance could be read from the change of the voltage output of the circuit as long as the current is constant. To ensure the constant current condition, the circuit contains a high impedance amplifier with $R_A = 10\Omega$. The complex output voltage $V(\omega, \chi)$ is

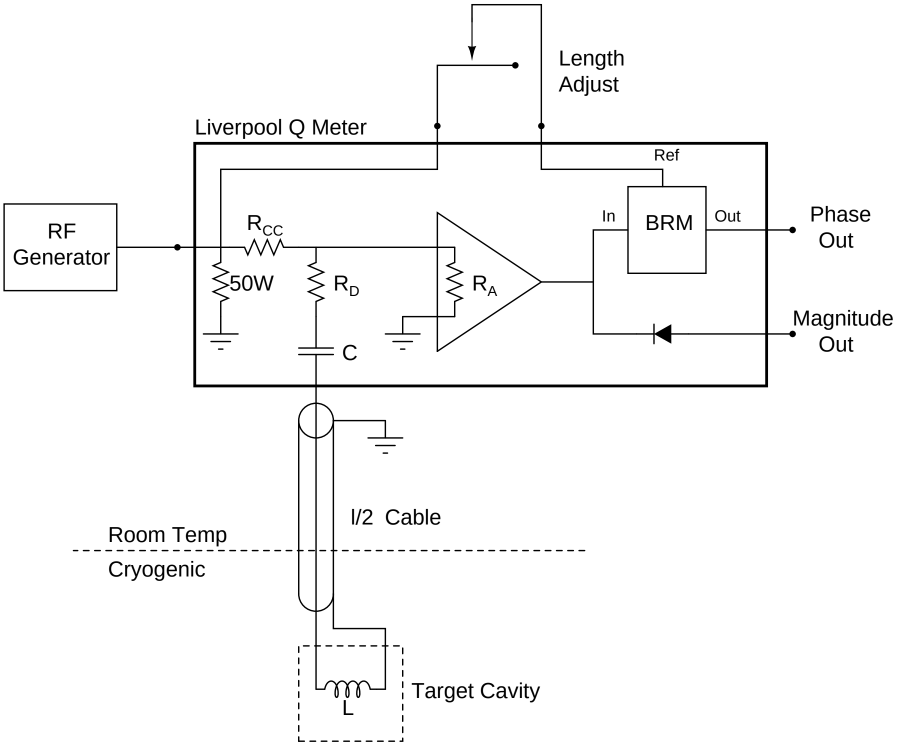

Figure 4.12: Liverpool Q-meter circuit diagram. The coil surrounding the target material inside a cryogenic target chamber is connected by a coaxial cable to the electronics of a Q-meter. The circuit is powered by a generator which sweeps the rf-frequency through the Larmor frequency of the target. As the target material absorbs or emits energy, the inductance of the coil changes, causing the impedance change of the circuit. The change in impedance could be read from the change of the voltage output of the circuit.

read from the diode output of the circuit. This output contains both dispersive and absorptive parts, so in order to isolate the absorptive part, the signal passes through a phase detector called the Balanced Ring Modulator (BRM). The phase detector compares the input rf signal and the output signal, and the phase between the two is set to zero by varying the length of an adjustable piece of cable from the generator to the BRM. After the real part of the voltage is selected, it contains χ'', and the so-called Q-curve, which is a background measurement of the Q-meter response to the input frequency away from the resonance, when χ is very small. The Q-curve is obtained by taking a measurement at the value of the external magnetic field B_0 which sets the Larmor frequency ω_0 of the target outside the frequency range of the sweep. In these conditions, χ'' is zero, and χ' is very small. The background Q-curve is subtracted from the resonant signal, and the resulting output is [30]:

$$S(\omega) = Re\left(V(\omega,\chi) - V(\omega,0)\right) \approx \chi''(\omega). \tag{4.27}$$

The baseline subtraction can be inaccurate for various reasons; in order to correct for it, a polynomial fit is made to the edges of the signal and subtracted. The result of these two subtractions is a so-called poly-subtracted signal. The resulting signal will still contain some multiplicative and additive constants due to the other components of the circuit, so it cannot be directly translated into the polarization of the sample. The system has to be calibrated first, and it is done using the thermal equilibrium measurements.

Table 4.2: NMR Parameters.

Name	Symbol	Value
Bohr Magneton	μ_B	$5.788 \times 10^{-11} MeV \cdot T^{-1}$
Nuclear Magneton	μ_N	$3.152 \times 10^{-14} MeV \cdot T^{-1}$
Electron Magnetic moment	μ_e	$1.001\mu_B$
Proton Magnetic moment	μ_p	$2.793\mu_N$
External Magnetic field	B_0	5.004 T
Larmor proton freq.	ω_0	212.17 MHz
Freq. sweep width	$\Delta\omega = \omega_2 - \omega_1$	400 KHz
RF input level	V	100 mV $< rms >$

Thermal Equilibrium Calibration

The calibration is performed by relating the calculable polarization P_{TE} to the area under the subtracted Q-curve of the TE signal. With no applied RF, the polarization at thermal equilibrium for the spin 1/2 protons is given by the Brillouin function:

$$P_{TE} = P_{1/2} = \tanh(\frac{\hbar\omega}{2k_BT}) = \tanh(\frac{\mu B_0}{k_BT}), \tag{4.28}$$

where k_B is the Boltzmann constant. At the magnetic field $B_0 = 5T$ and temperature $T = 1K$, the equilibrium polarization of the protons is 0.51%. Relevant parameters are shown in Table 4.2. A constant of proportionality C is obtained by relating the value of P_{TE} to the area under the NMR curve obtained at thermal equilibrium:

$$P_{TE} = C \cdot A_{TE} \approx C \cdot \int_{\omega_1}^{\omega_2} S_{TE} d\omega, \tag{4.29}$$

where ω_1 and ω_2 are the lower and upper limits of the rf-frequency range. This procedure is illustrated in Fig. 4.13.

During the DNP process, the resulting enhanced polarization is calculated:

$$P_{enh} = C \cdot \int_{\omega_1}^{\omega_2} S_{enh} d\omega. \tag{4.30}$$

Control software and system performance

The polarized target software consisted of two systems operating on two different computers. One system which controlled the flow of cryogens through the target is called the Experimental Physics and Industrial Control Software (EPICS). It ran on a VME-based single board computer, located in the experimental hall [34]. That computer was connected to the Jefferson Lab Local Area Network, and was accessible from any unix/linux machine on site. Most of the processes were controlled automatically with the shift workers informed of abnormal situations. Processes controlled by EPICS included filling the superconducting magnet and the refrigerator with LHe, and operation of the refrigerator valves to fill the target chamber. The second software system, using Labview 5.2, was installed on a PC computer in the experimental hall. The Labview program was used to control and record the NMR measurements, as well as to control the superconducting magnet, the microwave tube, and target insert motion. The Labview host computer was connected to another computer in the counting house to allow the shift workers to control the target without going to the hall. Communication was established between the Labview and EPICS computers, so that data could be passed from one system to another.

During the EG1b run, the target was operated for 7 months during 2000-2001. The target could operate continuously for a few days without human intervention, except when it was necessary to move the target insert, reverse direction of polarization, change targets or perform an anneal. During the experiment the typical proton polarization in the $^{15}NH_3$ target was $\sim$ 70%. The electron beam current ranged between 1 and 6 nA, so the target anneals were necessary approximately every 1 to 2 weeks. The target material was changed several times during the run.

NMR Signal Analysis

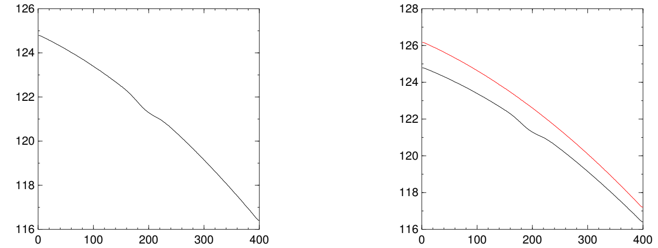

Signal is acquired by the NMR DAQ system

Baseline is subtracted from the signal

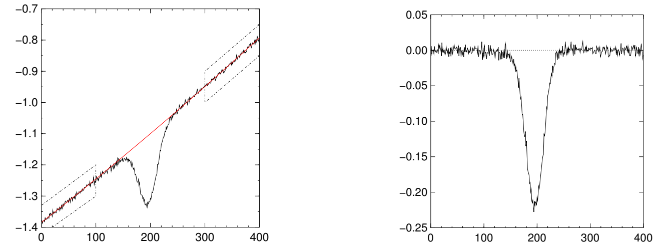

Polynomial is fit to wings of the signal

Polynomial is subtracted from the signal

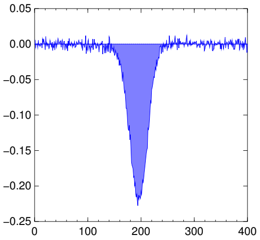

Area × CC = Polarization

Signal is integrated, giving area

Calibrating the NMR system gives polarization

Figure 4.13: Analysis of the NMR signal. A constant of proportionality CC is obtained by relating the value of P_{TE} to the area under the curve.

Chapter 5

CEBAF Large Acceptance Spectrometer

5.1 The Torus Magnet

Hall B houses the CEBAF Large Acceptance Spectrometer (CLAS), which was designed to detect multi-particle final states for the detailed study of nuclear and nucleon structure. The detector can operate with both electron and tagged-photon beams. The physics program of CLAS includes a study of nucleon resonances, search for missing resonances, measurements of the spin structure functions, and studies of nucleon correlations inside nuclei [35].

The detector's magnetic field has a toroidal configuration, instead of a more common dipole or solenoid options. This choice allows homogeneous geometrical coverage of charged particles at large angles, it provides good momentum and angle resolution and low background from electromagnetic interactions, and it leaves a field-free region around the target, which makes the operation of dynamically polarized targets possible. The magnetic field, pointing primarily in the ϕ direction, is produced by six superconducting coils arranged in a toroidal geometry around the beam line. The coils define six sectors of the detector with each sector independently instrumented to be an effective spectrometer. A diagram of the coils is shown in Fig. 5.1. The system is usually described using spherical coordinates, with the z-axis along the beam direction, the x-axis along the horizontal plane, and the y-axis along the vertical plane normal to the beam. θ is the polar scattering angle, and ϕ is the azimuthal angle. The magnet is approximately 5 m in diameter and 5 m in length. Each of its coils consists of 4 layers of 54 turns of aluminum-stabilized NbTi/Cu conductor [35]. The coils are cooled to a superconducting temperature of 4.5 K by liquid helium circulating through cooling tubes located at the edge of the windings. The heat load is

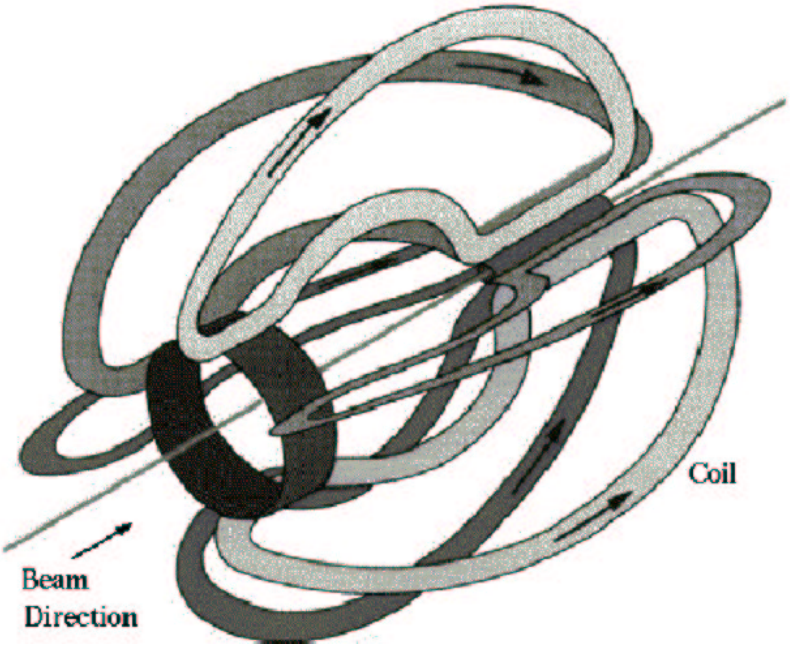

Figure 5.1: The layout of CLAS coils.

reduced by a liquid nitrogen shield and super-insulation. At the maximum allowed current of 2860 A, the integral magnetic field reaches 2.5 Tesla-meter in the forward direction, and decreases to 0.6 Tesla-meter at a scattering angle of 90°. A contour plot of magnetic field for CLAS in the midplane between two coils is shown in Fig 5.2. The magnetic field is transverse to the plane of the particle trajectory, leaving the ϕ angle unchanged. Because of zero field on the beam axis, forward going charged particles are not deflected, and the low energy particles such as Møller electrons can be deflected away by an additional magnetic field. A small normal-conducting 'mini-torus' surrounds the target to focus low momentum large angle electrons, produced by Møller scattering in the target, down the beam pipe. The mini-torus is used during the electron beam experiments, and is replaced by a scintillator start counter during the photon runs. The detector package consists of drift chambers to determine trajectories of charged particles, Cerenkov counters for electron identification, scintillation counter for measuring time of flight, and electromagnetic calorimeters to

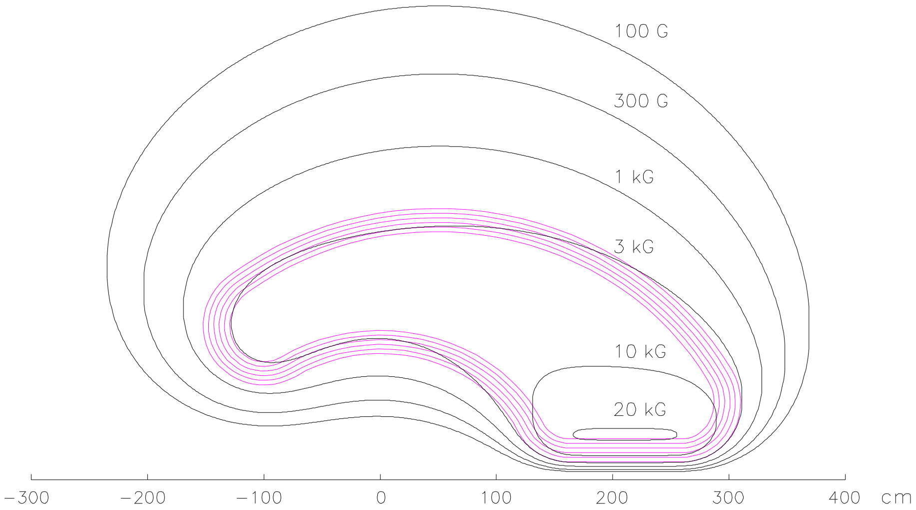

Figure 5.2: A contour of magnetic field for CLAS in the midplane between two coils.

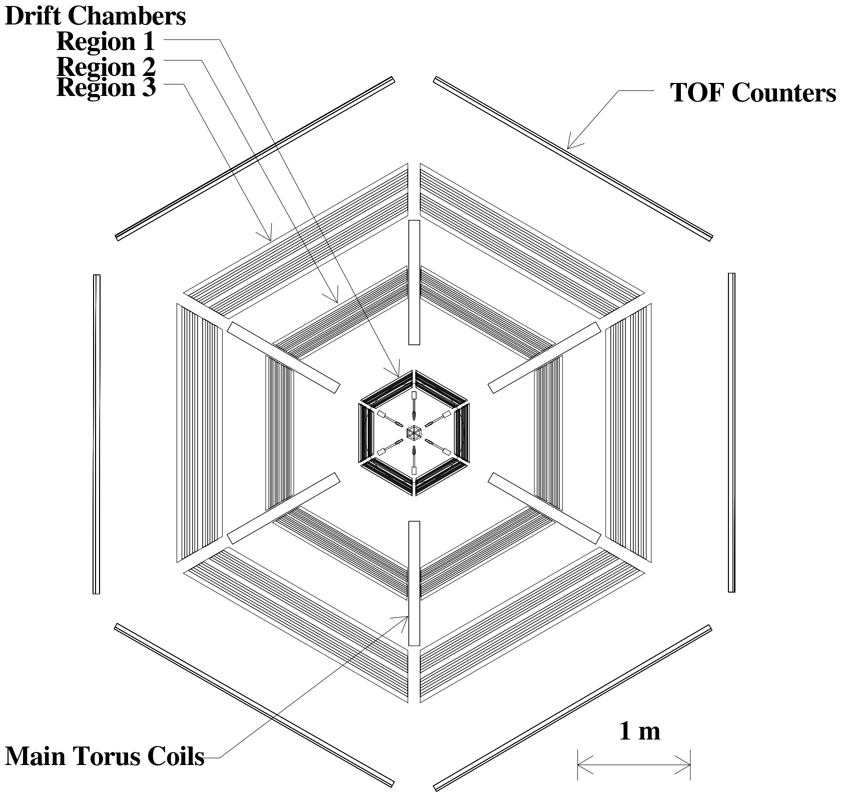

Figure 5.3: View of CLAS normal to the beam line.

detect showering particles. A view normal to the beam is shown in Fig 5.3.

5.2 Drift Chambers

The tracking of charged particles is performed by a drift chamber system. A drift chamber is a device that uses the drift time of electrons released by the ionization process in a gas to determine the spatial position of an ionizing particle. In a typical drift chamber, the chamber is filled with gas and is maintained at an electric field produced by the anode and cathode wires. The particle crossing the chamber, ionizes the gas atoms, releasing electrons which drift to the anode wire. While drifting, electrons produce more ionizations resulting in the amplification of the signal which can be detected. Electrons collect on the anode wire, producing a pulse at time t_f. The total drift time is $t_f - t_0$, where t_0 is the time when the first particle initiated the ionization. The distance from the point of ionization to the wire is determined from [36]:

$$x = \int_{t_0}^{t_f} w(t)dt, \tag{5.1}$$

where $w(t)$ is the drift velocity.

The CLAS drift chamber system consists of 18 separate chambers, located at three radial positions (called regions) in each of the six sectors. Region 1 is closest to the target, an area of low magnetic field, Region 2 is a high magnetic field region between the magnet coils, and Region 3 is a field-free region outside the magnet coils. The chambers contain wires stretched between two endplates, with the endplates tilted at 60° with respect to each other. The wires are strung in the azimuthal direction, perpendicular to the bend plane. The wire midpoints create concentric circular arcs, with the wire positions shifted by half the wire spacing in successive layers [35]. The arrangement of two field-wire layers and one sense-wire layer produces a quasi-hexagonal pattern, with six field-wires surrounding a sense-wire as shown in Figure 5.4. The distance between the field and sense wires increases with the radial distance from the target, with the average distance of 0.7 cm in Region 1, 1.5 cm in Region 2, and 2.0 cm in Region 3. The wires in each chamber are subdivided into two 'superlayers', with six wire layers in each 'superlayer'. One of the superlayers is axial to the magnetic field, while the other one is tilted by 6.5° to provide azimuthal information. Guard wires surrounding each superlayer, are at a potential, set to simulate the electric field of an infinite grid of hexagonal cells. The gas in the chambers is a 88%−12% mixture of argon and CO_2. Argon provides an ionization gain of $\sim 10^4$, and CO_2 is added for safety reasons, in order to prevent a cataclysmic ionization avalanche [37]. Constant pressure regardless of the atmospheric pressure is maintained by making adjustments to the out-flow [35]. A high voltage system maintains the sense-wires at a positive potential, and the field wires at a negative potential, 50% smaller than the positive one. Each sense wire is equipped with a single channel differential pre-amplifier, connected in groups of 48 to a printed circuit board on the chamber endplates. The circuit boards are then connected to the electronics in common crates.

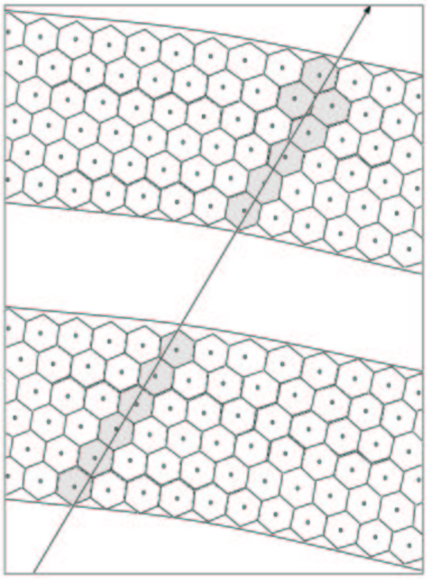

Figure 5.4: Section cut of drift chambers showing two superlayers each made of six hexagonal-celllayers. The cells are electrostatic boundaries created by the field wires at each corner of the hexagon. A charged particle is crossing the chamber, hitting cells marked in grey.

The tracking resolution is the deviation of the reconstructed momenta and angles of the charged particles from their true values at the interaction vertex [35]. The uncertainties can be caused by inaccurate knowledge of the true magnetic map of the torus field, by multiple secondary scattering in the material along the particle trajectory, by geometric misalignments, wire sagging and other reasons. The intrinsic resolution of the gas mixture in the chambers is $\sim 100\mu m$ [37]. The final space resolution is $\sim 500\mu m$, with resulting momentum resolution of $\sim .5 - 1.5\%$

5.2.1 Cerenkov Counters

The Cerenkov detector in CLAS is used to separate electrons from pions. The Cerenkov light is emitted when a particle travels through a dielectric medium at a speed exceeding the speed of light in that medium. Excited atoms in the vicinity of the traveling particle become polarized and emit photons at a fixed angle θ, determined by [36]:

$$cos\theta = 1/\beta n, \tag{5.2}$$

where $\beta = v/c$ and n is the index of refraction in that particular medium. A threshold Cerenkov detector detects particles whose velocity exceeds $1/n$. Gas radiator counters are often used when detection of particles with $\beta > .99$ is necessary. The gas counters are advantageous, because the indices of refraction in gas can be controlled by varying pressure. The CLAS Cerenkov detector is a threshold gas counter, filled with perfluorobutane (C_4F_{10}) at atmospheric pressure with index of refraction, $n = 1.00153$. The threshold energy is 9 MeV for electrons and 2.5 GeV for pions. The detector was designed to maximize solid angle coverage in each of the six sectors out to angle $\theta = 45°$. The light is collected by a system of mirrors and collected by photomultiplier tubes, placed in the regions of CLAS already obscured by the magnet coils, so they do not alter the acceptance. Since the azimuthal angle ϕ of scattered particles is practically unaffected by the torus field, the light collection optics focuses the light in the ϕ direction, leaving the polar angle θ unchanged. The polar angle range of each sector is divided into 18 regions, and each region is bisected by the symmetry plane through the center of each sector. This results in a total of 216 light-collecting modules. Each module contains one elliptical and one hyperbolic mirror for primary focusing, a cylindrical mirror to improve the focusing, and a light collection cone [35]. The detector response is calibrated in terms of the number of collected photoelectrons. For example, an inbending electron that crosses the active volume of

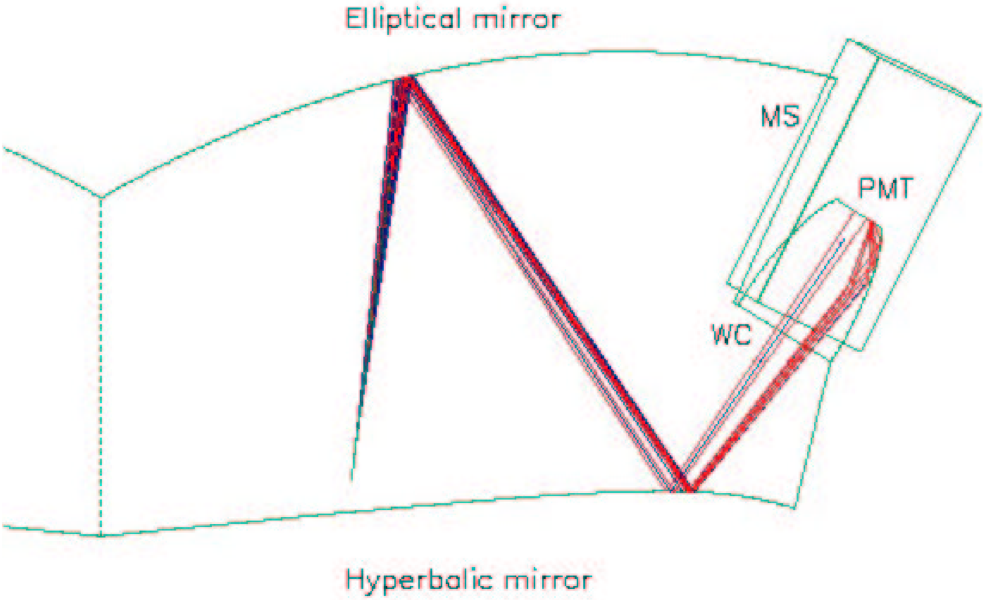

Figure 5.5: Optical arrangement of one module of the Cerenkov detector. The PMTs are hidden by the magnet coils.

the detector produces, on average, 4-5 photoelectrons.

5.2.2 Time-of-Flight Counters

The time-of-flight system consists of 288 scintillator counters with a photomultiplier tube on each end. When a particle hits the scintillator, a fraction of its energy can excite atoms in the scintillator material, which in turn can produce visible light [36]. The produced light is propagated through light guides and collected by a photomultiplier tube. The surface of the cathode of the tube is coated with a material that has a low work function, so that incident photons induce emission of electrons through the photoelectric effect. Emitted photoelectrons are multiplied to produce an electronic signal, which can then be used for triggering or timing measurement.

The TOF system of CLAS provides excellent timing resolution for particle identification, and is also used for triggering in coincidence with another detector system [38]. The design parameters were chosen with the requirement that pions and kaons can be separated up to 2 GeV/c. This translates into a time resolution of $\sigma = 120$ ps at small angles and $\sigma = 250$ ps at angles above 90° [38]. Both the time and pulse height are measured in each photomultiplier tube. The pulse height provides additional information on the energy released by the incident particle. This is important for slow particles with momenta less than 500 MeV/c, since the TOF energy resolution in this case is better that the resolution of tracking limited by multiple scattering at low momenta. The system is capable of operating in the high-rate environment of CLAS, with the average rate per scintillator of 100 kHZ. to An off-line analysis has been developed to identify particles, using the pulse time and height information along with the momentum and position measured by the drift chambers. The coun-

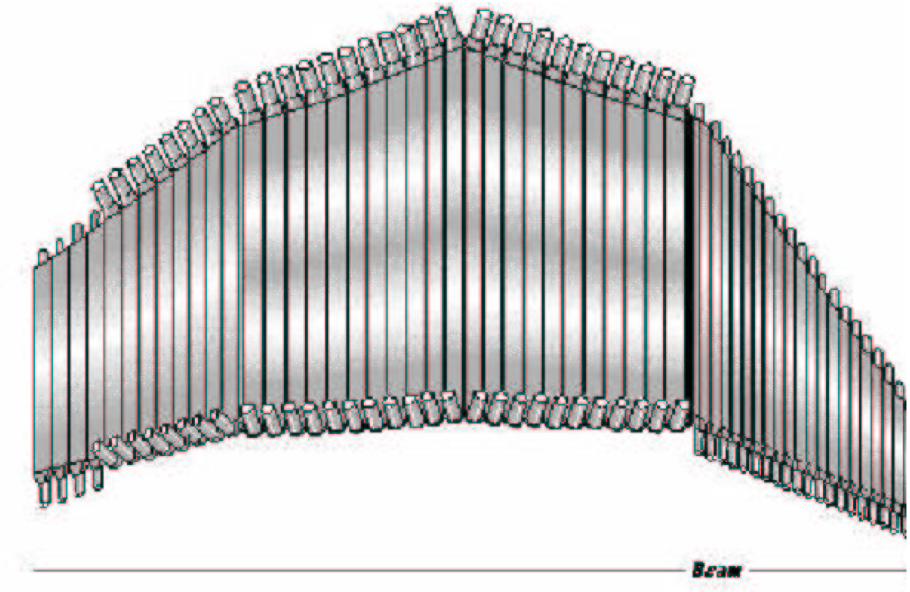

Figure 5.6: TOF counters in one sector of CLAS.

ters cover the entire azimuthal angular range, and the polar angular range between 8° and 142°, with the total area of the system of 206 m^2 [37]. The scintillators are located between the Cerenkov counters and electromagnetic calorimeters. Each scintillator is placed perpendicularly to the average particle trajectory, with an angular polar coverage of 1.5°. The scintillators have a thickness of 5.08 cm, selected to give a large signal for minimum-ionizing particles. The width varies between 15 cm for the small polar angles to 22 cm for large angles, and the length varies from 30 cm to 450 cm.

5.3 Electromagnetic calorimeter

The last part of the detector along the particle's trajectory is the electromagnetic calorimeter. The calorimeter is needed for pion rejection since the Cerenkov detector is not sufficient at high energies. A calorimeter is a device that measures the total energy deposited by a crossing particle. Calorimeters are useful in detecting neutral particles and distinguishing between electrons and hadrons. It is possible to distinguish between electrons and hadrons in the calorimeter due to their different mechanism of depositing energy. Electrons with energies higher that 100 MeV lose energy mostly through the pair production. Radiated photons produce electron-positron pairs which in turn can radiate photons. This process creates an electromagnetic shower consisting of many electrons and photons [36]. All of electrons energy is deposited in the calorimeter. On the other hand, fast hadrons such as pions have a different mechanism of interaction, and lose energy primarily through ionization. The total energy deposited in this process is independent of the beam energy, with the peak at the minimum ionizing energy. The function of the CLAS calorimeter is to detect neutrons, electrons with energies higher than 0.5 GeV, and photons with energies higher than 0.2 GeV. The calorimeter is also used to separate electrons from pions at high energies, when the Cerenkov detector does not distinguish between the two. The calorimeter is made of alternating layers of lead and scintillator material. The lead is a high Z metal that enhances the shower rate, and the scintillator material is necessary to sample the energy loss. CLAS has 8 calorimeter units, with one in each sector in the forward region (polar angle of $10-45^{\circ}$), and 2 of them at large angles ($50-70^{\circ}$) in sectors 1 and 2. The forward calorimeter has a lead to scintillator thickness ratio 1:5, with 40 cm of scintillator and 8 cm of lead per unit. The lead-scintillator configuration is shaped as a triangle in order to match the shape of CLAS. There are 39 layers of 10 mm scintillator and 2.2 mm lead in each. The ratio of radiation lengths of 10 mm scintillator and 2.2 mm lead is about $1:2$, so that 1/3

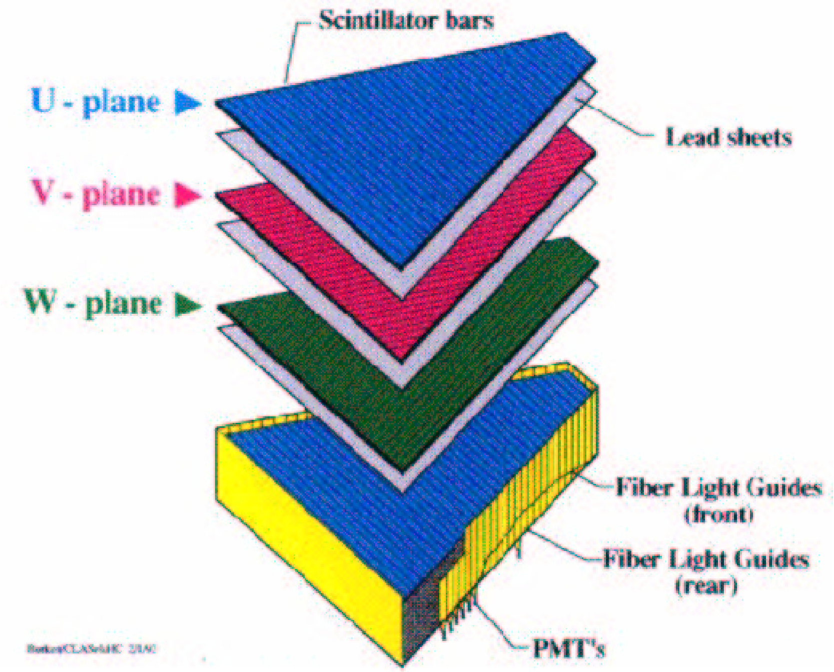

Figure 5.7: One of six modules of electromagnetic calorimeter.

of the energy is deposited in the scintillator, and 2/3 is deposited in the lead. The area of each successive layer increases to minimize the shower leakage. Each layer consists of 36 strips parallel to one side of the triangle, so that each orientation is rotated by 120° from another one. This makes a total of 3 orientations, each consisting of 13 layers providing a 2-dimensional information on the location of the energy deposition. Each set of 13 layers is divided into a stack of 5 inner layers and a stack of 8 outer layers. This is done to provide longitudinal sampling of the shower for better electron-pion separation [35]. The scintillator light is transmitted to PMTs, where the signal is sent to ADC and TDC boards. The sampling fraction of this calorimeter defined as the fraction of the shower energy collected by the active part of the detector is 0.27. The large angle calorimeter units are similar to the forward ones, but have a rectangular shape. Each consists of 33 layers; each layer has a 0.20 cm thick lead foil and 1.5 cm thick plastic scintillator. Each layer is rotated by 90°, forming a 40×24 net of cells. Each unit is vertically divided into an inner and outer part, with the bar width increasing from the inner to outer part.

5.4 Trigger System

A two-level trigger system serves the purpose of acquiring events of interest while rejecting the rest. The system is designed to minimize the deadtime of the detector. All signals from PMTs are used by the Level 1 trigger to determine if a desired event has occured. The information consists of the location of hits in the TOF detector, the signals in the Cerenkov detector, and energy deposited in the electromagnetic calorimeter. The information from these detectors is compared with the preloaded patterns. The Level 1 trigger processes the signals through a pipeline memory lookup within 90ns. The three stages of memory lookup are shown in Fig 1.5 and 1.6. The first stage starts with 62 bits of trigger data from each sector. The bits contain information on hits in various coarse angle bits in the TOF counters and in the Cerenkov counters. The bits also indicate events with the total energy deposited in the EC above some threshold, and in which layers the deposition was concentrated. Two consecutive lookup memory stages reduce the 62 bits to 4 groups of 3, determining the likelihood of some particles in that sector that are of interest, as defined by the preloaded trigger definitions. The third lookup stage correlates the patterns from each sector, and applies geometrical constraints on multi-particle events. The average processing period of Level 1 trigger is 90.5 ns [35]. After the Level 1 trigger signal

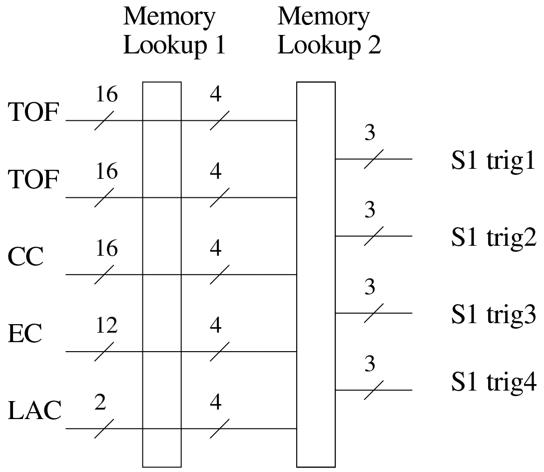

Sector-based trigger blocks for sector 1.

Figure 5.8: Trigger blocks.

has occured, the event is digitized, read out and passed to the Level 2 trigger. The Level 2 trigger finds 'likely tracks' in each sector, correlates them with the Level 1 trigger, and rejects hits without a likely track in DC. In order to find the likely tracks, a 'segment finder' continuously searches for track segments in overlapping regions of five superlayers in each sector. The segments are identified by comparing the DC hits with nine templates that were designed to catch all tracks passing through a superlayer up to angles of 60° [35]. A likely track in a sector is accepted if there are matching track segments found in 3 of 5 superlayers. If no track candidates are found, the Level 2 trigger issues a 'fast-clear' signal, and more triggers are accepted after that. The detector does not accept any triggers until either a fast-clear signal is issued or a digitization of a trigger is completed. The processing time of Level 2 trigger contributes to the deadtime of the detector. The Level 1 and Level 2 inputs are fed into a custom electronics board called the Trigger Supervisor (TS). TS has 12

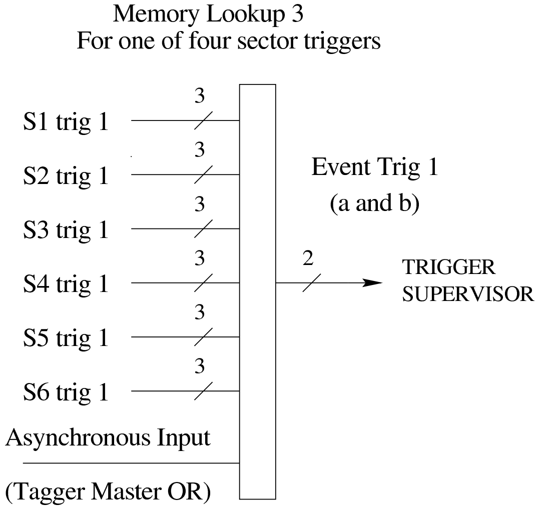

Figure 5.9: Memory Lookup.

trigger inputs, with 8 of them used by the Level 1 trigger, and other 4 used by other calibration triggers. There is also an input for a Level 2 trigger confirmation. The TS could be programmed to require only Level 1 input, or to require both the Level 1 input and Level 2 confirmation. EG1b did not use the Level 2 trigger.

5.5 Data Acquisition

When an event satisfies the trigger configuration, it is recorded by the data acquisition system. The signals from different components of the detector are sent to the Level 1 trigger. If the Level 1 is satisfied, the signals are sent to the Trigger Supervisor, digitized in 24 FASTBUS and VME crates, and collected by the 24 VME Readout Controllers (ROC1 to ROC24). The arrays of digitized values associated with a particular detector component are translated into tables in which each data value has a maximum of 16 bits. The tables are transfered to the CLAS online acquisition

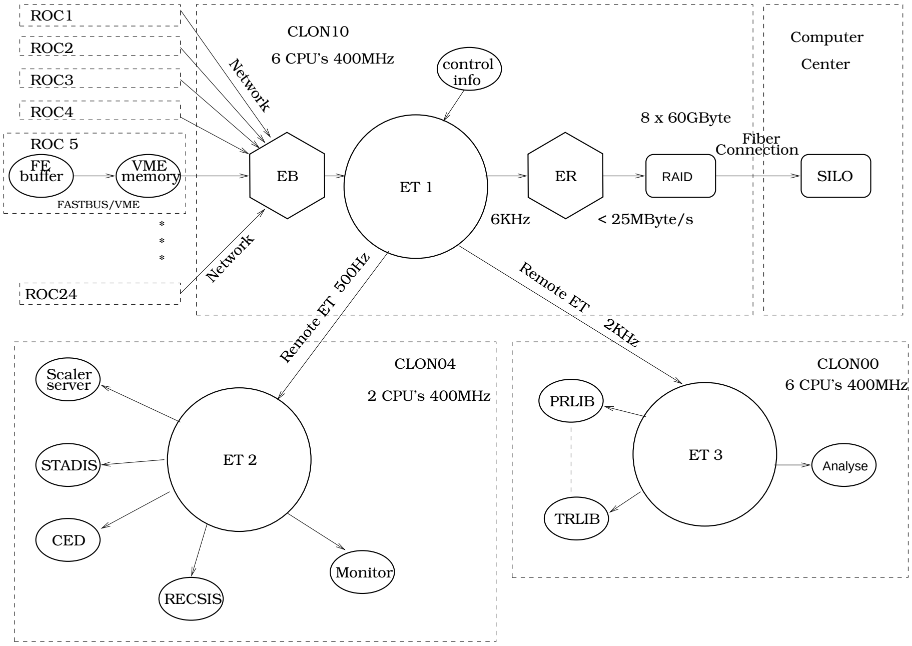

Figure 5.10: Data flow schematic 1.

computer (CLON10), located in the control room. There are three main processes in the acquisition computer: Event Builder (EB), Event Transport (ET), and Event Recorder (ER). The EB forms complete events out of incoming fragments. Each event is described by various tables of data called 'banks', each prefixed by a header that contains an alphanumeric name. The completed event is labeled by a run number, event number, event type, and the trigger bits contained in a header bank. Completed events are passed to shared memory (ET1) on the CLAS online computer.The shared memory is managed by the ET, which allows simultaneous access by various event producer and consumer processes. The ER collects all events for permanent storage. The ER writes the data in a single stream to a local disk. When the disk is full data are transfered to a remote tape silo managed by the computer center. Data transfers are performed in parallel, so that consecutive files may be transfered to different tapes.

The data flow involves approximately 100 processes running on a system of processors located around the detector, and several computers in the control room. The sequence of processes involved in acquiring one data run is shown in Fig. 5.9. Here, the DAQ components are configured, parameters and code are downloaded into the hardware components. The desired parameters are stored in a run configuration file; during the download procedure, all detector parameters, trigger configuration, trigger logic and the thresholds are obtained from the configuration file. Three keyboard commands are needed for the data acquisition. The 'prestart' command compares the configuration run parameters with the ones read back from hardware. A warning is sent in case of discrepancies. Basic run information regarding the beam and target type is recorded under the 'begin run' header in an online database. The 'prestart' command also reads and writes all run information into parameter files. The 'go' command enables the trigger, and data files are recorded in 2 GByte blocks. The data files contain physics events, along with scaler readings and 'slow controls' readings which are recorded periodically. The 'end' command completes the run, disables the trigger, and adds final scaler readings to the data file.

Some CLAS parameters are summarized in Table 5.1.

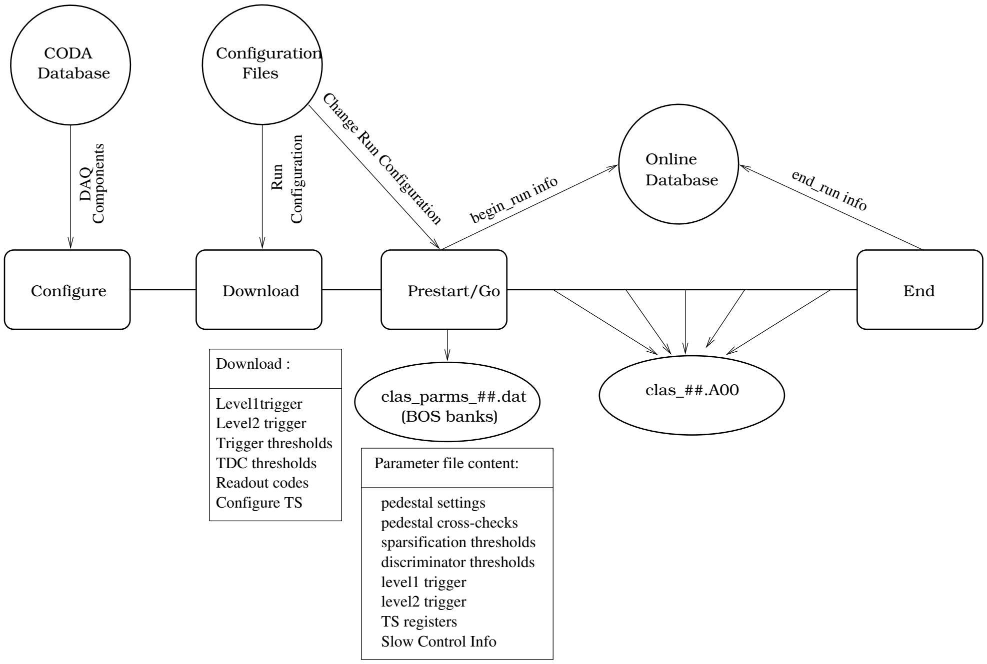

Figure 5.11: Data flow schematic 2.

Table 5.1: CLAS Parameters.

Capability	Quantity	Range
Coverage	charged particle angle charged particle momentum	$8° \leq \theta \leq 140°$ $p \geq 0.2$ GeV/c
Resolution	momentum ($\theta \leq 30°$) momentum ($\theta \geq 30°$) polar angle azimuthal angle time(charged particles)	$\sigma_p/p \approx 0.5\%$ $\sigma_p/p \approx 1 - 2\%$ $\sigma_\theta \approx 1$ mrad $\sigma_\phi \approx 4$ mrad $\sigma_t \approx 100 - 250$ ps
Particle ID	π/K separation π/p separation	$p \leq 2$ GeV/c $p \leq 3.5$ GeV/c
Luminosity	electron beam	L $\approx 10^{34}$ nucleon $cm^{-2}s^{-1}$
Data acquisition	event rate data rate	4 kHz 25 MB/s

Chapter 6

Event Reconstruction

6.1 Data Processing

The data accumulated during the experiment are stored in the form of TDC and ADC values from various parts of the detector. These so-called 'raw' data are converted into desired quantities such as energy and momentum of particles. This processing of the data, or event reconstruction, converts the raw digital data into the time of flight and trajectory parameters of the particles. This information is then used to extract the necessary physical quantities, and identify the particles. Event reconstruction of CLAS data consists of identification of charged and neutral particles, and of calculation of the components of their 3-momenta. Both the particle trajectory in the drift chambers and the time of flight are required for charged particle reconstruction. The flight path and particle momentum p are determined from the tracking information, while the particle's velocity is given by the time of flight if the path length is known.

This information is combined to give the particle's mass [35]:

$$m = p/\beta\gamma. \tag{6.1}$$

For a particle to be identified as an electron, its track must agree in time and position with a $\hat{C}$erenkov Counter hit, and with position and energy deposition in the Electromagnetic Calorimeter. Neutral particles can be detected in the calorimeter or the time-of-flight counters. The candidates for neutral particles are identified with the energy clusters in the outer detector parts that do not match any of the tracks. The photons deposit all their energy in the calorimeter, so their energy is calculated from the signal pulse-height. Momenta of the neutrons are calculated from their time of flight given by the time signal in EC or SC. The angle of the trajectory of a neutral particle is determined from the position of the energy cluster at the surface of the calorimeter.

The raw and reconstructed data are stored in BOS files, BOS being the Fortran-77 based dynamic memory management system [37]. The information in BOS files is divided into tables called 'banks', where 'banks' consist of the 'header' and the 'body'. The 'header' identifies the bank and its dimensions, while the 'body' contains the rows of data. The raw data banks contain the electronic information obtained from one system of the detector, or even one part of the system. After the reconstruction the new banks contain physical quantities. In the final output, the data consist of a few banks that contain four-vectors for each particle in each physical event, along with the information necessary for physics analysis.

The first part of data processing consists of the calibration of all detector systems.

For that purpose, a small sample of data is processed to check the detector behavior. The time and energy calibration are checked for every detector system, and the calibration constants are adjusted accordingly. This procedure has to be applied for each different run configuration of beam energy and torus magnetic field value. After this phase, calibration constants are 'frozen' in the calibration database, and the rest of the data is processed.

The files containing processed data are large, each occupying 10 MB of disk space, so a more compact version of data files is often used. Data storage tapes (DSTs) were created from the large BOS files. DSTs have a reduced number of banks, making them smaller and more flexible. These files have been used in the final analysis.

6.2 Track Reconstruction for Charged Particles

The reconstruction of charged particle tracks is a complex process, consisting of several steps. The first step is finding the group of adjacent hits called a cluster in each of the six superlayers. Each cluster may contain one or several track segments. The segments are found by using the look-up table to check if they are consistent with a track crossing a superlayer. Once the segments are found, they can be linked together using another look-up table generated through simulation. The segments form a track candidate if a match for at least 5 superlayers is found. The look-up table provides an estimate of initial parameters for that candidate. A candidate track is then fit using the cell centers as hit position, and propagated through the rest of the detector's magnetic field. The fitting procedure provides preliminary values for the particle's production angle and momentum. This procedure is called hit-based tracking (HBT). The result of HBT is improved by using the particle's time of flight given by the TOF scintillators. The corrected drift time is given by [37]:

$$t_{drift} = t_{start} + t_0 - t_{TDC} - t_{flight} - t_{prop} - t_{walk}, \tag{6.2}$$

where t_{start} is the event start time, t_0 is the known time delay for the wire, t_{TDC} is the time measured by the drift chamber's TDC, t_{flight} is the flight time of the particle from the vertex to the wire, t_{prop} is the time of propagation of the signal through the wire, and t_{walk} is the time-walk correction. The t_{TDC} is subtracted because all TDC's operate in the 'common stop mode', where the start signal is provided from the wire hits, and the stop signal is provided by a delayed version of the trigger [37].

The corrected drift times are converted to drift distances, and the corrected track positions in each cell are fit again in order to determine the final track parameters. This is called time-based tracking (TBT). At each superlayer, the distance-of-closest-approach (DOCA) of each track to the hit wire and to the position derived from TBT is calculated.

Five parameters define the trajectory of each charged particle: inverse momentum, polar and azimuthal angles with respect to the beam, and the interaction vertex, transverse and parallel to the beam direction. These parameters are determined from the fitting procedure, and stored in a vector $\vec{q}$. The positions from a reference trajectory $d_i(\vec{q})$ are fitted to the wire positions during HBT, and to the measured DOCA during TBT [35]. The χ^2 is minimized during the fitting [35]:

$$\chi^2 = \sum_i \frac{[d_{meas,i} - d_i(\vec{q})]^2}{\sigma_i^2}, \tag{6.3}$$

where the uncertainty σ is given by $\sigma_i \sim \text{cell size}/2\sqrt{12}$ for the HBT, and by a distance-dependent resolution for TBT. After the fitting procedure, there is still an ambiguity regarding which side of the wire the track was on. This question has to be resolved before the track can be propagated through CLAS. This is done separately within each superlayer. A straight line fit is made to different hit possibilities within one superlayer cluster; all left-right configurations are tried, and the one with highest probability is chosen. After the signs of all drift distances are determined, the final track is formed.

In the EG1b experiment, an additional magnetic field was introduced by the polarized target magnet, bending the charged particle's trajectories in the ϕ direction, which normally stays unchanged. Since the target field falls off rapidly with distance, the space mostly affected is in the region preceding the first layer of the drift chambers. The reconstruction code takes the target field into account by fitting the track from the first layer to the outside. to determine its momentum, after which the track is traced back to the interaction vertex to determine the initial angles of θ and ϕ [37].

6.3 Start Time Reconstruction

The start time of the interaction of an incoming electron with the target is calculated from the measured time of flight of the electron and its TDC signal. The primary scattered electron is identified without the time of flight information, using only the information from the electromagnetic calorimeter and the $\hat{C}$erenkov detector. The signal from these components of the detector is then matched with the negative track. After the electron is identified, the start time is calculated by using the time of flight signal and the path length l from the vertex to the hit scintillator counter [37]:

$$t_{start} = t_{tof} - \frac{l}{\beta c}, \tag{6.4}$$

where t_{tof} is the time corresponding to the electron signal in the scintillator, and $\beta = 1$ for the beam electrons. The resulting resolution is approximately 160 ps. The accuracy of the start time determination is improved by use of the RF structure of the beam. The time of arrival of each electron beam bucket is provided by the accelerator, and is recorded in the data stream. The electron beam buckets are separated by 2 ns. Ideally, the reconstructed start time should coincide with the arrival of one of the buckets, but due to the finite resolution the reconstructed times form a Gaussian distribution with a peak around the RF time, and mean width corresponding to the time resolution. Since the time resolution is much less that the bucket spacing, the reconstructed time can be replaced by the RF time. Taking the difference between the reconstructed start time and the arrival time of the closest bunch gives the RF correction:

$$t_{start} = t_{tof} - \frac{l}{\beta c} + t_{RF}. \tag{6.5}$$

6.4 Electron Selection

6.4.1 Helicity Physics

The helicity of the beam is pseudo-randomly selected with a frequency of 30 Hz. Each triggered physics event is labeled with the helicity state in the 'HEAD' bank, and the total beam charge is integrated over one helicity state. This information is passed

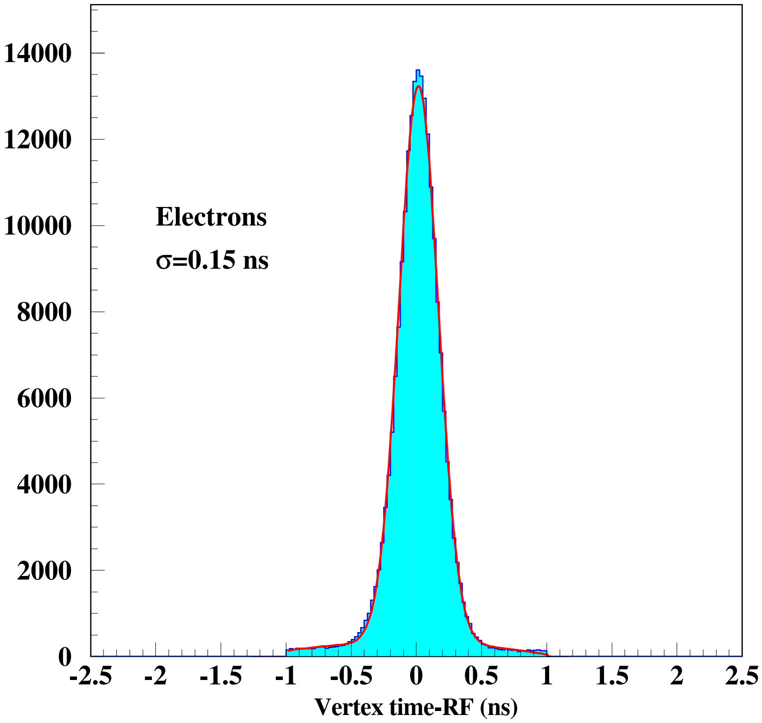

Figure 6.1: Difference between the start time reconstructed from the time-of-flight information and the accelerator RF signal. The resolution is approximately 160 ns.

into the data stream immediately after a helicity flip. Sometimes, this information is passed after 2 helicity flips depending on the status of the DAQ system. The Helicity Physics (HelP) algorithm is designed to 'realign' each physics event with the respective helicity information. For part of the run the helicity label failed to latch. However, helicity information is also stored in the 'HLS' bank, so it was possible to recover the proper helicity labels. Some additional problems with the helicity information were discovered while analyzing the data. While the Help program tries to align the helicity bit in the 'TGBI' bank with the information from the 'HLS' bank, it was found that the helicity scaler began to increment more than one count for some runs. To correct this problem, it was decided to rely on the appearance of the 'HLS' bank immediately after each helicity flip. Those events which did not have 'HLS' information present after the helicity flip were labeled as 'bad', and not used in the analysis. Another problem with the helicity information occured during the production of DSTs. When the DSTs are written, the physics events are grouped according to the beam helicity. Each DST file has a 'HELEVENT' bank, which contains information on the helicity of the physics events which appear in the next 'PHYS' bank. The 'HELEVENT' also contains the event number of the first (EvMin) and last (EvMax) physics events reconstructed during the helicity state. Occasionally the DST/HelP maker failed to read the tables correctly so that some physics events were written more than once in the 'HELEVENT' bank. When this problem occured, such events were discarded along with all events belonging to the same helicity state. Angela Biselli [39] provided a program which identified corrupted helicity states, and these helicity states were not used in the analysis.

6.4.2 Basic Cuts

Scattered electrons are used in the inclusive asymmetry analysis discussed in this thesis. An electron is identified and labeled by the reconstruction code as a negatively charged track with matching hits in the Electromagnetic Calorimeter, $\hat{C}$erenkov Counter and time of flight scintillator. The electron is also the event trigger, defining the start time of the event. The initial electron cuts are loose, so that the resulting sample can still contain other negative particles. More cuts are needed to clean the electron sample. These include the cuts on energy deposited in the calorimeter, number of photoelectrons in the $\hat{C}$erenkov detector, vertex cut and fiducial cut.

Electrons and pions can be distinguished in the calorimeter due to their different patterns of energy deposition. Electrons emit photons and produce electromagnetic showers, with the total deposited energy proportional to their momentum. Pions, on the other hand, are minimum ionizing particles (MIPs) losing energy at the rate of ~ 2 MeV/gm/cm^2. The calorimeter is made of 39 layers of 10 mm thick scintillator and 2.2 mm thick lead. Traveling through the calorimeter, pions lose 78 MeV of energy independent of their momentum. The patterns of energy loss in the calorimeter by electrons and pions is seen in the figure 6.2. The plot shows a linear momentum

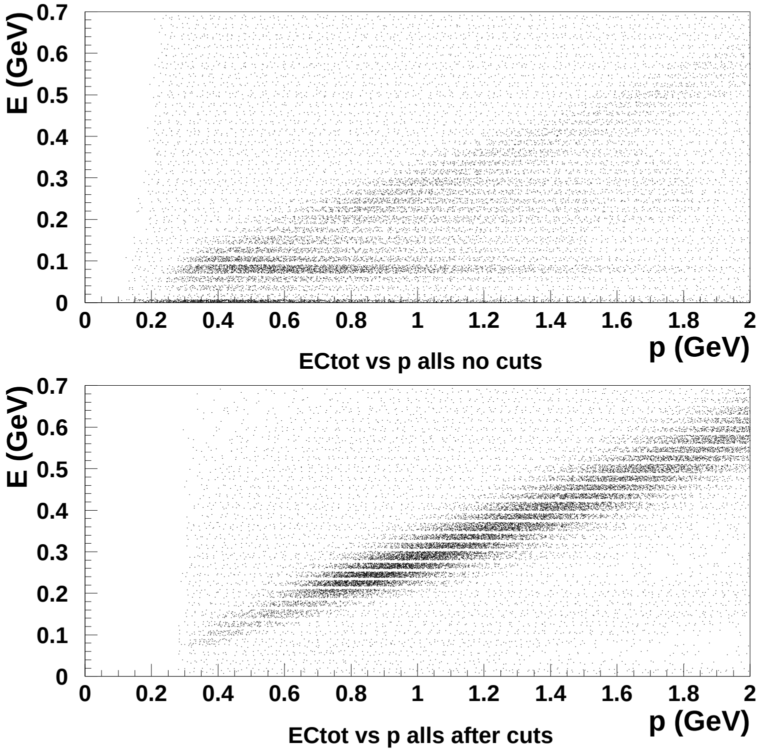

Figure 6.2: EC_{tot} vs p distribution before and after the EC cut. A constant signal of $EC_{tot} \sim 0.08$ GeV is produced by the MIPs and removed by the EC cut.

dependence of energy deposited by the electrons. The slope of the line is given by a sampling fraction ~ 0.27 [37], which is defined by the characteristics of the detector. On the same plot, we see a constant signal of $EC_{tot} \sim 0.08$ GeV, produced by the MIPs. In order to remove the MIPs from the sample, a cut of the following form is applied

$$EC_{tot} > 0.2 * p, \tag{6.6}$$

where p is the momentum of the particle. The cut can be slightly different for different energy/torus configuration. This cut alone is not sufficient, so more cuts are applied to the sample. The spatial pattern of energy deposition can also be exploited. Since the energy deposited by MIPs is related to the detector thickness, it is possible to correlate the energy collected in the inner (first 5) and outer (last 8) layers of the calorimeter. The correlation is

$$EC_{tot} : EC_{inner} = 13 : 5. \tag{6.7}$$

Particles that satisfy this condition are identified as contamination of the electron sample and removed by a cut in the EC_{tot} vs EC_{inner} distribution:

$$EC_{inner} > 0.08 * p. \tag{6.8}$$

An additional cut is provided by the $\hat{C}$erenkov detector which is efficient at distinguishing pions and electrons up to momentum of 2.5 GeV. Particles identified as electrons are required to have a signal in the $\hat{C}$erenkov detector. A typical photoelectron distribution is shown in Figure 6.4. The plotted distribution is due to the convolution of the Poissonian behavior that describes the emission of $\hat{C}$erenkov light

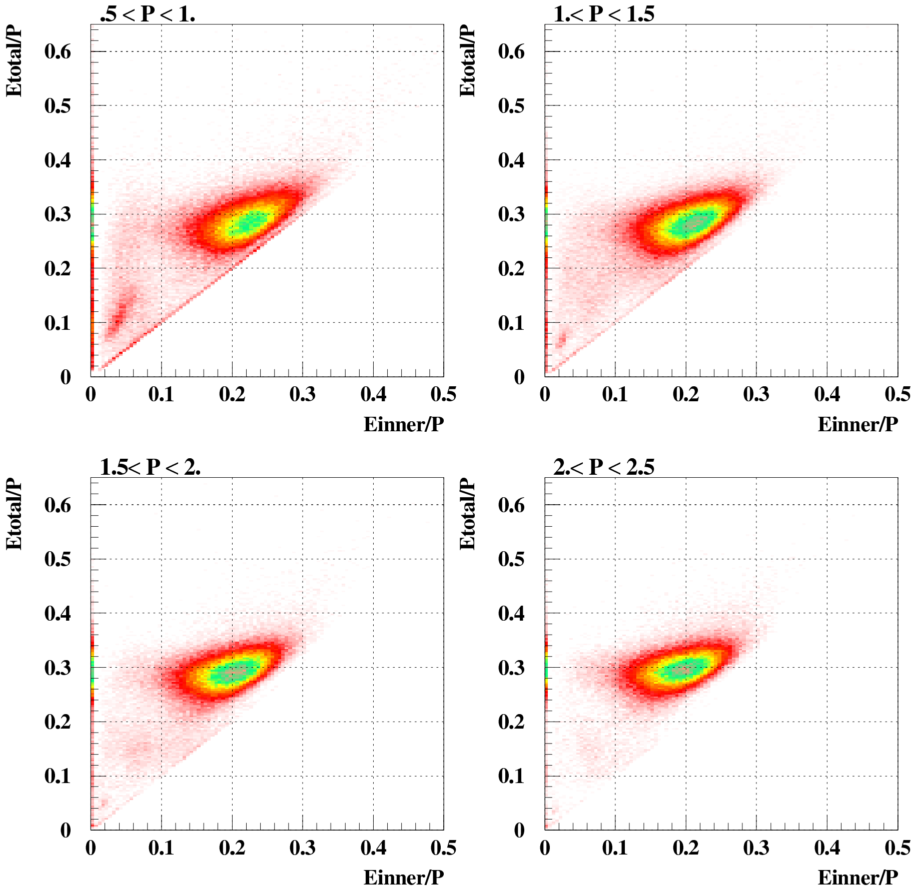

Figure 6.3: EC_{tot}/p vs EC_{inner}/p. Contamination in the left corner is removed by the EC cut. Plot is a courtesy of V.Dharmavardane.

[37]. The peak at ~ 2 photoelectrons is due to a bad collection of light that occurs at a particular kinematics. The $\hat{C}$erenkov PMTs cannot receive light for a particular combination of polar and azimuthal angles, which results in acceptance inefficiency which is usually removed by the fiducial cuts. The fiducial cuts will be discussed later in this chapter. In addition, a cut on the number of photoelectrons is used, usually nphe > 2.5. This cut removes the faulty peak, along with some high energy pions which have sufficient velocity to emit $\hat{C}$erenkov light. The plot in Fig 6.4 shows the

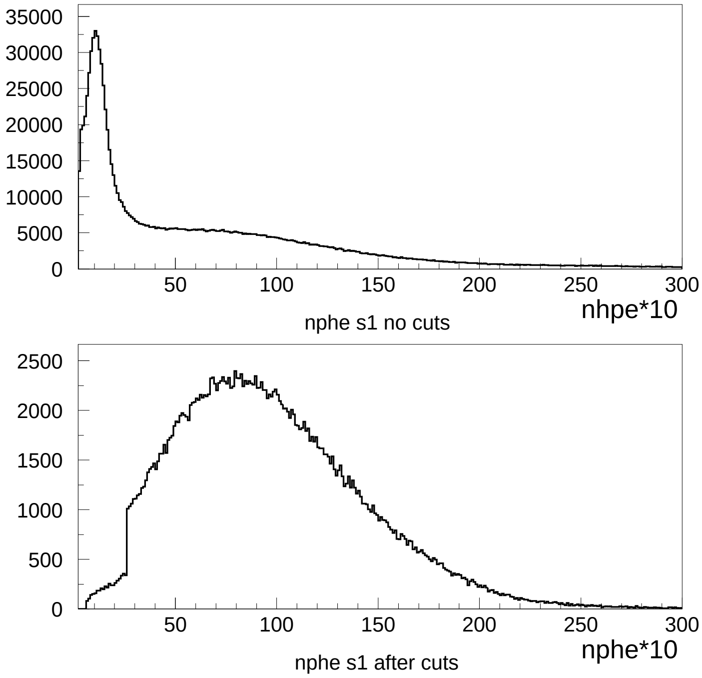

Figure 6.4: Photoelectron distribution before and after the cuts. The top plot shows original distribution, the bottom plot shows the distribution after electron cuts are applied.

effect of electron cuts on the $\hat{C}$erenkov distribution. The cuts used for each data set are listed in Table 6.1. The cuts are slightly different for low and high momentum particles. It is more difficult to distinguish pions and electrons at momentum higher than 2.5 GeV, but not many pions are expected to exist at that kinematics, so the cuts are looser for the high momentum particles. Some pion contamination still remains after the cuts. An estimate of this contamination is discussed in the Analysis section.

Table 6.1: Electron Cuts

Energy/Torus	mom (GeV)	EC_{tot}	EC_{inner}	$\hat{C}$erenkov cut
5.615,+2250	$p < 3$	$> 0.2 * p$	$> 0.08 * p$	$nphe > 2.5$
	$p > 3$	$> 0.24 * p$	$> 0.06 * p$	$nphe > 0.5$
5.725,+2250	$p < 3$	$> 0.2 * p$	$> 0.08 * p$	$nphe > 2.5$
	$p > 3$	$> 0.24 * p$	$> 0.06 * p$	$nphe > 0.5$
5.725,-2250	$p < 3$	$> 0.2 * p$	$> 0.08 * p$	$nphe > 2.5$
	$p > 3$	$> 0.24 * p$	$> 0.06 * p$	$nphe > 0.5$
5.743,-2250	$p < 3$	$> 0.2 * p$	$> 0.08 * p$	$nphe > 2.5$
	$p > 3$	$> 0.24 * p$	$> 0.06 * p$	$nphe > 0.5$
1.606,1500	$p < 3$	$> 0.27p - 0.071\sqrt{p}$	$> 0.08 * p$	$nphe > 2.0$
1.606,-1500	$p < 3$	run dependent func	$> 0.08 * p$	$nphe > 2.0$
1.723,-1500	$p < 3$	run dependent func	$> 0.08 * p$	$nphe > 2.0$

6.4.3 Raster and vertex correction

It is important to select electrons scattered from the polarized target, as opposed to the ones scattered from other materials in the beam path. For that reason, a raster calibration is performed, and a cut on the vertex distribution is made. During the experiment, the beam was rastered in a spiral pattern to avoid overheating local regions in the target. This was done using 2 magnets located upstream of the target. The values of the current going through the magnets are recorded by ADCs, and passed into the data stream. These numbers are stored in DSTs for every trigger. A procedure to translate the ADC values into the actual beam positions in (x, y) was developed by Peter Bosted [40].

Corrections are made to the tracking, which allows for better vertex reconstruction. Then, a cut on this distribution is made, choosing only a region corresponding to the target material. This procedure is briefly described here. A plot of the uncorrected and corrected vertex distributions is shown in Fig 6.5. The calibration

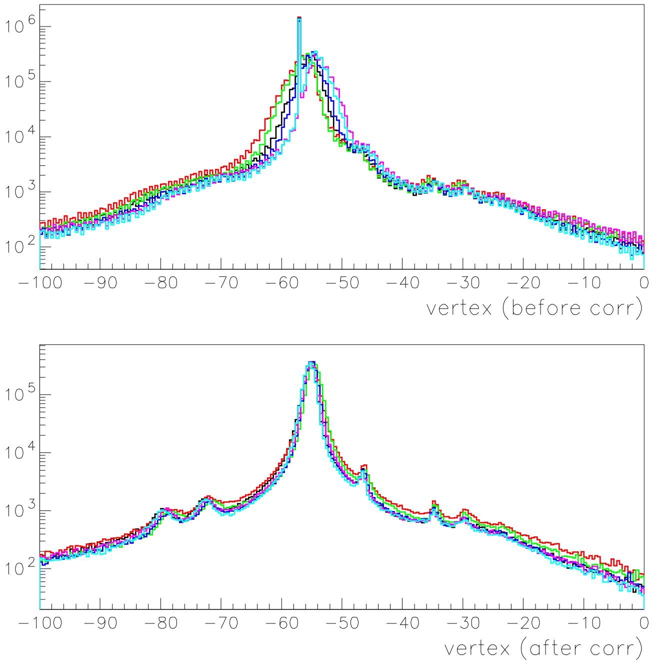

Figure 6.5: The top plot shows z-vertex distribution for 6 sectors before the raster correction. The bottom plot shows the same distribution after the correction was applied.

procedure assumes a linear relationship between the ADC values and positions of the beam. Then, the beam position in x and y has the following form [40]:

$$\begin{aligned} x &= (X - X_0) * c_x, \\ y &= (Y - Y_0) * c_y, \end{aligned} \tag{6.9}$$

where X and Y are the ADC values. Then, the corrected vertex position is defined:

$$z_c = z_{nom} + x'/\tan\theta, \tag{6.10}$$

where z_{nom} is the vertex position given by tracking, θ is the polar scattering angle, and x' is the distance along the track length that was not accounted for by the tracking:

$$x' = (x * \cos\phi_s + y * \sin\phi_s)/\cos(\phi - \phi_s), \tag{6.11}$$

where $\phi_s = (sector - 1) * 60$ is the sector angle, and ϕ is the particle's azimuthal angle given by the reconstruction code. The fit is performed by minimizing $\chi^2 = \sum_1^N (z_c - z_0)^2$, where z_0 is the fit parameter defining the center of the target. The four parameters, X_0, Y_0, c_x and c_y are optimized by the fit. These coefficients were found to vary slightly with the beam energy, but remained stable within each data set [40]. The raster correction improves the quality of vertex reconstruction. A tight cut is then applied to choose events that originate at the target cell:

$$-58 < v_z(i) < -52. \tag{6.12}$$

The raster correction also changes the calculated distance that particles travel in the magnetic field of the target, which in turn, changes the rotation of the azimuthal angle. The angle is corrected:

$$\phi_c = \phi_0 - (q)(50)(\frac{x'}{100})(\frac{1}{33.356})(\frac{1}{p\sin\theta}), \tag{6.13}$$

where q is the particle's charge, 50 is the value of the target magnetic filed in kG, $x'/100$ is the change in track length in cm, 33.356 is the inverse speed of light, and $p \sin \theta$ is the particle's transverse momentum. Having the proper values for x and y, a target image can be constructed, plotting the number of events as a function of x and y. An example of such a plot is shown in Figure 6.6. It is easy to see the distribution of target material in the cell. Similar plots were constructed for every analyzed run. Some runs showed a 'settling' of the target material, with the density decreasing on the top of the cell. It was also possible to find runs where the beam was over-rastered and hitting the walls of the cell. Such runs were not used in the dilution factor analysis.

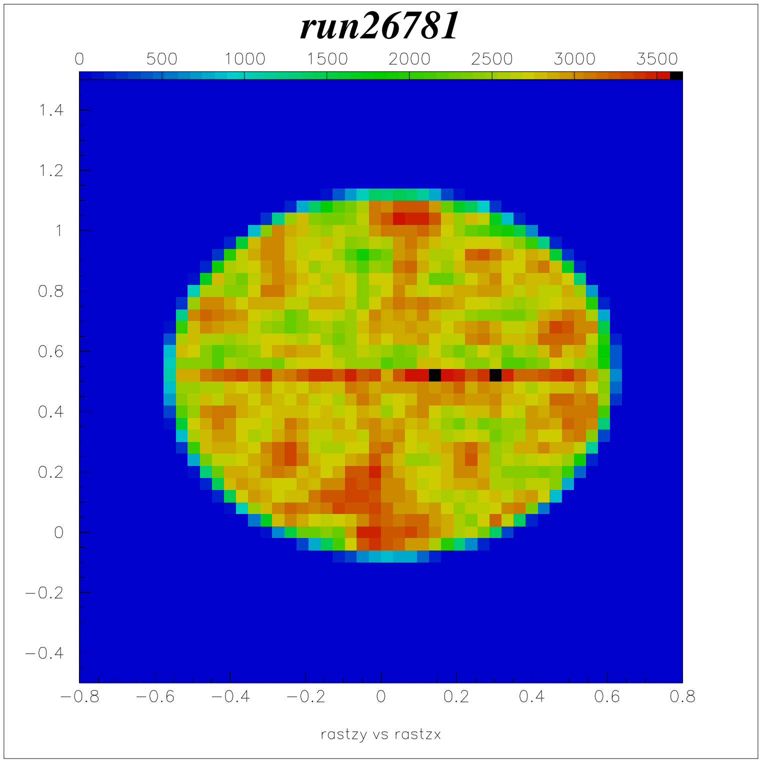

Figure 6.6: Target Image in x,y. Darker areas correspond to high count rates.

6.4.4 Fiducial Cuts

The detector contains some regions of acceptance inefficiency. These inefficiencies are caused by problems in different parts of the detector. In order to avoid introducing systematic offsets into the data, these inefficient regions are usually excluded from physics analysis.There is a certain combination of polar and azimuthal angles for which $\hat{C}$erenkov PMTs do not receive light. If an electron hit in the calorimeter is close to one of the edges, part of the shower's energy can 'leak', and will not be fully reconstructed. Other hardware problems like broken wires in the drift chambers, or dead time-of-flight PMTs can introduce additional inefficiencies in the acceptance.

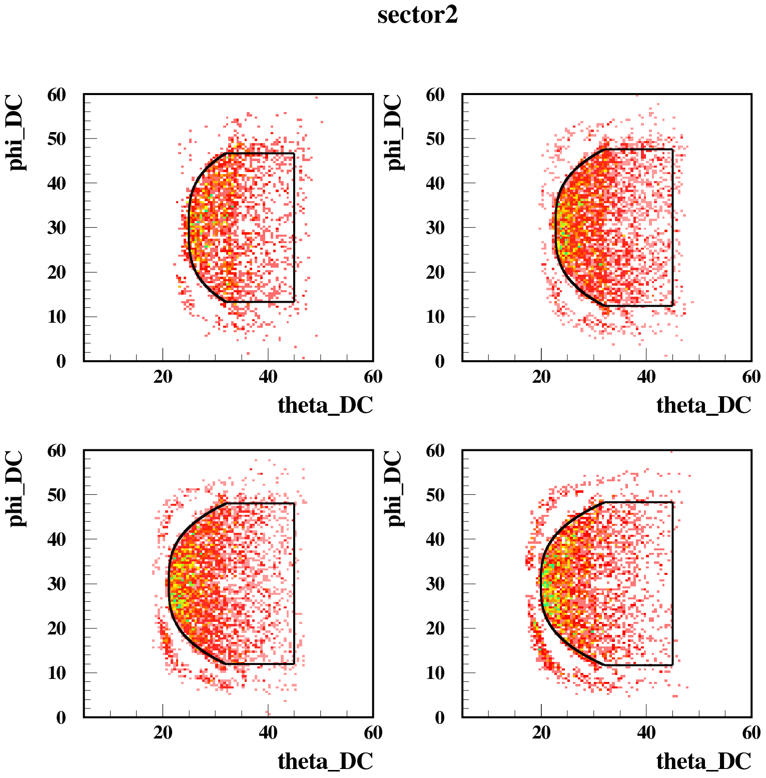

Figure 6.7: ϕ vs θ distribution for four momentum bins. Black line defines the fiducial region. Plot is a courtesy of V.Dharmavardane.

These problems are avoided by defining a safe fiducial region, which excludes regions with low detection rates. The fiducial cuts have been studied for each energy/torus data set, for each sector individually. The cuts are geometrical, with the fiducial region defined in terms of polar and azimuthal angle. The fiducial cut for EG1b data was developed by Volker Burkert and modified by Vipuli Dharmavardane [41]. Figure 6.7 shows an acceptance plot before and after the cut.

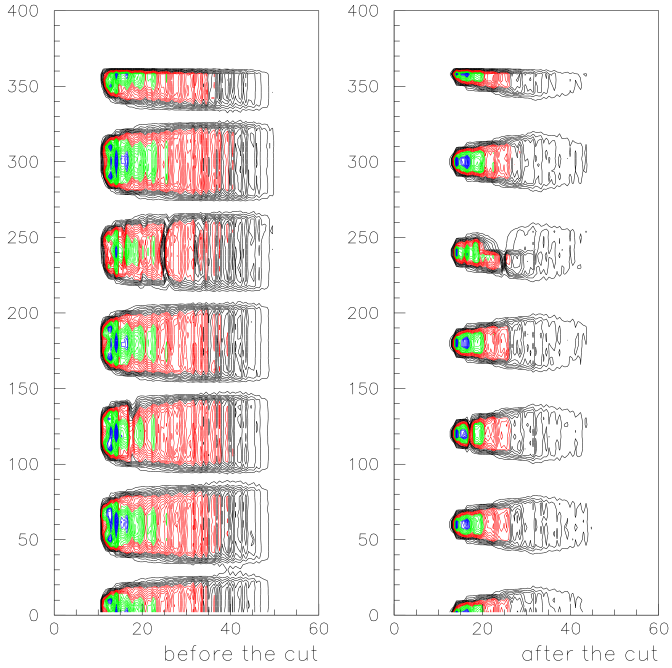

Figure 6.8: ϕ vs θ distribution before and after fiducial cuts. The regions of low efficiency are removed by the cut.

6.5 Momentum Correction

The particle's momentum given by the reconstruction code (RECSIS or A1c) is known to show deviations from the expected value. This effect can be seen by plotting a W distribution of inclusive electrons. The central value of the elastic peak is often shifted from its theoretical value $W_{elas} = m_p = 0.9382$ GeV. The peak is also broader than is expected from the intrinsic resolution of CLAS. This systematic shift depends on both the azimuthal and polar angles, and is caused by the inaccurate or incomplete knowledge of the magnetic field and the drift chamber positions. A correction algorithm was developed by A. Klimenko and S. Kuhn, and is described in reference [42]. The authors assume that both momenta and polar angles are systematically affected by the displacement of the drift chambers from their nominal positions, and by the magnetic field deviation from the field map used in the reconstruction code. Eight parameters (A-H) are adjusted to correct for these errors. The effect on the reconstructed track is written in terms of a change in the polar angle and a change in momentum:

$$\begin{aligned}\Delta\theta &= (A + B\phi)\frac{\cos\theta}{\cos\phi} + (C + D\phi)\sin\theta, \\ \frac{\Delta p}{p} &= \left[(E + F\phi)\frac{\cos\theta}{\cos\phi} + (G + H\phi)\sin\theta\right]\frac{p}{qB_{torus}}, \qquad (6.14)\end{aligned}$$

where p is the particle's momentum given by RECSIS, q is the particle's charge, and ϕ is the azimuthal angle which is kept unchanged in this scheme. An additional shift in reconstructed momenta caused by the inaccurate magnetic field map is included in the correction procedure by adding another function to the equation 6.14. This function $f(\theta, \phi)$ is parametrized with another 6 parameters (J-O):

$$f = (J\cos\theta + K\sin\theta + L\sin 2\theta)) + (M\cos\theta + N\sin\theta + O\sin 2\theta))\phi. \tag{6.15}$$

The 14 parameters A-O are determined for each sector by using a sample of exclusive events, in which all final particles are identified, and then applying 4-momentum conservation to each of them to evaluate and optimize the quality of the fit parameter χ^2. After the parameters are determined, the polar angles and momenta of the particles can be corrected:

$$\begin{aligned} \theta &\rightarrow \theta + \Delta\theta, \\ p &\rightarrow p(1 + \frac{\Delta p}{p}). \end{aligned} \tag{6.16}$$

A plot in Fig. 6.9 shows the W distribution of the inclusive electrons at the beam energy of 1.6 GeV, before and after the momentum correction. In the corrected version, the value of the elastic peak moves closer to its theoretical value, and the width of the peak is reduced.

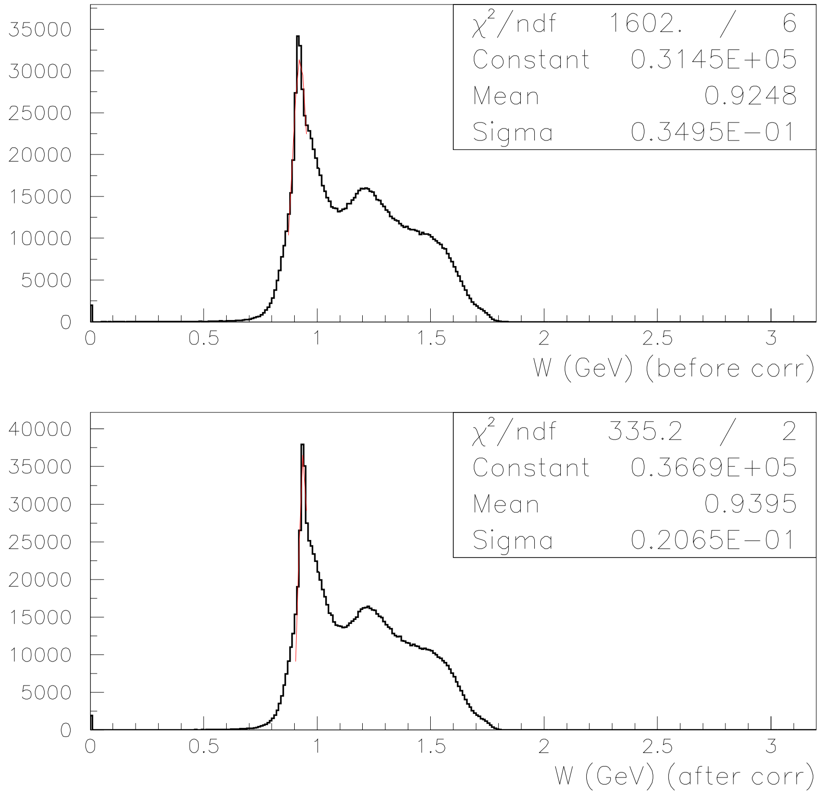

Figure 6.9: W distribution of inclusive electrons. The accuracy and resolution of the position of elastic peak is improved as a result of momentum corrections.

Chapter 7

Data Analysis

7.1 Electron Asymmetry

The first step in the data analysis is to form the raw spin asymmetries of the scattered electrons. After the final sample of electrons is selected, the asymmetry is calculated

$$A_{exp} = \frac{n^{\uparrow}/fc^{\uparrow} - n^{\downarrow}/fc^{\downarrow}}{n^{\uparrow}/fc^{\uparrow} + n^{\downarrow}/fc^{\downarrow}}, \tag{7.1}$$

where $n^{\uparrow}/fc^{\uparrow}(n^{\downarrow}/fc^{\downarrow})$ is the number of electrons with the spin up (down), normalized to the number of incident electrons with the spin up (down), given by the Faraday cup readings. The statistical error associated with the asymmetry is given by:

$$\Delta A_{exp} = \frac{2}{(n^{\uparrow}/fc^{\uparrow} + n^{\downarrow}/fc^{\downarrow})^2}\left[\frac{n^{\uparrow}}{(fc^{\uparrow})^2}{n^{\downarrow}}^2 + \frac{n^{\downarrow}}{(fc^{\downarrow})^2}{n^{\uparrow}}^2\right]^{\frac{1}{2}}. \tag{7.2}$$

The resulting asymmetry is binned in Q^2 and W bins, with the width of W bins being 50 MeV for 5.6 GeV data, and 20 MeV for 1.6 GeV data. The list of standard Q^2

Table 7.1: Q^2 bins

Bin#	Central Value	Min	Max	Bin #	Central Value	Min	Max
10	0.05	0.045	0.054	23	0.5	0.131	0.156
11	0.06	0.054	0.065	24	0.6	0.54	0.645
12	0.07	0.065	0.077	25	0.7	0.645	0.77
13	0.084	0.077	0.092	26	0.84	0.77	0.92
14	0.1	0.092	0.11	27	1.	0.92	1.10
15	0.12	0.11	0.131	28	1.2	1.1	1.31
16	0.14	0.131	0.156	29	1.4	1.31	1.56
17	0.17	0.045	0.054	30	1.7	1.56	1.87
18	0.2	0.054	0.065	31	2.	1.87	2.23
19	0.24	0.065	0.077	32	2.4	2.23	2.66
20	0.3	0.077	0.092	33	3.	2.66	3.17
21	0.35	0.092	0.11	34	3.5	3.17	3.79
22	0.42	0.11	0.131	35	4.2	3.79	4.52

bins is given in Table 7.1

Fig.7.1 shows the Q^2-averaged asymmetry plots for one of the seven data sets analyzed. The plot shows the elastic peak, and higher lying nucleon resonances. The asymmetry was evaluated for all filled Q^2 bins, for every NH_3 run in every data set analyzed. Along with the polarized NH_3 runs, every set contained some data runs obtained with the unpolarized carbon and ^{4}He targets, which are needed for the background subtraction. All runs analyzed for this thesis are listed in Table 7.2.

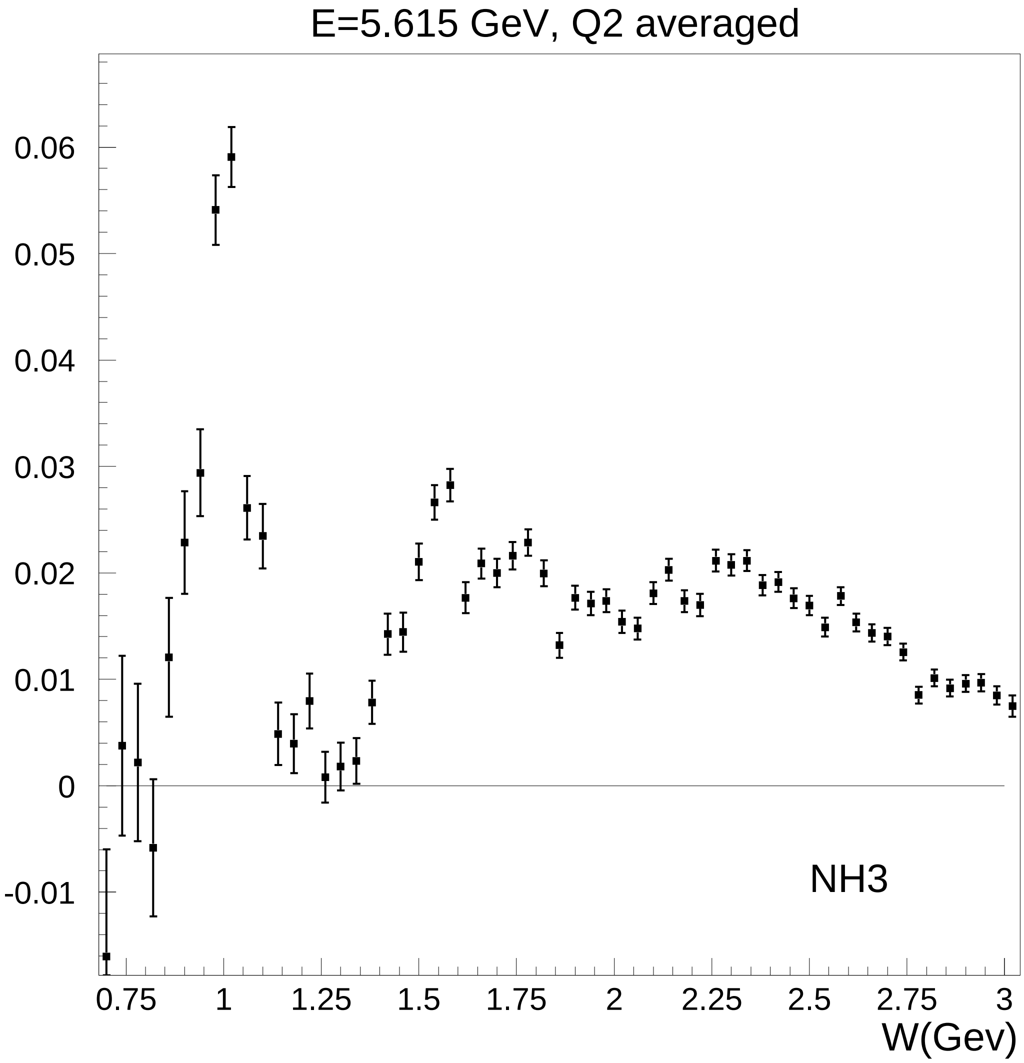

Figure 7.1: Electron Asymmetry $A_{exp} = \frac{n^{\uparrow}/fc^{\uparrow} - n^{\downarrow}/fc^{\downarrow}}{n^{\uparrow}/fc^{\uparrow} + n^{\downarrow}/fc^{\downarrow}}$.

Table 7.2: Run Numbers

Energy/Torus	Target	Run Numbers
1.605/+1500	NH_3	25600-25605,25669-25670,25672,25674-25679,25681,25697-25700,25702-25706,25747,25754,25767-25769,25771,25775-25780,25788-25802,25818,25819,25822-25830,25833-25840,25851-25865,25993,25999-26008,26016-26022,26054,26057-26063,26067,26071-26074,26076,260085,26087-26090,26093,26094,26096-26103,26105-26108,26110,26112
	^{12}C	25683-25686,25781,25785-25787,25813-25817,25841,25842,25867-25869,26010,26012,26013,26033-26035,26077,26078
	^4He	25809-25812,25871,26015,26028,26117
1.605/-1500	NH_3	26292-8,26303,26305-26311,26315,26318-26324
	^{12}C	26240,26241,26244,26245,26285-26287,26326,26327
	^4He	26239
1.723/-1500	NH_3	26292-8,26303,26305-26311,26315,26318-26324
	^{12}C	26240,26241,26244,26245,26285-26287,26326,26327
	^4He	26239
5.615/+2250	NH_3	27458-27464,27472-27484,27494-27499
	^{12}C	27425-27427, 27452-27453, 27455-27456 27466-27467,27491-27492
	^4He	27457,27485
	^{15}N	27364
5.725/+2250	NH_3	27074-27075,27078-27081,27084,27086-27089 27094-27100,27106-27109,27111-27112,27175-27183 27186-27195
	^{12}C	27101-27102,27172,27198
	^4He	27070,27114,27171,27184,27197
5.725/-2250	NH_3	26913-26916,26919-27920,26923-26934,26937-26949,26951-26958,26963-28966,26983-26989,27000-27008,27013-27015
	^{12}C	26904-26906, 26995-26996,27016-27017,27019
	^4He	26998,27020,27021
5.743/-2250	NH_3	26492,26493,26497,26501-26503,26507,26508,26517,26520,26521,26525-26527,26530-26532,26547-26552,26567,26576-26579,26583-26584,26586-26588,26704-26720,26778-26795,26800,26801-26816,26818-26819,26827-26828,26830-26835
	^{12}C	26554-26557,26721,26796,26797,26820,26821
	^4He	26560,26561,26798

Table 7.3: Faraday Cup Calibration

Target Type	2H01	2C24A	2C21A	Avg
empty	0.950	0.944	0.936	0.943
carbon	0.835	0.832	0.824	0.830
$^{15}NH_3$	0.829	0.828	0.814	0.823

7.2 Background Subtraction

7.2.1 Faraday Cup Correction

Measurements with different targets are used to determine the background. It is important that the Faraday Cup efficiency is independent of the target used. It was found, however, that due to multiple scattering there was some loss of beam from the FC, particularly at low beam energies. More beam is lost with the solid targets as opposed to the empty one, therefore, a correction factor is needed to make the counts from different targets compatible. In order to determine the correction factor, the upstream beam monitor readings were compared to the FC for the solid and empty targets. The FC loss factors were obtained from the 3 upstream beam monitors for the beam energy of 1.6 GeV, and their averages are given in Table 7.3.

To incorporate this correction into the data analysis, it was observed that the losses for the carbon and ammonia targets were approximately the same, and the FC reading for the empty target was corrected by multiplying it by 0.88. The correction for the 5 GeV is negligible. For the 1.7 GeV data the 1.6 GeV correction is modified by a factor of 1.6/1.7 since the multiple scattering in the first order is proportional to 1/E.

7.2.2 Dilution Factor

The measured asymmetry is formed by electrons scattered off the polarized protons in $^{15}\mathrm{NH}_3$, the unpolarized ^{15}N nucleus, liquid helium bath and target windows. To obtain the asymmetry for polarized electrons scattering off polarized protons, the other contributions need to be removed from the data. The unpolarized background contributes to the denominator of the asymmetry, thereby 'diluting' it. The 'undiluted' asymmetry is :

$$A_{undil} = \frac{n^{\uparrow}/fc^{\uparrow} - n^{\downarrow}/fc^{\downarrow}}{n^{\uparrow}/fc^{\uparrow} + n^{\downarrow}/fc^{\downarrow} - background}. \tag{7.3}$$

It is convenient to define a 'dilution factor' which represents a fraction of contributions from the polarized protons in ammonia and from all materials together.

$$DF = \frac{^{15}NH_3 - background}{^{15}NH_3} = \frac{n^{\uparrow}/fc^{\uparrow} + n^{\downarrow}/fc^{\downarrow} - background}{n^{\uparrow}/fc^{\uparrow} + n^{\downarrow}/fc^{\downarrow}}. \tag{7.4}$$

Then, the undiluted asymmetry can be written:

$$A_{undil} = \frac{n^{\uparrow}/fc^{\uparrow} - n^{\downarrow}/fc^{\downarrow}}{n^{\uparrow}/fc^{\uparrow} + n^{\downarrow}/fc^{\downarrow}} : \frac{n^{\uparrow}/fc^{\uparrow} + n^{\downarrow}/fc^{\downarrow} - background}{n^{\uparrow}/fc^{\uparrow} + n^{\downarrow}/fc^{\downarrow}} = A_{exp} * \frac{1}{DF}. \tag{7.5}$$

There are 3 polarized protons and a total of 18 nucleons in $^{15}NH_3$, so, in the absence of the helium bath and the target cell foils, and if the neutron cross sections were the same as for the proton, the dilution factor would be 1/6.

However, due to the presence of additional materials in the beam path, the calculation of the dilution factor is not so straightforward. The table of densities and thicknesses of these materials is given in Table 7.3. During the experiment, data were taken with the unpolarized ^{12}C target and the so-called 'empty' target filled with only

Table 7.4: Background Parameters

Parameter	Value	Comment
$\rho_f l_f$	Al:71+25+71 μm=0.045g/cm^2 Kapton:127+50+127 μm=0.0432g/cm^2 +80μm=0.055g/cm^2(after 27997) total m=0.0882g/cm^2(0.0996g/cm^2)	additional piece of Kapton was added after run 27997
$\rho_C l_C$	0.498 g/cm^2=0.0415 mol/cm^2)	
$f = \frac{\rho_f l_f}{\rho_C l_C}$	0.177(0.200)	
ρ_{He}	0.145g/cm^2=0.0362 mol/cm^2	
L	1.90 cm	calculated from n_{mt}/n_c
ρ_C	2.17g/cm^2=0.180mol/cm^2	
l_C	0.23 cm	
ρ_N	1.1 g/cm^2=0.07325 mol/cm^2	
l_N	0.65 cm	
ρ_{NH_3}	0.917g/cm^2=0.0508mol/cm^2	
l_{NH_3}	$\sim$ 0.55 cm	extracted from data

helium. Data were also taken with the ^{15}N target. Due to the limited statistics of the ^{15}N data, the ^{15}N background was simulated from the measurements with the other targets. ^{15}N data were used to check the quality of the simulation. The method used for background calculation is descibed in this section.

The first step is to express the number of detected electrons in terms of the contribution from each material. In this method, the density ρ is given in mol/cm^3, cross sections are in cm^2/nucleus, and the contribution of all foils is given as a fraction f of the ^{12}C contribution:$f = \frac{l_f \rho_f \sigma_f}{l_c \rho_c \sigma_c}$. The FC normalized counts obtained with the carbon target consist of the sum of counts from the foils (entrance and exit windows), the helium bath, and the carbon itself:

$$n_c = \rho_f l_f \sigma_f + \rho_{He}(L - l_c)\sigma_{He} + \rho_c l_c \sigma_c = \left[(1+f)\rho_c l_c \frac{\sigma_c}{\sigma_D} + \rho_{He}(L - l_c)\sigma_{He}\right]\sigma_D. \quad (7.6)$$

Similarly, the counts obtained with the helium filled target (called the empty target) are a sum of the contributions from the foils and the helium bath:

$$n_{mt} = \rho_f l_f \sigma_f + \rho_{He} L \sigma_{He} = \left[\rho_c l_c f \frac{\sigma_c}{\sigma_D} + \rho_{He} L \frac{\sigma_{He}}{\sigma_D}\right] \sigma_D. \tag{7.7}$$

An additional correction was applied to the empty target counts to account for the difference in radiation length between it and the solid targets. The empty target has thickness of 0.006 r.l., while ^{12}C and ^{15}NH$_3$ (together with He bath and foils) have thickness of 0.018 r.l. The measured empty target counts were corrected by calculating fully radiated cross sections for He for two target thicknesses. The counts from helium in the 'empty' target are multiplied by the correction factor to get what they would have been if the target were 1.8 % in r.l.

The counts obtained with a nitrogen filled target are then given by:

$$n_N = \rho_f l_f \sigma_f + \rho_{He}(L - l_N)\sigma_{He} + \rho_N l_N \sigma_N = \left[\rho_c l_c f \frac{\sigma_c}{\sigma_D} + \rho_{He}(L - l_N)\sigma_{He} + \rho_N l_N \frac{\sigma_N}{\sigma_D}\right] \sigma_D. \tag{7.8}$$

By comparing rates obtained with the ^{12}C target and the empty target it is possible to calculate the separate contibutions of the ^{12}C and He:

$$\begin{aligned} n'_c &= \frac{L}{L + f l_c} n_c - \frac{L - l_c}{L + f l_c} n_{mt}, \\ n'_{He} &= \frac{1 + f}{L + f l_c} n_{mt} - \frac{f}{L + f l_c} n_c, \end{aligned} \tag{7.9}$$

where $n'_c = \rho_c l_c \sigma_c$ and $n'_{He} = \rho_{He} l_{He} \sigma_{He}$. To determine the contribution of the ^{15}N using our measured data, we used a model. Since ^{15}N contains 7 protons and 8 neutrons while ^{12}C contains 6 protons and 6 neutrons, we assumed the following relation:

$$\begin{aligned} \sigma_N &= 7\sigma_D + 1\sigma_n, \\ \sigma_C &= 6\sigma_D, \\ \sigma_N &= \frac{7\sigma_D + 1\sigma_n}{6\sigma_D}\sigma_c = (a + b\frac{\sigma_n}{\sigma_D})\sigma_c, \end{aligned} \tag{7.10}$$

where σ_D is the deuteron cross section and σ_n is the neutron cross section. The parameters a and b have been introduced to allow for deviations from these simple relationships. The ratio, σ_D/σ_n, was obtained from a fit to world data carried out by S. Kuhn [43]. With this model the expected rate with the ^{15}N target is

$$\begin{aligned} n_N &= \left[\rho_c l_c f\frac{\sigma_c}{\sigma_D} + \rho_{He}(L - l_N)\sigma_{He} + \rho_N l_N\frac{\sigma_N}{\sigma_D}\right]\sigma_D \\ &= n'_c f + n'_{He}L - l_N n'_{He} + \rho_N l_N\frac{\sigma_N}{\sigma_D}\sigma_D \\ &= n_{mt} - l_N n'_{He} + l_N\frac{\rho_N}{\rho_c l_c}(a + b\frac{\sigma_n}{\sigma_D}n'_c). \end{aligned} \tag{7.11}$$

This equation was fit to the ^{15}N data, allowing a and b to vary. Attempts to fit with l_N as a free parameter were unstable. Independent fits were carried out for different Q^2 values and the resulting values of a and b were averaged. These average values were $a = 1.1965$ and $b = 0.22665$, which are close to their theoretical values of 7/6 and 1/6 respectively. A sample of the fit is shown in Fig. 7.2.

With this model for ^{15}N we can now write an expression for the contributions from all materials in the beam other than polarized protons in the ammonia $^{15}NH_3$ target, namely the foils, the helium bath and the ^{15}N part of the $^{15}NH_3$ target. The total background counts are: $n_b = n_N + n_{He} + n_{foils}$. Each of these components is

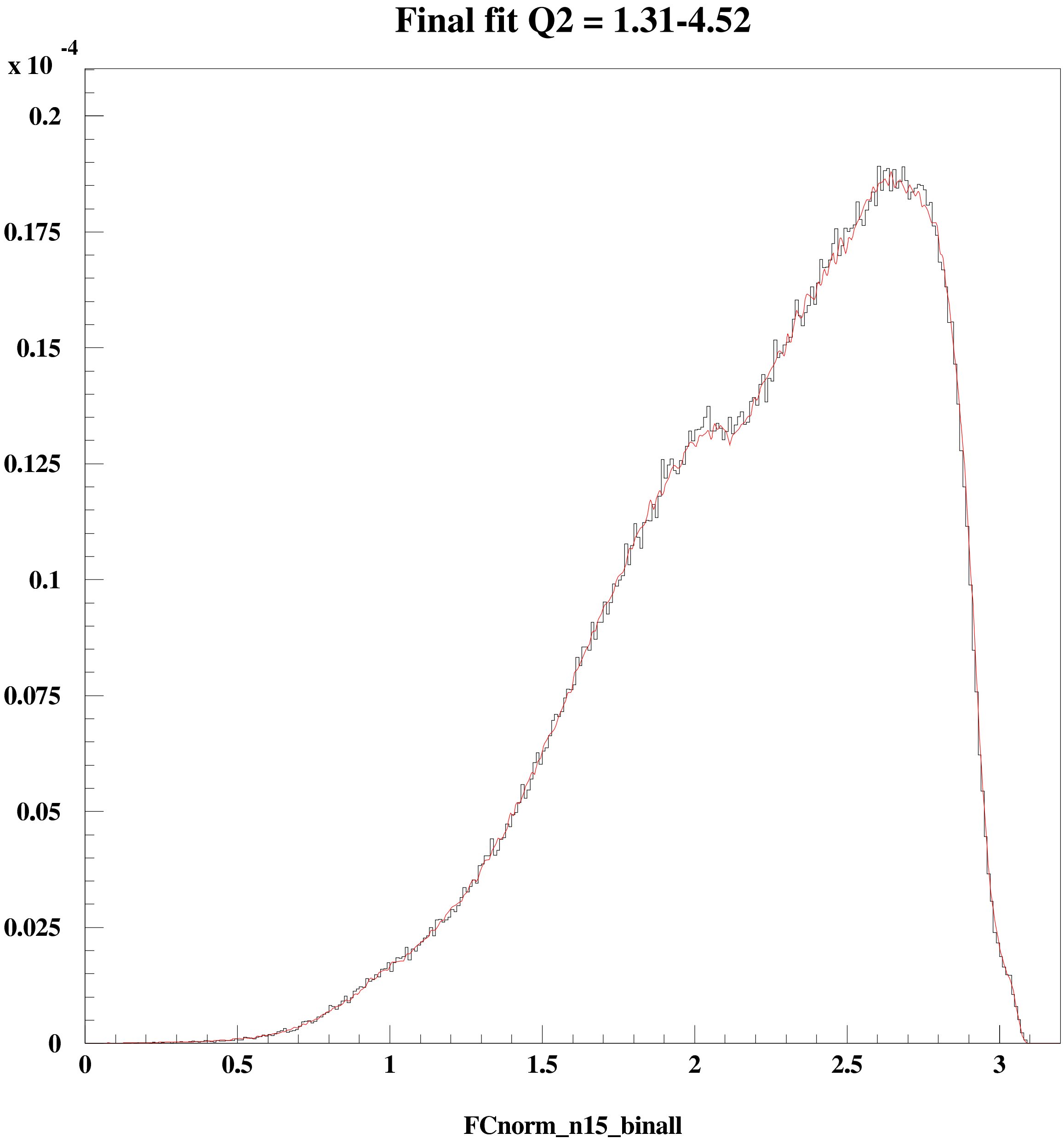

Figure 7.2: Counts normalized to the Faraday Cup vs W. The measured ^{15}N W spectrum is plotted in black. The simulated ^{15}N W spectrum obtained with ^{12}C data is shown in red. Plot is a courtesy of V. Dharmavardane.

known, so that the background can be calculated explicitly:

$$\begin{aligned}
n_{He} &= (L - l_A)n'_{He}, \qquad (7.12)\\
n_{foils} &= f n'_c,\\
n_N &= \rho_A l_A \frac{n'_c}{\rho_c l_c}(a + b\frac{\sigma_n}{\sigma_D}),\\
n_b &= n_{mt} + l_A \left[\left[\frac{\rho_A}{\rho_c l_c}(a + b\frac{\sigma_n}{\sigma_D})\right] n'_c - n'_{He}\right].
\end{aligned}$$

All variables in the last equation are known except for the length, l_A, of the ammonia target. Since the target material consists of crystal beads, the actual thickness is less than the physical length of the cell. The ratio of the actual thickness to the length of the target is called the packing fraction. For our target the physical length is 1 cm, so l_A is also the packing fraction. The packing fraction can be extracted from data using the ^{15}NH$_3$, ^{12}C and ^{4}He runs. The method used to extract l_A used a high W region, above the resonances, and it was assumed that the ratios of cross sections can be approximated by the number of protons and neutrons in each. Since ^{15}NH$_3$ consists of one nitrogen and 3 hydrogens, the cross sections can be related by using our model for ^{15}N:

$$\begin{aligned}
\sigma_A &= \sigma_N + 3\sigma_H = \sigma_c(a + b\frac{\sigma_n}{\sigma_D} + 3\frac{\sigma_H}{\sigma_c}), \qquad (7.13)\\
\sigma_H &= (1 - \frac{\sigma_n}{\sigma_D})\sigma_D = (1 - \frac{\sigma_n}{\sigma_D})\frac{\sigma_c}{6},\\
3\frac{\sigma_H}{\sigma_c} &= 3(1 - \frac{\sigma_n}{\sigma_D})\frac{\sigma_D}{\sigma_c} = 0.5(1 - \frac{\sigma_n}{\sigma_D}).
\end{aligned}$$

Then, the spectrum obtained with the ammonia target is:

$$\begin{aligned} n_A &= n_{mt} + l_A \left[\frac{\rho_A}{\rho_c l_c} (a + b\frac{\sigma_n}{\sigma_D} + 3\frac{\sigma_H}{\sigma_c}) n'_c - n'_{He} \right], \qquad (7.14) \\ n_A &= n_{mt} + l_A \left[\frac{\rho_A}{\rho_c l_c} \left[a + b\frac{\sigma_n}{\sigma_D} + 0.5(1 - \frac{\sigma_n}{\sigma_D}) \right] n'_c - n'_{He} \right]. \end{aligned}$$

Solving the last equation for l_A:

$$l_A = \frac{n_A - n_{mt}}{\frac{\rho_A}{\rho_c l_c} \left[a + b\frac{\sigma_n}{\sigma_D} + 0.5(1 - \frac{\sigma_n}{\sigma_D}) \right] n'_c - n'_{He}}. \qquad (7.15)$$

In order to determine the packing fraction l_A for a particular data set, a subset of ammonia, carbon and helium runs for which the electron counts per FC are stable was selected. This step eliminated runs with a problem in one of the sectors. After the selection, the W spectra for each target material are statistically similar. These spectra were used to plot the packing fraction as defined in equation 7.15. It is plotted separately for each relevant Q^2 bin, and each sector separately. For each sector, the packing fraction is averaged over all available Q^2 bins, using statistical weighting. No dependence of the packing fraction on the Q^2 value was observed. After that, the l_A is averaged over sectors, excluding sectors that had a problem during the run. A typical plot of l_A vs W is shown in Fig. 7.3. A straight line is fit to a high W region of l_A, and the value of the fitting parameter is taken to be the value of the packing fraction. The value of the packing fraction varied from 0.54 to 0.61. Once the packing fraction has been evaluated, the contribution of all background materials can be calculated and added. There are two plots in Fig. 7.4. The first one shows the calculated W spectra for the simulated ^{15}N, total background including ^{15}N, foils and helium bath,

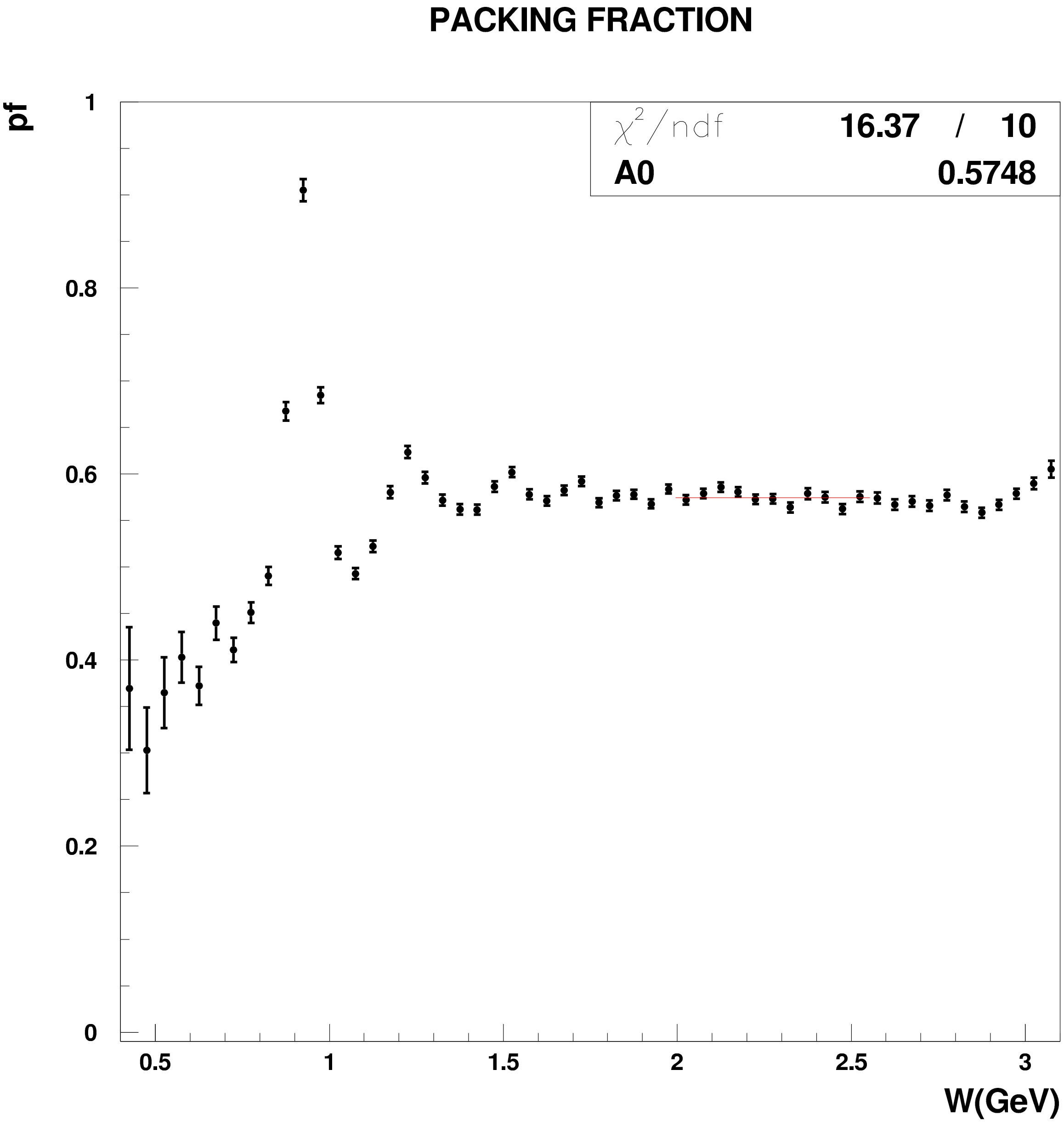

Figure 7.3: Q^2-averaged packing fraction for the E=5.725 GeV, inbending data.

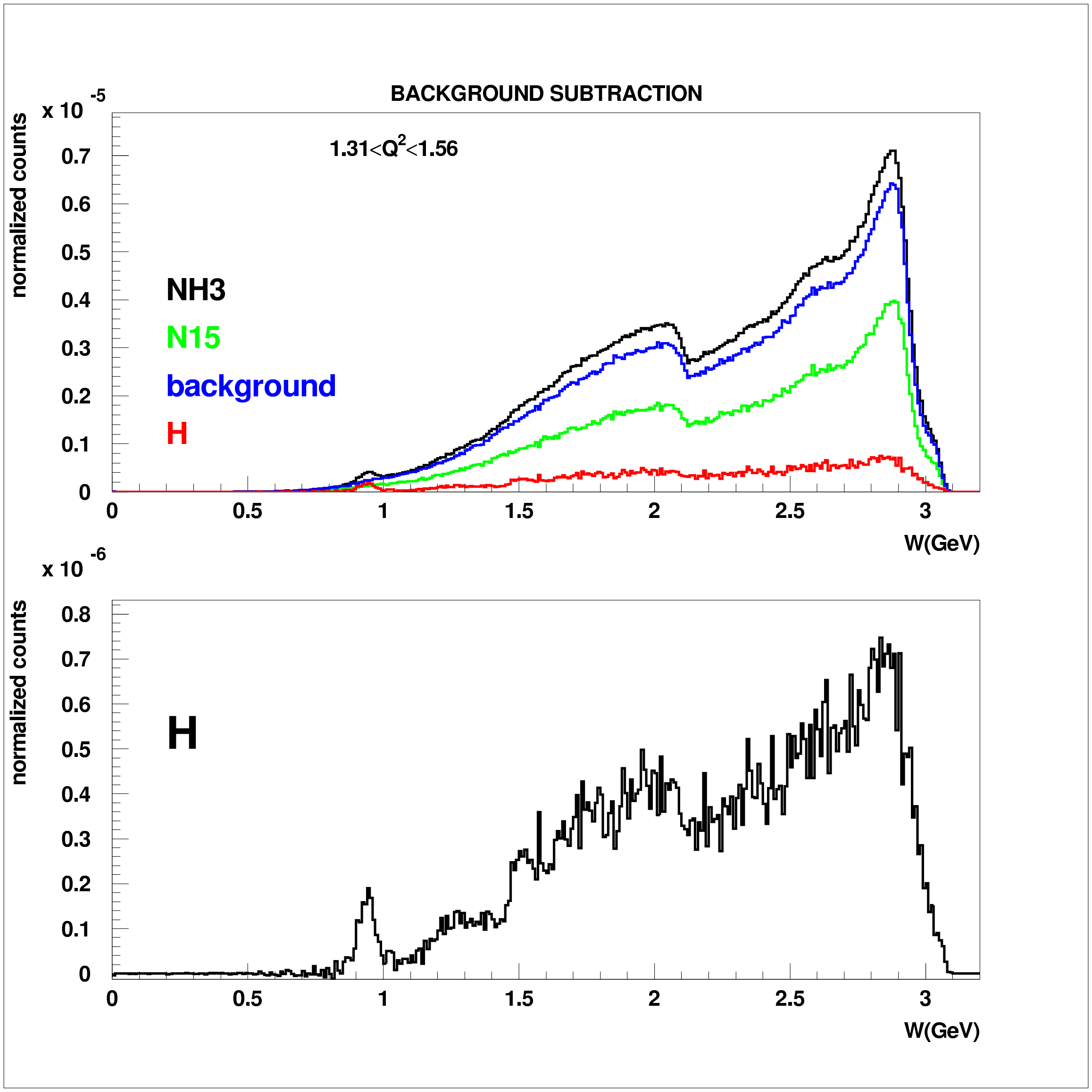

Figure 7.4: Background subtraction for data set with E=5.615 GeV. The top plot shows W spectra for $^{15}NH_3$ (black), ^{15}N (green), total background (blue) and H=($^{15}NH_3$-background) in red. The bottom plot shows H on the smaller scale.

$^{15}NH_3$ spectra, and the result of subtracting the total background from $^{15}NH_3$. The resulting plot should contain the hydrogen contribution only. The second plot shows the subtracted result on a smaller scale.

Finally, the dilution factor can be evaluated using the subtracted and unsubtracted spectra. The dilution factor is evaluated separately for every Q^2 bin and every sector. For each Q^2 bin, the dilution factor is averaged over all sectors, excluding the problematic ones:

$$\begin{aligned} DF &= 1 - \frac{n_b}{n_A} = 1 - \frac{n_{mt} + l_A\left[1.227(a + b\frac{\sigma_n}{\sigma_D})n'_c - n'_{He}\right]}{n_A}, \qquad (7.16) \\ n'_c &= 0.979n_c - 0.861n_{mt}, \\ n'_{He} &= 0.606(0.616)n_{mt} - 0.091(0.103)n_c. \end{aligned}$$

The numbers in the parentheses refer to runs after 27997, when an additional layer of Kapton foil was wrapped around the ammonia target. These runs were not used in this analysis. For convenience, the quantity $l_A * 1.227(a + b\frac{\sigma_n}{\sigma_D})$ is labeled as C. Then, the statistical error associated with the dilution factor is

$$\begin{aligned} \Delta DF &= \frac{1}{(n_b)^2}\left[(\Delta n_b)^2 * n_A^2 + (\Delta n_A)^2 * n_b^2\right]^{1/2}, \qquad (7.17) \\ (\Delta n_b)^2 &= (\Delta n_{mt})^2(1 - .861C - .606l_A)^2 + (\Delta n_c)^2(.979C + .091l_A)^2, \\ \Delta DF &= \frac{1}{(n_A)^2}\left[\frac{n_{mt}}{fc_{mt}}(1 - .861C - .606l_A)^2 + \frac{n_c}{fc_c}(.979C + .091l_A)^2\right]^{1/2}. \end{aligned}$$

The ammonia n_A and the background n_b counts necessary to calculate the dilution factor are found for every Q^2 and W bin. Since the data runs used for this calculation are restricted to those with very stable conditions, the statistics are limited, and

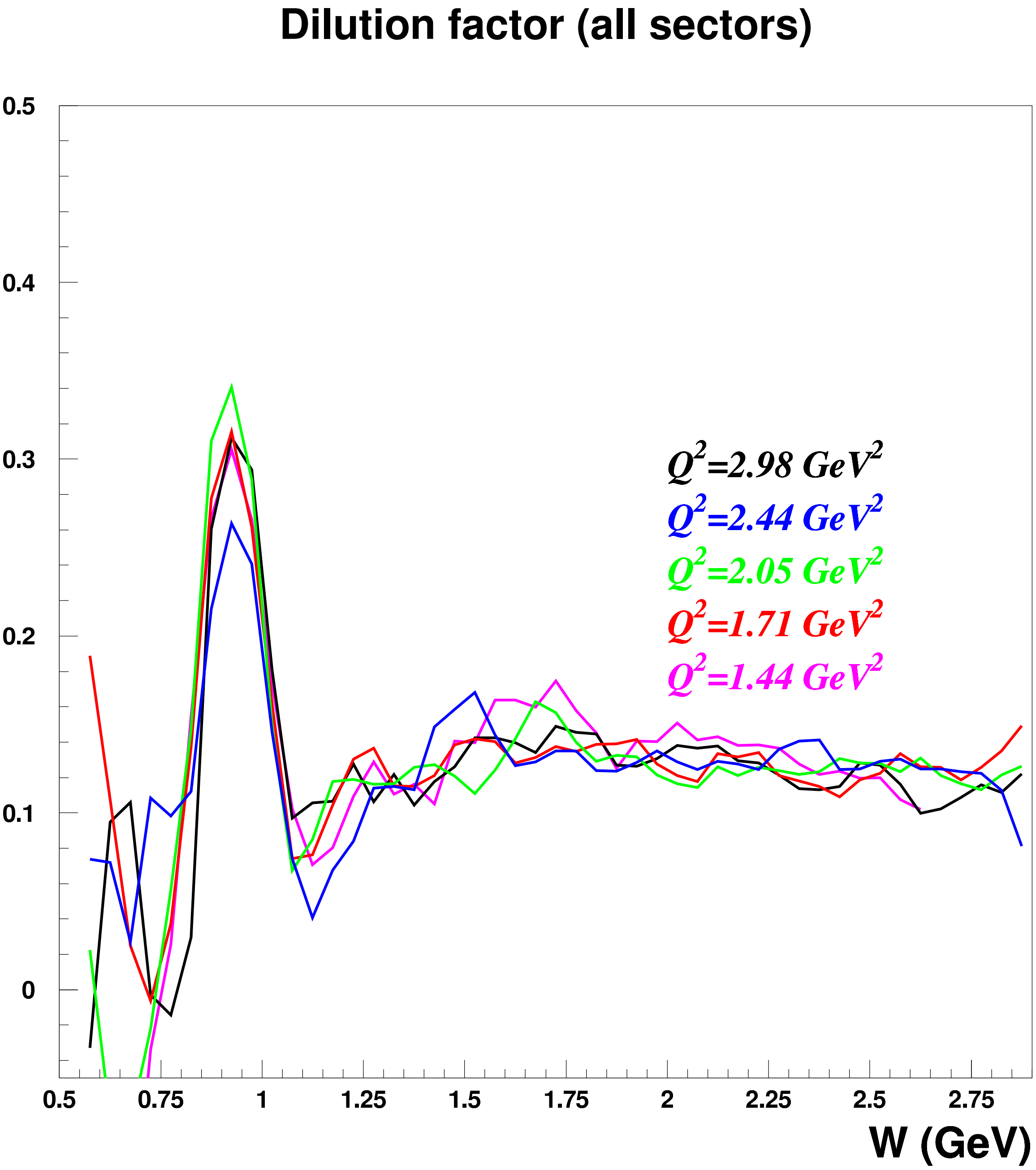

Figure 7.5: Dilution factor for different Q^2 bins in data set with E=5.615 GeV. No significant variation with Q^2 is observed.

unphysically large fluctuations can be observed from one W bin to another. In order to remedy this situation, a 'smoothing' procedure was used, where each W bin was replaced by a sum of that bin and the two adjacent ones. This was applied to both the ammonia and the background spectra before calculating the dilution factor. A plot of the dilution factor before and after the 'smoothing' procedure is shown in Fig. 7.6. A 'smoothing' over high Q^2 bins was also applied to the high Q^2 bins with low statistics.

The value of the dilution factor varied from 0.11 to 0.13, depending on the value of Q^2, and the data set. A statistical error associated with the dilution factor was not propagated in calculating the undiluted asymmetry. The uncertainty associated with evaluation of dilution factor is included in the systematic error analysis.

7.3 Beam and Target Polarization

After the background has been estimated, the experimental asymmetry can be 'undiluted':

$$\begin{aligned} A_{undil} &= A_{exp} * \frac{1}{DF}, \\ \Delta A_{undil} &= \Delta A_{exp} * \frac{1}{DF}. \end{aligned} \tag{7.18}$$

A plot of the 'undiluted' asymmetry is shown in Fig. 7.7. The next step is to use the undiluted asymmetry to extract the product of beam and target polarization $P_b P_t$. The measurement of the target and beam polarizations was performed independently during the experiment. The electron beam polarization was measured by a Møller polarimeter, while the target polarization was monitored by the NMR system, dis-

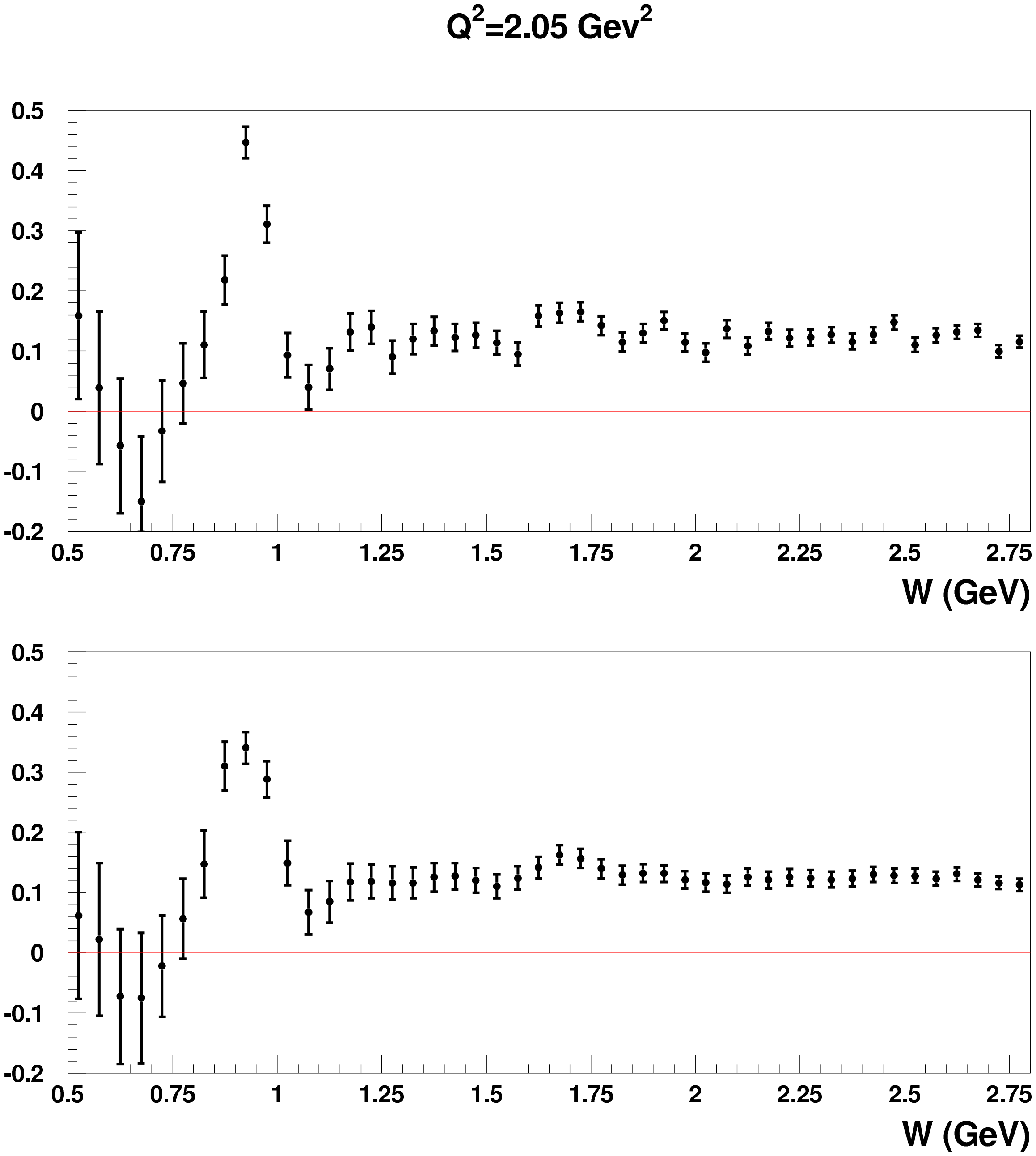

Figure 7.6: Dilution factor before and after 'smoothing', as described in section 7.2.2

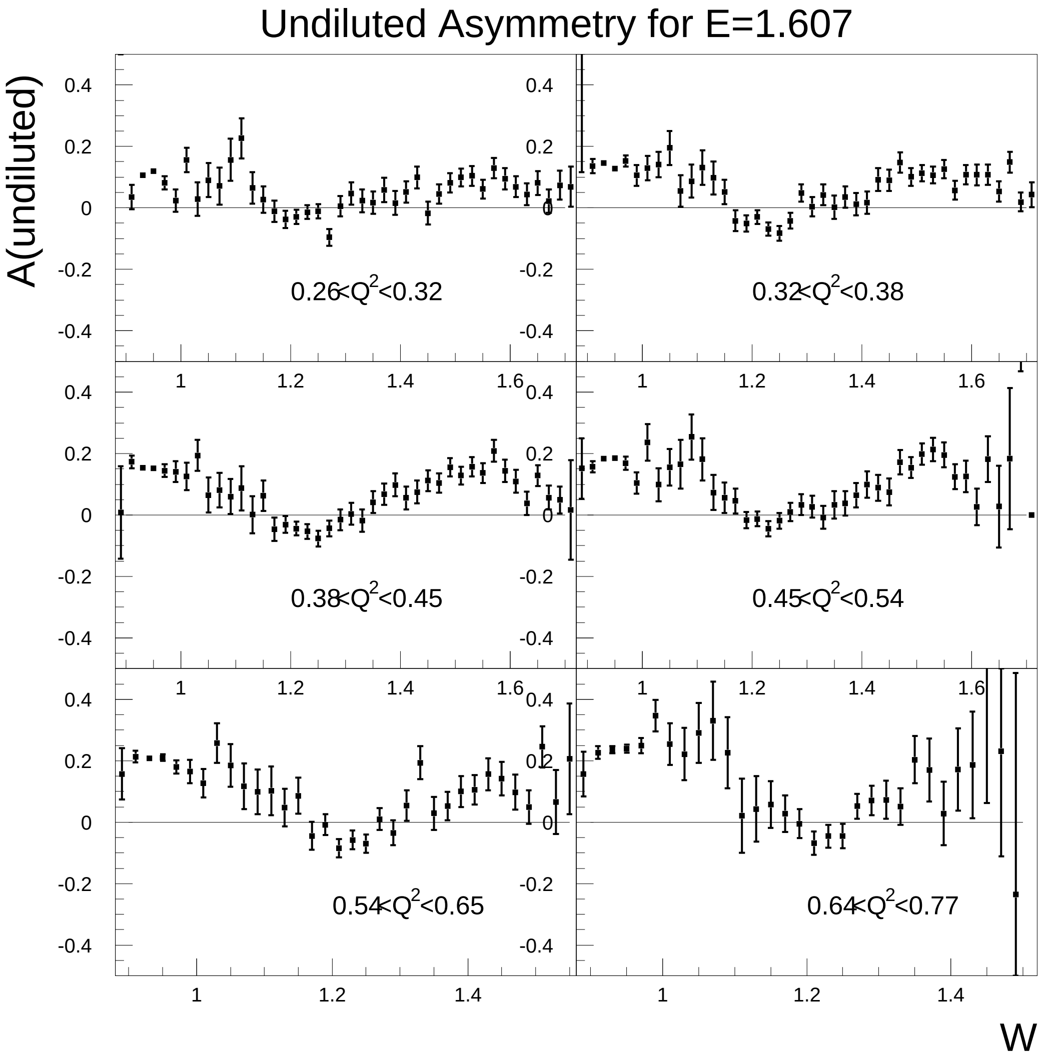

Figure 7.7: $A_{undil} = A_{exp} * \frac{1}{DF}$ for different Q^2 bins in data set with E=1.607 GeV, I=1500 Amps

cussed in the Target chapter. While the determination of the beam polarization is considered accurate, the NMR measurement was affected by several uncertainties. The electron beam causes radiation damage of the material, which can lead to a depolarized region within the target cell. Since the NMR coils are located outside of the cell, the measurement is mostly sensitive to the polarization of the outer layer of target material. Also, the technique depends on the value of the signal size at thermal equilibrium, producing additional uncertainties due to the small size of the TE signal. [44]. Therefore, an independent method of extracting polarization is highly desirable.

The method to determine P_bP_t used in this analysis is based on the knowledge of the theoretical value of asymmetry in the elastic process at given kinematics. The method is discussed in reference [45]. It predicts the value of the elastic asymmetry [46]:

$$A_{||} = \frac{2\tau r * \left[\frac{m_p}{e} + r(\tau\frac{m_p}{e} + (1+\tau)\tan^2(\frac{\theta}{2}))\right]}{1+\tau\frac{r^2}{\epsilon}}, \tag{7.19}$$

where $\tau = \frac{Q^2}{4m_p^2}$, e is the beam energy, θ is the electron scattering angle, $\epsilon = 1/(1 + 2(1+\tau)\tan^2(\frac{\theta}{2})$, and $r = \frac{G_{M_p}}{G_{E_p}} \approx 2.79$. The predicted asymmetry is evaluated for every beam energy setting, and every relevant Q^2 bin. By comparing the theoretical value with the one extracted from data, it is possible to obtain the product of beam and target polarization:

$$P_bP_t = \frac{A_{measured}}{A_{predicted}}. \tag{7.20}$$

This was done separately for each Q^2 bin, after which an average was taken to obtain one value of P_bP_t for each data set. The extraction of the elastic asymmetry is done using two methods. In the first one, elastic events are selected by detecting only the scattered electron, reconstructing the mass of the final state W , and using a cut on that mass $0.9 < W < 1.0$ GeV. In this approach, the elastic asymmetry is extracted by evaluating the undiluted asymmetry in the elastic W region. In the second method, both the scattered electron and proton are detected in the final state, and their azimuthal angle correlation is used to select elastic events. In order to select $e - p$ coincidence events, an elastic electron is first identified by using the standard electron cuts, and restricting the W range to the elastic region. As a second step, the expected momentum and scattering angle of the elastic proton are calculated. The final energy of the elastically scattered electron is calculated:

$$E_{out} = \frac{m_p E_{beam}}{m + p + 2E_{beam}\sin^2(\theta/2)}. \tag{7.21}$$

Using the conservation of energy (E_{beam}+m_p=E_{out}+E'_p), the energy of the elastically scattered proton is given by:

$$E'_p = E_{beam} + m_p - \frac{m_p E_{beam}}{m_p + 2E_{beam}\sin^2(\theta/2)}. \tag{7.22}$$

The 3-momentum can now be found by using $\mathbf{p}$=$\sqrt{E'^2_p - m^2_p}$. In order to find the proton's scattering angle, conservation of 3-momentum along the z-axis (beam direction) is used:

$$\begin{aligned} E_{beam} &= E_{out}\cos\theta_e + \mathbf{p}\cos\theta_p, \\ \cos\theta_p &= \frac{E_{beam} - E_{out}\cos\theta_e}{\sqrt{E'^2 2_p - m^2_p}}. \end{aligned} \tag{7.23}$$

The protons with the momentum within 0.2 GeV of the predicted elastic value, and angle within 1.25° on the expected value were selected. Finally, after selecting elastic

Table 7.5: Target and Beam Polarization

Data Set	P_bP_t(incl)	P_bP_T(excl)
5.615/+2250	0.5507 ± 0.034	0.6043 ± 0.027
5.725/+2250	0.5064 ± 0.028	0.5128 ± 0.015
5.725/-2250	0.4958 ± 0.013	0.5072 ± 0.023
5.743/+2250	0.5145 ± 0.014	0.4750 ± 0.029
1.606/+1500	0.5420 ± 0.005	
1.606/-1500	0.5367 ± 0.01	
1.723/-1500	0.5639 ± 0.008	

ep candidates, the difference between their azimuthal angles was plotted for each electron helicity separately. The distribution in such plots was centered around 180° as would be expected for these events. All events between $\phi = 178°$ and $\phi = 182°$ were counted to contribute to $nh_3^{\uparrow}$ or $nh_3^{\downarrow}$ counts, while events between $\phi = 175°$ and $\phi = 177°$ plus events between $\phi = 183°$ and $\phi = 185°$ contributed to the background counts. The elastic asymmetry is then:

$$A_{el} = \frac{nh_3^{\uparrow} - nh_3^{\downarrow}}{nh_3^{\uparrow} + nh_3^{\downarrow} - background}. \tag{7.24}$$

The inclusive and exclusive methods produced results which agreed within the statistical error. While the inclusive method had the advantage of large statistics, the exclusive one used a cleaner sample of hydrogen counts. The agreement is illustrated in Fig.7.8

After the value of P_bP_t is evaluated, $A_{||}$ is found:

$$A_{||} = A_{undil}/P_bP_t, \tag{7.25}$$

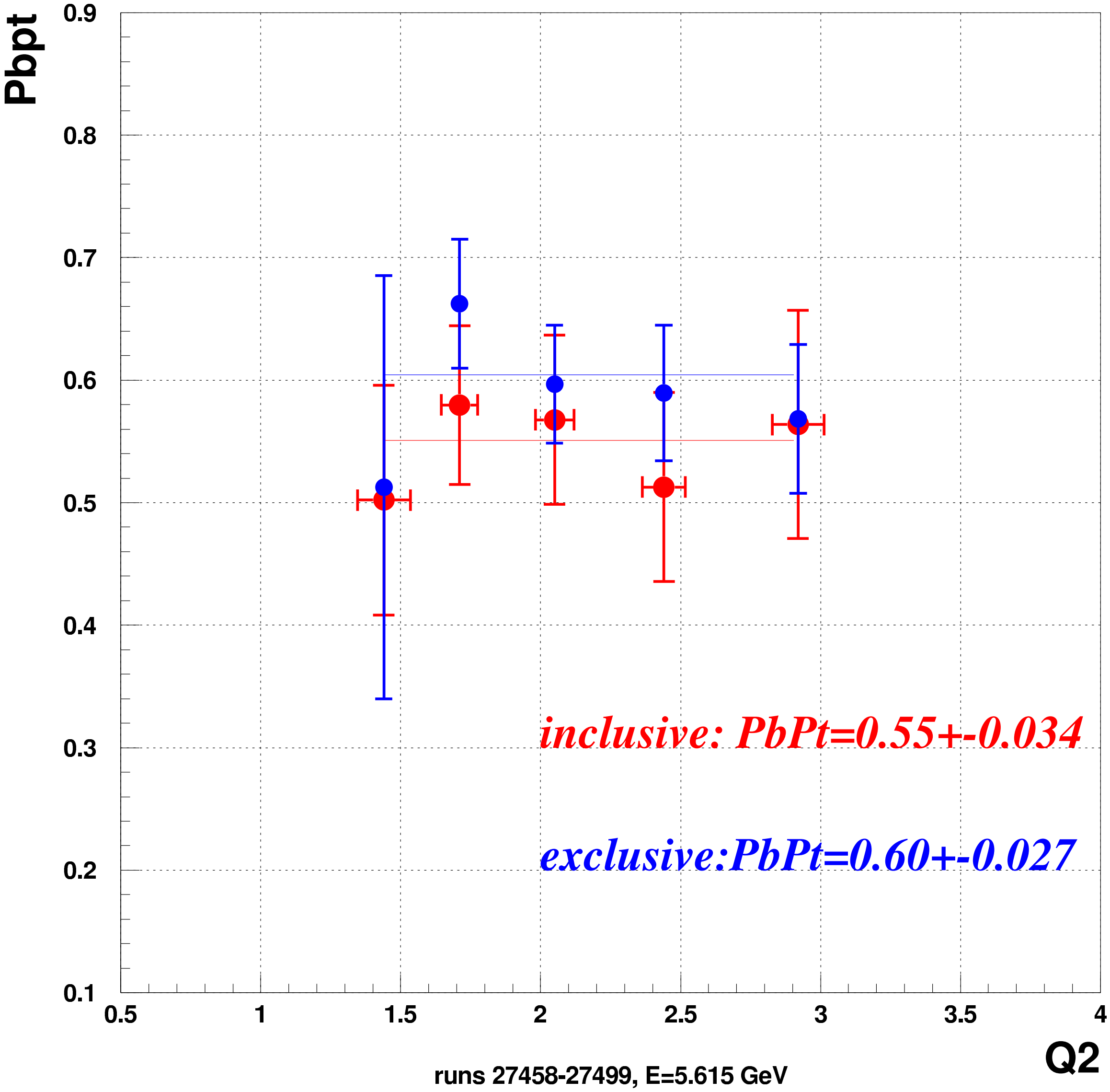

Figure 7.8: P_bP_t evaluated by two methods. The inclusive and exclusive results agree within the statistical error.

$$\Delta A_{\parallel} \;=\; \Delta A_{undil}/P_b P_t.$$

7.4 Corrections to $A_{\parallel}$

7.4.1 Nuclear Correction

Along with the polarized hydrogen protons, the target contains another polarizable nuclear component, a ^{15}N nucleus. Electrons scattered off ^{15}N contribute to the measured spin asymmetry, therefore a correction is needed to take that fact into account. The spin in ^{15}N is carried by an unpaired proton, whose polarization needs to be calculated. According to the EST theory described in section 4.2.3, the polarization of the ^{15}N nucleus can be estimated from the knowledge of the proton polarization in the same material:

$$P_{^{15}N} = P_p * \frac{\mu_{^{15}N}}{\mu_p} = P_p * \frac{-0.264\mu_N}{2.793\mu_N} = -0.0945P_p. \tag{7.26}$$

As the proton polarization grows, $P_{^{15}N}$ behavior exhibits deviations from the EST prediction. During the E143 experiment at SLAC, the polarizations of ^{15}N and $^{15}NH_3$ were measured independently in one material sample, and a fit was obtained based on this data [47]:

$$P_{^{15}N} = -(0.13561 * P_p - 0.18286 * P_p^2 + 0.33482 * P_p^3). \tag{7.27}$$

Ammonia has three hydrogen atoms for each nitrogen, and the free proton in ^{15}N is expected to be anti-aligned with the nuclear spin one third of the time [48], therefore, polarization of the proton in ^{15}N is $-\frac{1}{3}\frac{1}{3}P_{^{15}N}$. The nuclear correction to $A_{||}$ is calculated as a factor C_1 [47]:

$$C_1 = 1.0 - \frac{P_{^{15}N}}{P_p} * \frac{1}{3}\frac{1}{3}. \tag{7.28}$$

The asymmetry is then divided by C_1. Using a typical value of proton polarization of $P_p = 75\%$, C_1 is 1.009, so that this correction is relatively small.

7.4.2 Pion contamination

The electron asymmetry also needs to be corrected for the pion contamination. Some basic cuts were applied to the electron sample to differentiate between electrons and pions, in particular, the cut on the number of photoelectrons in the Cerenkov detector ($nphe > 2.5$), and the cut on the ratio of total energy deposited in the Electromagnetic Calorimeter to the momentum of the particle ($EC_{tot}/p > 0.2$). These cuts were discussed in detail in Section 6.4. However, some contamination of the electron sample with pions still occurs, particularly at the low electron momentum. The procedure to estimate the fraction of pions misidentified as electrons is outlined below.

In the first step, a distribution of photoelectrons (multiplied by 10) is plotted for particles that passed all electron cuts discussed earlier, excluding the Cerenkov cut ($nphe > 2.5$). This plot is shown in the bottom left corner of Fig 7.9. In order to see what particles are causing the peak of photoelectrons in the range $0.5 < nphe < 2.5$, their EC profile needs to be examined. This is done by plotting E/p fraction for these events. The plot is shown in upper left corner of Fig 7.9. The plot appears to be a combination of pions and electrons. A Gaussian plus an exponential are fitted to this distribution in order to see what fraction of the sample consists of electrons. Two fitting parameters (mean and width) of the distribution are bounded by the parameters obtained from fitting a 'pure' electron sample (shown in the upper right corner of Fig 7.9). The total number of particles N_{tot} is obtained by calculating the total area under the curve (upper left plot), while the number of electrons N_e in this sample is calculated by finding the area under the Gaussian. Then, the fraction of pions is $f = 1 - N_e/N_{tot}$. Next, a photoelectron distribution is plotted for particles defined as pions (bottom right corner of Fig. 7.9). Here the pions are defined as negatively charged particles with mass greater than 100 MeV that pass the vertex and fiducial cuts, but not the EC cut. This plot is used to calculate the normalization factor N. N is calculated by integrating the nphe spectra over the interval $0.5 < nphe < 2.5$ for both the pion and contaminated electron samples (plots in the bottom right and left corners correspondingly): $N = \int_{0.5}^{2.0} nphe(e) * bin_{size} / \int_{0.5}^{2.0} nphe(\pi) * bin_{size}$. Finally, a fraction of electrons x that pass the CC cut but are actually pions is calculated :

$$x = \frac{\pi}{e} = f * N * \frac{\int_{2.5}^{300} nphe(\pi) * bin_{size}}{\int_{2.5}^{300} nphe(e) * bin_{size}}. \tag{7.29}$$

This fraction is calculated for various Q^2 and momentum bins for both the inbending and outbending 5.6 GeV runs. Results are shown in Fig.7.10. The correction is then applied to $A_{||}$ as follows:

$$A_{||}^{corr} = A_{||} * \frac{1 - xA_{\pi}/A_{||}}{1 - x}, \tag{7.30}$$

where A_{π} is the pion asymmetry, assumed to be zero in this analysis.

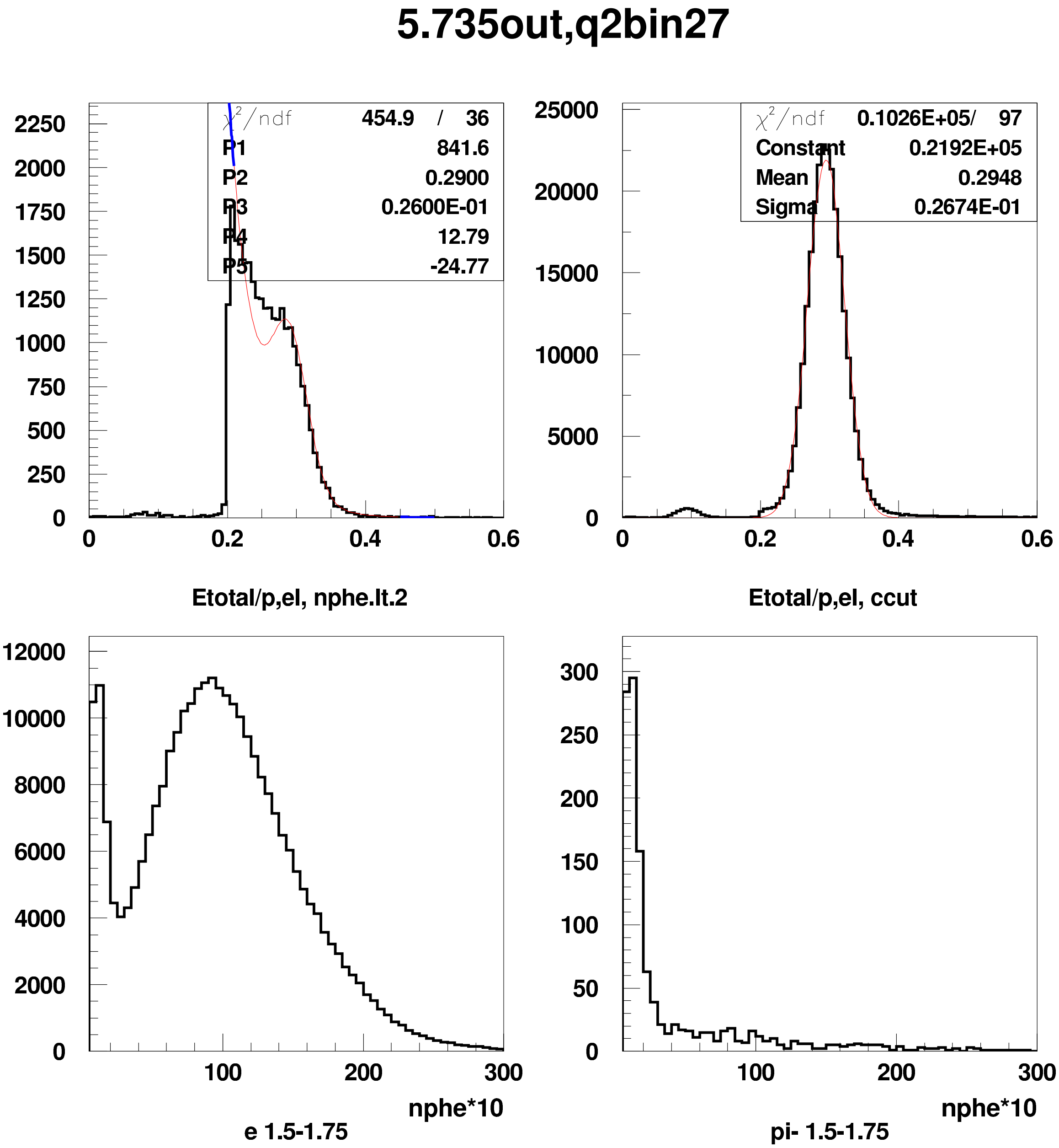

Figure 7.9: Pion contamination. Plots clockwise from upper left corner: 1. E/p distribution for the standard electron definition, but reversed Cerenkov Cut. 2. Same plot for the standard electron definition 3. Photoelectron distribution for electrons for one momentum bin 4.Photoelectron distribution for pions for the same momentum bin.

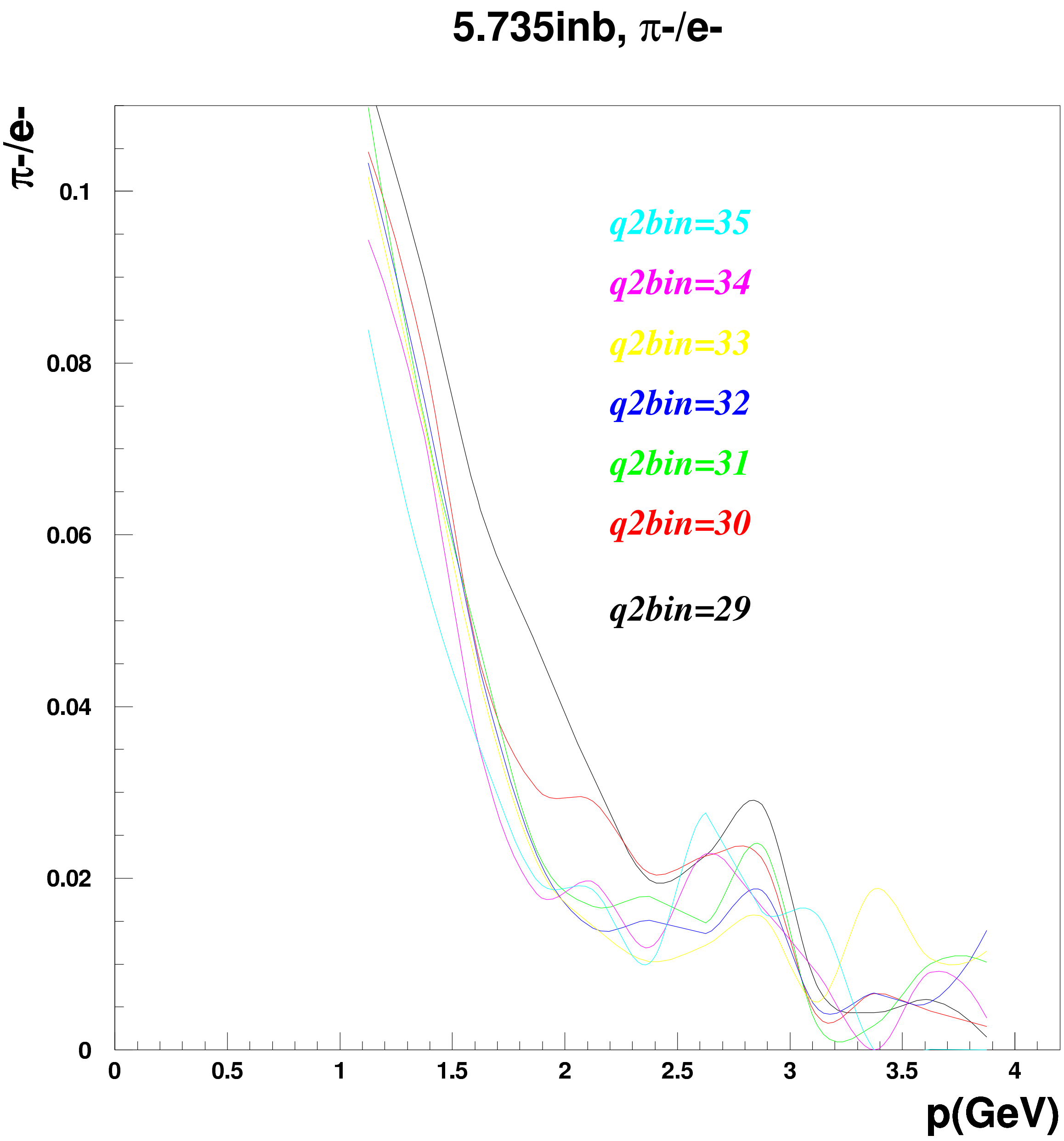

Figure 7.10: Pion contamination $\frac{\pi}{e}$ for the inbending runs with E=5.7 GeV. Q^2 bins are defined in Table 7.1.

7.5 Pair-symmetric correction

Electrons produced in pair-symmetric processes can contaminate the scattered electron sample. This contamination needs to be taken into account in the inclusive asymmetry analysis. The main background is created by the neutral pion decay reactions, such as $\pi^0 \to \gamma\gamma$ and $\pi^0 \to e^+e^-\gamma$. The lepton pair production from bremsstrahlung photons was calculated to be negligible, and is neglected in the analysis [49]. The pair-symmetric correction to the raw inclusive asymmetry can be written as:

$$A_{||} = A_{||}^{raw}(1 - R_r R_a / A_{||})/(1 - R_r), \tag{7.31}$$

where R_r is the ratio of measured e^+/e^- rates, and R_a is the ratio of raw asymmetries for e^+ and e^-: $R_a = A_{||}^{pos}/A_{||}^{neg}$. R_r and R_a were evaluated by Peter Bosted in his pair-symmetric analysis, outlined in Ref. [49]. The procedure requires production runs with electrons as trigger particles and runs with positrons as trigger particles. Approximately 50 runs of each type were processed, with the helicity dependent total charge and counts stored in bins of W and Q^2. The counts are compared for runs with opposite torus current, choosing the combinations so that both e^+ and e^- are inbending or outbending. Standard electron cuts are applied to each sample, and then the e^+/e^- ratios are formed, giving the desired quantity R_r. The value of R_a was found to be consistent with zero. The pair-symmetric correction has to be applied to the raw electron asymmetries before A_1 can be extracted. This correction becomes more important at high W.

7.6 Radiative corrections

In our analysis we approximate the scattering process as a one photon exchange, also called Born scattering. In reality, there are higher order processes contributing to the total measured cross sections and asymmetries. These effects are taken into account by calculating radiative corrections. The radiative corrections can be broken into two kinds: internal and external. The internal processes occur within the field of the scattering nucleus and consist of the bremsstrahlung, vertex correction, vacuum polarization, and elastic and quasi-elastic scattering contributions [47]. Some of the diagrams contributing to the internal correction are shown in Fig. 7.11 and Fig. 7.12. The radiative corrections require the evaluation of both polarized and unpolarized components for Born, internally radiated and fully radiated cross sections and asymmetries. Polarization-dependent internal radiative cross sections were calculated using the code developed by Kuchto and Shumeiko [50]. The radiated cross sections can be decomposed as [51]:

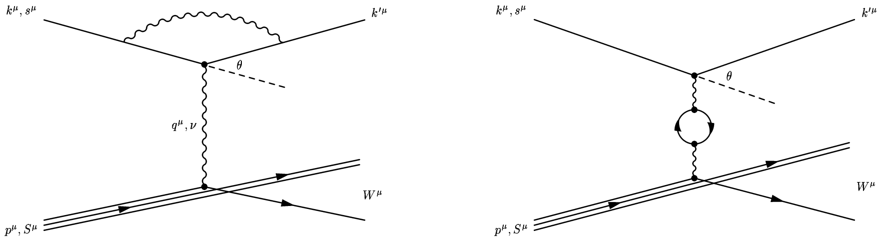

Figure 7.11: Vertex correction and Vacuum polarization

$$\begin{aligned} \sigma_r^p &= \sigma_0^p(1+\delta_v) + \sigma_{el}^p + \sigma_q^p + \sigma_{in}^p, \qquad (7.32) \\ \sigma_r^u &= \sigma_0^u(1+\delta_v) + \sigma_{el}^u + \sigma_q^u + \sigma_{in}^u, \end{aligned}$$

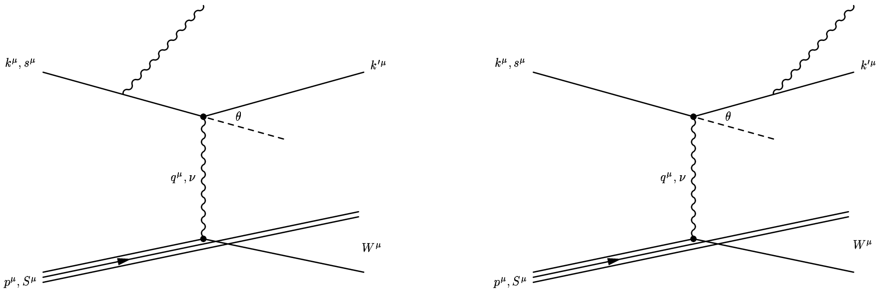

Figure 7.12: Internal radiative processes

where δ_v contains corrections for the electron vertex and vacuum polarization contributions, along with the term left after the infrared-divergent contributions are cancelled out [51]. The terms σ_{el}, σ_q, σ_{in} are due to the internal bremsstrahlung radiation for elastic, quasi-elastic and inelastic processes respectively. The deep-inelastic component of the polarized cross sections is modeled using Q^2-dependent fits to A_1. The polarized resonance region model is based on the parametrization of existing data. The unpolarized cross sections are modeled from fits to structure function data in the deep inelastic region, and fits to cross sections in the resonance region.

The external processes consist of the energy losses of electrons traveling through materials. The external corrections were based on the work of Ref. [52]. In the case of inclusive scattering the main effect of external radiation is the widening of the elastic peak called the elastic radiative tail. This occurs because the elastic cross section grows rapidly with the decreasing beam energy causing the high probability for radiation of a high energy photon followed by elastic scattering [37]. In our correction scheme, the radiative corrections are broken into an additive correction A_{RC} and a 'radiative dilution factor' f_{RC}. The additive piece A_{RC} contains the quasi-elastic radiative tail, while radiative tails of inelastic states are treated as a multiplicative correction to the cross sections. The dilution factor f_{RC} gets small at low x where the radiative corrections are significant from the quasi-elastic tails, and the statistical error bars in this region increase accordingly. The radiatively corrected asymmetry is then given by

$$A_{corr} = A_{uncorr}/f_{RC} - A_{RC}. \tag{7.33}$$

The result of radiative corrections is shown in Fig 7.13.

7.7 Models

Once $A_{||}$ has been calculated and appropriately corrected, A_1 and g_1 can be extracted using formulas in equations 2.105-2.107. However, some quantities in the formulas were not measured during our experiment. In particular, F_1, R and A_2 were not measured, so they had to be estimated from previous experiments. Also, the deep inelastic contribution to the integral over g_1 had to be estimated. A 'model', designed to provide quantities necessary for our analysis, is outlined in Ref. [53]. The model parametrizes the measured world data, producing predictions for the unmeasured regions. The 'model' values for F_1, R and A_2 are used to calculate g_1 and Γ_1, and the 'model' prediction for A_1 is used to compare the measured quantity with the model. The structure function $F_1(x, Q^2)$ is well known in the DIS region. It is extrapolated into the low Q^2 regime by noticing that it approximately scales with modified x variable: $\xi = (1 + 0.272/Q^2)x$ [53]. The structure function $R(x, Q^2)$ is calculated using the SLAC/Whitlow fit, and is assumed to be constant below $Q^2 = 0.3$. In the resonance region, $F_1(x, Q^2)$ is obtained by using the most recent fit to world data, and $R(x, Q^2)$ is obtained by using the Whitlow fit again, but it only multiplies

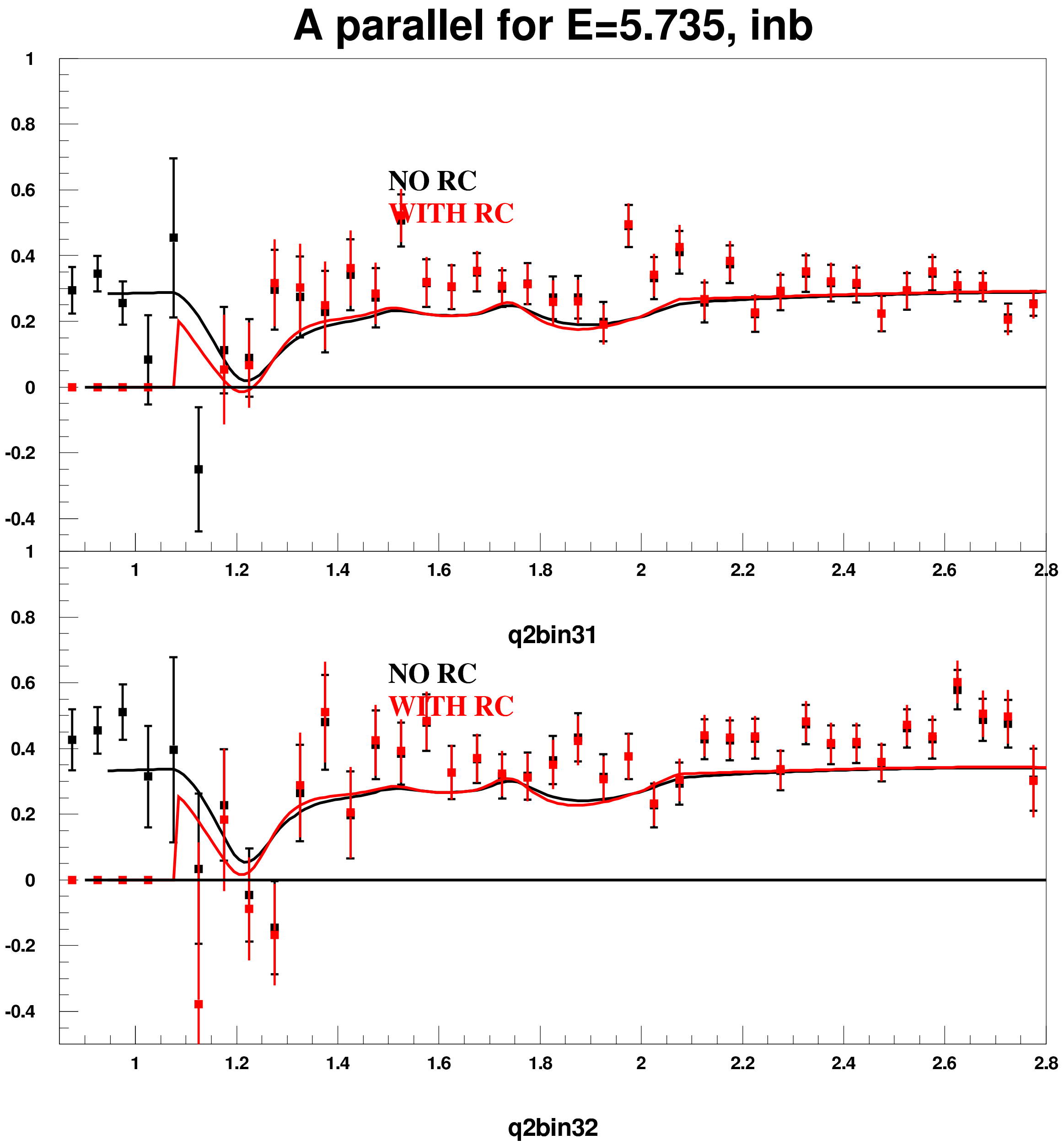

Figure 7.13: $A_{||}$ vs W. Effect of radiative corrections on $A_{||}$ for the data set with E=5.735 GeV, I=2250 Amps. The most significant change occurs in the Δ (1232 MeV) region

.

the non-resonant part of the cross section, since $R(x, Q^2)$ is assumed to be zero in the resonance region. The combined DIS/resonance model uses the DIS values for $W^2 > 4.3$, the resonance values for $W^2 < 3.5$, and interpolation for the intermediate W.

The photon-nucleon asymmetry A_1^p is fit to the world data in the DIS region as a function of variable ξ defined above. The fit uses data from E80, E130, E143, E155, EMC and SMC experiments, as well as data from EG1b in the $W > 2$ GeV region. The fit is constrained to give $A_1 = 1$ at the pion photoproduction threshold, and is also constrained at the real photon point by the Bianchi prediction for the high energy part of the GDH sum rule. In the resonance region, A_1^p is parametrized using two ingredients: an extrapolation of the DIS fit (as function of x and Q^2), and the output from the AO code (as function of W and Q^2) without the non-resonant Born terms. The reference 'model' uses the DIS fit for the non-resonant part of the cross section and the AO output for the resonant part. The combination is used in the $W < 2$ region, and the DIS fit is used in the region of $W^2 > 4.3$, with an interpolation in between [53]. The resulting A_1^p is used for comparison with the measured asymmetry. The second photon-nucleon asymmetry A_2^p was not measured by the EG1b experiment, but is needed is order to extract g_1 from the data. Unfortunately, there is very little experimental data on A_2^p, particularly in the resonance region. An important guideline for predicting A_2 (which is related to g_2) is the Wandzura-Wilczek prediction for the DIS region:

$$g_2(x, Q^2) = -g1(x, Q^2) + \int_x^1 \frac{dy}{y} g_1(y, Q^2) + g_2^{HT}(x, Q^2). \tag{7.34}$$

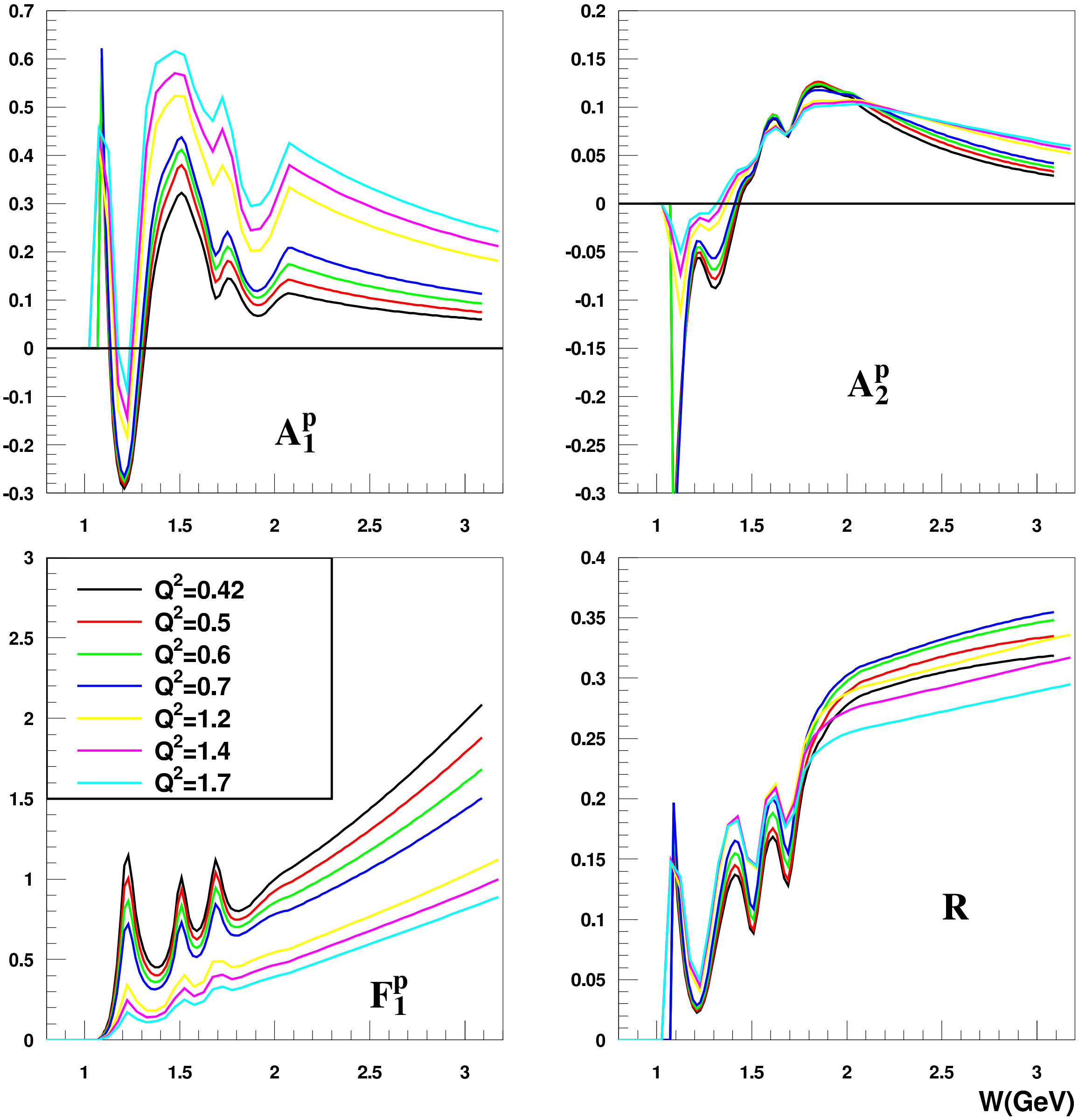

Figure 7.14: Structure functions A_1^p, A_2^p,F_1^p and R plotted as a function of invariant mass W and Q^2.

The first two terms of the equation are known as g_2^{WW} and contain a leading twist contribution to g_2, while the last term contains twist-three and higher contribution. g_2^{WW} (and, consequently, A_2^{WW}) is determined by the integral over $\frac{g_1(y)}{y}$, integrated from the point of interest x up to the elastic peak, including the peak itself. In the 'Models' A_2^p is estimated by the MAID2000 fit in the resonance region, and g_2^{WW} in the DIS region, with a smooth interpolation between the two above W = 1.7 GeV.

7.8 Asymmetry $A_1^p(x, Q^2)$

The desired virtual photon-nucleon asymmetry $A_1^p(x, Q^2)$ can be obtained from the measured lepton asymmetry $A_{||}$, model values for A_2 and R, and the depolarization factor D:

$$\begin{aligned}
A_1 &= (A_{||}/D - \eta A_2), \qquad (7.35)\\
D &= [1-(1-y)\epsilon]/(1+\epsilon R),\\
y &= \frac{\nu}{E},\\
R &= \frac{\sigma_L}{\sigma_T},\\
\epsilon &= [4(1-y)-\gamma^2 y^2]/[2y^2+4(1-y)+\gamma^2 y^2],\\
\eta &= \epsilon\gamma y/[1-\epsilon(1-y)].
\end{aligned}$$

It is important to study the behavior of $A_1^p(x, Q^2)$ as a function of x because of its potential to distinguish between the different models of valence spin structure of the proton. A plot of $A_1^p(x, Q^2)$ is shown in Fig. 7.15, along with several model predictions for its behavior. There is a number of different predictions for the numerical value

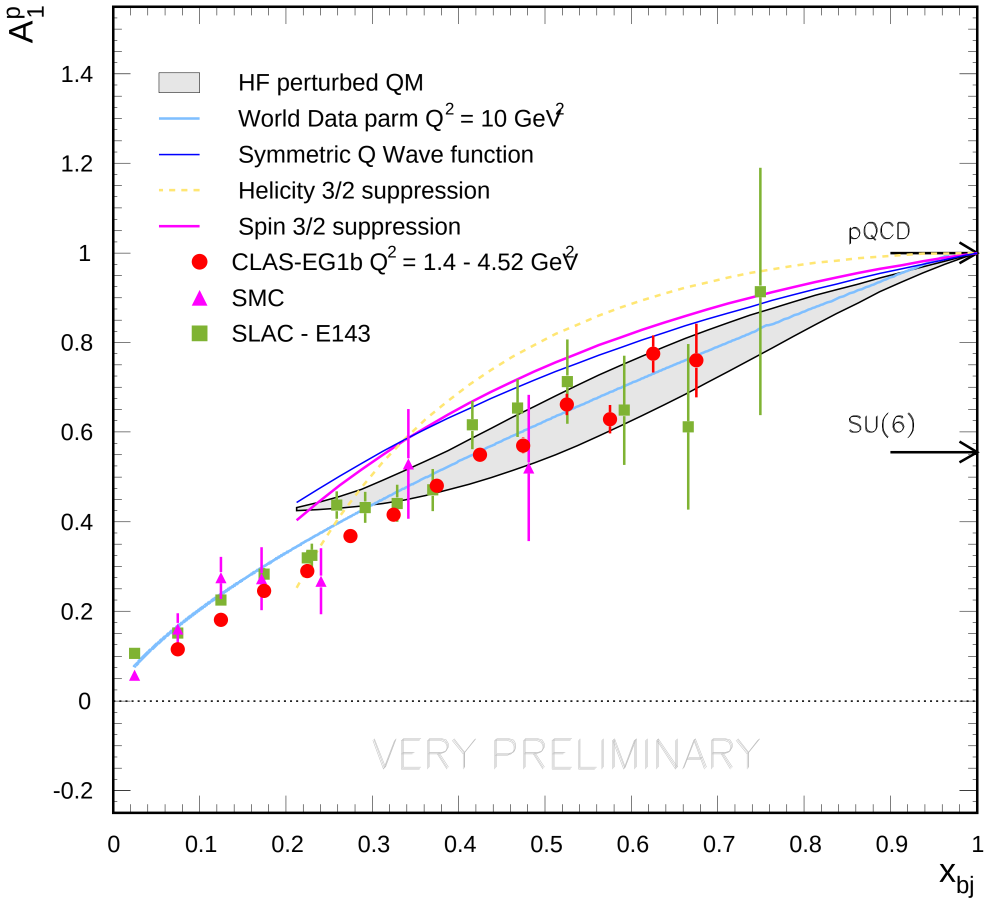

Figure 7.15: Asymmetry A_1^p plotted vs x could differentiate between the different models of valence spin structure of the proton. Two main predictions are indicated on the plot: pQCD: $A_1^p(x \to 1) \to 1$ and SU(6): $A_1^p = 5/9$.

of A_1^p. Two main values are indicated on the plot: the perturbative QCD prediction of $A_1^p(x \to 1) = 1$, and the SU(6) prediction of $A_1^p(x) = 5/9$. In the lowest order in the quark parton model, A_1^p is given by the ratio of the spin-dependent to spin-independent quark distribution functions:

$$A_1 = \frac{\Sigma_i e_i^2[q_i^\uparrow - q_i^\downarrow]}{\Sigma_i e_i^2[q_i^\uparrow + q_i^\downarrow]}. \tag{7.36}$$

Assuming that the nucleon obeys an SU(6) symmetry generates a prediction for A_1^p. The wave functions for the $J^P = \frac{1}{2}^+$ baryon octet are symmetric under simultaneous interchange of the spin and flavor of any quark pair. For the proton, the two u-quark and one d-quark configuration is symmetrized by making a cyclic permutation, resulting in the following wavefunction:

$$|p^\uparrow\rangle = \frac{1}{\sqrt{18}}(2u^\uparrow u^\uparrow d^\downarrow - u^\uparrow u^\downarrow d^\uparrow - u^\downarrow u^\uparrow d^\uparrow + 2\text{permutations}). \tag{7.37}$$

Using this wavefunction, the following probabilities of finding a quark of a particular flavor and spin are found:

$$u^\uparrow = \frac{5}{9}, \quad u^\downarrow = \frac{1}{9}, \quad d^\uparrow = \frac{1}{9}, \quad d^\downarrow = \frac{2}{9}. \tag{7.38}$$

Weighting these probabilities with the charge-squared factors for the u and d quarks gives the prediction of $A_1^p(x) = 5/9$. While the SU(6) predictions are approximately valid at $x \sim 0.3$, the symmetry is strongly broken, which is particularly evident at large x. Several non-perturbative mechanisms have been used to account for this observation by explicitly breaking SU(6) at the quark level, which results in different weighting of components of the wavefunction, and consequently different x dependences for the spin and flavor distributions [54]. Some of these mechanisms are described in ref [54], involving the suppression of transitions to states in the lowest even and odd parity multiplets with combined quark spin $S = 3/2$, to states with helicity $h = 3/2$, and to states which couple only through symmetric components of the spin-flavor wavefunction. Predictions from each of these model are indicated in Figure 7.15. Also shown on the plot is the prediction of the hyperfine-perturbed quark model, which involves spin-spin interaction between the quarks, mediated by the one-gluon or pion exchange [55]. The value of $A_1^p(x)$ extracted from the EG1b data shows a preference for the pQCD limit as $x \to 1$, as opposed to the SU(6) prediction of 5/9, and is also consistent with the hyperfine-perturbed quark model.

7.9 Spin structure function $g_1^p(x, Q^2)$

The evaluation of $g_1^p(x, Q^2)$ is now straightforward:

$$g_1 = \frac{F_1}{1+\gamma^2}[A_{||}/D + (\gamma - \eta)A_2], \tag{7.39}$$

where $\gamma = \frac{Q}{\nu}$, $A_{||}$ is measured, and F_1 and A_2 come from the 'Models'. One plot of $g_1^p(x, Q^2)$ is shown in Fig. 7.16. The red curve on each plot is the $g_1^p(x, Q^2)$ given by the 'Models'. A strong resonant structure is evident from Fig. 7.16, with the $\Delta(1232)$ being the most prominent resonance. As Q^2 increases, the resonances become 'smoothed out'. At low Q^2 the hadronic degrees of freedom are expected to be more relevant than the partonic degrees of freedom. In general, according to the DGLAP equations discussed in section 2.2.3, g_1^p evolves logarithmically with Q^2, and

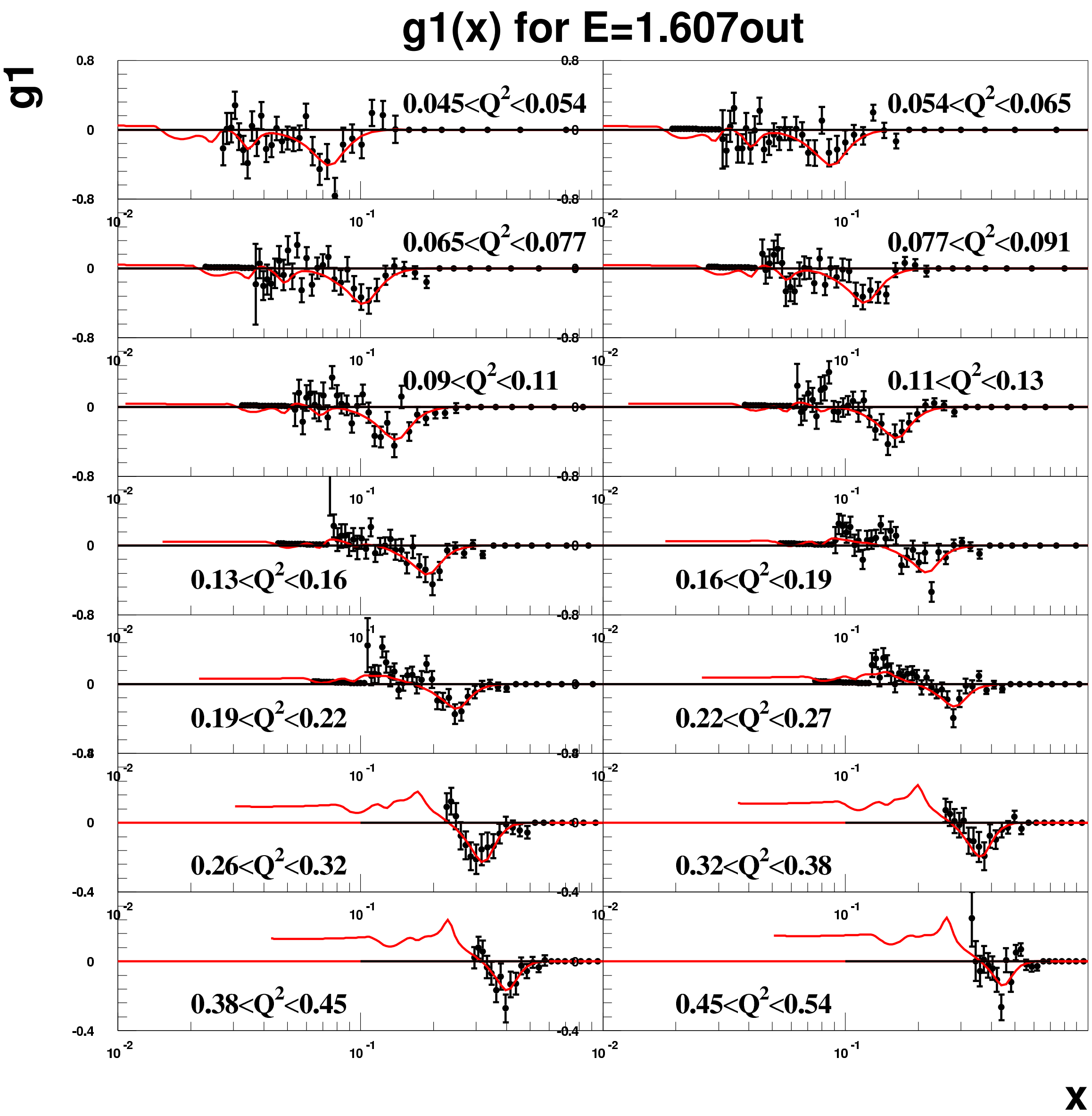

Figure 7.16: Structure function g_1^p plotted vs x for the data set with E=1.6 GeV, outbending. Strong resonant structure is observed at low Q^2.

is expected to grow with Q^2 at low x, and decrease with Q^2 at high x. This pattern is also predicted and observed for the spin-averaged structure function $F_1(x, Q^2)$. However, the splitting functions for the polarized and unpolarized cases are different, so that g_1^p/F_1^p is expected to vary with Q^2. The ratio g_1^p/F_1^p has been found by previous experiments to vary little with Q^2, and EG1b data shows similar behavior. Fig. 7.17 shows results for g_1^p/F_1^p as a function of Q^2, in coarse bins of x. The results from E155 experiments are plotted for comparison, along with a fit of that data. The peak of the $\Delta(W = 1232)$ resonance is marked by a solid black triangle, while the $W = 2$ GeV is indicated by a solid black square. Below $W = 2$ GeV, the ratio g_1^p/F_1^p decreases slightly with decreasing Q^2, and it becomes negative near the Δ resonance.

Another interesting aspect of the structure functions is the quark-hadron duality. This phenomenon refers to the observation made by Bloom and Gilman [56], that the resonance form factors and nucleon inelastic structure functions have the same Q^2-dependence when plotted as a function of $w' = w + m_p^2/Q^2$. When the structure functions in the resonance region are averaged over a finite region of w', they follow behavior of the structure functions measured at higher Q^2 where x-scaling is observed. x-scaling is violated at low Q^2 by resonance excitation and other higher-twist effects, and at higher Q^2 by logarithmic dependence of the strong coupling constant . In order to study the QCD scaling violations at finite Q^2, it is necessary to separate them from the low-Q^2 scaling violations caused by higher-twist effects. Georgi and Politzer [57] showed that in order to study the scaling violations, the Nachtmann variable $\xi = \frac{2x}{1+\sqrt{1+4m_p^2x^2/Q^2}}$ was the appropriate variable to use. Using ξ instead of x at finite Q^2 accounts for the finite target mass effects. Fig. 7.18 shows a plot of g_1^p as a function of Nachtmann variable ξ. The red curve plotted on top of the data is

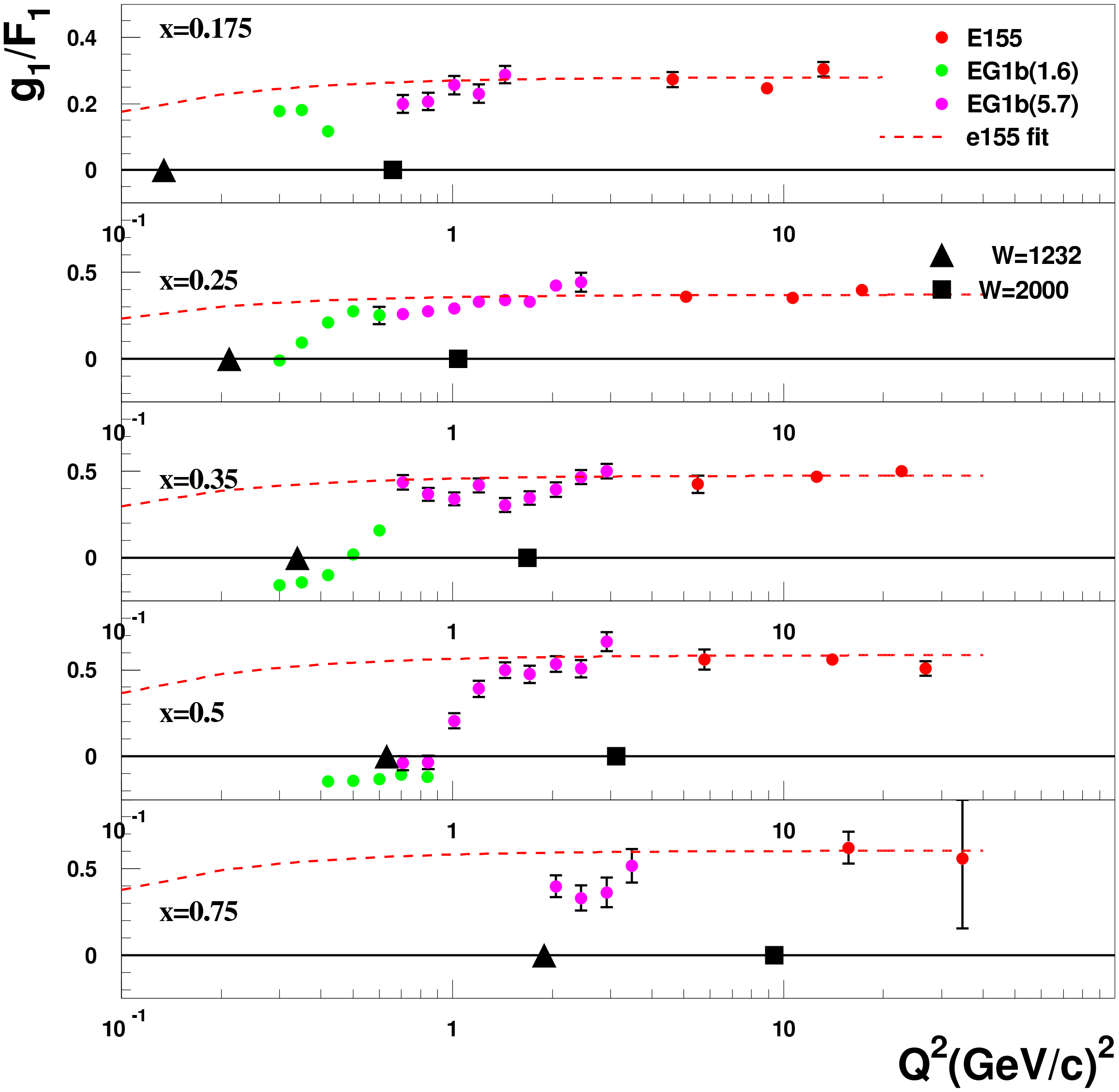

Figure 7.17: g_1^p/F_1^p plotted vs Q^2. There is no clear Q^2 dependence for the ratio for $W > 2GeV$, indicated by black squares. Below that value, there is a tendency for the ratio to decrease, in agreement with the E155 fit. Near the $\Delta(1232)$ region, indicated by black triangle, the ratio becomes negative as expected. The evolution equations (2.52) are not valid in this region.

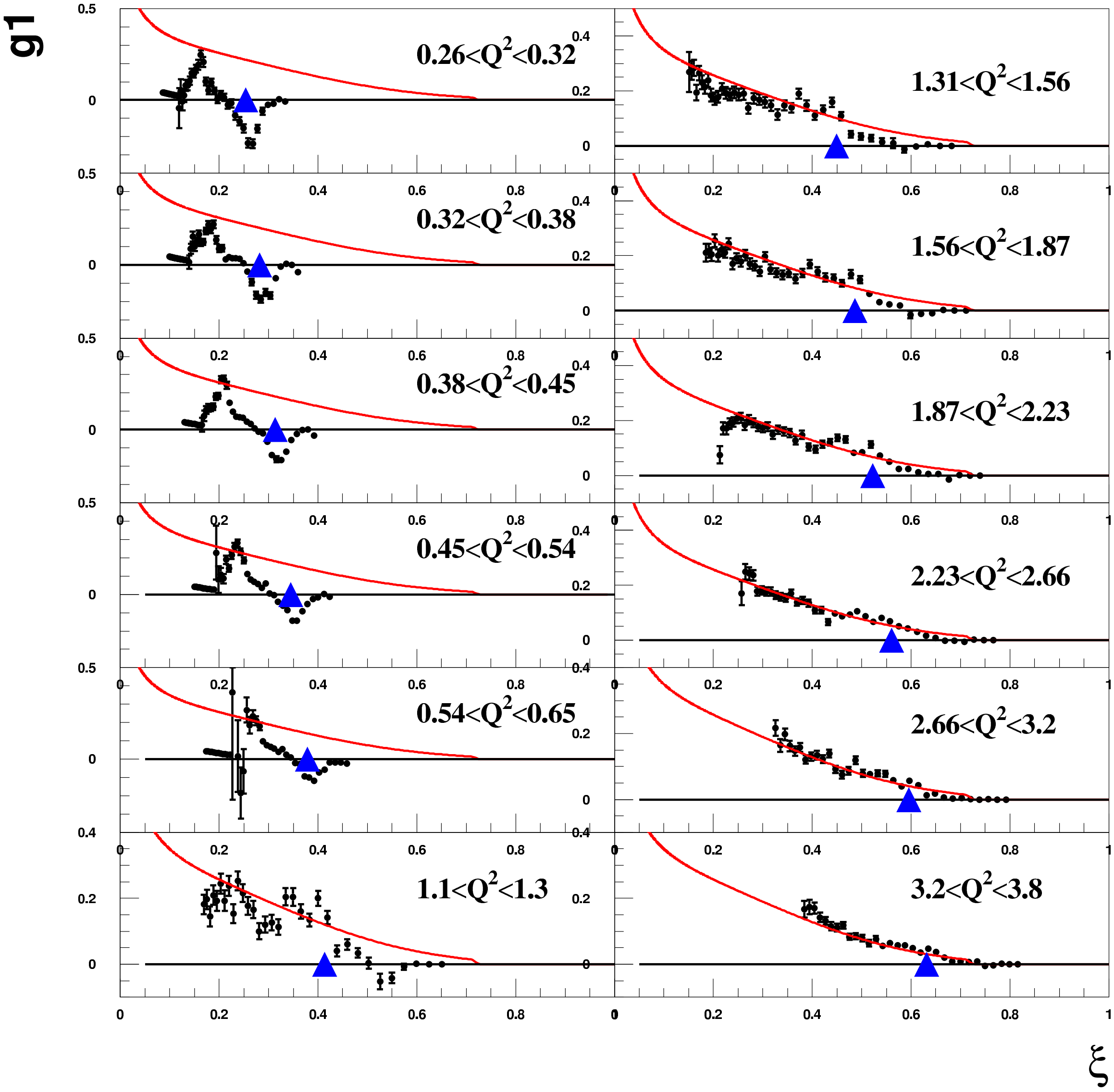

Figure 7.18: g_1^p plotted vs ξ and the parametrization of the DIS world data at $Q^2 = 10$ GeV^2. g_1^p becomes consistent with the DIS parametrization at $Q^2 \sim 1.5$ GeV^2. The duality of polarized structure functions is known to be broken because the $\Delta(1232)$ resonance is negative at low Q^2 and positive at high Q^2.

obtained from the 'Models' at $Q^2 = 10$ GeV^2.

7.10 First Moment $\Gamma_1^p(Q^2)$

The first moment is evaluated by integrating the structure function $g_1(x, Q^2)$ over the entire range of x:

$$\Gamma_1^p(Q^2) = \int_0^1 g_1^p(x, Q^2)dx. \tag{7.40}$$

In this analysis, $\Gamma_1^p(Q^2)$ is considered without the elastic contribution, so the integration starts at the pion photoproduction threshold $W = 1.075$ GeV. The upper limit of integration (over data) depends on Q^2. The cutoff value for the 5.6 GeV energy sets is based on the condition that the energy of scattered electron E' is larger than 0.15*Ebeam. For the 1.6 GeV data the condition is $E' > 0.5$ GeV. These conditions were chosen to avoid pion and positron contamination of the low energy electron sample. Translating this condition into the W cutoff gives for the 5.6 GeV energy data:

$$W^{cut} = \sqrt{m_p^2 + 2m_p\nu - Q^2} = \sqrt{m_p^2 + 2 * 0.85 m_p Ebeam - Q^2} \tag{7.41}$$

For the 1.6 GeV data the cutoff is

$$W^{cut} = \sqrt{m_p^2 + 2m_p\nu - Q^2} = \sqrt{m_p^2 + 2m_p(Ebeam - 0.5) - Q^2} \tag{7.42}$$

Since the data are binned in W, the integral is rearranged:

$$\Gamma_1^p(Q^2) = -\int_{1.075}^{W^{cut}} g_1(W, Q^2)dW\frac{dx}{dW}, \tag{7.43}$$

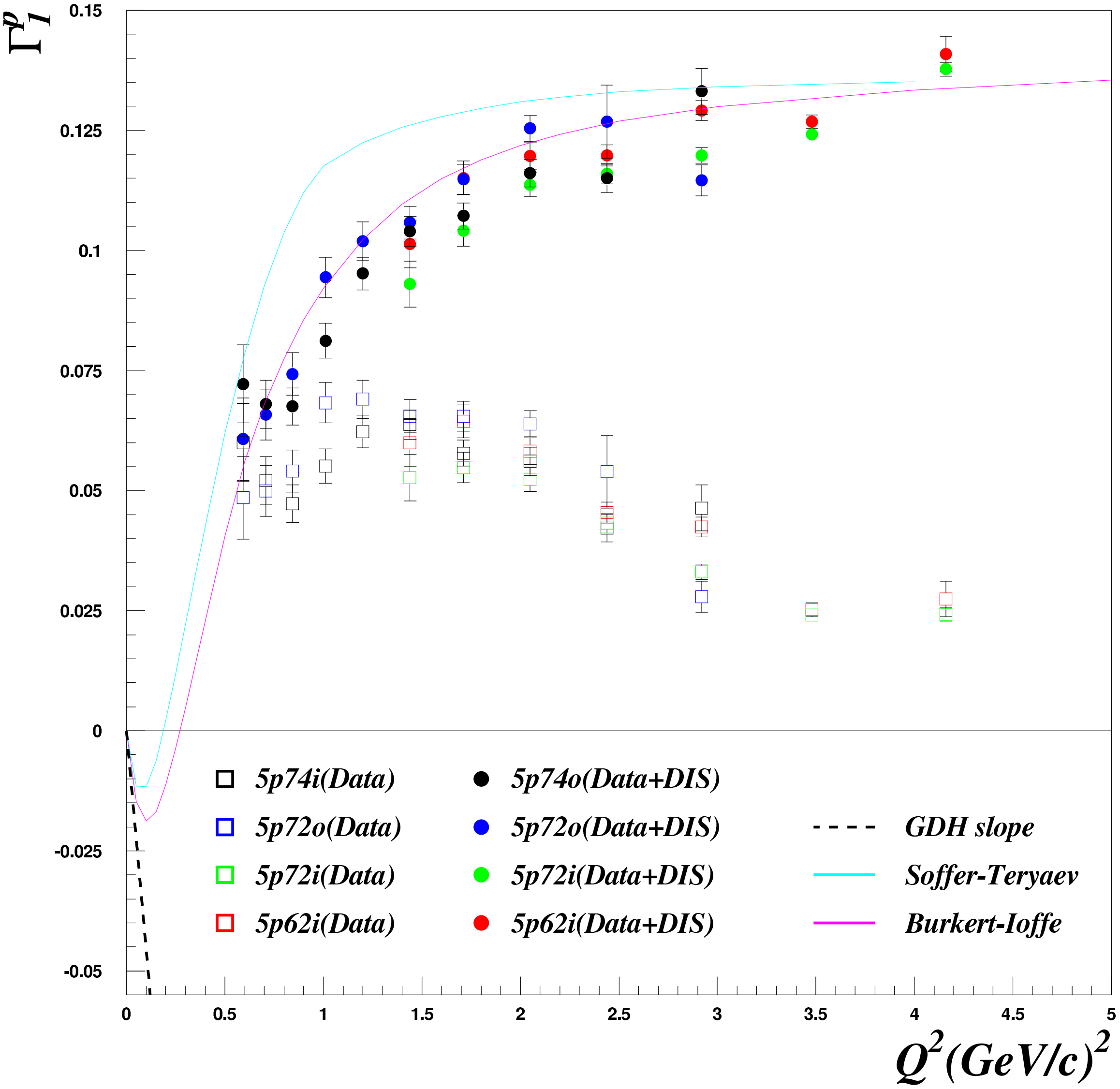

Figure 7.19: Γ_1^p obtained with 4 sets of 5.6(7) GeV data; here 'o' stands for the outbending data, and 'i' stands for the inbending data. Points shown by open squares are values of g_1^p integrated over the data down to the lowest available value of x. The missing part of the integral in DIS is obtained by integrating the 'Model'g_1^p down to $x = 0.001$. The two parts are added, and the sum is shown by filled circles.

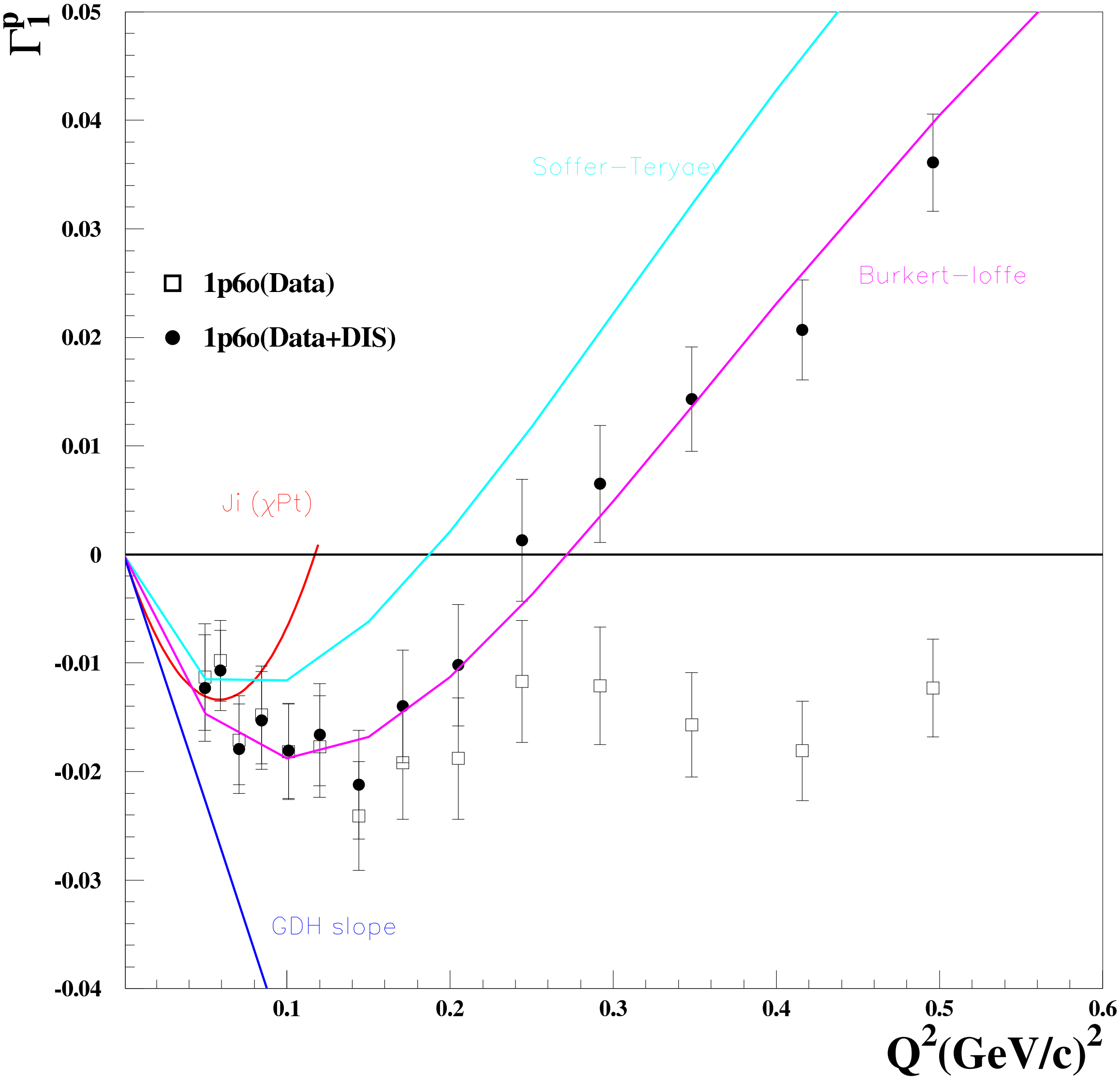

Figure 7.20: Γ_1^p obtained with the 1.6 GeV, outbending set. Open squares show values of g_1^p integrated over data points, closed circles show the full value of integral. Most of the integral in this region is obtained with experimental g_1^p.

where $\frac{dx}{dW} = \frac{-2Wx}{W^2+Q^2-m_p^2}$ and dW is the size of the bin. After integrating data over the available kinematic region, the rest of the integral is obtained from the 'Models' and added to the experimental piece. The lower limit of integration for the 'Model' part is $x = 10^{-3}$. Another quantity of interest is what fraction of integral comes from the data relative to the total contribution. A variable *Ratio* is defined as

$$Ratio = \frac{\int_{data} |g_1(x)|dx}{\int_{all} |g_1(x)|dx}. \tag{7.44}$$

Ratio is evaluated for high and low energy data sets, and is plotted in Fig. 7.21

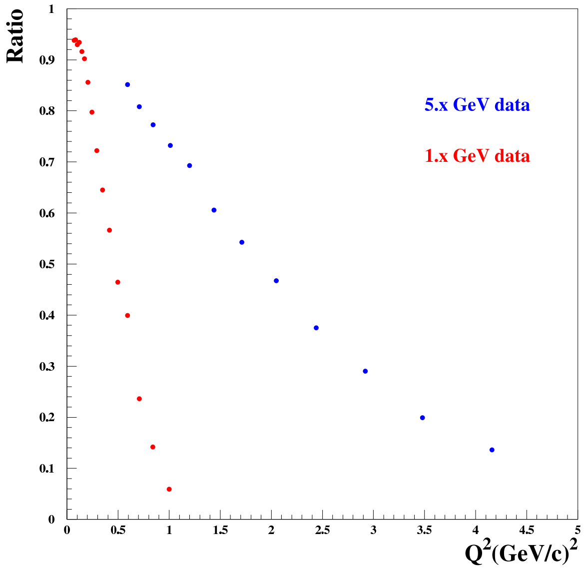

Figure 7.21: Ratio as defined in equation 7.44.

7.11 Error Analysis

7.11.1 Statistical Error

The statistical error associated with $A_1^p(x)$, $g_1^p(x, Q^2)$ and $\Gamma_1^p(Q^2)$ is calculated from the number of electron counts detected in every Q^2 bin. The statistical error on the raw electron asymmetry is given by

$$\Delta A_{exp} = \frac{2}{(n^+ + n^-)^2} \left[\frac{n^+}{fc^+} {n^-}^2 + \frac{n^-}{fc^-} {n^+}^2 \right]^{\frac{1}{2}}, \tag{7.45}$$

where $n^+/fc^+(n^-/fc^-)$ is the number of electrons with the spin up (down), normalized to the number of incident electrons with the spin up (down), given by the faraday cup readings. The next two steps in the analysis consist of finding the dilution factor DF and the product of target and beam polarization $P_b P_t$. Both of these procedures have statistical and systematic uncertainties, however, they are treated as systematic uncertainties only, and do not enter the statistical error on the final result. The error on the electron asymmetry $A_{||}$ is then:

$$\Delta A_{||} = \Delta A_{exp} \frac{1}{P_b P_t * DF}. \tag{7.46}$$

After $A_{||}$ is corrected for the ^{15}N polarization, and pion and positron contamination, the error is modified:

$$\Delta A_{||}^{corr} = \Delta A_{||} * \frac{1}{C_1} * \frac{1}{1-x} * \frac{1}{1-R_r}, \tag{7.47}$$

where $C_1 = 1.0 - \frac{P_{15_N}}{P_p} * \frac{1}{3}\frac{1}{3}$, $x = \pi^-/e^-$ and $R_r = e^+/e^-$. The radiative corrections introduce another multiplicative factor:

$$\Delta A_{||}^{corr+RC} = \Delta A_{||}^{corr} \frac{1}{f_{RC}} \tag{7.48}$$

The error associated with the photon asymmetry $A_1(x)$ is obtained by dividing the above equation by the depolarization factor D:

$$\Delta A_1 = \Delta A_{||}^{corr+RC}/D \tag{7.49}$$

The error associated with the structure function $g_1(x, Q^2)$ is

$$\Delta g_1 = \Delta A_1 * \frac{F_1}{1+\gamma^2} \tag{7.50}$$

Finally, the error associated with the first moment Γ_1 is

$$\Delta\Gamma_1 = \Delta W * \sqrt{\sum_W (\Delta g_1 * \frac{-2Wx}{W^2 - m_p^2 + Q^2})^2} \tag{7.51}$$

7.11.2 Systematic Error

There are several sources of systematic uncertainty in this analysis, arising from calculation of the dilution factor, evaluation of P_bP_t, the 'Models' input and electron contamination correction factors.

The dilution factor calculation involves several parameters, whose values had some uncertainty. These parameters were varied by an appropriate amount, and the resulting DF was recalculated. Since the inclusive method of extracting the product P_bP_t

Table 7.6: Dilution Factor Uncertainty

Parameter	Nominal	Alternative
L	$1.9cm$	$2.1cm$
a,b	7/6,1/6	1.1965,0.2266
fit region	varied	varied
σ_n/σ_d	model	$\frac{1+0.75x}{2-0.75x}$

depends on DF, the variation in the quantity $DF * P_bP_t$ was calculated. A list of parameters subject to variation is given in Table 7.6. The banjo length L was varied by 10%, a and b were changed from their nominal values to values obtained by fitting a simulated ^{15}N spectrum to the measured one. The ratio of cross sections σ_n/σ_d was changed from the nominal value to one given by the DIS parametrization. Also, the fitting region for finding the packing fraction was varied. One parameter was changed at a time, and the product $DF * P_bP_t$ recalculated. This procedure resulted in the nominal $DF * P_bP_t$ and 4 alternative values. The difference between the nominal value and each of the alternative values was found, and the total systematic error from the dilution factor was estimated. For convenience, the product $DF * P_bP_t$ is labeled as f

$$\Delta_s f = \sqrt{(f_{nom} - f_1)^2 + (f_{nom} - f_2)^2 + (f_{nom} - f_3)^2 + (f_{nom} - f_4)^2} \tag{7.52}$$

Next, the value of P_bP_t was varied by one standard deviation given by the statistical error associated with calculation of P_bP_t. The total systematic error from the

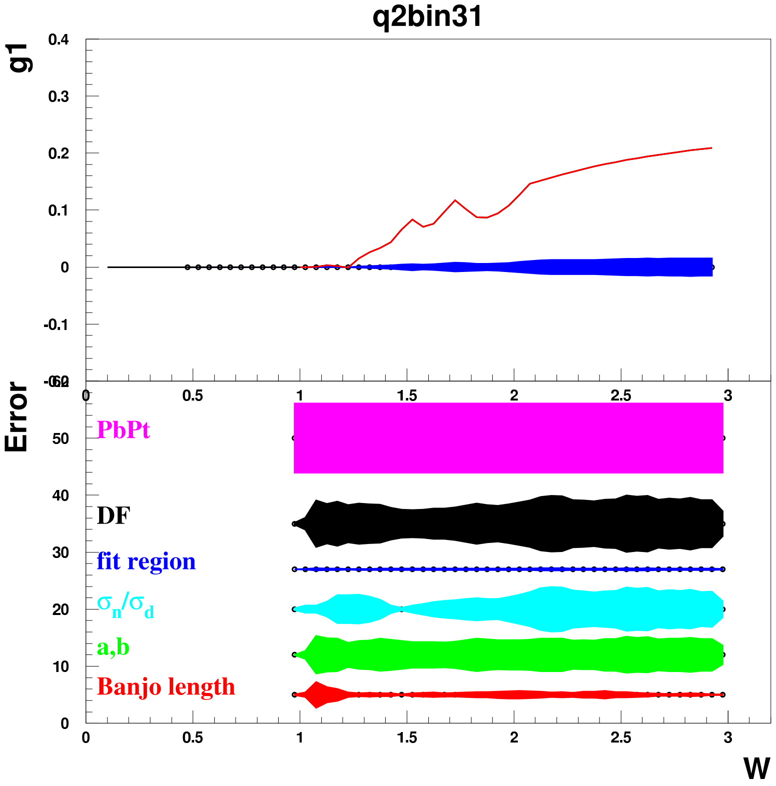

Figure 7.22: Statistical uncertainty in g_1 caused by uncertainty in several parameters determining DF and uncertainty in P_bP_t. The bottom plot shows contributions to the systematic error resulting from varying parameters involved in the calculation of the dilution factor DF, and the error associated with extraction of $PbPT$. The range, and not the absolute value of the error on the bottom plot is important. The top plot shows the effect of this error on the value of g_1. The blue band shows $\Delta_s * g_1$, where Δ_s is given by equation 7.53.

product of the dilution factor and P_bP_t is:

$$\Delta_s = \sqrt{(\frac{\Delta_s f}{f_{nom}})^2 + (\frac{\Delta P_bP_t}{P_bP_t})^2} * 100\% \tag{7.53}$$

In order to find the effect of this systematic uncertainty on the value of g_1, the value of g_1 is multiplied by Δ_s: $\Delta_s g_1 = \Delta_s * g_1$. To avoid bin-to-bin fluctuations which are present in the experimental value of g_1, the 'Models' output for g_1 was used. The plot in Fig. 7.22 shows the total systematic uncertainty in g_1 resulting from varying each of the components that go into calculation of DF and P_bP_t.

The systematic uncertainty associated with the pion and positron background correction was estimated by Peter Bosted and described in ref. [58]. If all background in described by a single dilution factor $f = (\pi^- + e^+)/e^-$, and assuming the the ratio of π^-/π^+ is on the order of 1, the correction can be described as follows:

$$A_{corr} = A_{raw}(1 + f) \tag{7.54}$$

The background asymmetry is zero, but it has an uncertainty dA_b/A_e, which translates into the systematic error on the correction:

$$\delta A_{corr} = A_{raw} * \sqrt{(df)^2 + (f(dA_b/A_e))^2} \tag{7.55}$$

The systematic errors associated with the use of the 'Models' were evaluated by using different versions of the models, and finding the difference between resulting g_1 and Γ_1. Several sources of uncertainty are introduced by using the 'Models': the values of A_2, R and unpolarized structure functions F_1, F_2.

Table 7.7: Uncertainty in π^-,e^+ correction

E(GeV)	torus	df	dA_b/A_e
1.6	+1500	$0.5f$	0.2
1.6	-1500	$0.5f$	0.2
5.7	+2250	$0.3f$	0.1
5.7	-2250	$0.3f$	0.2

To find the error associated with A_2 seven different variations of estimating A_2 were used. The version 'v4' uses the MAID 2000 fit in the resonance region and twist two calculation in the DIS region [59]. Version 'v5' assumes $A_2 = 0$ in both the resonance and DIS region. Version 'v6' uses only the resonance contribution to A_2 in the resonance region and twist two in DIS. Version 'v7' adds a twist three term to the DIS region and uses the standard value of A_2 in the resonance region (MAID 2000 fit combined with the extrapolation of DIS results) [59]. Version 'v8' uses twist two in the DIS region and the Dubna-Mainz-Taipei dynamical model in the resonance region. [53]. Version 'v10' uses the upper Soffer bound $A_2 = \sqrt{(1 + A_1)/2R}$ divided by W in both the resonance and DIS region [59] . The results are shown in Figure 7.23.

To find the error associated with the uncertainty in the unpolarized structure functions F_1 and F_2 and in R, six alternative versions of the 'Models' were used in addition to the standard one. The standard version 'v1' uses R from R1998 SLAC fit, F2NMC-NEW fit for DIS and H2MODEL for the resonance region [53]. Version 'v2' uses R1998+ΔR where ΔR is the uncertainty in the R1998 fit. Version 'v3' uses the older SLAC parametrization 'F2global' for the DIS region instead of NMC parametrization [59]. Version 'v4' uses RRicco fit instead of R1998 in the resonance

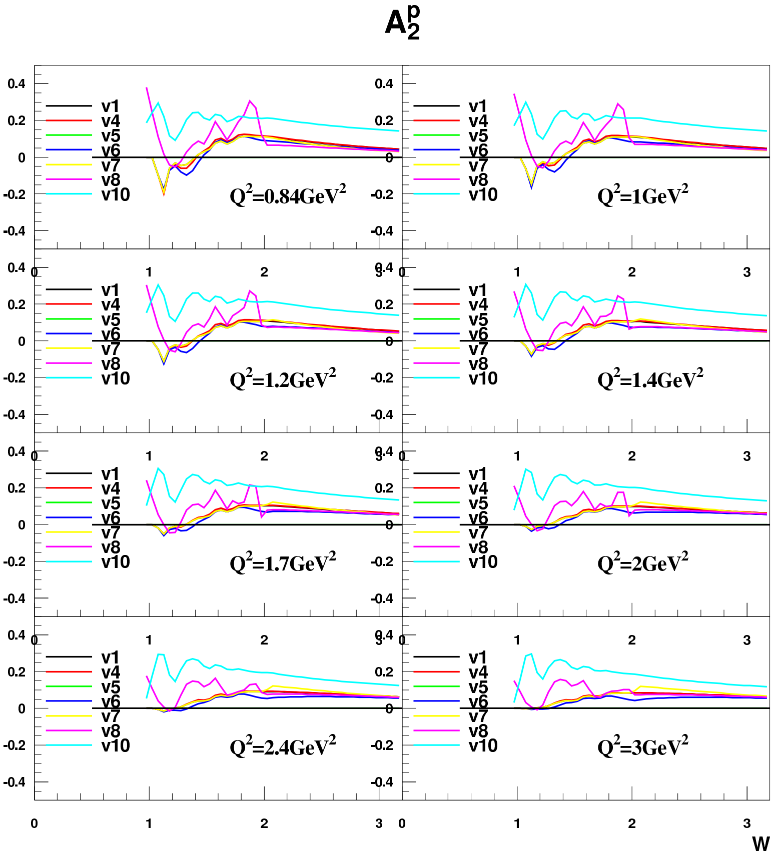

Figure 7.23: Results for A_2^p from various versions of 'Models' as described in section 7.11.2.

region [59] . Version 'v5' uses the Bodek parametrization instead of H2MODEL for F_2 and R in the resonance region. Version 'v6' uses the new Hall C parametrization of F_1 and F_L in the resonance region to get F_2 and R. Version 'v7' uses R1998 down to $Q^2 = 0$ instead of assuming that it is constant below $Q^2 = 0.3$ and decreases linearly to zero as it is done in the standard version. The results are shown in Figure 7.24 In order to estimate the effect these variations have on g_1 and Γ, each version was used to calculate the radiative corrections and the quantities needed to extract g_1 and Γ_1 from $A_{\|}$. The difference between the nominal value and each alternative value is

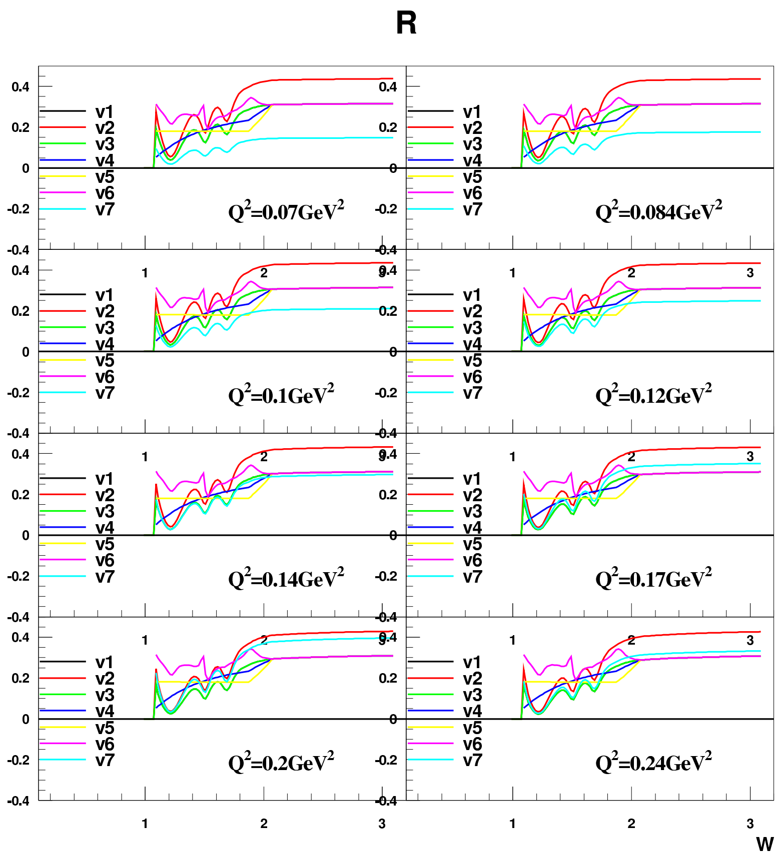

Figure 7.24: Results for $R = F_1/F_2$ from various versions of 'Models' as described in section 7.11.2.

found for g_1 and Γ. The results are shown in Fig. 7.25. The top plot shows g_1^p as predicted by the 'Model' with the blue line being a total systematic error associated with the 'Model' quantities A_2, R, F_1 and F_2. The bottom plot shows individual contributions to the error in %. The average systematic error is around 5-7 % of the g_1^p value.

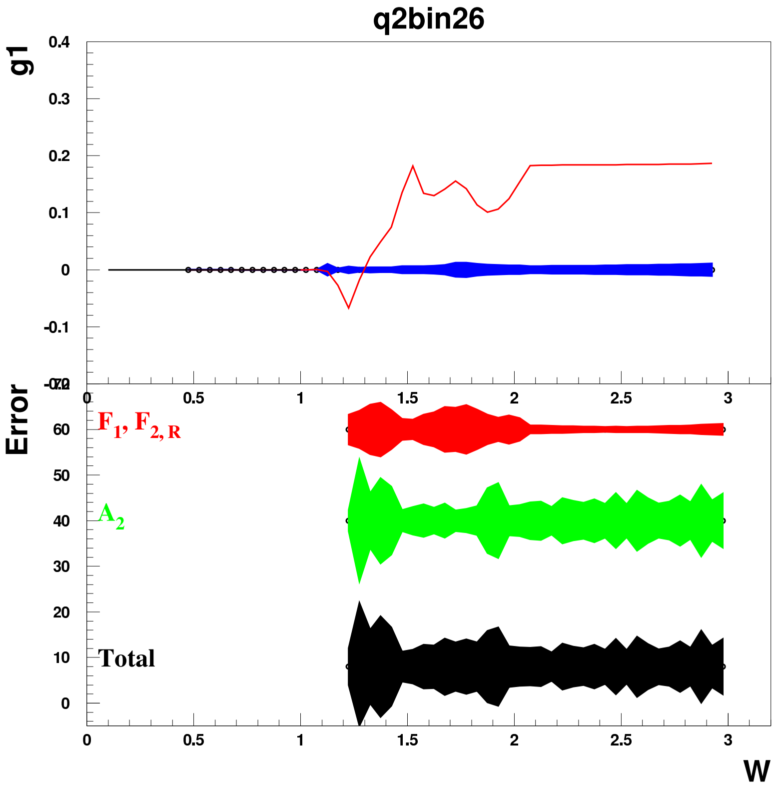

Figure 7.25: Systematic errors associated with the 'Models' input. The bottom plot shows relative contribution to systematic error from variations in F_1, F_2, R and A_2. The range and not the absolute value is important on the bottom plot. The top plot shows the effect of systematic errors associated with 'Models' on g_1^p.

7.11.3 Combining Data Sets

In the final step of the analysis, data sets with similar but slightly different beam energies needed to be combined. This thesis is based on 7 groups of runs, listed in Table 7.8. The asymmetries are scaled to the common beam energy; in this case, the common beam energies are 5.7 GeV for the last 4 sets and 1.64 GeV for the first 3 sets. The scaling is done by multiplying asymmetries by a ratio of depolarization factors $D_{E_{nom}}/D_{E_{set}}$. Then, the scaled asymmetries from different groups are combined using

Table 7.8: Data groups

set #	E(GeV)	torus
1	1.607	+1500
2	1.607	-1500
3	1.723	-1500
4	5.615	+2250
5	5.725	+2250
6	5.725	-2250
7	5.743	-2250

the weighted mean with the weighted statistical error:

$$\begin{aligned} A_{\|}^{raw}(mean) &= \sum_{groups} \frac{A_{\|}^{raw}(group)}{\sigma^2_{A_{\|}^{raw}(group)}} * \sigma^2_{A_{\|}^{raw}(mean)} \\ \sigma^2_{A_{\|}^{raw}(mean)} &= \left[\sum_{groups} \frac{1}{\sigma^2_{A_{\|}^{raw}(group)}}\right]^{-1/2} \end{aligned} \tag{7.56}$$

After the raw asymmetries are combined, radiative corrections are applied, and the quantities of interest such as $A_1 + \eta A_2$ and g_1 are extracted. This can be done with the final combined asymmetry because the error propagation involves only multiplicative constant factors.

7.12 Results and Conclusion

The final results are shown in the plots in this section. The results are divided into a 'low energy' set and a 'high energy' set. The low energy set is comprised of the three data sets, obtained at beam energies of 1.606 GeV and 1.723 GeV. These data fill the standard Q^2 bins 10 to 27 ($0.05 \leq Q^2 \leq 1.0$ GeV^2), with the inbending data contributing to bins 16 through 27 ($0.14 \leq Q^2 \leq 1.0$ GeV^2), and the outbending data contributing to bins 10 through 25 ($0.05 \leq Q^2 \leq 0.7$ GeV^2). The high energy set consists of the four data sets obtained at the beam energies of 5.615, 5.725 and 5.743 GeV. The inbending sets contributed to the Q^2 bins 28 through 35 ($1.2 \leq Q^2 \leq 4.2$ GeV^2), while the outbending data contributed to bins 24 through 32. ($0.6 \leq Q^2 \leq 2.4$ GeV^2)

The extracted spin structure function g_1^p shows a clear resonant structure at low values of Q^2 (Fig. 7.26, 7.27). The resonances become 'smoothed out' as Q^2 get larger. The ratio g_1^p/F_1^p plotted as a function of Q^2 in bins of x does not show any significant Q^2 variation above $W = 2$ GeV. When g_1^p is plotted as a function of Nachtmann scaling variable ξ, it becomes consistent with the DIS data (Q^2=10 GeV^2) at $Q^2 \geq 1$ GeV.

The first moment Γ_1^p was evaluated for the Q^2 range of $0.05 \leq Q^2 \leq 3.5$ GeV^2. The obtained values follow closely the Ioffe-Burkert Model discussed in section 2.5.2. When plotted as a function of Q^2, the slope of Γ_1^p becomes negative at $Q^2 \sim 0.15$ GeV^2 (Fig.7.28). A first degree polynomial was fitted to the values of Γ_1^p at four lowest Q^2 points (as shown in Fig.7.31), and the slope was found to be -0.3329 ± 0.1199. Adding a hypothetical point $\Gamma_1^p(Q^2 = 0) = 0$ resulted in slope of -0.256 ± 0.0246. In comparison, the generalized GDH Sum Rule predicts a slope of -0.427. More measurements at low Q^2 values will be provided by the next experiment which is expected to reach Q^2 as low as 0.01 GeV^2.

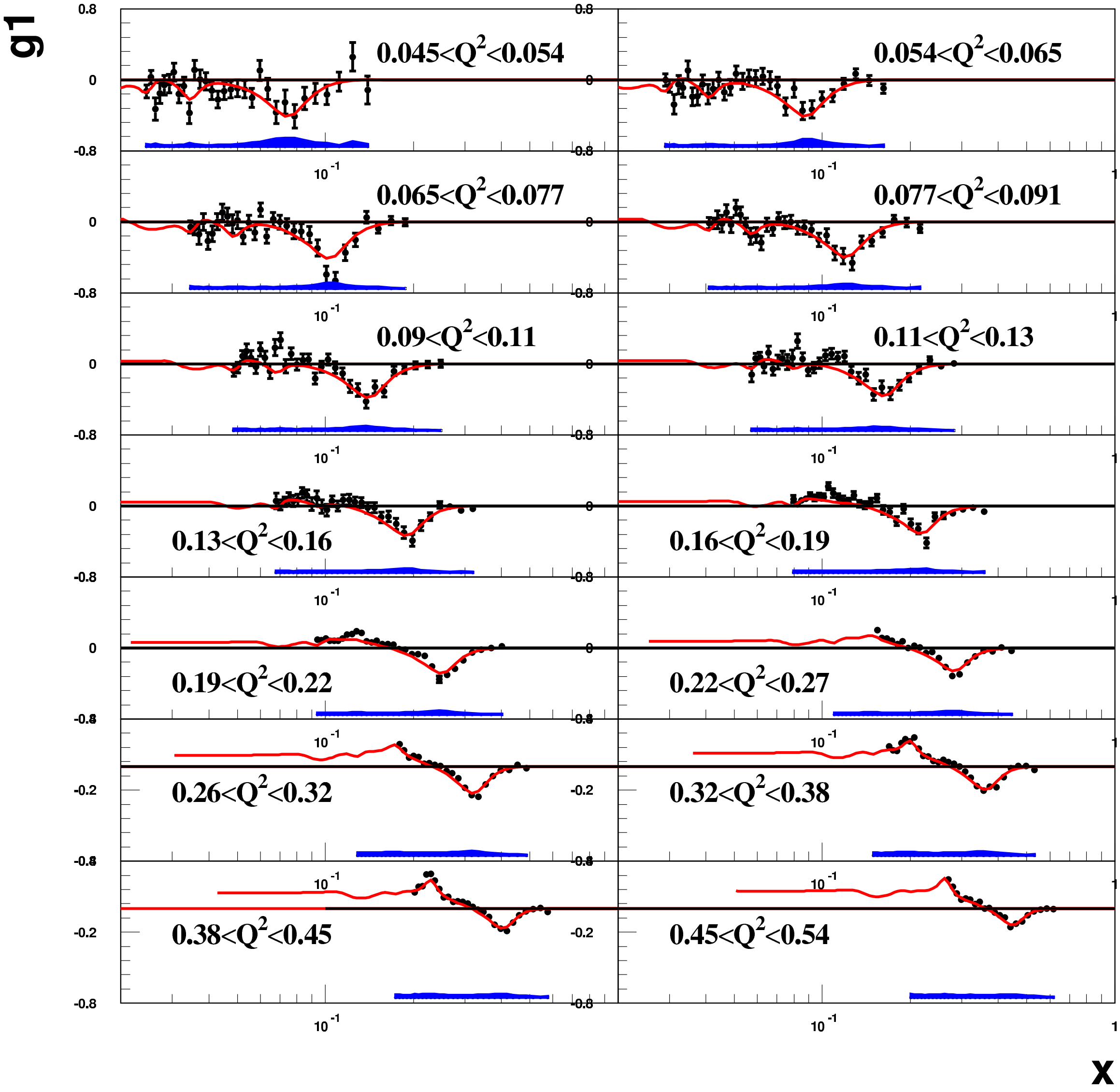

Figure 7.26: Spin structure function $g_1^p(x, Q^2)$ for the low energy set. Strong resonant structure is evident at low Q^2, with the $\Delta(1232)$ resonance being the most prominent one. Total systematic error is shown by a blue band on the bottom of each plot. g_1^p from the 'Models' is shown by the red curve on each plot.

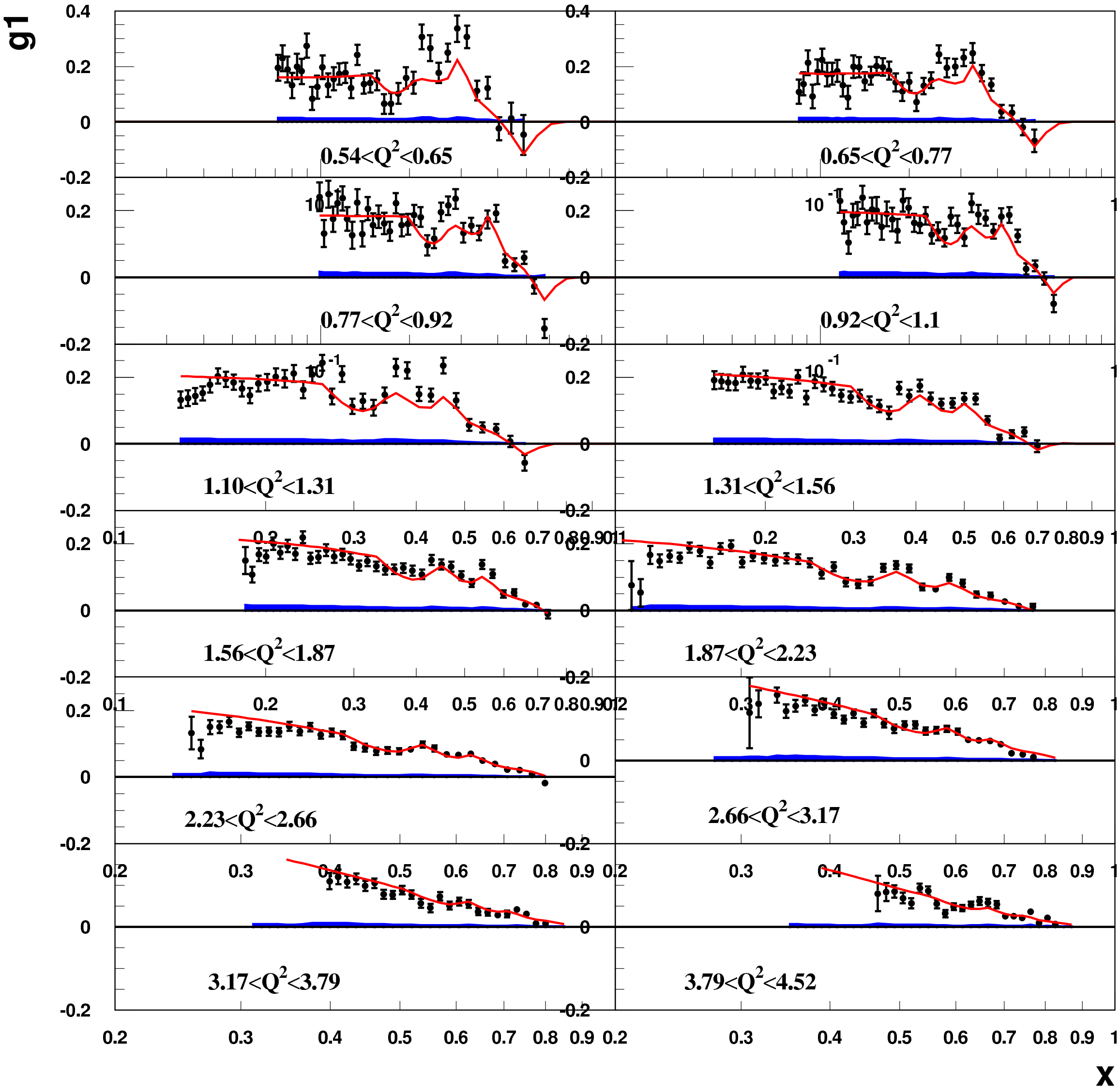

Figure 7.27: Spin structure function $g_1^p(x, Q^2)$ for the high energy set. Resonances become 'smoothed out' as Q^2 gets larger. Total systematic error is shown by a blue band on the bottom of each plot. g_1^p from the 'Models' is shown by the red curve on each plot.

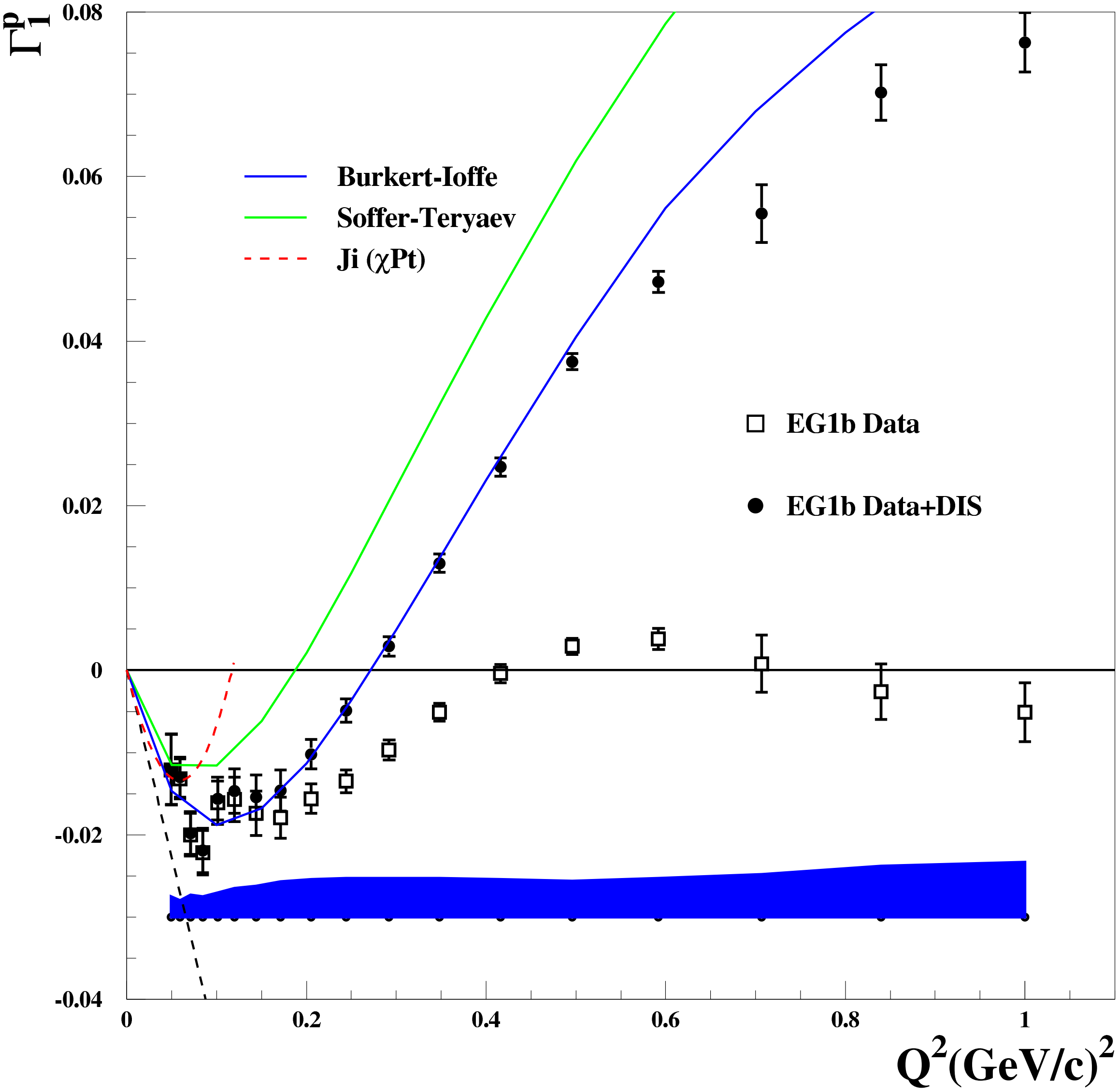

Figure 7.28: First moment for the low energy set. Values of g_1^p, extracted from the data and integrated down to the lowest available value of x are shown by the open squares. The rest of the integral is obtained by integrating 'Models' g_1^p down to $x = 0.001$. Total values of Γ_1^p are shown by filled circles. Systematic error is shown by a blue band on the bottom of the plot. Models shown on the plot are discussed in Section 2.5.2.

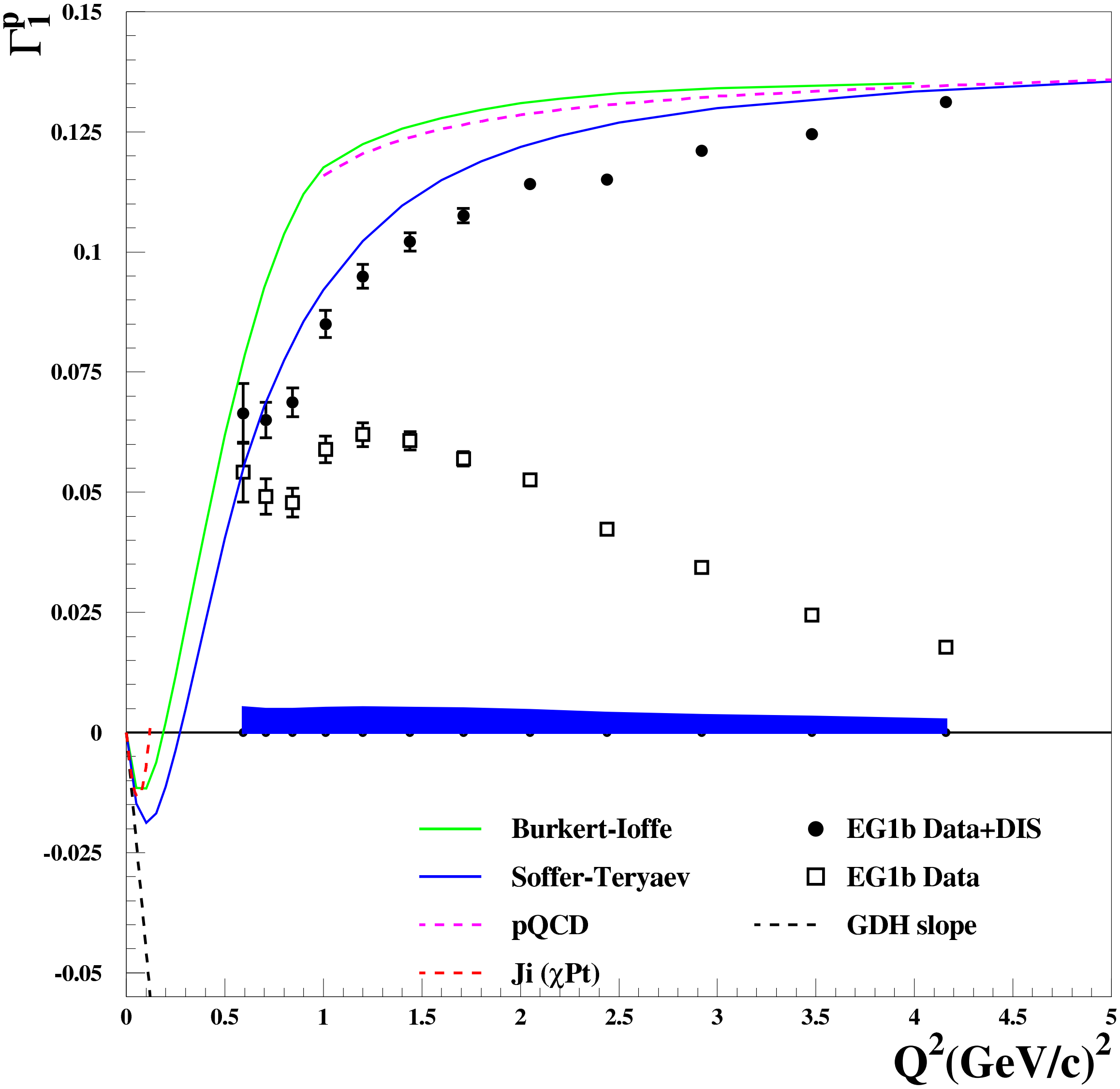

Figure 7.29: First moment for the high energy set. Values of g_1^p, extracted from the data and integrated down to the lowest available value of x are shown by the open squares. The rest of the integral is obtained by integrating 'Models' g_1^p down to $x = 0.001$. Total values of Γ_1^p are shown by filled circles. Systematic error is shown by a blue band on the bottom of the plot. Models shown on the plot are discussed in Section 2.5.2.

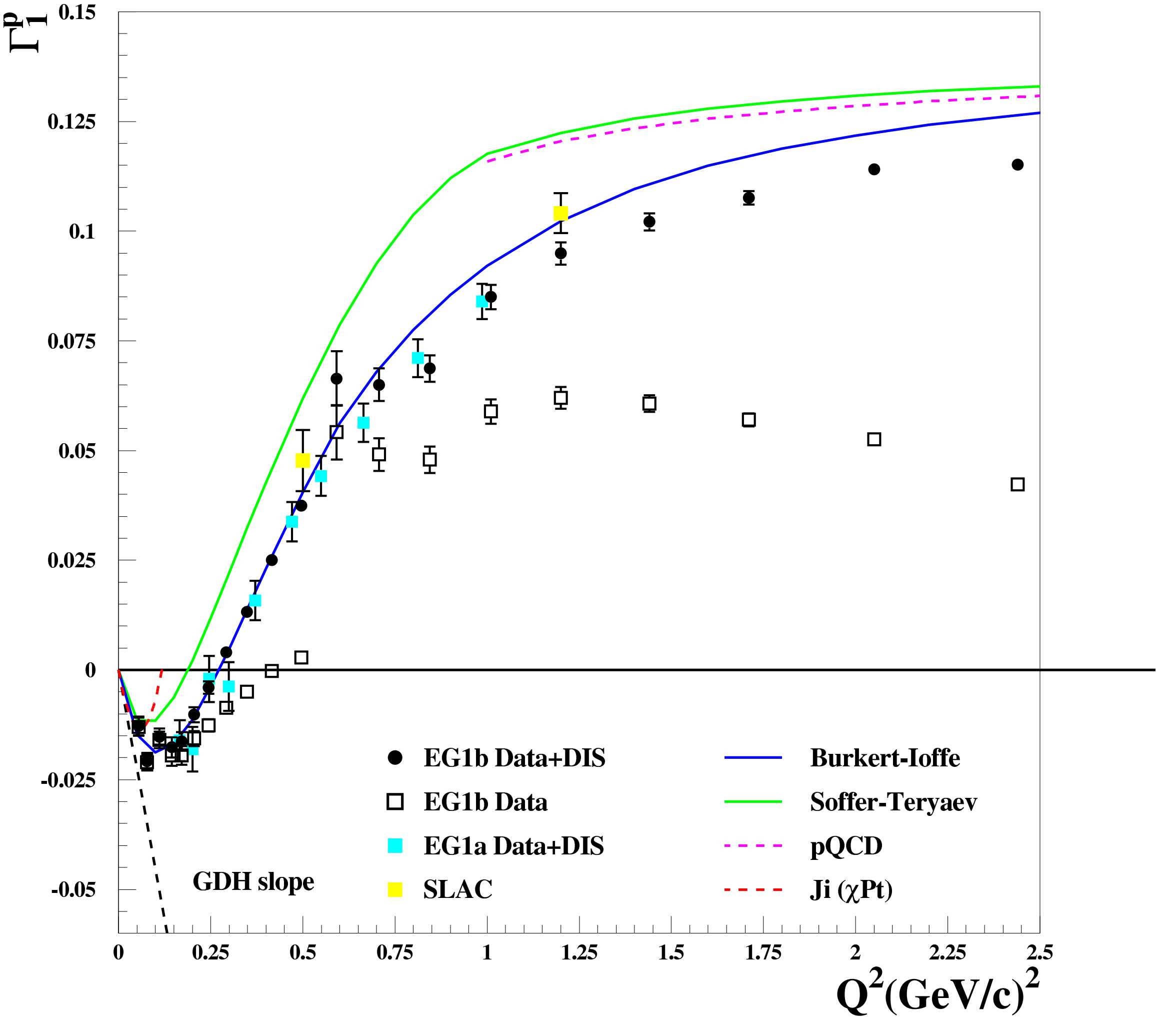

Figure 7.30: First moment for all data. Values of g_1^p, extracted from the data and integrated down to the lowest available value of x are shown by the open black squares. The rest of the integral is obtained by integrating 'Models' g_1^p down to $x = 0.001$. Total values of Γ_1^p are shown by filled black circles. Resuls from the EG1a experiment are shown by filled teal squares, and the results from SLAC are shown by filled yellow squares. The values of Γ_1^p obtained from EG1b data are consistent with results from EG1a and SLAC.

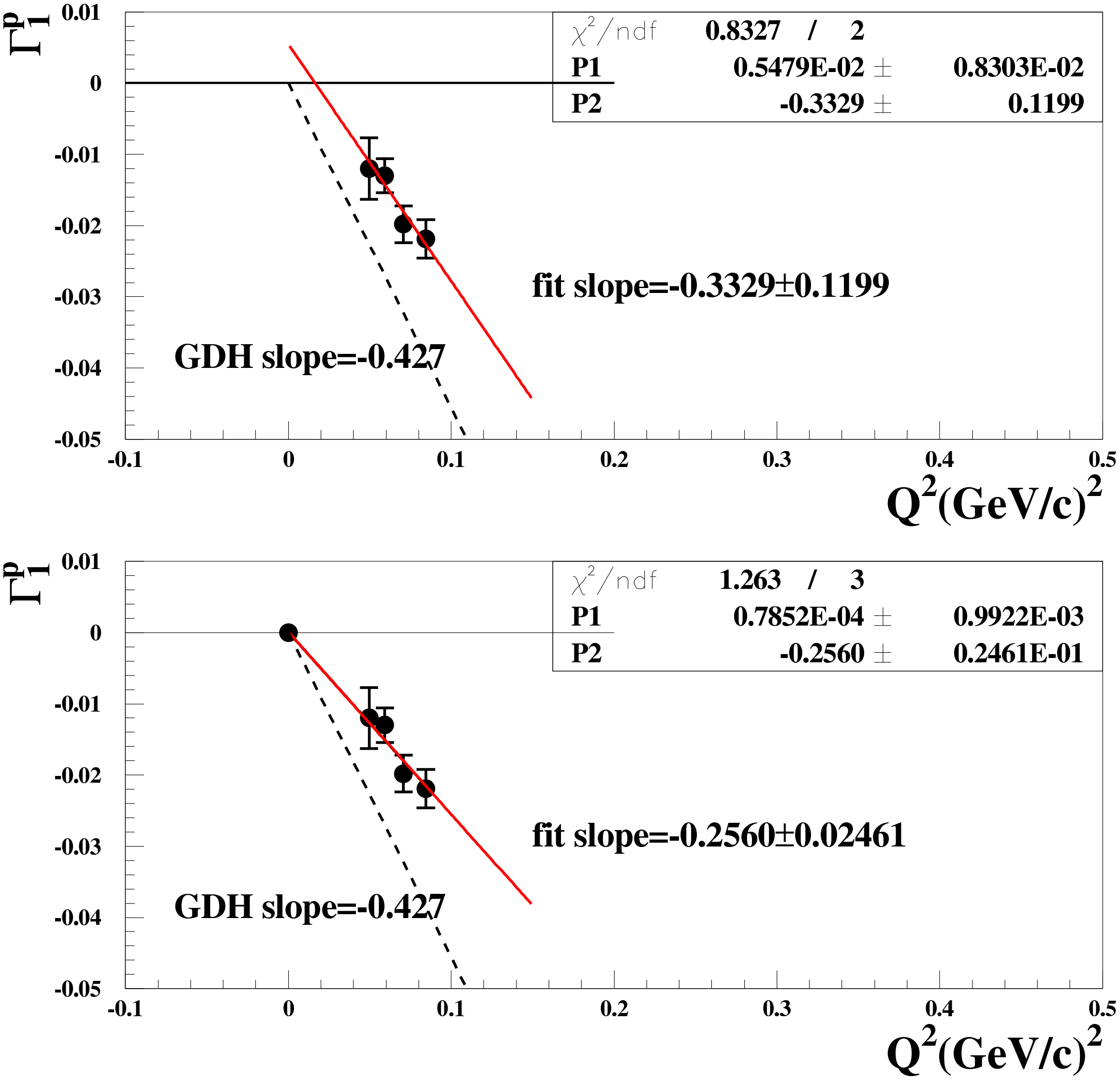

Figure 7.31: Values of Γ_1^p for the four lowest Q^2 points. If a polynomial of first degree is fitted though these points the resulting slope is 0.3329 ± 0.1199. If a hypothetical point $\Gamma_1^p(Q^2 = 0) = 0$ is added, the slope is 0.256 ± 0.0246. The generalized GDH Sum Rule predicts a slope of -0.427.

Appendix A

From $A_{\|}$ to A_1

The cross sections involved in polarized electron scattering were derived in section one:

$$\begin{aligned}
\frac{\sigma^2 x}{dxdQ^2} &= \frac{4\pi\alpha^2}{Q^4 x}\left[(1-\frac{Q^2}{2MEx}-\frac{Q^2}{4E^2})F_2+\frac{Q^4}{4M^2E^2x}F_1\right] \\
\frac{\Delta\sigma^2 x}{dxdQ^2} &= \frac{4\pi\alpha^2}{MEQ^2x}\left[(2-\frac{Q^2}{2MEx}-\frac{Q^2}{2E^2})g_1-\frac{2Mx}{E}g_2\right],
\end{aligned} \tag{A.1}$$

where the structure functions F_1, F_2, g_1, g_2 are implied to be functions of x, Q^2. Utilizing the definitions of Bjorken variables $x = \frac{Q^2}{2m\nu}$ and $y = \frac{\nu}{E}$, the cross sections are rewritten:

$$\begin{aligned}
\frac{\sigma^2 x}{dxdQ^2} &= \frac{2\pi\alpha^2}{MEx^2y^2}\left[(1-y-\frac{Mxy}{2E})F_2+xy^2F_1\right] \\
\frac{\Delta\sigma^2 x}{dxdQ^2} &= \frac{4\pi\alpha^2}{MExy}\left[(2-y-\frac{Mxy}{E})g_1-\frac{2Mx}{E}g_2\right]
\end{aligned} \tag{A.2}$$

The electron spin asymmetry is formed:

$$A_{||} = \frac{\Delta\sigma}{2\sigma} = xy\frac{(2 - y - \frac{Mxy}{E})g_1 - \frac{2Mx}{E}g_2}{(1 - y - \frac{Mxy}{2E})F_2 + xy^2F_1} \tag{A.3}$$

The virtual photon absorption cross sections are written as:

$$\begin{aligned}
\sigma^T_{\frac{1}{2}} &= \frac{4\pi^2\alpha}{MK}(F_1 + g_1 - \frac{2Mx}{\nu}g_2) \\
\sigma^T_{\frac{3}{2}} &= \frac{4\pi^2\alpha}{MK}(F_1 - g_1 + \frac{2Mx}{\nu}g_2) \\
\sigma^L_{\frac{1}{2}} &= \frac{4\pi^2\alpha}{K}(\frac{F_2}{\nu}(1 + \frac{\nu^2}{Q^2} - \frac{1}{M}F_1) \\
\sigma^{LT}_{\frac{1}{2}} &= \frac{4\pi^2\alpha}{K}\frac{Q}{M\nu}(g_1 + g_2)
\end{aligned} \tag{A.4}$$

2 photon-nucleon asymmetries are formed:

$$\begin{aligned}
A_1 &= \frac{\sigma^T_{\frac{1}{2}} - \sigma^T_{\frac{3}{2}}}{\sigma^T_{\frac{1}{2}} + \sigma^T_{\frac{3}{2}}} = \frac{\Delta\sigma^t}{2\sigma^T} \\
A_2 &= \frac{\sigma^{TL}}{\sigma^T}
\end{aligned} \tag{A.5}$$

The photon cross sections are $\sigma^T = \frac{4\pi^2\alpha}{MK}F_1$ and $\Delta\sigma^T = \frac{4\pi^2\alpha}{MK}(2g_1 - \frac{4Mx}{\nu}g_2)$. Substituting these equations gives:

$$\begin{aligned}
A_1 &= \frac{g_1 - \gamma^2 g_2}{F_1} \\
A_2 &= \frac{\gamma(g_1 + g_2)}{F_1},
\end{aligned} \tag{A.6}$$

where $\gamma = \frac{Q^2}{\nu^2}$. A variable R is defined:

$$R = \frac{\sigma^L}{\sigma_T} = \frac{1+\gamma^2}{2xF_1}F_2 - 1, \tag{A.7}$$

so that

$$F_1 = \frac{1+\gamma_2}{2x(1+R)}F_2 \tag{A.8}$$

The spin structure functions can now be rewritten:

$$\begin{aligned} g_1 &= \frac{F_1}{1+\gamma^2} = (A_1 + \gamma A_2)\frac{F_2}{2x(1+R)} \\ g_2 &= = \frac{F_1}{1+\gamma^2}(\frac{A_2}{\gamma} - A_1) = (\frac{A_2}{\gamma} - A_1)\frac{F_2}{2x(1+R)} \end{aligned} \tag{A.9}$$

Substituting these into the expression for $A_{||}$ gives:

$$\begin{aligned} A_{||} &= A_1 \times xy\frac{(2 - y - \frac{\gamma^2}{2})\frac{1}{2x(1+R)} + \frac{\gamma^2}{2xy(1+R)}}{(1 - y - \frac{\gamma^2}{4} + xy^2\frac{1+\gamma^2}{2x(1+R)}} \\ &+ A_2 \times xy\frac{(2 - y - \frac{\gamma^2}{2})\frac{\gamma}{2x(1+R)} - \frac{\gamma}{2xy(1+R)}}{(1 - y - \frac{\gamma^2}{4} + xy^2\frac{1+\gamma^2}{2x(1+R)}} \end{aligned} \tag{A.10}$$

or

$$\begin{aligned} A_{||} &= D(A_1 + \eta A_2) \\ D &= \frac{y(2-y)(1+\frac{1}{2}\gamma^2 y)}{(1+\gamma^2)(2(1-y-\frac{\gamma^2 y^2}{4})\frac{1+R}{1+\gamma^2} + y^2)} \\ \eta &= \frac{2\gamma(1-y-\frac{1}{4}\gamma^2 y^2)}{(2-y)(1+\frac{1}{2}\gamma^2 y)} \end{aligned} \tag{A.11}$$

Appendix B

Operator Product Expansion

Hadronic tensor with proper normalization is :

$$W_{\mu\nu} = \frac{1}{2\pi} \int d^4x e^{iqx} < p|j_\mu(x) j_\nu(0)|p > \tag{B.1}$$

For physical processes $E > E'$and $q_0 > 0$, so $< p|j_\mu(x)j_\nu(0)|p >$ for $q_0 > 0$ is considered. Using the completeness condition, translational invariance, and the fact that for $q_0 > 0$

$$\int d^4x e^{iqx} < p|j_\nu(0) j_\mu(x)|p >= 0 \tag{B.2}$$

the hadronic tensor can be rewritten using the commutator of the currents.

$$W_{\mu\nu} = \frac{1}{2\pi} \int d^4x e^{iqx} < p|[j_\mu(x), j_\nu(0)]|p > \tag{B.3}$$

Causality requires that the commutator vanishes for space-like x($x^2 < 0$),

$$[j_\mu(x), j_\nu(0)] = 0 \tag{B.4}$$

Therefore, only the region of $x^2 < 0$ is relevant for the scattering process. Moreover, it can be shown, that for deep inelastic scatterings in which $-q^2 \rightarrow \infty$ with $\frac{-q^2}{\nu}$ fixed, the dominant contribution comes from the region $0 \leq x^2 \leq \frac{const}{-q^2}$, where the constant comes from the integration. This is an important detail that needs to be elaborated. In order to show this, we look at the integration in the expression for the hadronic tensor, and see what region gives the dominant contribution in the limit $-q^2 \rightarrow \infty$, $\frac{-q^2}{\nu}$ fixed. The kinematic region where $|q \cdot x| \rightarrow \infty$ makes vanishing contributions to the integral, because $exp(iq \cdot x)$ oscillates without bound. Also, in the laboratory frame

$$\vec{q} \cdot \vec{x} = r|\vec{q}| = \sqrt{-q^2 + q_0^2} = rq_0\sqrt{1 - \frac{q^2}{q_0^2}} \qquad r = \frac{\vec{q} \cdot \vec{x}}{|\vec{q}|} \tag{B.5}$$

In the limit $q^2 \rightarrow \infty$ and $\xi = -\frac{q^2}{2Mq_0}$ fixed

$$q \cdot x \sim \; q_0(x_0 - r) - \xi M r \tag{B.6}$$

Keeping $|q \cdot x|$ finite leads to the following conditions:

$$|x_0 - r| \leq \frac{const}{q_0} \qquad |r| \leq \frac{const}{\xi} \tag{B.7}$$

Therefore, we obtain

$$x_0^2 \leq (r + \frac{const}{q_0})^2 = r^2 + 2const\frac{r}{q_0} + \frac{const^2}{q_0^2} \leq \vec{x}^2 + \frac{const}{\xi q_0} \tag{B.8}$$

$$0 \leq x^2 \leq \frac{-const}{q^2} \tag{B.9}$$

The conclusion is that the deep inelastic scattering is determined by the product of currents near the light cone.

Another important property of the hadronic tensor is that it is related to the absorptive part of the Compton scattering amplitude $T_{\mu\nu}$

$$T_{\mu\nu} = i \int d^4x e^{iq\cdot x} < q|T[j_\mu(x) j_\nu(0)]|p > \tag{B.10}$$

The main difference between $W_{\mu\nu}$ and $T_{\mu\nu}$ is that the product of currents is time-ordered for $T_{\mu\nu}$, and that fact makes the perturbative field theory applicable to the analysis. In particular, the Feynman Rules can be applied. Conventionally, the Compton amplitude is used for the description of DIS.

$T_{\mu\nu}$ contains a time-ordered product of currents $T[\mathrm{j}_\nu(x) j_\nu(0)]$. Each current can be wriiten in terms of the fields

$$j_\mu(x) = \Psi(x)\gamma_\mu\Psi(x) \qquad j_\nu(0) = \Psi(0)\gamma_\nu\Psi(0) \tag{B.11}$$

The product of currents is consequently a product of 4 fields. Such products are called the 'composite operators' and, in general, are not well defined, since their vacuum expectation value given as a momentum integral diverges at the same space-time point ($x \to 0$). Operator Product Expansion gives a meaningful definition of a composite operator. Product of operators A(x) and B(y) is expanded in a series of well-defined local operators $O_i(x)$ with singular number coefficients $C_i(x)$:

$$A(x)B(y) = \sum_{i=0}^{\infty} C_i(x-y)\hat{O}_i(\frac{x+y}{z}) \tag{B.12}$$

This method provides a powerful tool in the analysis of the deep inelastic scattering

The first step is to use Wick's Theorem to relate the time-ordered product to the normal product of fields. For the time-ordered product of 4 free fermion fields it gives a normal product of the 4 fields and all possible contractions. The expression 'all possible contractions' means that there is a term in the sum for each possible way of contracting the 4 fields into pairs. This way, Wick's Theorem allows us to turn a time-ordered product of 4 fields into a sum of products of Feynman propagators.

$$\begin{aligned} T\left[\bar\Psi(x)\gamma_\mu\Psi(x)\bar\Psi(0)\gamma_\nu\Psi(0)\right] &= N\Big[\bar\Psi(x)\Psi(x)\bar\Psi(0)\Psi(0) + \overbrace{\bar\Psi(x)\Psi(x)}\,\bar\Psi(0)\Psi(0) \\ +\overbrace{\bar\Psi(x)\Psi(x)\bar\Psi(0)}\,\Psi(0) &+ \overbrace{\bar\Psi(x)\Psi(x)\bar\Psi(0)\Psi(0)} + \bar\Psi(x)\,\overbrace{\Psi(x)\bar\Psi(0)}\,\Psi(0) \\ +\bar\Psi(x)\,\overbrace{\Psi(x)\bar\Psi(0)\Psi(0)} &+ \bar\Psi(x)\Psi(x)\,\overbrace{\bar\Psi(0)\Psi(0)} + \overbrace{\bar\Psi(x)\Psi(x)\bar\Psi(0)}\,\Psi(0) \\ +\overbrace{\bar\Psi(x)\Psi(x)}\,\overbrace{\bar\Psi(0)\Psi(0)} &+ \overbrace{\bar\Psi(x)\,\overbrace{\Psi(x)\bar\Psi(0)}\,\Psi(0)}\Big] \end{aligned}$$

$$\begin{aligned} &= -Tr\,[< 0|T[\Psi(0)\Psi(x)]|0 > \gamma_\mu < 0|T[\Psi(x)\Psi(0)]|0 > \gamma_\nu] \\ &+ \Psi(x)\gamma_\mu < 0|T[\Psi(x)\Psi(0)]|0 > \gamma_\nu\Psi(0) + \Psi(0)\gamma_\nu < 0|T[\Psi(0)\Psi(x)]|0 > \gamma_\mu\Psi(x) \\ &+ \Psi(x)\gamma_\mu\Psi(x)\Psi(0)\gamma_\mu\Psi(0) \end{aligned} \tag{B.13}$$

Each term can be evaluated using the Feynman propagator for the free quark field Ψ

$$< 0|T[\Psi(x)\Psi(0)]|0 >= -iS(x) = \int \frac{d^4p}{(2\pi)^4}\frac{1}{m-\not p - i\varepsilon}e^{-ip\cdot x} = (i\not\partial + m)\frac{1}{4\pi^2 i}\frac{1}{x^2 - i\varepsilon} \tag{B.14}$$

The time-ordered product is evaluated and the products of fields are expressed in terms of regular bilocal operators.

$$T[j_\mu(x)j_\nu(0)] = \frac{x^2 g_{\mu\nu} - 2x_\mu x_\nu}{\pi^4(x^2 - i\varepsilon)^4} + \frac{ix^\lambda}{2\pi^2(x^2 - i\epsilon)^2}\sigma_{\mu\lambda\nu\rho}O^\rho_\nu(x,0) \tag{B.15}$$

$$+\frac{x^\lambda}{2\pi^2(x^2 - i\varepsilon)^2}\varepsilon_{\mu\lambda\nu\rho}O^\rho_A(x,0) + O_{\mu\nu}(x,0)(1)$$

where the bilocal operators are defined as

$$\begin{aligned} O^\mu_V(x,y) &= \Psi(x)\gamma^\mu\Psi(y) - \Psi(y)\gamma^\mu\Psi(x) \\ O^\mu_A(x,y) &= \Psi(x)\gamma^\mu\gamma_5\Psi(y) + \Psi(y)\gamma^\mu\gamma_5\Psi(x) \\ O_{\mu\nu}(x,y) &= \Psi(x)\gamma_\mu\Psi(x)\Psi(y)\gamma_\nu\Psi(y) \end{aligned} \tag{B.16}$$

The object of interest for the deep inelastic scattering is a commutator of fields, and it can be evaluated from the time ordered product. Using the fact that the electromagnetic current is hermitian, and applying the residue calculus gives:

$$\begin{aligned} \pm[j_\mu(x), j_\nu(0)] &= \frac{i}{3\pi^3}(2x_\mu x_\nu - x^2 g_{\mu\nu})\delta^{(3)}(x^2) + \frac{1}{\pi}x^\lambda\delta^{(1)}(x^2)\sigma_{\mu\lambda\nu\rho}O^\rho_V(x,0) \\ &- \frac{i}{\pi}x^\lambda\delta^{(1)}(x^2)\varepsilon_{\mu\lambda\nu\rho}O^\rho_A(x,0) + O_{\mu\nu}(x,0) - O_{\nu\mu}(0,x) \end{aligned} \tag{B.17}$$

where

$$\delta^n(y) = \frac{d^n}{d(y)^n}\delta(y) \tag{B.18}$$

This expression can be used now to evaluate the hadronic tensor, defined through the commutator of currents.

$$W_{\mu\nu} = \frac{1}{2\pi}\int d^4x e^{iq\cdot x} < p|[j_\mu(x), j_\nu(0)]|p > \tag{B.19}$$

$$\begin{aligned} W_{\mu\nu} = \frac{i}{3\pi^2}(2x_\mu x_\nu - x^2 g_{\mu\nu})\delta^{(3)}(x^2) < p|p > - \qquad \text{(B.20)} \\ -\frac{1}{2\pi^2}\int d^4x e^{iq\cdot x} x^\lambda \delta^{(1)}(x^2)\cdot < p| - \sigma_{\mu\lambda\rho\nu} O^\rho_\nu(x,0) + i\varepsilon_{\mu\lambda\nu\rho} O^\rho_A(x,0)|p > + \\ +\frac{1}{2\pi}\int d^4x e^{iq\cdot x}\cdot < p|O_{\mu\nu}(x,0) - O_{\nu\mu}(0,x)|p > \end{aligned}$$

Diagrammatic representation of matrix element is shown in Figure 2.10. Operators $O^\rho_V(x,0)$ and $O^\rho_A(x,0)$ are regular bilocal operators which can be Taylor expanded around x=0. This is done by expanding the free quark fields around $x \sim 0$, and plugging the result into the definition of the operators. The result is an infinite series of local operators:

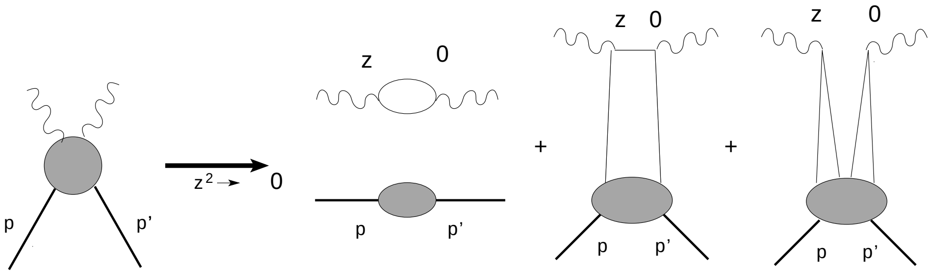

Figure B.1: Leading order graphs for $W_{\mu\nu}$

$$O^\rho_V(x,0) = \sum_{n=0}^{\infty} \frac{1}{n!} x^{\mu_1} \dots x^{\mu_n} O^\rho_{V\mu_1\dots\mu_n}(0) \tag{B.21}$$

$$O^\rho_A(x,0) = \sum_{n=0}^{\infty} \frac{1}{n!} x^{\mu_1} \dots x^{\mu_n} O^\rho_{A\mu_1\dots\mu_n}(0) \tag{B.22}$$

where the local operators are

$$O^\rho_{V\mu_1\dots\mu_n}(x) = (\partial_{\mu_1}\dots\partial_{\mu_n}\Psi(x))\gamma^\rho\Psi(x) - \Psi(x)\gamma^\rho\partial_{\mu_1}\dots\partial_{\mu_n}\Psi(x) \tag{B.23}$$

$$O^\rho_{A\mu_1\dots\mu_n}(x) = (\partial_{\mu_1}\dots\partial_{\mu_n}\Psi(x))\gamma^\rho\Psi_5\Psi(x) - \Psi(x)\gamma^\rho\gamma_5\partial_{\mu_1}\dots\partial_{\mu_n}\Psi(x) \tag{B.24}$$

In general, a product of currents takes the following form:

$$j(x)j(0) = \sum_{i,n} C_n^{(i)}(x^2)x^{\mu_1}......x^{\mu_n}O^{(i)}_{\mu_1.....\mu_n}(0) \tag{B.25}$$

The mass dimension of the current $j(x)$ is d_{jo} and the mass dimension of $O^{(i)}_{\mu_1.....\mu_n}$ is $d^i_{O(n)}$. Matching both sides of this equation in their mass dimensions gives:

$$[m]^{2djo} = [C(x^2)]m^{-n+d^i_{O(n)}} \tag{B.26}$$

$$[C_n^{(i)}(x^2)] = [m]^{2d_{jo}+n-d^i_{O(n)}}$$

$$[C_n^{(i)}(x^2)] \stackrel{x^2\to 0}{\to} (\frac{1}{x^2})^{\frac{1}{2}(2d_{jo}-d_{O(n)}+n}$$

$$\to (x^2)^{\frac{1}{2}(-2d_{jo}-n+d^i_{O(n)})}$$

The strength of the singularity is determined by the number $\tau = d^i_{O(n)} - n$, called the 'twist' of the operator $O_n^{(i)}$. The lowest twist corresponds to the largest contribution in the expansion. In analyzing a product of currents, the operators $O_n^{(i)}$ are at least bilinear in fields, with the lowest twist $\tau = 2$ [5]. Operators are usually labeled by their spin n and twist τ, but in this discussion the twist label is suppressed and the leading twist $\tau = 2$ is implied Keeping the 2 lowest order terms the hadronic tensor can now be rewritten as

$$\begin{aligned} W_{\mu\nu} &= -\frac{1}{2\pi^2}\sum_{n=0}^{\infty}\frac{1}{n!}\int d^4x e^{iq\cdot x}x^\lambda \delta^{(1)} x_1^{\mu_1}...x^{\mu_n} \times (-\sigma_{\mu\lambda\rho\nu} < p|O^\rho_{V\mu_1...\mu_n}(0)|p > + \\ &+ i\varepsilon_{\mu\lambda\nu\rho} < p|O^\rho_{A\mu_1...\mu_n}(0)|p > \end{aligned} \tag{B.27}$$

Last term in this expression contains a totally antisymmetric tensor, which vanishes when contracted with the symmetric leptonic tensor. Therefore this term is relevant only for the polarized scattering experiments when both leptonic and hadronic antisymmetric tensors contribute.

The matrix elements such as $< p|O^{\rho}_{V\mu_1...\mu_n}(0)|p >$ are not known because they depend on the unknown properties of the hadronic state $|P >$. However we can deduce the tensor structure of such matrix element based on the fact that it must be traceless, symmetric , and can only depend on p_μ. Using these properties gives:

$$W_{\mu\nu} = \frac{1}{2\pi^2}\sigma_{\mu\lambda\nu\rho}p^{\rho}\int d^4x e^{iq\cdot x}x^{\lambda}\delta^{(1)}(x^2)\sum_{n=0}^{\infty} a_n p_{\mu_1}...p_{\mu_n}x^{\mu_1}...x^{\mu_n} \tag{B.28}$$

The summation can be absorbed into a function:

$$f(p\cdot x) = \sum_{n=0}^{\infty}\frac{1}{n!}a_n(p\cdot x)^n \tag{B.29}$$

For later convenience, the function is rewritten as a Fourier Transform:

$$f(p\cdot x) = \int_{-\infty}^{\infty}\tilde{f}(\xi)e^{i\xi(p\cdot x)} \tag{B.30}$$

Finally, the hadronic tensor can be expressed as

$$W_{\mu\nu} = \frac{1}{2\pi^2}\sigma_{\mu\lambda\nu\rho}p^{\rho}\int d^4x e^{i(q+\xi p)\cdot x}x^{\lambda}\delta^{(1)}(x^2)\int\tilde{f}(\xi)d\xi \tag{B.31}$$

$$W_{\mu\nu} = \int_{-\infty}^{\infty}\tilde{f}(\xi)d\xi\left[p_\nu p_\mu + p_\mu p_\nu + 2\xi p_\nu p_\mu - g_{\mu\nu}(p\cdot q + 2\xi M^2)\right]\delta(q^2 + 2\xi p\cdot q + \xi^2 M^2) \tag{B.32}$$

In the Bjorken limit, the mass can be neglected and $\xi = -\frac{q^2}{2p\cdot q}$, so that:

$$W_{\mu 0} = \frac{1}{2}\tilde{f}(\xi)(-g_{\mu\nu} - \frac{q^2}{(p\cdot q)^2}p_\mu p_\nu + \frac{p_\mu p_\nu + p_\nu p_\mu}{p\cdot q}) \tag{B.33}$$

Equation (103) is equivalent to equation (18) that was derived earlier:

$$W_{\mu\nu} = \frac{1}{2}\tilde{f}(\xi)(\frac{q_\mu q_\nu}{q^2} - g_{\mu\nu}) + \frac{1}{p\cdot q}\xi\tilde{f}(\xi)(p_\mu - \frac{p\cdot q}{q^2}q_\mu)(p_\nu - \frac{p\cdot q}{q^2}q_\nu) \tag{B.34}$$

It can be seen now, that this analysis leads to the Bjorken scaling , where the structure functions W_1 and W_2 depend only on the variable ξ.

$$\begin{aligned} W_1 &= \frac{1}{2}\tilde{f}(\xi) \equiv F_1(\xi) \\ W_2 &= \frac{1}{2}\xi\tilde{f}(\xi) \equiv F_2(\xi) \end{aligned} \tag{B.35}$$

Therefore, the operator product expansion with the free quark fields recovers the parton model predictions.

The next step is to generalize the argument to the interacting fields. The important difference between the expansion of the free and the interacting fields is that in the case of the interacting fields, the coefficient functions will be different for each term in the Taylor expansion. This fact prevents the series from summing into a regular bilocal operator. The consequence of this is that the free field theory results in exact scaling, while the interacting fields produce logarithmic scaling. Time ordered product of the interacting fields is given by:

$$T[j_\mu(x), j_\nu(x')] = (\partial_\mu \partial'_\nu - g_{\mu\nu}\partial\cdot\partial')O_L(x,x')$$

$$+(g_{\mu\lambda})\partial_\rho\partial'_\nu + g_{\rho\nu}\partial_\mu\partial'_\lambda - g_{\mu\lambda}g_{\rho\nu}\partial\cdot\partial' - g_{\mu\nu}\partial_\lambda\partial'_\rho)O_2^{\lambda\rho}(x,x')$$
$$+antisymmetric \quad terms \tag{B.36}$$

The operators are expanded near the light cone:

$$\begin{aligned} O_L(x,x') &= \sum_{i,n} C^{(i)}_{L,n}(y^2)y^{\mu_1}....y^{\mu_n}O^{(i)}_{L\mu_1...\mu_n}(\frac{x+x'}{2}) \quad y = x - x' \\ O_2^{\lambda\rho}(x,x') &= \sum_{i,n} C^{(i)}_{2,n}(y^2)y^{\mu_1}....y^{\mu_n}O^{(i)\lambda\rho}_{2\mu_1...\mu_n}(\frac{x+x'}{2}) \end{aligned} \tag{B.37}$$

The forward virtual Compton amplitude $T_{\mu\nu}$ is obtained by taking a Fourier transform of equation (106). For the symmetric part of matrix element that gives:

$$\begin{aligned} iT_{\mu\nu} \quad &= \int d^4xe^{iqx}\langle p|T[j_\mu(x)j_\nu(0)|p\rangle = \\ &= (q_\mu q_\nu - q^2 g_{\mu\nu})\sum_{i,n}\langle p|O^{(i)}_{L\mu_1...\mu_n}(0)|p\rangle \int d^4xe^{iqx}x_{\mu_1}...x_{\mu_n}C^{(i)}_{L,n}(x^2) \\ &+(g_{\mu\lambda}q_\rho q_\nu + g_{\rho\nu}q_\mu q_\lambda - q^2 g_{\mu\lambda}g_{\rho\nu} - g_{\mu\nu}q_\lambda q_\rho) \\ &\times\sum_{i,n}\langle p|O_{(i)\lambda\rho 2\mu_1...\mu_n}(0)|p\rangle \int d^4xe^{iqx}x_{\mu_1}...x_{\mu_n}C^{(i)}_{2,n}(x^2) \end{aligned} \tag{B.38}$$

The Fourier Transforms of the coefficient functions are defined as follows:

$$\begin{aligned} \int d^4e^{iq\cdot x}x^{\mu_1}....x^{\mu_n}C^{(i)}_{i,n}(x^2) &= \tilde{C}^{(i)}_{2,n}(-q^2)q^{\mu_1}...q^{\mu_n}(-i)(\frac{q^2}{2})^{-n-1} \\ \int d^4xe^{iq\cdot x}x^{\mu_1}....x^{\mu_n}C^{(i)}_{2,n}(x^2) &= \tilde{C}^{(i)}_{2,n+2}(-q^2)q^{\mu_1}....q^{\mu_n}(-2i)(-\frac{q^2}{2})^{-n-2} \end{aligned}$$

The matrix elements of the composite operators are:

$$< p|O^{(i)}_{L_{\mu_1....\mu_n}}|p> \;=\; A^{(i)}_{L,n}p_{\mu_1}....p_{\mu_n} - traces$$

$$< p|O^{(i)\lambda\rho}_{2_{\mu_1....\mu_n}}|p > \ = \ A^{(i)}_{2,n+2}p^\lambda p^\rho p_{\mu_1}....p_{\mu_n} - traces \tag{B.39}$$

Using the formulas above, the forward Compton amplitude, and consequently, the hadronic tensor can be evaluated. The forward Compton amplitude is [60]:

$$T_{\mu\nu} = 2\sum_{i,n}\left[e_{\mu\nu}A^i_{L,n}\tilde{C}^{(i)}_{L,n}(-q^2) + d_{\mu\nu}A^{(i)}_{2,n}\tilde{C}^{(i)}_{2,n}\right] \tag{B.40}$$

where

$$\begin{aligned} w &= \frac{2p\cdot q}{-q^2} = 1/\xi && \text{(B.41)} \\ e_{\mu\nu} &= g_{\mu\nu} - \frac{q_\mu q_\nu}{q^2} \\ d_{\mu\nu} &= g_{\mu\nu} - p_\mu p_\nu\frac{q^2}{p\cdot q} + \frac{p_\mu q_\nu + p_\nu q_\mu}{p\cdot q} \end{aligned}$$

(B.42)

The hadronic tensor is determined using $W_{\mu\nu} = \frac{1}{\pi}$ Abs $T_{\mu\nu}$, where the $Abs(T_{\mu\nu})$ is the discontinuity of $T_{\mu\nu}$ across the cut along the $q_0 > 0$ line in the complex plane [60]:

$$AbsT_{\mu\nu} = \frac{1}{2i}\left[T_{\mu\nu}(q_0 + i\epsilon) - T_{\mu\nu}(q_0 - i\epsilon)\right] \tag{B.43}$$

Applying Cauchy integration to both sides of equation(113) and using expression (115) results in the relations which describe the Q^2 dependence of the moments of the structure functions:

$$\int_0^1 d\xi\xi^{n-2}F_L(\xi, Q^2) \ = \ \sum_i A^{(i)}_{L,n}\tilde{C}^{(i)}_{L,n}(Q^2)$$

$$\int_0^1 d\xi \xi^{n-2} F_2(\xi, Q^2) \quad = \quad \sum_i A_{2,n}^{(i)} \tilde{C}_{2,n}^{(i)}(Q^2) \tag{B.44}$$

Appendix C

Altarelli-Parisi Equations

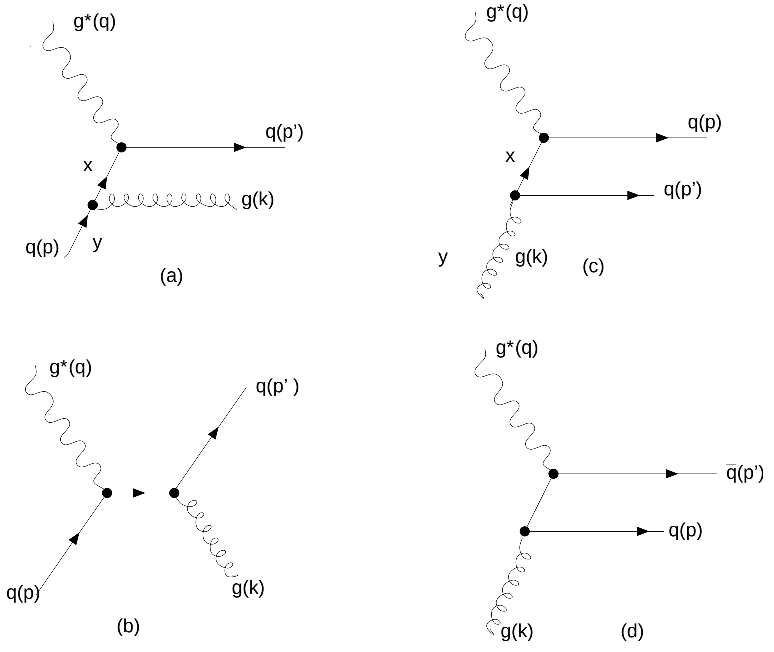

Figure C.1: Leading order processes for AP equations

The evolution of the distribution functions can be formally described by the Altarelli-Parisi equations. Leading order diagrams for this evolution are shown below: The

Altarelli-Parisi equations are derived by analyzing the parton cross-sections for the leading order transitions causing the Q^2-evolution of the distribution functions, which subsequently lead to scaling violations. These are

$$\begin{aligned} \gamma^*(q) + q(p) &\rightarrow q(p') + g(k) \\ \gamma^*(q) + g(k) &\rightarrow q(p) + \bar{q}(p') \end{aligned} \tag{C.1}$$

The first process is similar to the Compton scattering, apart from the color factor, and the fact that the photon is virtual. This is shown in Figure 2.8 (a,b). The matrix element has the following form

$$\mathcal{M}_{fi} = -ie^2 \varepsilon_\alpha \varepsilon_\beta \Psi_f \left[\frac{\gamma^\beta (\not p + \not k)\gamma^\alpha}{(p+q)^2} + \frac{\gamma^\alpha (\not p - \not k')\gamma^\beta}{(q-k)^2} \right] \Psi_i \tag{C.2}$$

Using the trace techniques, summing over the photon polarization states, and averaging over the initial spins gives:

$$|\mathcal{M}_{fi}|^2 = 32\pi^2\alpha^2 \left[\frac{(-(q-k)^2)}{(p+q)^2} + \frac{(p+q)^2}{(-(q-k)^2)} + \frac{2(q-p')Q^2}{(p+q)^2(q-k)^2} \right] \tag{C.3}$$

The color factor C_F needs to be taken into account, so the coupling constant at the qg vertex is modified, and the spin and color-averaged differential cross section for $\gamma^*(q) + q(p) \rightarrow q(p') + g(k)$ can be obtained.

$$\frac{d\sigma}{d\Omega} = \frac{C_F e_q^2 \alpha \alpha_s}{2(p+q)^2} \left[\frac{(-(q-p')^2)}{(p+q)^2} + \frac{(p+q)^2}{(-(q-p')^2)} + \frac{2(q-k)^2 Q^2}{(p+q)^2(q-p')^2} \right] \tag{C.4}$$

The emission of the gluon in the process described above, followed by the subse-

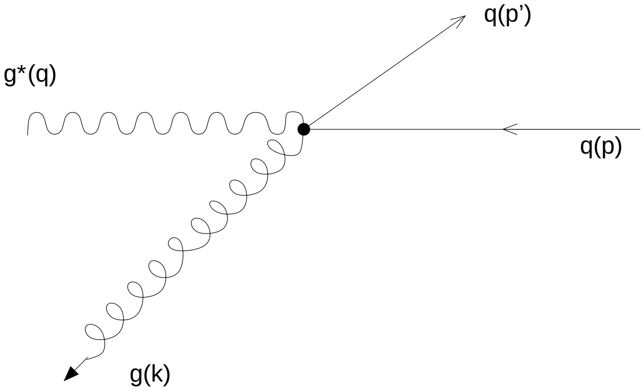

Figure C.2: Kinematics of the gluon emission in the cms

quent scattering of the quark at an angle θ gives rise to the transverse momentum, and changes the longitudinal momentum fraction carried by the quark. The transverse momentum of the quark is $p_T = p' sin\theta$, and the differential cross section is approximated for small θ as

$$\frac{d\sigma}{dp_T^2} = \frac{2\pi}{(p+q)^4} C_F e_q^2 \alpha\alpha_s \frac{1}{(p'-q)^2} \left[(p+q)^2 + \frac{2((p+q)^2+Q)Q^2}{(p+q)^2} \right] \tag{C.5}$$

Two new quantities can be defined for convenience. A variable z, which represents the fraction by which the momentum of the quark is reduced through the gluon emission.

$$z = \frac{Q^2}{2p \cdot q} \tag{C.6}$$

Also, a splitting function $P_{qq}(z)$ is defined as

$$P_{qq}(z) = C_F \frac{1+z^2}{1-z} \tag{C.7}$$

Then, the differential cross section is rewritten as

$$\frac{d\sigma}{dp_T^2} = (\frac{4\pi^2\alpha e_q^2}{(p+q)^2})\frac{\alpha_s}{2\pi}\frac{1}{p_T^2}P_{qq}(z) \tag{C.8}$$

In order to obtain the total cross section, the expression above is integrated over the relevant momentum range, from an imposed infrared cut-off point (λ^2) to the maximum allowed value approximated by Q^2. The resulting parton cross section has a logarithmic dependence on Q^2:

$$\sigma = \frac{4\pi^2\alpha e_q^2}{(p+q)^2}\frac{\alpha_s}{2\pi}P_{qq}(z)\ln(Q^2/\lambda^2) \tag{C.9}$$

The total nucleon cross section σ_n is calculated by considering a nucleon to be a collection of quarks of momentum fraction y, emitting gluons, and reducing their momentum to x, so that $z = y/x$

$$\sigma_n(x,Q^2) = \int_0^1 dz \int_0^1 dy\; q(y)\delta(x-zy)\sigma(z,Q^2) \tag{C.10}$$

Finally, the quark density distribution is deduced:

$$q(x,Q^2) = F_2/x = q(x) + \int_x^1 \frac{dy}{y}q(y)\left[\frac{\alpha_s}{2\pi}P_{qq}(\frac{x}{y})\ln(\frac{Q^2}{\lambda^2})\right] \tag{C.11}$$

A splitting function $P_{qq}(\frac{x}{y})$ may be interpreted as the probability for a quark with momentum fraction y to radiate a gluon, leaving the quark with momentum fraction x. A resulting conclusion is that the gluon emission results in the logarithmic Q^2 dependence of the quark distribution functions. The above equation is rewritten to demonstrate this dependence explicitly:

$$\frac{dq(x,Q^2)}{d\ln Q^2} = \frac{\alpha_s}{2\pi}\int_x^1 \frac{dy}{y} q(y,Q^2)P_{qq}(x/y) \tag{C.12}$$

The resulting equation is one of the Altarelli-Parisi equations for the non-singlet quark distribution. A flavor non-singlet distribution refers to the one which does not mix with gluons, or the valence distribution. For example, $g \to q\bar{q}$ does not change the number of the valence quarks, but the structure functions involve $q + \bar{q}$, and the total number of $q\bar{q}$ pairs increases with Q^2. Such distributions mix with gluons, and are known as flavor singlet distributions. In order to describe them, three additional splitting functions are introduced:

$$\begin{aligned} P_{qg}(z) &= C_F\left[z^2 + (1-z)^2\right] \\ P_{gq}(z) &= \frac{4}{3}\left[\frac{1+(1-z)^2}{z}\right] \\ P_{gg}(z) &= 6\left[\frac{z}{1-z} + \frac{1-z}{z} + z(1-z)\right] \end{aligned} \tag{C.13}$$

Finally, summing over all quark flavors, the flavor singlet Altarelli-Parisi equations are written in the leading order:

$$\begin{aligned} \frac{dq_i(x,Q^2)}{d\ln Q^2} &= \frac{\alpha_s(Q^2)}{2\pi}\int_z^1 \frac{dy}{y}\left[P_{qq}(\frac{x}{y})q_i(y,Q^2) + P_{qg}(\frac{x}{y})g(y,Q^2)\right] \\ \frac{dg(x,Q^2)}{d\ln Q^2} &= \frac{\alpha_s(Q^2)}{2\pi}\int_z^1 \frac{dy}{y}\left[\sum_j P_{gq}(\frac{x}{y})q_j(y,Q^2) + P_{gg}(\frac{x}{y})g(y,Q^2)\right] \end{aligned} \tag{C.14}$$

Appendix D

Data Tables for E=5.6 GeV

Q^2_{bin}	W_{bin}	Q^2	W	g_1^p	Δg_1^p	$\Delta_s g_1^p$
24	22	0.5920E+00	0.1075E+01	0.1955E-01	0.8658E-02	0.9937E-02
24	23	0.5920E+00	0.1125E+01	-0.1757E-01	0.2600E-01	0.4973E-02
24	24	0.5920E+00	0.1175E+01	-0.6024E-01	0.4375E-01	0.5183E-02
24	25	0.5920E+00	0.1225E+01	-0.4669E-01	0.7132E-01	0.8042E-02
24	26	0.5920E+00	0.1275E+01	0.1364E-01	0.5632E-01	0.5685E-02
24	27	0.5920E+00	0.1325E+01	-0.2409E-01	0.4161E-01	0.4560E-02
24	28	0.5920E+00	0.1375E+01	0.1232E+00	0.3937E-01	0.9569E-02
24	29	0.5920E+00	0.1425E+01	0.1131E+00	0.3463E-01	0.8733E-02
24	30	0.5920E+00	0.1475E+01	0.3062E+00	0.4067E-01	0.1438E-01
24	31	0.5920E+00	0.1525E+01	0.3363E+00	0.4728E-01	0.1612E-01
24	32	0.5920E+00	0.1575E+01	0.2502E+00	0.3287E-01	0.1189E-01
24	33	0.5920E+00	0.1625E+01	0.1762E+00	0.3622E-01	0.1148E-01
24	34	0.5920E+00	0.1675E+01	0.2662E+00	0.4620E-01	0.1606E-01
24	35	0.5920E+00	0.1725E+01	0.3066E+00	0.4413E-01	0.1679E-01
24	36	0.5920E+00	0.1775E+01	0.1411E+00	0.3901E-01	0.1228E-01
24	37	0.5920E+00	0.1825E+01	0.1589E+00	0.3832E-01	0.1150E-01
24	38	0.5920E+00	0.1875E+01	0.1024E+00	0.3740E-01	0.1175E-01
24	39	0.5920E+00	0.1925E+01	0.6654E-01	0.3684E-01	0.1044E-01
24	40	0.5920E+00	0.1975E+01	0.6511E-01	0.3568E-01	0.9965E-02
24	41	0.5920E+00	0.2025E+01	0.1498E+00	0.3493E-01	0.1187E-01
24	42	0.5920E+00	0.2075E+01	0.1401E+00	0.3418E-01	0.1252E-01

continued on next page

Q^2_{bin}	W_{bin}	Q^2	W	g_1^p	Δg_1^p	$\Delta_s g_1^p$
24	43	0.5920E+00	0.2125E+01	0.1370E+00	0.3467E-01	0.1276E-01
24	44	0.5920E+00	0.2175E+01	0.2416E+00	0.3572E-01	0.1277E-01
24	45	0.5920E+00	0.2225E+01	0.1221E+00	0.3708E-01	0.1280E-01
24	46	0.5920E+00	0.2275E+01	0.1771E+00	0.3665E-01	0.1280E-01
24	47	0.5920E+00	0.2325E+01	0.1723E+00	0.3809E-01	0.1295E-01
24	48	0.5920E+00	0.2375E+01	0.1551E+00	0.4140E-01	0.1312E-01
24	49	0.5920E+00	0.2425E+01	0.1326E+00	0.4311E-01	0.1328E-01
24	50	0.5920E+00	0.2475E+01	0.1975E+00	0.4204E-01	0.1323E-01
24	51	0.5920E+00	0.2525E+01	0.1256E+00	0.4108E-01	0.1321E-01
24	52	0.5920E+00	0.2575E+01	0.8467E-01	0.4143E-01	0.1332E-01
24	53	0.5920E+00	0.2625E+01	0.2745E+00	0.4379E-01	0.1367E-01
24	54	0.5920E+00	0.2675E+01	0.1822E+00	0.4500E-01	0.1410E-01
24	55	0.5920E+00	0.2725E+01	0.1997E+00	0.4514E-01	0.1417E-01
24	56	0.5920E+00	0.2775E+01	0.1323E+00	0.4548E-01	0.1444E-01
24	57	0.5920E+00	0.2825E+01	0.1884E+00	0.4663E-01	0.1449E-01
24	58	0.5920E+00	0.2875E+01	0.2293E+00	0.4606E-01	0.1488E-01
24	59	0.5920E+00	0.2925E+01	0.1944E+00	0.4640E-01	0.1503E-01
24	60	0.5920E+00	0.2975E+01	0.1497E+00	0.4604E-01	0.1525E-01
24	61	0.5920E+00	0.3025E+01	0.2142E+00	0.4676E-01	0.1555E-01
24	62	0.5920E+00	0.3075E+01	0.1021E+00	0.5439E-01	0.1556E-01
24	63	0.5920E+00	0.3125E+01	0.1923E+00	0.8929E-01	0.1594E-01
25	22	0.7070E+00	0.1075E+01	0.8208E-02	0.3709E-02	0.4120E-02
25	23	0.7070E+00	0.1125E+01	-0.3250E-01	0.1343E-01	0.8984E-02
25	24	0.7070E+00	0.1175E+01	-0.4522E-01	0.2316E-01	0.3934E-02
25	25	0.7070E+00	0.1225E+01	-0.6770E-01	0.3988E-01	0.6584E-02
25	26	0.7070E+00	0.1275E+01	-0.1893E-01	0.2916E-01	0.4483E-02
25	27	0.7070E+00	0.1325E+01	0.3358E-01	0.2502E-01	0.4425E-02
25	28	0.7070E+00	0.1375E+01	0.3796E-01	0.2312E-01	0.5117E-02
25	29	0.7070E+00	0.1425E+01	0.1346E+00	0.2280E-01	0.7922E-02
25	30	0.7070E+00	0.1475E+01	0.1764E+00	0.2912E-01	0.9642E-02
25	31	0.7070E+00	0.1525E+01	0.2482E+00	0.3540E-01	0.1279E-01
25	32	0.7070E+00	0.1575E+01	0.2306E+00	0.2860E-01	0.1050E-01
25	33	0.7070E+00	0.1625E+01	0.1983E+00	0.2928E-01	0.1040E-01
25	34	0.7070E+00	0.1675E+01	0.1947E+00	0.3469E-01	0.1378E-01
25	35	0.7070E+00	0.1725E+01	0.2442E+00	0.3149E-01	0.1530E-01
25	36	0.7070E+00	0.1775E+01	0.1497E+00	0.2844E-01	0.1186E-01
25	37	0.7070E+00	0.1825E+01	0.1295E+00	0.2855E-01	0.1028E-01
25	38	0.7070E+00	0.1875E+01	0.7136E-01	0.3184E-01	0.1070E-01

continued on next page

Q^2_{bin}	W_{bin}	Q^2	W	g_1^p	Δg_1^p	$\Delta_s g_1^p$
25	39	0.7070E+00	0.1925E+01	0.1449E+00	0.3200E-01	0.1061E-01
25	40	0.7070E+00	0.1975E+01	0.1091E+00	0.3304E-01	0.1023E-01
25	41	0.7070E+00	0.2025E+01	0.1428E+00	0.3201E-01	0.1217E-01
25	42	0.7070E+00	0.2075E+01	0.1852E+00	0.3241E-01	0.1350E-01
25	43	0.7070E+00	0.2125E+01	0.1980E+00	0.3170E-01	0.1319E-01
25	44	0.7070E+00	0.2175E+01	0.2008E+00	0.3198E-01	0.1311E-01
25	45	0.7070E+00	0.2225E+01	0.1669E+00	0.3187E-01	0.1293E-01
25	46	0.7070E+00	0.2275E+01	0.1468E+00	0.3275E-01	0.1323E-01
25	47	0.7070E+00	0.2325E+01	0.1970E+00	0.3697E-01	0.1358E-01
25	48	0.7070E+00	0.2375E+01	0.2000E+00	0.4049E-01	0.1423E-01
25	49	0.7070E+00	0.2425E+01	0.8821E-01	0.4178E-01	0.1424E-01
25	50	0.7070E+00	0.2475E+01	0.1320E+00	0.4027E-01	0.1394E-01
25	51	0.7070E+00	0.2525E+01	0.1837E+00	0.3996E-01	0.1409E-01
25	52	0.7070E+00	0.2575E+01	0.1733E+00	0.3957E-01	0.1388E-01
25	53	0.7070E+00	0.2625E+01	0.1708E+00	0.4268E-01	0.1454E-01
25	54	0.7070E+00	0.2675E+01	0.2232E+00	0.4136E-01	0.1461E-01
25	55	0.7070E+00	0.2725E+01	0.1816E+00	0.4480E-01	0.1502E-01
25	56	0.7070E+00	0.2775E+01	0.9216E-01	0.4231E-01	0.1463E-01
25	57	0.7070E+00	0.2825E+01	0.2135E+00	0.4382E-01	0.1520E-01
25	58	0.7070E+00	0.2875E+01	0.1373E+00	0.4171E-01	0.1509E-01
25	59	0.7070E+00	0.2925E+01	0.1088E+00	0.4334E-01	0.1532E-01
25	60	0.7070E+00	0.2975E+01	0.4673E-01	0.4265E-01	0.1529E-01
25	61	0.7070E+00	0.3025E+01	0.1195E+00	0.4727E-01	0.1551E-01
25	62	0.7070E+00	0.3075E+01	0.1682E+00	0.5399E-01	0.1561E-01
25	63	0.7070E+00	0.3125E+01	0.8579E-01	0.1199E+00	0.1570E-01
26	22	0.8440E+00	0.1075E+01	-0.3020E-03	0.2919E-02	0.1532E-03
26	23	0.8440E+00	0.1125E+01	-0.3741E-01	0.1054E-01	0.1037E-01
26	24	0.8440E+00	0.1175E+01	-0.8307E-02	0.1773E-01	0.2635E-02
26	25	0.8440E+00	0.1225E+01	-0.1532E+00	0.2909E-01	0.6786E-02
26	26	0.8440E+00	0.1275E+01	-0.2686E-01	0.2179E-01	0.3816E-02
26	27	0.8440E+00	0.1325E+01	0.5925E-01	0.1881E-01	0.4898E-02
26	28	0.8440E+00	0.1375E+01	0.3777E-01	0.1940E-01	0.4859E-02
26	29	0.8440E+00	0.1425E+01	0.4941E-01	0.1928E-01	0.5472E-02
26	30	0.8440E+00	0.1475E+01	0.1923E+00	0.2548E-01	0.8896E-02
26	31	0.8440E+00	0.1525E+01	0.1737E+00	0.2683E-01	0.1066E-01
26	32	0.8440E+00	0.1575E+01	0.1335E+00	0.2193E-01	0.9244E-02
26	33	0.8440E+00	0.1625E+01	0.1557E+00	0.2315E-01	0.9889E-02
26	34	0.8440E+00	0.1675E+01	0.1340E+00	0.3005E-01	0.1129E-01

continued on next page

Q^2_{bin}	W_{bin}	Q^2	W	g_1^p	Δg_1^p	$\Delta_s g_1^p$
26	35	0.8440E+00	0.1725E+01	0.2357E+00	0.2947E-01	0.1525E-01
26	36	0.8440E+00	0.1775E+01	0.2157E+00	0.2773E-01	0.1527E-01
26	37	0.8440E+00	0.1825E+01	0.1965E+00	0.2818E-01	0.1237E-01
26	38	0.8440E+00	0.1875E+01	0.1167E+00	0.2950E-01	0.1097E-01
26	39	0.8440E+00	0.1925E+01	0.9571E-01	0.3012E-01	0.1045E-01
26	40	0.8440E+00	0.1975E+01	0.1809E+00	0.2958E-01	0.1111E-01
26	41	0.8440E+00	0.2025E+01	0.1867E+00	0.3054E-01	0.1246E-01
26	42	0.8440E+00	0.2075E+01	0.1595E+00	0.3173E-01	0.1356E-01
26	43	0.8440E+00	0.2125E+01	0.1563E+00	0.3239E-01	0.1378E-01
26	44	0.8440E+00	0.2175E+01	0.2223E+00	0.3048E-01	0.1341E-01
26	45	0.8440E+00	0.2225E+01	0.1383E+00	0.2929E-01	0.1314E-01
26	46	0.8440E+00	0.2275E+01	0.1626E+00	0.3219E-01	0.1356E-01
26	47	0.8440E+00	0.2325E+01	0.1826E+00	0.3420E-01	0.1369E-01
26	48	0.8440E+00	0.2375E+01	0.1573E+00	0.3448E-01	0.1377E-01
26	49	0.8440E+00	0.2425E+01	0.2066E+00	0.3412E-01	0.1372E-01
26	50	0.8440E+00	0.2475E+01	0.1307E+00	0.3804E-01	0.1419E-01
26	51	0.8440E+00	0.2525E+01	0.2245E+00	0.3956E-01	0.1467E-01
26	52	0.8440E+00	0.2575E+01	0.1271E+00	0.4024E-01	0.1461E-01
26	53	0.8440E+00	0.2625E+01	0.1758E+00	0.3594E-01	0.1401E-01
26	54	0.8440E+00	0.2675E+01	0.2374E+00	0.3600E-01	0.1422E-01
26	55	0.8440E+00	0.2725E+01	0.2219E+00	0.3583E-01	0.1471E-01
26	56	0.8440E+00	0.2775E+01	0.1747E+00	0.3803E-01	0.1507E-01
26	57	0.8440E+00	0.2825E+01	0.2496E+00	0.4025E-01	0.1552E-01
26	58	0.8440E+00	0.2875E+01	0.1320E+00	0.4050E-01	0.1571E-01
26	59	0.8440E+00	0.2925E+01	0.2421E+00	0.4334E-01	0.1619E-01
26	60	0.8440E+00	0.2975E+01	0.1882E+00	0.4079E-01	0.1589E-01
26	61	0.8440E+00	0.3025E+01	0.1432E+00	0.4378E-01	0.1562E-01
26	62	0.8440E+00	0.3075E+01	0.9905E-01	0.6317E-01	0.1573E-01
26	63	0.8440E+00	0.3125E+01	-0.3642E+00	0.2056E+00	0.1688E-01
27	22	0.1010E+01	0.1075E+01	0.7255E-02	0.2504E-02	0.3609E-02
27	23	0.1010E+01	0.1125E+01	-0.2337E-01	0.9302E-02	0.6469E-02
27	24	0.1010E+01	0.1175E+01	-0.1992E-01	0.1566E-01	0.2238E-02
27	25	0.1010E+01	0.1225E+01	-0.7890E-01	0.2590E-01	0.4116E-02
27	26	0.1010E+01	0.1275E+01	-0.3157E-02	0.1833E-01	0.3054E-02
27	27	0.1010E+01	0.1325E+01	0.3444E-01	0.1605E-01	0.3932E-02
27	28	0.1010E+01	0.1375E+01	0.2565E-01	0.1657E-01	0.4222E-02
27	29	0.1010E+01	0.1425E+01	0.1246E+00	0.1833E-01	0.7707E-02
27	30	0.1010E+01	0.1475E+01	0.1877E+00	0.2361E-01	0.8719E-02

continued on next page

Q^2_{bin}	W_{bin}	Q^2	W	g_1^p	Δg_1^p	$\Delta_s g_1^p$
27	31	0.1010E+01	0.1525E+01	0.1819E+00	0.2605E-01	0.9893E-02
27	32	0.1010E+01	0.1575E+01	0.1381E+00	0.2177E-01	0.9448E-02
27	33	0.1010E+01	0.1625E+01	0.1778E+00	0.2329E-01	0.1142E-01
27	34	0.1010E+01	0.1675E+01	0.1894E+00	0.2839E-01	0.1242E-01
27	35	0.1010E+01	0.1725E+01	0.2231E+00	0.2778E-01	0.1445E-01
27	36	0.1010E+01	0.1775E+01	0.1205E+00	0.2585E-01	0.1195E-01
27	37	0.1010E+01	0.1825E+01	0.1592E+00	0.2645E-01	0.1196E-01
27	38	0.1010E+01	0.1875E+01	0.1824E+00	0.2645E-01	0.1209E-01
27	39	0.1010E+01	0.1925E+01	0.1189E+00	0.2653E-01	0.1026E-01
27	40	0.1010E+01	0.1975E+01	0.1383E+00	0.2757E-01	0.1042E-01
27	41	0.1010E+01	0.2025E+01	0.1291E+00	0.2735E-01	0.1159E-01
27	42	0.1010E+01	0.2075E+01	0.1849E+00	0.2685E-01	0.1284E-01
27	43	0.1010E+01	0.2125E+01	0.1591E+00	0.2614E-01	0.1295E-01
27	44	0.1010E+01	0.2175E+01	0.1638E+00	0.2646E-01	0.1315E-01
27	45	0.1010E+01	0.2225E+01	0.2096E+00	0.2899E-01	0.1352E-01
27	46	0.1010E+01	0.2275E+01	0.2315E+00	0.3357E-01	0.1406E-01
27	47	0.1010E+01	0.2325E+01	0.1400E+00	0.3513E-01	0.1446E-01
27	48	0.1010E+01	0.2375E+01	0.1738E+00	0.3495E-01	0.1454E-01
27	49	0.1010E+01	0.2425E+01	0.1906E+00	0.3665E-01	0.1505E-01
27	50	0.1010E+01	0.2475E+01	0.1522E+00	0.3847E-01	0.1539E-01
27	51	0.1010E+01	0.2525E+01	0.2014E+00	0.3924E-01	0.1567E-01
27	52	0.1010E+01	0.2575E+01	0.2050E+00	0.3482E-01	0.1517E-01
27	53	0.1010E+01	0.2625E+01	0.1655E+00	0.3502E-01	0.1526E-01
27	54	0.1010E+01	0.2675E+01	0.2402E+00	0.3517E-01	0.1547E-01
27	55	0.1010E+01	0.2725E+01	0.1909E+00	0.3466E-01	0.1531E-01
27	56	0.1010E+01	0.2775E+01	0.1856E+00	0.3588E-01	0.1536E-01
27	57	0.1010E+01	0.2825E+01	0.1047E+00	0.3446E-01	0.1547E-01
27	58	0.1010E+01	0.2875E+01	0.1658E+00	0.3471E-01	0.1618E-01
27	59	0.1010E+01	0.2925E+01	0.2298E+00	0.3576E-01	0.1603E-01
27	60	0.1010E+01	0.2975E+01	0.1092E+00	0.3568E-01	0.1581E-01
27	61	0.1010E+01	0.3025E+01	0.4830E-01	0.4442E-01	0.1547E-01
27	62	0.1010E+01	0.3075E+01	0.1723E+00	0.8085E-01	0.1547E-01
28	22	0.1200E+01	0.1075E+01	-0.1608E-02	0.2502E-02	0.8044E-03
28	23	0.1200E+01	0.1125E+01	-0.2723E-01	0.9579E-02	0.7321E-02
28	24	0.1200E+01	0.1175E+01	-0.4049E-01	0.1528E-01	0.2416E-02
28	25	0.1200E+01	0.1225E+01	-0.5668E-01	0.2303E-01	0.2978E-02
28	26	0.1200E+01	0.1275E+01	0.7725E-02	0.1712E-01	0.2614E-02
28	27	0.1200E+01	0.1325E+01	0.4501E-01	0.1426E-01	0.4160E-02

continued on next page

Q^2_{bin}	W_{bin}	Q^2	W	g_1^p	Δg_1^p	$\Delta_s g_1^p$
28	28	0.1200E+01	0.1375E+01	0.4928E-01	0.1525E-01	0.4864E-02
28	29	0.1200E+01	0.1425E+01	0.5709E-01	0.1719E-01	0.5260E-02
28	30	0.1200E+01	0.1475E+01	0.1304E+00	0.2147E-01	0.7822E-02
28	31	0.1200E+01	0.1525E+01	0.2354E+00	0.2349E-01	0.1149E-01
28	32	0.1200E+01	0.1575E+01	0.1466E+00	0.1922E-01	0.1050E-01
28	33	0.1200E+01	0.1625E+01	0.1496E+00	0.2124E-01	0.1100E-01
28	34	0.1200E+01	0.1675E+01	0.2208E+00	0.2518E-01	0.1304E-01
28	35	0.1200E+01	0.1725E+01	0.2294E+00	0.2548E-01	0.1447E-01
28	36	0.1200E+01	0.1775E+01	0.1473E+00	0.2296E-01	0.1349E-01
28	37	0.1200E+01	0.1825E+01	0.1083E+00	0.2337E-01	0.1024E-01
28	38	0.1200E+01	0.1875E+01	0.1282E+00	0.2309E-01	0.1072E-01
28	39	0.1200E+01	0.1925E+01	0.1126E+00	0.2319E-01	0.9958E-02
28	40	0.1200E+01	0.1975E+01	0.2096E+00	0.2372E-01	0.1171E-01
28	41	0.1200E+01	0.2025E+01	0.1420E+00	0.2340E-01	0.1155E-01
28	42	0.1200E+01	0.2075E+01	0.2439E+00	0.2317E-01	0.1318E-01
28	43	0.1200E+01	0.2125E+01	0.2074E+00	0.2349E-01	0.1331E-01
28	44	0.1200E+01	0.2175E+01	0.1626E+00	0.2511E-01	0.1385E-01
28	45	0.1200E+01	0.2225E+01	0.2117E+00	0.2597E-01	0.1349E-01
28	46	0.1200E+01	0.2275E+01	0.1952E+00	0.2614E-01	0.1367E-01
28	47	0.1200E+01	0.2325E+01	0.2016E+00	0.2543E-01	0.1374E-01
28	48	0.1200E+01	0.2375E+01	0.1855E+00	0.2456E-01	0.1390E-01
28	49	0.1200E+01	0.2425E+01	0.1811E+00	0.2329E-01	0.1378E-01
28	50	0.1200E+01	0.2475E+01	0.1451E+00	0.2248E-01	0.1401E-01
28	51	0.1200E+01	0.2525E+01	0.1653E+00	0.2231E-01	0.1417E-01
28	52	0.1200E+01	0.2575E+01	0.1851E+00	0.2257E-01	0.1448E-01
28	53	0.1200E+01	0.2625E+01	0.1940E+00	0.2314E-01	0.1445E-01
28	54	0.1200E+01	0.2675E+01	0.2040E+00	0.2307E-01	0.1484E-01
28	55	0.1200E+01	0.2725E+01	0.1778E+00	0.2273E-01	0.1508E-01
28	56	0.1200E+01	0.2775E+01	0.1521E+00	0.2145E-01	0.1527E-01
28	57	0.1200E+01	0.2825E+01	0.1441E+00	0.2314E-01	0.1572E-01
28	58	0.1200E+01	0.2875E+01	0.1373E+00	0.2321E-01	0.1605E-01
28	59	0.1200E+01	0.2925E+01	0.1328E+00	0.2428E-01	0.1570E-01
28	60	0.1200E+01	0.2975E+01	0.9203E-01	0.2457E-01	0.1536E-01
28	61	0.1200E+01	0.3025E+01	0.1676E+00	0.4356E-01	0.1523E-01
28	62	0.1200E+01	0.3075E+01	-0.1017E-01	0.8704E-01	0.1588E-01
28	63	0.1200E+01	0.3125E+01	0.4547E+00	0.1670E+00	0.1316E-01
29	22	0.1440E+01	0.1075E+01	0.7139E-02	0.2172E-02	0.3608E-02
29	23	0.1440E+01	0.1125E+01	0.1702E-02	0.7012E-02	0.7537E-03

continued on next page

Q^2_{bin}	W_{bin}	Q^2	W	g_1^p	Δg_1^p	$\Delta_s g_1^p$
29	24	0.1440E+01	0.1175E+01	-0.2550E-01	0.1144E-01	0.1550E-02
29	25	0.1440E+01	0.1225E+01	-0.6685E-02	0.1713E-01	0.2217E-02
29	26	0.1440E+01	0.1275E+01	0.3675E-01	0.1341E-01	0.2756E-02
29	27	0.1440E+01	0.1325E+01	0.2917E-01	0.1186E-01	0.3456E-02
29	28	0.1440E+01	0.1375E+01	0.1525E-01	0.1293E-01	0.3652E-02
29	29	0.1440E+01	0.1425E+01	0.7059E-01	0.1302E-01	0.5941E-02
29	30	0.1440E+01	0.1475E+01	0.1349E+00	0.1565E-01	0.8842E-02
29	31	0.1440E+01	0.1525E+01	0.1357E+00	0.1648E-01	0.8959E-02
29	32	0.1440E+01	0.1575E+01	0.1224E+00	0.1450E-01	0.9219E-02
29	33	0.1440E+01	0.1625E+01	0.1203E+00	0.1513E-01	0.9626E-02
29	34	0.1440E+01	0.1675E+01	0.1365E+00	0.1834E-01	0.9538E-02
29	35	0.1440E+01	0.1725E+01	0.1748E+00	0.1798E-01	0.1169E-01
29	36	0.1440E+01	0.1775E+01	0.1449E+00	0.1759E-01	0.1242E-01
29	37	0.1440E+01	0.1825E+01	0.1683E+00	0.1855E-01	0.1266E-01
29	38	0.1440E+01	0.1875E+01	0.9391E-01	0.1834E-01	0.9282E-02
29	39	0.1440E+01	0.1925E+01	0.1136E+00	0.1804E-01	0.9311E-02
29	40	0.1440E+01	0.1975E+01	0.1254E+00	0.1768E-01	0.9329E-02
29	41	0.1440E+01	0.2025E+01	0.1447E+00	0.1782E-01	0.1033E-01
29	42	0.1440E+01	0.2075E+01	0.1413E+00	0.1680E-01	0.1123E-01
29	43	0.1440E+01	0.2125E+01	0.1455E+00	0.1789E-01	0.1168E-01
29	44	0.1440E+01	0.2175E+01	0.1662E+00	0.1963E-01	0.1221E-01
29	45	0.1440E+01	0.2225E+01	0.1787E+00	0.2053E-01	0.1280E-01
29	46	0.1440E+01	0.2275E+01	0.1873E+00	0.1986E-01	0.1298E-01
29	47	0.1440E+01	0.2325E+01	0.1394E+00	0.1985E-01	0.1320E-01
29	48	0.1440E+01	0.2375E+01	0.2012E+00	0.1972E-01	0.1361E-01
29	49	0.1440E+01	0.2425E+01	0.1582E+00	0.1980E-01	0.1384E-01
29	50	0.1440E+01	0.2475E+01	0.1695E+00	0.2073E-01	0.1416E-01
29	51	0.1440E+01	0.2525E+01	0.1584E+00	0.2077E-01	0.1447E-01
29	52	0.1440E+01	0.2575E+01	0.1988E+00	0.2149E-01	0.1529E-01
29	53	0.1440E+01	0.2625E+01	0.1888E+00	0.2226E-01	0.1562E-01
29	54	0.1440E+01	0.2675E+01	0.1905E+00	0.2183E-01	0.1586E-01
29	55	0.1440E+01	0.2725E+01	0.2088E+00	0.2269E-01	0.1561E-01
29	56	0.1440E+01	0.2775E+01	0.1828E+00	0.2158E-01	0.1559E-01
29	57	0.1440E+01	0.2825E+01	0.1841E+00	0.2350E-01	0.1605E-01
29	58	0.1440E+01	0.2875E+01	0.1876E+00	0.2172E-01	0.1586E-01
29	59	0.1440E+01	0.2925E+01	0.1915E+00	0.2698E-01	0.1571E-01
29	60	0.1440E+01	0.2975E+01	0.9095E-01	0.4160E-01	0.1495E-01
29	61	0.1440E+01	0.3025E+01	0.1941E+00	0.1394E+00	0.1314E-01

continued on next page

Q^2_{bin}	W_{bin}	Q^2	W	g_1^p	Δg_1^p	$\Delta_s g_1^p$
29	62	0.1440E+01	0.3075E+01	0.3954E+00	0.1428E+00	0.1225E-01
29	63	0.1440E+01	0.3125E+01	0.3711E+00	0.8640E+00	0.1139E-01
30	22	0.1710E+01	0.1075E+01	0.4693E-02	0.1837E-02	0.2408E-02
30	23	0.1710E+01	0.1125E+01	0.3239E-02	0.6704E-02	0.8096E-03
30	24	0.1710E+01	0.1175E+01	-0.2701E-01	0.1018E-01	0.1279E-02
30	25	0.1710E+01	0.1225E+01	-0.1102E-01	0.1245E-01	0.1676E-02
30	26	0.1710E+01	0.1275E+01	0.1658E-01	0.9345E-02	0.2031E-02
30	27	0.1710E+01	0.1325E+01	0.1763E-01	0.8529E-02	0.2744E-02
30	28	0.1710E+01	0.1375E+01	0.5375E-01	0.1013E-01	0.4785E-02
30	29	0.1710E+01	0.1425E+01	0.4956E-01	0.1077E-01	0.4746E-02
30	30	0.1710E+01	0.1475E+01	0.1099E+00	0.1249E-01	0.8015E-02
30	31	0.1710E+01	0.1525E+01	0.1373E+00	0.1357E-01	0.9206E-02
30	32	0.1710E+01	0.1575E+01	0.8191E-01	0.1209E-01	0.7154E-02
30	33	0.1710E+01	0.1625E+01	0.1046E+00	0.1348E-01	0.8686E-02
30	34	0.1710E+01	0.1675E+01	0.1312E+00	0.1563E-01	0.8868E-02
30	35	0.1710E+01	0.1725E+01	0.1383E+00	0.1481E-01	0.1000E-01
30	36	0.1710E+01	0.1775E+01	0.1518E+00	0.1481E-01	0.1188E-01
30	37	0.1710E+01	0.1825E+01	0.1084E+00	0.1455E-01	0.8983E-02
30	38	0.1710E+01	0.1875E+01	0.1198E+00	0.1476E-01	0.8994E-02
30	39	0.1710E+01	0.1925E+01	0.1277E+00	0.1421E-01	0.8558E-02
30	40	0.1710E+01	0.1975E+01	0.1234E+00	0.1483E-01	0.8696E-02
30	41	0.1710E+01	0.2025E+01	0.1222E+00	0.1444E-01	0.9196E-02
30	42	0.1710E+01	0.2075E+01	0.1327E+00	0.1433E-01	0.1021E-01
30	43	0.1710E+01	0.2125E+01	0.1476E+00	0.1512E-01	0.1062E-01
30	44	0.1710E+01	0.2175E+01	0.1345E+00	0.1555E-01	0.1112E-01
30	45	0.1710E+01	0.2225E+01	0.1549E+00	0.1638E-01	0.1176E-01
30	46	0.1710E+01	0.2275E+01	0.1683E+00	0.1660E-01	0.1217E-01
30	47	0.1710E+01	0.2325E+01	0.1615E+00	0.1794E-01	0.1304E-01
30	48	0.1710E+01	0.2375E+01	0.1815E+00	0.1730E-01	0.1309E-01
30	49	0.1710E+01	0.2425E+01	0.1607E+00	0.1744E-01	0.1353E-01
30	50	0.1710E+01	0.2475E+01	0.1572E+00	0.1691E-01	0.1396E-01
30	51	0.1710E+01	0.2525E+01	0.2193E+00	0.1781E-01	0.1433E-01
30	52	0.1710E+01	0.2575E+01	0.1696E+00	0.1805E-01	0.1439E-01
30	53	0.1710E+01	0.2625E+01	0.1944E+00	0.1871E-01	0.1465E-01
30	54	0.1710E+01	0.2675E+01	0.1738E+00	0.1837E-01	0.1505E-01
30	55	0.1710E+01	0.2725E+01	0.1999E+00	0.1869E-01	0.1507E-01
30	56	0.1710E+01	0.2775E+01	0.1611E+00	0.1840E-01	0.1521E-01
30	57	0.1710E+01	0.2825E+01	0.1676E+00	0.2005E-01	0.1545E-01

continued on next page

Q^2_{bin}	W_{bin}	Q^2	W	g_1^p	Δg_1^p	$\Delta_s g_1^p$
30	58	0.1710E+01	0.2875E+01	0.1079E+00	0.2349E-01	0.1558E-01
30	59	0.1710E+01	0.2925E+01	0.1498E+00	0.4019E-01	0.1617E-01
30	60	0.1710E+01	0.2975E+01	-0.1159E+00	0.6458E-01	0.1096E-01
30	61	0.1710E+01	0.3025E+01	-0.6653E-01	0.1618E+00	0.1117E-01
30	62	0.1710E+01	0.3075E+01	-0.6816E+00	0.7817E+00	0.1052E-01
31	22	0.2050E+01	0.1075E+01	0.1450E-02	0.1034E-02	0.7593E-03
31	23	0.2050E+01	0.1125E+01	-0.1210E-01	0.4862E-02	0.2040E-02
31	24	0.2050E+01	0.1175E+01	-0.5218E-02	0.6761E-02	0.8014E-03
31	25	0.2050E+01	0.1225E+01	0.1093E-01	0.9503E-02	0.1281E-02
31	26	0.2050E+01	0.1275E+01	0.1300E-01	0.7611E-02	0.1751E-02
31	27	0.2050E+01	0.1325E+01	0.2630E-01	0.7439E-02	0.2832E-02
31	28	0.2050E+01	0.1375E+01	0.4355E-01	0.9608E-02	0.4252E-02
31	29	0.2050E+01	0.1425E+01	0.4781E-01	0.9551E-02	0.4451E-02
31	30	0.2050E+01	0.1475E+01	0.8188E-01	0.1091E-01	0.6536E-02
31	31	0.2050E+01	0.1525E+01	0.9928E-01	0.1034E-01	0.7467E-02
31	32	0.2050E+01	0.1575E+01	0.6463E-01	0.9024E-02	0.5796E-02
31	33	0.2050E+01	0.1625E+01	0.7069E-01	0.9758E-02	0.6335E-02
31	34	0.2050E+01	0.1675E+01	0.1261E+00	0.1195E-01	0.8065E-02
31	35	0.2050E+01	0.1725E+01	0.1363E+00	0.1250E-01	0.9432E-02
31	36	0.2050E+01	0.1775E+01	0.1284E+00	0.1180E-01	0.9529E-02
31	37	0.2050E+01	0.1825E+01	0.8806E-01	0.1222E-01	0.7285E-02
31	38	0.2050E+01	0.1875E+01	0.7975E-01	0.1242E-01	0.6790E-02
31	39	0.2050E+01	0.1925E+01	0.8547E-01	0.1292E-01	0.6959E-02
31	40	0.2050E+01	0.1975E+01	0.1317E+00	0.1369E-01	0.7853E-02
31	41	0.2050E+01	0.2025E+01	0.1106E+00	0.1422E-01	0.8467E-02
31	42	0.2050E+01	0.2075E+01	0.1433E+00	0.1414E-01	0.9612E-02
31	43	0.2050E+01	0.2125E+01	0.1542E+00	0.1420E-01	0.1016E-01
31	44	0.2050E+01	0.2175E+01	0.1567E+00	0.1483E-01	0.1082E-01
31	45	0.2050E+01	0.2225E+01	0.1505E+00	0.1545E-01	0.1144E-01
31	46	0.2050E+01	0.2275E+01	0.1562E+00	0.1487E-01	0.1158E-01
31	47	0.2050E+01	0.2325E+01	0.1628E+00	0.1516E-01	0.1196E-01
31	48	0.2050E+01	0.2375E+01	0.1447E+00	0.1512E-01	0.1212E-01
31	49	0.2050E+01	0.2425E+01	0.1942E+00	0.1565E-01	0.1273E-01
31	50	0.2050E+01	0.2475E+01	0.1863E+00	0.1635E-01	0.1337E-01
31	51	0.2050E+01	0.2525E+01	0.1439E+00	0.1614E-01	0.1346E-01
31	52	0.2050E+01	0.2575E+01	0.1787E+00	0.1550E-01	0.1383E-01
31	53	0.2050E+01	0.2625E+01	0.1884E+00	0.1471E-01	0.1397E-01
31	54	0.2050E+01	0.2675E+01	0.1581E+00	0.1500E-01	0.1410E-01

continued on next page

Q^2_{bin}	W_{bin}	Q^2	W	g_1^p	Δg_1^p	$\Delta_s g_1^p$
31	55	0.2050E+01	0.2725E+01	0.1627E+00	0.1672E-01	0.1425E-01
31	56	0.2050E+01	0.2775E+01	0.1485E+00	0.1962E-01	0.1434E-01
31	57	0.2050E+01	0.2825E+01	0.1666E+00	0.2768E-01	0.1423E-01
31	58	0.2050E+01	0.2875E+01	0.5293E-01	0.4061E-01	0.1033E-01
31	59	0.2050E+01	0.2925E+01	0.7498E-01	0.7299E-01	0.1054E-01
31	60	0.2050E+01	0.2975E+01	0.2394E+00	0.2018E+00	0.1042E-01
32	22	0.2440E+01	0.1075E+01	0.1053E-02	0.1093E-02	0.5642E-03
32	23	0.2440E+01	0.1125E+01	-0.3455E-02	0.4640E-02	0.1097E-02
32	24	0.2440E+01	0.1175E+01	-0.4696E-03	0.5958E-02	0.6366E-03
32	25	0.2440E+01	0.1225E+01	-0.1855E-01	0.7628E-02	0.1416E-02
32	26	0.2440E+01	0.1275E+01	0.8334E-02	0.5952E-02	0.1563E-02
32	27	0.2440E+01	0.1325E+01	0.2029E-01	0.6521E-02	0.2536E-02
32	28	0.2440E+01	0.1375E+01	0.2245E-01	0.6922E-02	0.2799E-02
32	29	0.2440E+01	0.1425E+01	0.3930E-01	0.7410E-02	0.3738E-02
32	30	0.2440E+01	0.1475E+01	0.4852E-01	0.8190E-02	0.4405E-02
32	31	0.2440E+01	0.1525E+01	0.7028E-01	0.8834E-02	0.5599E-02
32	32	0.2440E+01	0.1575E+01	0.6563E-01	0.8194E-02	0.5288E-02
32	33	0.2440E+01	0.1625E+01	0.6741E-01	0.8583E-02	0.5577E-02
32	34	0.2440E+01	0.1675E+01	0.8568E-01	0.9513E-02	0.6002E-02
32	35	0.2440E+01	0.1725E+01	0.9727E-01	0.9805E-02	0.7226E-02
32	36	0.2440E+01	0.1775E+01	0.8309E-01	0.9279E-02	0.6403E-02
32	37	0.2440E+01	0.1825E+01	0.7658E-01	0.9439E-02	0.5965E-02
32	38	0.2440E+01	0.1875E+01	0.7981E-01	0.1003E-01	0.5809E-02
32	39	0.2440E+01	0.1925E+01	0.7794E-01	0.1093E-01	0.5772E-02
32	40	0.2440E+01	0.1975E+01	0.8807E-01	0.1121E-01	0.6198E-02
32	41	0.2440E+01	0.2025E+01	0.9171E-01	0.1082E-01	0.6829E-02
32	42	0.2440E+01	0.2075E+01	0.1253E+00	0.1142E-01	0.7934E-02
32	43	0.2440E+01	0.2125E+01	0.1330E+00	0.1181E-01	0.8585E-02
32	44	0.2440E+01	0.2175E+01	0.1276E+00	0.1290E-01	0.9530E-02
32	45	0.2440E+01	0.2225E+01	0.1502E+00	0.1289E-01	0.9932E-02
32	46	0.2440E+01	0.2275E+01	0.1377E+00	0.1315E-01	0.1035E-01
32	47	0.2440E+01	0.2325E+01	0.1521E+00	0.1286E-01	0.1079E-01
32	48	0.2440E+01	0.2375E+01	0.1347E+00	0.1222E-01	0.1073E-01
32	49	0.2440E+01	0.2425E+01	0.1365E+00	0.1257E-01	0.1129E-01
32	50	0.2440E+01	0.2475E+01	0.1349E+00	0.1179E-01	0.1134E-01
32	51	0.2440E+01	0.2525E+01	0.1523E+00	0.1235E-01	0.1180E-01
32	52	0.2440E+01	0.2575E+01	0.1332E+00	0.1291E-01	0.1204E-01
32	53	0.2440E+01	0.2625E+01	0.1658E+00	0.1536E-01	0.1263E-01

continued on next page

Q^2_{bin}	W_{bin}	Q^2	W	g_1^p	Δg_1^p	$\Delta_s g_1^p$
32	54	0.2440E+01	0.2675E+01	0.1501E+00	0.1734E-01	0.1290E-01
32	55	0.2440E+01	0.2725E+01	0.1500E+00	0.2114E-01	0.1411E-01
32	56	0.2440E+01	0.2775E+01	0.8343E-01	0.2804E-01	0.9290E-02
32	57	0.2440E+01	0.2825E+01	0.1320E+00	0.4939E-01	0.9476E-02
32	58	0.2440E+01	0.2875E+01	-0.1410E+00	0.1702E+00	0.9677E-02
32	59	0.2440E+01	0.2925E+01	-0.8171E+00	0.1128E+01	0.9315E-02
33	22	0.2920E+01	0.1075E+01	0.1155E-02	0.7197E-03	0.6319E-03
33	23	0.2920E+01	0.1125E+01	-0.2812E-02	0.2909E-02	0.1100E-02
33	24	0.2920E+01	0.1175E+01	-0.3543E-02	0.4746E-02	0.7388E-03
33	25	0.2920E+01	0.1225E+01	-0.4580E-02	0.6915E-02	0.8856E-03
33	26	0.2920E+01	0.1275E+01	-0.6165E-02	0.4628E-02	0.1303E-02
33	27	0.2920E+01	0.1325E+01	0.8103E-02	0.4225E-02	0.1611E-02
33	28	0.2920E+01	0.1375E+01	0.1369E-01	0.4309E-02	0.1994E-02
33	29	0.2920E+01	0.1425E+01	0.1661E-01	0.4750E-02	0.2197E-02
33	30	0.2920E+01	0.1475E+01	0.3817E-01	0.6167E-02	0.3631E-02
33	31	0.2920E+01	0.1525E+01	0.4730E-01	0.7462E-02	0.4078E-02
33	32	0.2920E+01	0.1575E+01	0.4775E-01	0.7108E-02	0.3915E-02
33	33	0.2920E+01	0.1625E+01	0.4985E-01	0.7221E-02	0.4151E-02
33	34	0.2920E+01	0.1675E+01	0.6886E-01	0.7724E-02	0.4912E-02
33	35	0.2920E+01	0.1725E+01	0.7572E-01	0.7961E-02	0.5777E-02
33	36	0.2920E+01	0.1775E+01	0.7228E-01	0.7878E-02	0.4942E-02
33	37	0.2920E+01	0.1825E+01	0.7064E-01	0.8472E-02	0.4864E-02
33	38	0.2920E+01	0.1875E+01	0.8527E-01	0.9232E-02	0.5095E-02
33	39	0.2920E+01	0.1925E+01	0.8404E-01	0.9967E-02	0.5060E-02
33	40	0.2920E+01	0.1975E+01	0.7580E-01	0.9946E-02	0.5352E-02
33	41	0.2920E+01	0.2025E+01	0.8881E-01	0.9873E-02	0.6081E-02
33	42	0.2920E+01	0.2075E+01	0.1126E+00	0.9851E-02	0.6897E-02
33	43	0.2920E+01	0.2125E+01	0.9017E-01	0.9852E-02	0.7228E-02
33	44	0.2920E+01	0.2175E+01	0.1123E+00	0.9980E-02	0.7812E-02
33	45	0.2920E+01	0.2225E+01	0.9808E-01	0.9590E-02	0.7924E-02
33	46	0.2920E+01	0.2275E+01	0.1116E+00	0.1022E-01	0.8609E-02
33	47	0.2920E+01	0.2325E+01	0.1370E+00	0.1062E-01	0.9149E-02
33	48	0.2920E+01	0.2375E+01	0.1205E+00	0.1180E-01	0.1011E-01
33	49	0.2920E+01	0.2425E+01	0.1440E+00	0.1260E-01	0.1040E-01
33	50	0.2920E+01	0.2475E+01	0.1310E+00	0.1414E-01	0.1139E-01
33	51	0.2920E+01	0.2525E+01	0.1183E+00	0.1626E-01	0.1069E-01
33	52	0.2920E+01	0.2575E+01	0.1568E+00	0.1835E-01	0.1125E-01
33	53	0.2920E+01	0.2625E+01	0.2377E+00	0.2485E-01	0.8229E-02

continued on next page

Q^2_{bin}	W_{bin}	Q^2	W	g_1^p	Δg_1^p	$\Delta_s g_1^p$
33	54	0.2920E+01	0.2675E+01	0.1358E+00	0.3289E-01	0.8405E-02
33	55	0.2920E+01	0.2725E+01	0.1143E+00	0.8511E-01	0.9199E-02
33	56	0.2920E+01	0.2775E+01	0.6365E+00	0.6388E+00	0.8195E-02
34	22	0.3480E+01	0.1075E+01	-0.3754E-03	0.1031E-02	0.2088E-03
34	23	0.3480E+01	0.1125E+01	0.3006E-02	0.4972E-02	0.7734E-03
34	24	0.3480E+01	0.1175E+01	-0.8090E-02	0.4497E-02	0.8746E-03
34	25	0.3480E+01	0.1225E+01	0.8998E-03	0.7032E-02	0.7157E-03
34	26	0.3480E+01	0.1275E+01	0.7713E-02	0.4986E-02	0.1072E-02
34	27	0.3480E+01	0.1325E+01	0.8551E-02	0.6089E-02	0.1432E-02
34	28	0.3480E+01	0.1375E+01	0.7655E-02	0.6061E-02	0.1511E-02
34	29	0.3480E+01	0.1425E+01	0.3127E-01	0.6216E-02	0.2762E-02
34	30	0.3480E+01	0.1475E+01	0.4134E-01	0.6448E-02	0.4618E-02
34	31	0.3480E+01	0.1525E+01	0.3087E-01	0.7924E-02	0.3241E-02
34	32	0.3480E+01	0.1575E+01	0.2843E-01	0.7224E-02	0.2757E-02
34	33	0.3480E+01	0.1625E+01	0.3521E-01	0.7736E-02	0.3157E-02
34	34	0.3480E+01	0.1675E+01	0.3697E-01	0.8463E-02	0.3569E-02
34	35	0.3480E+01	0.1725E+01	0.5537E-01	0.9240E-02	0.4888E-02
34	36	0.3480E+01	0.1775E+01	0.6073E-01	0.9484E-02	0.4064E-02
34	37	0.3480E+01	0.1825E+01	0.5139E-01	0.9182E-02	0.3775E-02
34	38	0.3480E+01	0.1875E+01	0.7348E-01	0.1010E-01	0.4304E-02
34	39	0.3480E+01	0.1925E+01	0.4526E-01	0.1023E-01	0.3960E-02
34	40	0.3480E+01	0.1975E+01	0.5682E-01	0.1084E-01	0.4433E-02
34	41	0.3480E+01	0.2025E+01	0.7706E-01	0.1024E-01	0.4890E-02
34	42	0.3480E+01	0.2075E+01	0.8830E-01	0.9942E-02	0.5367E-02
34	43	0.3480E+01	0.2125E+01	0.7681E-01	0.9857E-02	0.5740E-02
34	44	0.3480E+01	0.2175E+01	0.7837E-01	0.1047E-01	0.6314E-02
34	45	0.3480E+01	0.2225E+01	0.1049E+00	0.1124E-01	0.6892E-02
34	46	0.3480E+01	0.2275E+01	0.9844E-01	0.1179E-01	0.7346E-02
34	47	0.3480E+01	0.2325E+01	0.1156E+00	0.1278E-01	0.7960E-02
34	48	0.3480E+01	0.2375E+01	0.1086E+00	0.1461E-01	0.8832E-02
34	49	0.3480E+01	0.2425E+01	0.1204E+00	0.1741E-01	0.9667E-02
34	50	0.3480E+01	0.2475E+01	0.1097E+00	0.1956E-01	0.9775E-02
34	51	0.3480E+01	0.2525E+01	0.5341E-01	0.2704E-01	0.9913E-02
34	52	0.3480E+01	0.2575E+01	0.1580E+00	0.4773E-01	0.1002E-01
34	53	0.3480E+01	0.2625E+01	-0.5290E-01	0.2316E+00	0.6576E-02
35	22	0.4160E+01	0.1075E+01	0.1328E-02	0.5832E-03	0.7425E-03
35	23	0.4160E+01	0.1125E+01	-0.4155E-04	0.2998E-02	0.2130E-03
35	24	0.4160E+01	0.1175E+01	-0.3415E-02	0.5265E-02	0.5820E-03

continued on next page

Q^2_{bin}	W_{bin}	Q^2	W	g_1^p	Δg_1^p	$\Delta_s g_1^p$
35	25	0.4160E+01	0.1225E+01	0.2978E-02	0.3578E-02	0.7598E-03
35	26	0.4160E+01	0.1275E+01	0.4658E-02	0.3665E-02	0.8609E-03
35	27	0.4160E+01	0.1325E+01	0.6240E-02	0.3215E-02	0.9525E-03
35	28	0.4160E+01	0.1375E+01	0.2158E-01	0.4893E-02	0.2084E-02
35	29	0.4160E+01	0.1425E+01	0.1008E-01	0.5463E-02	0.1559E-02
35	30	0.4160E+01	0.1475E+01	0.3709E-01	0.7263E-02	0.5684E-02
35	31	0.4160E+01	0.1525E+01	0.2185E-01	0.6453E-02	0.2860E-02
35	32	0.4160E+01	0.1575E+01	0.2611E-01	0.5614E-02	0.2580E-02
35	33	0.4160E+01	0.1625E+01	0.2520E-01	0.6089E-02	0.2587E-02
35	34	0.4160E+01	0.1675E+01	0.5363E-01	0.8562E-02	0.4653E-02
35	35	0.4160E+01	0.1725E+01	0.5782E-01	0.9942E-02	0.5628E-02
35	36	0.4160E+01	0.1775E+01	0.6217E-01	0.9137E-02	0.4351E-02
35	37	0.4160E+01	0.1825E+01	0.5263E-01	0.8493E-02	0.3640E-02
35	38	0.4160E+01	0.1875E+01	0.4521E-01	0.7629E-02	0.3244E-02
35	39	0.4160E+01	0.1925E+01	0.4867E-01	0.8328E-02	0.3330E-02
35	40	0.4160E+01	0.1975E+01	0.3230E-01	0.8812E-02	0.3428E-02
35	41	0.4160E+01	0.2025E+01	0.5494E-01	0.1033E-01	0.4326E-02
35	42	0.4160E+01	0.2075E+01	0.8652E-01	0.1045E-01	0.4869E-02
35	43	0.4160E+01	0.2125E+01	0.9264E-01	0.1095E-01	0.5294E-02
35	44	0.4160E+01	0.2175E+01	0.5680E-01	0.1161E-01	0.5630E-02
35	45	0.4160E+01	0.2225E+01	0.6929E-01	0.1264E-01	0.5821E-02
35	46	0.4160E+01	0.2275E+01	0.8567E-01	0.1486E-01	0.5902E-02
35	47	0.4160E+01	0.2325E+01	0.8350E-01	0.2185E-01	0.6624E-02
35	48	0.4160E+01	0.2375E+01	0.7997E-01	0.4234E-01	0.7860E-02
35	49	0.4160E+01	0.2425E+01	-0.2102E+00	0.1184E+00	0.4781E-02

Appendix E

Data Tables for E=1.6 GeV

Q^2_{bin}	W_{bin}	Q^2	W	g_1^p	Δg_1^p	$\Delta_s g_1^p$
10	55	0.4960E-01	0.1090E+01	-0.1139E+00	0.1572E+00	0.2432E-01
10	56	0.4960E-01	0.1110E+01	0.2588E+00	0.1613E+00	0.5580E-01
10	57	0.4960E-01	0.1130E+01	-0.1892E-01	0.1058E+00	0.1115E-01
10	58	0.4960E-01	0.1150E+01	-0.1665E+00	0.1104E+00	0.3987E-01
10	59	0.4960E-01	0.1170E+01	-0.1540E+00	0.1122E+00	0.4111E-01
10	60	0.4960E-01	0.1190E+01	-0.2117E+00	0.1258E+00	0.6562E-01
10	61	0.4960E-01	0.1210E+01	-0.4109E+00	0.1333E+00	0.9253E-01
10	62	0.4960E-01	0.1230E+01	-0.2517E+00	0.1345E+00	0.9280E-01
10	63	0.4960E-01	0.1250E+01	-0.3681E+00	0.1255E+00	0.8658E-01
10	64	0.4960E-01	0.1270E+01	-0.1040E+00	0.1201E+00	0.6643E-01
10	65	0.4960E-01	0.1290E+01	0.1058E+00	0.1110E+00	0.5193E-01
10	66	0.4960E-01	0.1310E+01	-0.2031E+00	0.1052E+00	0.4446E-01
10	67	0.4960E-01	0.1330E+01	-0.1053E+00	0.9615E-01	0.3121E-01
10	68	0.4960E-01	0.1350E+01	-0.9391E-01	0.9497E-01	0.2264E-01
10	69	0.4960E-01	0.1370E+01	-0.1083E+00	0.9236E-01	0.1713E-01
10	70	0.4960E-01	0.1390E+01	-0.1249E+00	0.9504E-01	0.1555E-01
10	71	0.4960E-01	0.1410E+01	-0.2235E+00	0.9560E-01	0.2089E-01
10	72	0.4960E-01	0.1430E+01	-0.1233E+00	0.9928E-01	0.1479E-01
10	73	0.4960E-01	0.1450E+01	-0.1641E-01	0.9931E-01	0.1304E-01
10	74	0.4960E-01	0.1470E+01	0.7723E-02	0.1027E+00	0.1655E-01
10	75	0.4960E-01	0.1490E+01	0.1099E+00	0.1108E+00	0.2371E-01

continued on next page

Q^2_{bin}	W_{bin}	Q^2	W	g_1^p	Δg_1^p	$\Delta_s g_1^p$
10	76	0.4960E-01	0.1510E+01	-0.3747E+00	0.1148E+00	0.3499E-01
10	77	0.4960E-01	0.1530E+01	-0.7177E-01	0.1044E+00	0.2016E-01
10	78	0.4960E-01	0.1550E+01	-0.1585E+00	0.9986E-01	0.1748E-01
10	79	0.4960E-01	0.1570E+01	0.8470E-01	0.1007E+00	0.1357E-01
10	80	0.4960E-01	0.1590E+01	-0.4199E-01	0.1036E+00	0.1197E-01
10	81	0.4960E-01	0.1610E+01	-0.6029E-01	0.1086E+00	0.1275E-01
10	82	0.4960E-01	0.1630E+01	-0.1493E+00	0.1178E+00	0.1871E-01
10	83	0.4960E-01	0.1650E+01	-0.3284E+00	0.1274E+00	0.2947E-01
10	84	0.4960E-01	0.1670E+01	0.3142E-01	0.7446E-01	0.1871E-01
10	85	0.4960E-01	0.1690E+01	-0.1275E+00	0.7269E-01	0.2697E-01
10	86	0.4960E-01	0.1710E+01	0.1680E-02	0.8413E-01	0.2684E-01
11	55	0.5920E-01	0.1090E+01	-0.9693E-01	0.5380E-01	0.2108E-01
11	56	0.5920E-01	0.1110E+01	-0.7590E-02	0.5507E-01	0.5048E-02
11	57	0.5920E-01	0.1130E+01	0.6723E-01	0.5554E-01	0.1833E-01
11	58	0.5920E-01	0.1150E+01	-0.4505E-01	0.6144E-01	0.2208E-01
11	59	0.5920E-01	0.1170E+01	-0.1747E+00	0.6944E-01	0.3824E-01
11	60	0.5920E-01	0.1190E+01	-0.2164E+00	0.8255E-01	0.5732E-01
11	61	0.5920E-01	0.1210E+01	-0.3320E+00	0.9592E-01	0.7932E-01
11	62	0.5920E-01	0.1230E+01	-0.3504E+00	0.9732E-01	0.7966E-01
11	63	0.5920E-01	0.1250E+01	-0.9632E-01	0.9745E-01	0.4813E-01
11	64	0.5920E-01	0.1270E+01	-0.3029E+00	0.9721E-01	0.4011E-01
11	65	0.5920E-01	0.1290E+01	-0.6997E-01	0.1012E+00	0.2247E-01
11	66	0.5920E-01	0.1310E+01	-0.5593E-02	0.9771E-01	0.1851E-01
11	67	0.5920E-01	0.1330E+01	0.3890E-01	0.9215E-01	0.1658E-01
11	68	0.5920E-01	0.1350E+01	0.1353E-01	0.8987E-01	0.1503E-01
11	69	0.5920E-01	0.1370E+01	0.2040E-01	0.9057E-01	0.1394E-01
11	70	0.5920E-01	0.1390E+01	-0.1772E-01	0.9036E-01	0.1294E-01
11	71	0.5920E-01	0.1410E+01	0.6533E-01	0.9114E-01	0.1320E-01
11	72	0.5920E-01	0.1430E+01	-0.8243E-01	0.8758E-01	0.1346E-01
11	73	0.5920E-01	0.1450E+01	-0.1395E+00	0.8929E-01	0.1588E-01
11	74	0.5920E-01	0.1470E+01	-0.2852E-02	0.9228E-01	0.1552E-01
11	75	0.5920E-01	0.1490E+01	-0.1008E+00	0.1015E+00	0.2198E-01
11	76	0.5920E-01	0.1510E+01	-0.1619E+00	0.1074E+00	0.2465E-01
11	77	0.5920E-01	0.1530E+01	-0.5332E-01	0.1059E+00	0.1867E-01
11	78	0.5920E-01	0.1550E+01	-0.1818E+00	0.1026E+00	0.1731E-01
11	79	0.5920E-01	0.1570E+01	-0.1894E+00	0.1002E+00	0.1677E-01
11	80	0.5920E-01	0.1590E+01	0.1072E+00	0.1046E+00	0.1397E-01
11	81	0.5920E-01	0.1610E+01	-0.9167E-01	0.1062E+00	0.1437E-01

continued on next page

Q^2_{bin}	W_{bin}	Q^2	W	g_1^p	Δg_1^p	$\Delta_s g_1^p$
11	82	0.5920E-01	0.1630E+01	-0.5281E-01	0.1031E+00	0.1393E-01
11	83	0.5920E-01	0.1650E+01	-0.2763E+00	0.1089E+00	0.2575E-01
11	84	0.5920E-01	0.1670E+01	-0.7038E-01	0.7001E-01	0.1771E-01
11	85	0.5920E-01	0.1690E+01	-0.3323E-02	0.6997E-01	0.2442E-01
11	86	0.5920E-01	0.1710E+01	0.1071E+00	0.8366E-01	0.2364E-01
12	55	0.7070E-01	0.1090E+01	-0.5137E-02	0.4268E-01	0.2430E-02
12	56	0.7070E-01	0.1110E+01	0.1437E-01	0.4523E-01	0.6229E-02
12	57	0.7070E-01	0.1130E+01	-0.7614E-01	0.5314E-01	0.1850E-01
12	58	0.7070E-01	0.1150E+01	0.5234E-01	0.6452E-01	0.1594E-01
12	59	0.7070E-01	0.1170E+01	-0.2008E+00	0.7457E-01	0.2382E-01
12	60	0.7070E-01	0.1190E+01	-0.3475E+00	0.8626E-01	0.3504E-01
12	61	0.7070E-01	0.1210E+01	-0.6589E+00	0.9345E-01	0.6520E-01
12	62	0.7070E-01	0.1230E+01	-0.5952E+00	0.9961E-01	0.6483E-01
12	63	0.7070E-01	0.1250E+01	-0.2949E+00	0.9242E-01	0.4277E-01
12	64	0.7070E-01	0.1270E+01	-0.1409E+00	0.9125E-01	0.3070E-01
12	65	0.7070E-01	0.1290E+01	-0.1072E+00	0.8804E-01	0.2562E-01
12	66	0.7070E-01	0.1310E+01	-0.1009E+00	0.8605E-01	0.2207E-01
12	67	0.7070E-01	0.1330E+01	-0.4368E-01	0.8045E-01	0.1850E-01
12	68	0.7070E-01	0.1350E+01	-0.2346E-02	0.7936E-01	0.1670E-01
12	69	0.7070E-01	0.1370E+01	0.2853E-01	0.8064E-01	0.1550E-01
12	70	0.7070E-01	0.1390E+01	-0.1642E+00	0.7860E-01	0.1820E-01
12	71	0.7070E-01	0.1410E+01	0.1359E+00	0.7653E-01	0.1641E-01
12	72	0.7070E-01	0.1430E+01	-0.1224E+00	0.7735E-01	0.1527E-01
12	73	0.7070E-01	0.1450E+01	-0.8213E-02	0.8032E-01	0.1366E-01
12	74	0.7070E-01	0.1470E+01	-0.1628E+00	0.8592E-01	0.1808E-01
12	75	0.7070E-01	0.1490E+01	0.1790E-01	0.9304E-01	0.1884E-01
12	76	0.7070E-01	0.1510E+01	-0.2231E-01	0.1016E+00	0.2027E-01
12	77	0.7070E-01	0.1530E+01	0.6033E-01	0.9847E-01	0.1730E-01
12	78	0.7070E-01	0.1550E+01	0.1082E+00	0.9140E-01	0.1500E-01
12	79	0.7070E-01	0.1570E+01	0.2113E-02	0.9369E-01	0.1287E-01
12	80	0.7070E-01	0.1590E+01	-0.1337E+00	0.8980E-01	0.1520E-01
12	81	0.7070E-01	0.1610E+01	-0.2158E+00	0.9505E-01	0.2110E-01
12	82	0.7070E-01	0.1630E+01	-0.1260E-02	0.9619E-01	0.1368E-01
12	83	0.7070E-01	0.1650E+01	-0.1364E+00	0.1177E+00	0.1793E-01
12	84	0.7070E-01	0.1670E+01	-0.7658E-01	0.6955E-01	0.1761E-01
12	85	0.7070E-01	0.1690E+01	-0.5643E-01	0.6953E-01	0.2287E-01
12	86	0.7070E-01	0.1710E+01	0.1544E+00	0.1005E+00	0.2204E-01
13	55	0.8440E-01	0.1090E+01	-0.7464E-01	0.4721E-01	0.1653E-01

continued on next page

Q^2_{bin}	W_{bin}	Q^2	W	g_1^p	Δg_1^p	$\Delta_s g_1^p$
13	56	0.8440E-01	0.1110E+01	-0.4625E-02	0.4971E-01	0.5107E-02
13	57	0.8440E-01	0.1130E+01	0.2482E-01	0.5062E-01	0.1003E-01
13	58	0.8440E-01	0.1150E+01	-0.1164E+00	0.5452E-01	0.2637E-01
13	59	0.8440E-01	0.1170E+01	-0.2132E+00	0.5981E-01	0.2469E-01
13	60	0.8440E-01	0.1190E+01	-0.2278E+00	0.6812E-01	0.2930E-01
13	61	0.8440E-01	0.1210E+01	-0.4600E+00	0.7979E-01	0.4982E-01
13	62	0.8440E-01	0.1230E+01	-0.3839E+00	0.8643E-01	0.4836E-01
13	63	0.8440E-01	0.1250E+01	-0.3501E+00	0.8099E-01	0.4690E-01
13	64	0.8440E-01	0.1270E+01	-0.1528E+00	0.7789E-01	0.3152E-01
13	65	0.8440E-01	0.1290E+01	-0.1995E+00	0.7553E-01	0.3010E-01
13	66	0.8440E-01	0.1310E+01	-0.8796E-01	0.7526E-01	0.2319E-01
13	67	0.8440E-01	0.1330E+01	-0.6557E-01	0.7499E-01	0.2049E-01
13	68	0.8440E-01	0.1350E+01	-0.6620E-01	0.7316E-01	0.1857E-01
13	69	0.8440E-01	0.1370E+01	0.1537E-02	0.7018E-01	0.1665E-01
13	70	0.8440E-01	0.1390E+01	-0.7352E-02	0.6800E-01	0.1559E-01
13	71	0.8440E-01	0.1410E+01	0.3735E-01	0.6891E-01	0.1503E-01
13	72	0.8440E-01	0.1430E+01	-0.7903E-01	0.7019E-01	0.1502E-01
13	73	0.8440E-01	0.1450E+01	-0.2963E-01	0.7519E-01	0.1444E-01
13	74	0.8440E-01	0.1470E+01	-0.2350E+00	0.7837E-01	0.1948E-01
13	75	0.8440E-01	0.1490E+01	-0.1496E+00	0.8498E-01	0.1968E-01
13	76	0.8440E-01	0.1510E+01	-0.1591E+00	0.9075E-01	0.2055E-01
13	77	0.8440E-01	0.1530E+01	-0.4419E-01	0.8972E-01	0.1688E-01
13	78	0.8440E-01	0.1550E+01	0.8339E-01	0.8873E-01	0.1517E-01
13	79	0.8440E-01	0.1570E+01	0.1578E+00	0.8588E-01	0.1566E-01
13	80	0.8440E-01	0.1590E+01	-0.3342E-01	0.8557E-01	0.1351E-01
13	81	0.8440E-01	0.1610E+01	0.1080E+00	0.8832E-01	0.1584E-01
13	82	0.8440E-01	0.1630E+01	-0.2062E-01	0.9371E-01	0.1457E-01
13	83	0.8440E-01	0.1650E+01	0.2266E-01	0.1017E+00	0.1539E-01
13	84	0.8440E-01	0.1670E+01	-0.1647E-01	0.6025E-01	0.1730E-01
13	85	0.8440E-01	0.1690E+01	-0.1397E-01	0.6150E-01	0.2081E-01
13	86	0.8440E-01	0.1710E+01	-0.7468E-02	0.1317E+00	0.2022E-01
14	55	0.1010E+00	0.1090E+01	0.2791E-02	0.3949E-01	0.2464E-02
14	56	0.1010E+00	0.1110E+01	-0.6051E-02	0.3919E-01	0.5301E-02
14	57	0.1010E+00	0.1130E+01	-0.1882E-01	0.4129E-01	0.9103E-02
14	58	0.1010E+00	0.1150E+01	-0.6349E-01	0.4500E-01	0.1767E-01
14	59	0.1010E+00	0.1170E+01	-0.8070E-01	0.5325E-01	0.1864E-01
14	60	0.1010E+00	0.1190E+01	-0.3101E+00	0.6229E-01	0.3126E-01
14	61	0.1010E+00	0.1210E+01	-0.2615E+00	0.7415E-01	0.3782E-01

continued on next page

Q^2_{bin}	W_{bin}	Q^2	W	g_1^p	Δg_1^p	$\Delta_s g_1^p$
14	62	0.1010E+00	0.1230E+01	-0.4204E+00	0.7553E-01	0.5041E-01
14	63	0.1010E+00	0.1250E+01	-0.2922E+00	0.7206E-01	0.4260E-01
14	64	0.1010E+00	0.1270E+01	-0.2542E+00	0.6808E-01	0.3744E-01
14	65	0.1010E+00	0.1290E+01	-0.1050E+00	0.6310E-01	0.2688E-01
14	66	0.1010E+00	0.1310E+01	-0.4217E-01	0.6524E-01	0.2354E-01
14	67	0.1010E+00	0.1330E+01	0.4800E-01	0.6287E-01	0.2168E-01
14	68	0.1010E+00	0.1350E+01	-0.3391E-01	0.6384E-01	0.1982E-01
14	69	0.1010E+00	0.1370E+01	-0.1657E+00	0.6185E-01	0.2070E-01
14	70	0.1010E+00	0.1390E+01	0.4808E-01	0.6357E-01	0.1745E-01
14	71	0.1010E+00	0.1410E+01	0.4631E-01	0.6369E-01	0.1660E-01
14	72	0.1010E+00	0.1430E+01	-0.6777E-02	0.6411E-01	0.1586E-01
14	73	0.1010E+00	0.1450E+01	0.1140E+00	0.6664E-01	0.1650E-01
14	74	0.1010E+00	0.1470E+01	-0.2569E-01	0.7503E-01	0.1613E-01
14	75	0.1010E+00	0.1490E+01	0.2683E+00	0.8632E-01	0.2367E-01
14	76	0.1010E+00	0.1510E+01	0.1832E+00	0.9047E-01	0.2143E-01
14	77	0.1010E+00	0.1530E+01	-0.8215E-01	0.8475E-01	0.1754E-01
14	78	0.1010E+00	0.1550E+01	0.6710E-01	0.7961E-01	0.1583E-01
14	79	0.1010E+00	0.1570E+01	0.1625E+00	0.7721E-01	0.1645E-01
14	80	0.1010E+00	0.1590E+01	-0.3117E-01	0.7880E-01	0.1444E-01
14	81	0.1010E+00	0.1610E+01	0.6734E-01	0.8379E-01	0.1538E-01
14	82	0.1010E+00	0.1630E+01	0.1458E+00	0.8219E-01	0.1948E-01
14	83	0.1010E+00	0.1650E+01	0.9017E-01	0.5856E-01	0.1603E-01
14	84	0.1010E+00	0.1670E+01	-0.4033E-01	0.5981E-01	0.1775E-01
14	85	0.1010E+00	0.1690E+01	-0.7285E-01	0.6551E-01	0.2021E-01
14	86	0.1010E+00	0.1710E+01	-0.5332E+00	0.4702E+00	0.1968E-01
15	55	0.1200E+00	0.1090E+01	0.6342E-02	0.3300E-01	0.2831E-02
15	56	0.1200E+00	0.1110E+01	-0.2427E-01	0.3392E-01	0.7511E-02
15	57	0.1200E+00	0.1130E+01	0.4218E-01	0.3750E-01	0.1331E-01
15	58	0.1200E+00	0.1150E+01	-0.6894E-01	0.4114E-01	0.1832E-01
15	59	0.1200E+00	0.1170E+01	-0.1557E+00	0.4911E-01	0.2109E-01
15	60	0.1200E+00	0.1190E+01	-0.2393E+00	0.5840E-01	0.2811E-01
15	61	0.1200E+00	0.1210E+01	-0.3357E+00	0.6953E-01	0.4079E-01
15	62	0.1200E+00	0.1230E+01	-0.2631E+00	0.7151E-01	0.4046E-01
15	63	0.1200E+00	0.1250E+01	-0.3427E+00	0.6666E-01	0.4606E-01
15	64	0.1200E+00	0.1270E+01	-0.1221E+00	0.6631E-01	0.3143E-01
15	65	0.1200E+00	0.1290E+01	-0.1618E+00	0.6385E-01	0.2984E-01
15	66	0.1200E+00	0.1310E+01	-0.8733E-01	0.6413E-01	0.2515E-01
15	67	0.1200E+00	0.1330E+01	0.8539E-01	0.6144E-01	0.2298E-01

continued on next page

Q^2_{bin}	W_{bin}	Q^2	W	g_1^p	Δg_1^p	$\Delta_s g_1^p$
15	68	0.1200E+00	0.1350E+01	0.7155E-01	0.6077E-01	0.2115E-01
15	69	0.1200E+00	0.1370E+01	0.1152E+00	0.5935E-01	0.2066E-01
15	70	0.1200E+00	0.1390E+01	0.9508E-01	0.6032E-01	0.1932E-01
15	71	0.1200E+00	0.1410E+01	0.9106E-02	0.5999E-01	0.1761E-01
15	72	0.1200E+00	0.1430E+01	-0.4173E-01	0.6131E-01	0.1724E-01
15	73	0.1200E+00	0.1450E+01	-0.6701E-01	0.6588E-01	0.1713E-01
15	74	0.1200E+00	0.1470E+01	0.5604E-01	0.7006E-01	0.1714E-01
15	75	0.1200E+00	0.1490E+01	0.2562E+00	0.8184E-01	0.2274E-01
15	76	0.1200E+00	0.1510E+01	0.6817E-01	0.8623E-01	0.1970E-01
15	77	0.1200E+00	0.1530E+01	0.2061E-01	0.8321E-01	0.1796E-01
15	78	0.1200E+00	0.1550E+01	0.6515E-01	0.7797E-01	0.1688E-01
15	79	0.1200E+00	0.1570E+01	0.2138E-01	0.7691E-01	0.1575E-01
15	80	0.1200E+00	0.1590E+01	-0.5584E-01	0.7318E-01	0.1559E-01
15	81	0.1200E+00	0.1610E+01	0.1241E+00	0.7477E-01	0.1765E-01
15	82	0.1200E+00	0.1630E+01	-0.2612E-01	0.7424E-01	0.1666E-01
15	83	0.1200E+00	0.1650E+01	0.7779E-01	0.5384E-01	0.1669E-01
15	84	0.1200E+00	0.1670E+01	0.6254E-01	0.5714E-01	0.1794E-01
15	85	0.1200E+00	0.1690E+01	-0.1201E+00	0.7892E-01	0.1982E-01
16	55	0.1440E+00	0.1090E+01	-0.2857E-01	0.2635E-01	0.6541E-02
16	56	0.1440E+00	0.1110E+01	-0.4878E-01	0.2862E-01	0.1230E-01
16	57	0.1440E+00	0.1130E+01	-0.7340E-02	0.3222E-01	0.8266E-02
16	58	0.1440E+00	0.1150E+01	0.1225E-01	0.3679E-01	0.1229E-01
16	59	0.1440E+00	0.1170E+01	-0.1210E+00	0.4539E-01	0.1933E-01
16	60	0.1440E+00	0.1190E+01	-0.2213E+00	0.5573E-01	0.2705E-01
16	61	0.1440E+00	0.1210E+01	-0.3876E+00	0.6525E-01	0.4259E-01
16	62	0.1440E+00	0.1230E+01	-0.2995E+00	0.6647E-01	0.4236E-01
16	63	0.1440E+00	0.1250E+01	-0.2034E+00	0.6292E-01	0.3806E-01
16	64	0.1440E+00	0.1270E+01	-0.1172E+00	0.5812E-01	0.3097E-01
16	65	0.1440E+00	0.1290E+01	-0.1291E+00	0.5848E-01	0.2875E-01
16	66	0.1440E+00	0.1310E+01	-0.2018E-01	0.5747E-01	0.2449E-01
16	67	0.1440E+00	0.1330E+01	-0.2169E-01	0.5809E-01	0.2292E-01
16	68	0.1440E+00	0.1350E+01	0.3734E-01	0.5530E-01	0.2164E-01
16	69	0.1440E+00	0.1370E+01	0.4259E-01	0.5717E-01	0.2063E-01
16	70	0.1440E+00	0.1390E+01	0.7017E-01	0.5947E-01	0.2010E-01
16	71	0.1440E+00	0.1410E+01	0.7032E-01	0.5512E-01	0.1942E-01
16	72	0.1440E+00	0.1430E+01	0.2354E-02	0.5708E-01	0.1848E-01
16	73	0.1440E+00	0.1450E+01	0.5436E-01	0.5849E-01	0.1844E-01
16	74	0.1440E+00	0.1470E+01	-0.4574E-01	0.6630E-01	0.1828E-01

continued on next page

Q^2_{bin}	W_{bin}	Q^2	W	g_1^p	Δg_1^p	$\Delta_s g_1^p$
16	75	0.1440E+00	0.1490E+01	-0.5876E-02	0.7369E-01	0.1953E-01
16	76	0.1440E+00	0.1510E+01	0.9055E-01	0.7808E-01	0.2084E-01
16	77	0.1440E+00	0.1530E+01	0.2063E-01	0.7185E-01	0.1932E-01
16	78	0.1440E+00	0.1550E+01	0.1167E+00	0.6593E-01	0.1865E-01
16	79	0.1440E+00	0.1570E+01	0.1497E+00	0.6082E-01	0.1819E-01
16	80	0.1440E+00	0.1590E+01	0.6661E-01	0.6379E-01	0.1643E-01
16	81	0.1440E+00	0.1610E+01	0.5804E-01	0.6160E-01	0.1628E-01
16	82	0.1440E+00	0.1630E+01	0.8138E-01	0.7155E-01	0.1810E-01
16	83	0.1440E+00	0.1650E+01	0.4858E-01	0.5287E-01	0.1756E-01
16	84	0.1440E+00	0.1670E+01	0.1409E-01	0.5522E-01	0.1837E-01
16	85	0.1440E+00	0.1690E+01	0.5644E-01	0.8838E-01	0.1984E-01
16	86	0.1440E+00	0.1710E+01	0.2999E+00	0.1641E+00	0.1926E-01
16	87	0.1440E+00	0.1730E+01	0.1657E+00	0.1590E+00	0.1902E-01
16	88	0.1440E+00	0.1750E+01	0.3331E-01	0.1689E+00	0.1816E-01
16	89	0.1440E+00	0.1770E+01	0.1394E+00	0.2055E+00	0.1783E-01
16	90	0.1440E+00	0.1790E+01	-0.8903E-01	0.4184E+00	0.1848E-01
16	91	0.1440E+00	0.1810E+01	0.3558E+01	-0.2981E+01	0.1930E-01
16	92	0.1440E+00	0.1830E+01	-0.2395E+00	-0.3412E+00	0.1985E-01
17	55	0.1710E+00	0.1090E+01	-0.6431E-01	0.2633E-01	0.1414E-01
17	56	0.1710E+00	0.1110E+01	-0.1921E-01	0.2593E-01	0.6719E-02
17	57	0.1710E+00	0.1130E+01	-0.3734E-01	0.2833E-01	0.1167E-01
17	58	0.1710E+00	0.1150E+01	-0.8332E-01	0.3280E-01	0.2099E-01
17	59	0.1710E+00	0.1170E+01	-0.1084E+00	0.3900E-01	0.1916E-01
17	60	0.1710E+00	0.1190E+01	-0.1220E+00	0.4606E-01	0.2507E-01
17	61	0.1710E+00	0.1210E+01	-0.4174E+00	0.5561E-01	0.4470E-01
17	62	0.1710E+00	0.1230E+01	-0.2611E+00	0.5659E-01	0.4042E-01
17	63	0.1710E+00	0.1250E+01	-0.2009E+00	0.5609E-01	0.3764E-01
17	64	0.1710E+00	0.1270E+01	-0.3062E-01	0.5211E-01	0.2995E-01
17	65	0.1710E+00	0.1290E+01	-0.1722E+00	0.4986E-01	0.3117E-01
17	66	0.1710E+00	0.1310E+01	-0.6989E-01	0.4821E-01	0.2572E-01
17	67	0.1710E+00	0.1330E+01	-0.4411E-01	0.4761E-01	0.2371E-01
17	68	0.1710E+00	0.1350E+01	0.8808E-01	0.4697E-01	0.2301E-01
17	69	0.1710E+00	0.1370E+01	0.4306E-01	0.4374E-01	0.2137E-01
17	70	0.1710E+00	0.1390E+01	0.1126E-01	0.4048E-01	0.2034E-01
17	71	0.1710E+00	0.1410E+01	0.2563E-01	0.4009E-01	0.1984E-01
17	72	0.1710E+00	0.1430E+01	0.1190E+00	0.4265E-01	0.2050E-01
17	73	0.1710E+00	0.1450E+01	0.4600E-01	0.4267E-01	0.1941E-01
17	74	0.1710E+00	0.1470E+01	0.6612E-01	0.4466E-01	0.1944E-01

continued on next page

Q^2_{bin}	W_{bin}	Q^2	W	g_1^p	Δg_1^p	$\Delta_s g_1^p$
17	75	0.1710E+00	0.1490E+01	0.9248E-01	0.4685E-01	0.2113E-01
17	76	0.1710E+00	0.1510E+01	0.1453E+00	0.4901E-01	0.2258E-01
17	77	0.1710E+00	0.1530E+01	0.2233E+00	0.4285E-01	0.2235E-01
17	78	0.1710E+00	0.1550E+01	0.1019E+00	0.3714E-01	0.1988E-01
17	79	0.1710E+00	0.1570E+01	0.1069E+00	0.3571E-01	0.1876E-01
17	80	0.1710E+00	0.1590E+01	0.9321E-01	0.3557E-01	0.1776E-01
17	81	0.1710E+00	0.1610E+01	0.1181E+00	0.3539E-01	0.1920E-01
17	82	0.1710E+00	0.1630E+01	0.8474E-01	0.2599E-01	0.1791E-01
17	83	0.1710E+00	0.1650E+01	0.6050E-01	0.2636E-01	0.1912E-01
17	84	0.1710E+00	0.1670E+01	0.2059E-01	0.3000E-01	0.1899E-01
17	85	0.1710E+00	0.1690E+01	0.7843E-01	0.4041E-01	0.2000E-01
17	86	0.1710E+00	0.1710E+01	0.8447E-01	0.3914E-01	0.1959E-01
17	87	0.1710E+00	0.1730E+01	0.8534E-01	0.3798E-01	0.1930E-01
17	88	0.1710E+00	0.1750E+01	0.2540E-01	0.4255E-01	0.1854E-01
17	89	0.1710E+00	0.1770E+01	0.3053E-01	0.6338E-01	0.1840E-01
17	90	0.1710E+00	0.1790E+01	-0.6819E-01	0.1486E+00	0.1928E-01
17	91	0.1710E+00	0.1810E+01	-0.9455E+01	0.6782E+01	0.2029E-01
17	92	0.1710E+00	0.1830E+01	0.4157E+00	-0.5607E+00	0.2096E-01
18	55	0.2050E+00	0.1090E+01	0.2211E-01	0.1976E-01	0.5611E-02
18	56	0.2050E+00	0.1110E+01	0.2714E-02	0.1895E-01	0.5288E-02
18	57	0.2050E+00	0.1130E+01	-0.1861E-01	0.2025E-01	0.9071E-02
18	58	0.2050E+00	0.1150E+01	-0.5231E-01	0.2222E-01	0.1604E-01
18	59	0.2050E+00	0.1170E+01	-0.1351E+00	0.2468E-01	0.2053E-01
18	60	0.2050E+00	0.1190E+01	-0.2352E+00	0.2927E-01	0.2783E-01
18	61	0.2050E+00	0.1210E+01	-0.3001E+00	0.3310E-01	0.3833E-01
18	62	0.2050E+00	0.1230E+01	-0.3520E+00	0.3501E-01	0.4471E-01
18	63	0.2050E+00	0.1250E+01	-0.2057E+00	0.3267E-01	0.3718E-01
18	64	0.2050E+00	0.1270E+01	-0.8995E-01	0.2962E-01	0.3053E-01
18	65	0.2050E+00	0.1290E+01	-0.6893E-01	0.2788E-01	0.2780E-01
18	66	0.2050E+00	0.1310E+01	-0.6760E-01	0.2727E-01	0.2581E-01
18	67	0.2050E+00	0.1330E+01	-0.1965E-01	0.2692E-01	0.2379E-01
18	68	0.2050E+00	0.1350E+01	-0.9812E-02	0.2555E-01	0.2243E-01
18	69	0.2050E+00	0.1370E+01	0.4066E-01	0.2394E-01	0.2167E-01
18	70	0.2050E+00	0.1390E+01	0.4539E-01	0.2299E-01	0.2104E-01
18	71	0.2050E+00	0.1410E+01	0.4291E-01	0.2326E-01	0.2050E-01
18	72	0.2050E+00	0.1430E+01	0.8301E-01	0.2403E-01	0.2065E-01
18	73	0.2050E+00	0.1450E+01	0.6460E-01	0.2437E-01	0.2028E-01
18	74	0.2050E+00	0.1470E+01	0.7738E-01	0.2586E-01	0.2043E-01

continued on next page

Q^2_{bin}	W_{bin}	Q^2	W	g_1^p	Δg_1^p	$\Delta_s g_1^p$
18	75	0.2050E+00	0.1490E+01	0.1692E+00	0.2886E-01	0.2325E-01
18	76	0.2050E+00	0.1510E+01	0.1917E+00	0.3028E-01	0.2462E-01
18	77	0.2050E+00	0.1530E+01	0.1593E+00	0.2728E-01	0.2310E-01
18	78	0.2050E+00	0.1550E+01	0.1545E+00	0.2510E-01	0.2184E-01
18	79	0.2050E+00	0.1570E+01	0.1073E+00	0.2444E-01	0.1979E-01
18	80	0.2050E+00	0.1590E+01	0.8043E-01	0.2435E-01	0.1824E-01
18	81	0.2050E+00	0.1610E+01	0.8420E-01	0.2341E-01	0.1951E-01
18	82	0.2050E+00	0.1630E+01	0.8449E-01	0.1742E-01	0.1934E-01
18	83	0.2050E+00	0.1650E+01	0.1065E+00	0.1911E-01	0.2105E-01
18	84	0.2050E+00	0.1670E+01	0.9064E-01	0.2377E-01	0.2034E-01
18	85	0.2050E+00	0.1690E+01	0.9482E-01	0.2617E-01	0.2039E-01
18	86	0.2050E+00	0.1710E+01	0.8857E-01	0.2431E-01	0.1993E-01
18	87	0.2050E+00	0.1730E+01	0.1475E+00	0.2251E-01	0.1956E-01
18	88	0.2050E+00	0.1750E+01	0.1177E+00	0.2375E-01	0.1902E-01
18	89	0.2050E+00	0.1770E+01	0.7518E-01	0.3473E-01	0.1924E-01
18	90	0.2050E+00	0.1790E+01	0.1777E+00	0.8328E-01	0.2041E-01
18	91	0.2050E+00	0.1810E+01	-0.1263E+00	0.4765E+00	0.2171E-01
18	92	0.2050E+00	0.1830E+01	-0.2629E+01	0.5719E+01	0.2262E-01
19	55	0.2440E+00	0.1090E+01	-0.3212E-01	0.1309E-01	0.7550E-02
19	56	0.2440E+00	0.1110E+01	0.4947E-02	0.1349E-01	0.5254E-02
19	57	0.2440E+00	0.1130E+01	-0.3686E-01	0.1431E-01	0.1145E-01
19	58	0.2440E+00	0.1150E+01	-0.3398E-01	0.1669E-01	0.1347E-01
19	59	0.2440E+00	0.1170E+01	-0.9441E-01	0.1890E-01	0.1844E-01
19	60	0.2440E+00	0.1190E+01	-0.1609E+00	0.2106E-01	0.2502E-01
19	61	0.2440E+00	0.1210E+01	-0.2971E+00	0.2481E-01	0.3674E-01
19	62	0.2440E+00	0.1230E+01	-0.3128E+00	0.2464E-01	0.4107E-01
19	63	0.2440E+00	0.1250E+01	-0.2106E+00	0.2278E-01	0.3640E-01
19	64	0.2440E+00	0.1270E+01	-0.1136E+00	0.2043E-01	0.3047E-01
19	65	0.2440E+00	0.1290E+01	-0.4551E-01	0.2056E-01	0.2677E-01
19	66	0.2440E+00	0.1310E+01	-0.5321E-01	0.1958E-01	0.2491E-01
19	67	0.2440E+00	0.1330E+01	0.6539E-02	0.1832E-01	0.2316E-01
19	68	0.2440E+00	0.1350E+01	0.2489E-01	0.1928E-01	0.2205E-01
19	69	0.2440E+00	0.1370E+01	-0.2024E-02	0.1913E-01	0.2108E-01
19	70	0.2440E+00	0.1390E+01	0.7782E-01	0.1912E-01	0.2135E-01
19	71	0.2440E+00	0.1410E+01	0.4166E-01	0.1888E-01	0.2037E-01
19	72	0.2440E+00	0.1430E+01	0.8029E-01	0.1897E-01	0.2065E-01
19	73	0.2440E+00	0.1450E+01	0.1086E+00	0.1968E-01	0.2094E-01
19	74	0.2440E+00	0.1470E+01	0.1133E+00	0.2165E-01	0.2118E-01

continued on next page

Q^2_{bin}	W_{bin}	Q^2	W	g_1^p	Δg_1^p	$\Delta_s g_1^p$
19	75	0.2440E+00	0.1490E+01	0.2026E+00	0.2480E-01	0.2467E-01
19	76	0.2440E+00	0.1510E+01	0.2343E+00	0.2615E-01	0.2630E-01
19	77	0.2440E+00	0.1530E+01	0.2172E+00	0.2395E-01	0.2509E-01
19	78	0.2440E+00	0.1550E+01	0.1675E+00	0.2127E-01	0.2318E-01
19	79	0.2440E+00	0.1570E+01	0.1440E+00	0.2157E-01	0.2155E-01
19	80	0.2440E+00	0.1590E+01	0.9190E-01	0.2171E-01	0.2008E-01
19	81	0.2440E+00	0.1610E+01	0.1093E+00	0.2085E-01	0.1960E-01
19	82	0.2440E+00	0.1630E+01	0.1450E+00	0.2303E-01	0.2169E-01
19	83	0.2440E+00	0.1650E+01	0.9551E-01	0.2631E-01	0.2006E-01
19	84	0.2440E+00	0.1670E+01	0.4012E-01	0.3192E-01	0.2011E-01
19	85	0.2440E+00	0.1690E+01	0.6970E-01	0.3430E-01	0.2097E-01
19	86	0.2440E+00	0.1710E+01	0.1015E+00	0.3347E-01	0.2090E-01
19	87	0.2440E+00	0.1730E+01	0.1197E+00	0.3515E-01	0.2015E-01
19	88	0.2440E+00	0.1750E+01	0.1818E+00	0.5466E-01	0.2044E-01
19	89	0.2440E+00	0.1770E+01	0.1663E+00	0.3875E-01	0.1986E-01
19	90	0.2440E+00	0.1790E+01	0.1507E+00	0.1320E+00	0.2152E-01
19	91	0.2440E+00	0.1810E+01	-0.7695E+01	0.5013E+01	0.2376E-01
20	55	0.2920E+00	0.1090E+01	-0.1313E-01	0.1051E-01	0.3789E-02
20	56	0.2920E+00	0.1110E+01	0.1254E-01	0.1105E-01	0.5935E-02
20	57	0.2920E+00	0.1130E+01	-0.2756E-01	0.1175E-01	0.9736E-02
20	58	0.2920E+00	0.1150E+01	-0.3199E-01	0.1241E-01	0.1267E-01
20	59	0.2920E+00	0.1170E+01	-0.8257E-01	0.1435E-01	0.1691E-01
20	60	0.2920E+00	0.1190E+01	-0.1521E+00	0.1784E-01	0.2279E-01
20	61	0.2920E+00	0.1210E+01	-0.2560E+00	0.1958E-01	0.3174E-01
20	62	0.2920E+00	0.1230E+01	-0.2436E+00	0.2058E-01	0.3423E-01
20	63	0.2920E+00	0.1250E+01	-0.1785E+00	0.1934E-01	0.3223E-01
20	64	0.2920E+00	0.1270E+01	-0.1010E+00	0.1815E-01	0.2837E-01
20	65	0.2920E+00	0.1290E+01	-0.5810E-01	0.1837E-01	0.2556E-01
20	66	0.2920E+00	0.1310E+01	-0.3923E-01	0.1788E-01	0.2368E-01
20	67	0.2920E+00	0.1330E+01	0.4684E-02	0.1812E-01	0.2225E-01
20	68	0.2920E+00	0.1350E+01	0.1228E-01	0.1743E-01	0.2117E-01
20	69	0.2920E+00	0.1370E+01	0.2713E-01	0.1664E-01	0.2049E-01
20	70	0.2920E+00	0.1390E+01	0.2135E-01	0.1662E-01	0.2001E-01
20	71	0.2920E+00	0.1410E+01	0.7821E-01	0.1652E-01	0.2059E-01
20	72	0.2920E+00	0.1430E+01	0.9026E-01	0.1736E-01	0.2068E-01
20	73	0.2920E+00	0.1450E+01	0.7368E-01	0.1755E-01	0.2067E-01
20	74	0.2920E+00	0.1470E+01	0.1377E+00	0.2047E-01	0.2169E-01
20	75	0.2920E+00	0.1490E+01	0.1869E+00	0.2117E-01	0.2470E-01

continued on next page

Q^2_{bin}	W_{bin}	Q^2	W	g_1^p	Δg_1^p	$\Delta_s g_1^p$
20	76	0.2920E+00	0.1510E+01	0.2587E+00	0.2265E-01	0.2683E-01
20	77	0.2920E+00	0.1530E+01	0.2067E+00	0.2039E-01	0.2577E-01
20	78	0.2920E+00	0.1550E+01	0.2030E+00	0.1839E-01	0.2473E-01
20	79	0.2920E+00	0.1570E+01	0.1506E+00	0.1740E-01	0.2254E-01
20	80	0.2920E+00	0.1590E+01	0.1147E+00	0.1805E-01	0.2084E-01
20	81	0.2920E+00	0.1610E+01	0.1016E+00	0.1815E-01	0.1975E-01
20	82	0.2920E+00	0.1630E+01	0.5962E-01	0.1890E-01	0.1993E-01
20	83	0.2920E+00	0.1650E+01	0.9430E-01	0.2474E-01	0.2042E-01
20	84	0.2920E+00	0.1670E+01	0.1094E+00	0.3054E-01	0.1951E-01
20	85	0.2920E+00	0.1690E+01	0.1473E+00	0.3216E-01	0.2259E-01
20	86	0.2920E+00	0.1710E+01	0.1319E+00	0.3247E-01	0.2189E-01
20	87	0.2920E+00	0.1730E+01	0.1114E+00	0.3208E-01	0.2038E-01
20	88	0.2920E+00	0.1750E+01	0.1581E+00	0.2964E-01	0.1969E-01
20	89	0.2920E+00	0.1770E+01	0.8885E-01	0.6349E-01	0.2111E-01
20	90	0.2920E+00	0.1790E+01	-0.1198E+00	0.8065E+00	0.2384E-01
21	55	0.3480E+00	0.1090E+01	-0.3038E-01	0.8782E-02	0.8304E-02
21	56	0.3480E+00	0.1110E+01	0.2400E-02	0.9986E-02	0.4683E-02
21	57	0.3480E+00	0.1130E+01	0.2589E-02	0.1057E-01	0.7271E-02
21	58	0.3480E+00	0.1150E+01	-0.1558E-01	0.1115E-01	0.1064E-01
21	59	0.3480E+00	0.1170E+01	-0.8857E-01	0.1292E-01	0.1595E-01
21	60	0.3480E+00	0.1190E+01	-0.1766E+00	0.1521E-01	0.2128E-01
21	61	0.3480E+00	0.1210E+01	-0.1692E+00	0.1821E-01	0.2641E-01
21	62	0.3480E+00	0.1230E+01	-0.2058E+00	0.1873E-01	0.2984E-01
21	63	0.3480E+00	0.1250E+01	-0.1649E+00	0.1711E-01	0.2902E-01
21	64	0.3480E+00	0.1270E+01	-0.9448E-01	0.1547E-01	0.2571E-01
21	65	0.3480E+00	0.1290E+01	-0.4461E-01	0.1511E-01	0.2345E-01
21	66	0.3480E+00	0.1310E+01	-0.5450E-04	0.1432E-01	0.2195E-01
21	67	0.3480E+00	0.1330E+01	0.2147E-01	0.1407E-01	0.2085E-01
21	68	0.3480E+00	0.1350E+01	0.3699E-01	0.1450E-01	0.2009E-01
21	69	0.3480E+00	0.1370E+01	0.5569E-01	0.1461E-01	0.1971E-01
21	70	0.3480E+00	0.1390E+01	0.3798E-01	0.1455E-01	0.1916E-01
21	71	0.3480E+00	0.1410E+01	0.4842E-01	0.1529E-01	0.1915E-01
21	72	0.3480E+00	0.1430E+01	0.8254E-01	0.1600E-01	0.1991E-01
21	73	0.3480E+00	0.1450E+01	0.8833E-01	0.1680E-01	0.2036E-01
21	74	0.3480E+00	0.1470E+01	0.1496E+00	0.1792E-01	0.2153E-01
21	75	0.3480E+00	0.1490E+01	0.2447E+00	0.1966E-01	0.2502E-01
21	76	0.3480E+00	0.1510E+01	0.2126E+00	0.1994E-01	0.2704E-01
21	77	0.3480E+00	0.1530E+01	0.2282E+00	0.1803E-01	0.2616E-01

continued on next page

Q^2_{bin}	W_{bin}	Q^2	W	g_1^p	Δg_1^p	$\Delta_s g_1^p$
21	78	0.3480E+00	0.1550E+01	0.1960E+00	0.1628E-01	0.2494E-01
21	79	0.3480E+00	0.1570E+01	0.1309E+00	0.1693E-01	0.2399E-01
21	80	0.3480E+00	0.1590E+01	0.1347E+00	0.1733E-01	0.2183E-01
21	81	0.3480E+00	0.1610E+01	0.1700E+00	0.1819E-01	0.2368E-01
21	82	0.3480E+00	0.1630E+01	0.1438E+00	0.2267E-01	0.2243E-01
21	83	0.3480E+00	0.1650E+01	0.1528E+00	0.2559E-01	0.1904E-01
21	84	0.3480E+00	0.1670E+01	0.2171E+00	0.3108E-01	0.2068E-01
21	85	0.3480E+00	0.1690E+01	0.1601E+00	0.3372E-01	0.2374E-01
21	86	0.3480E+00	0.1710E+01	0.1590E+00	0.3702E-01	0.2334E-01
21	87	0.3480E+00	0.1730E+01	0.1285E+00	0.3646E-01	0.2031E-01
21	88	0.3480E+00	0.1750E+01	0.1143E+00	0.8476E-01	0.2078E-01
21	89	0.3480E+00	0.1770E+01	-0.1645E+01	0.7058E+00	0.2291E-01
22	55	0.4160E+00	0.1090E+01	-0.2806E-01	0.8073E-02	0.8446E-02
22	56	0.4160E+00	0.1110E+01	0.5901E-02	0.9137E-02	0.4753E-02
22	57	0.4160E+00	0.1130E+01	-0.6324E-02	0.1008E-01	0.6907E-02
22	58	0.4160E+00	0.1150E+01	-0.2237E-01	0.1112E-01	0.1072E-01
22	59	0.4160E+00	0.1170E+01	-0.5573E-01	0.1156E-01	0.1415E-01
22	60	0.4160E+00	0.1190E+01	-0.1169E+00	0.1393E-01	0.1841E-01
22	61	0.4160E+00	0.1210E+01	-0.1894E+00	0.1558E-01	0.2464E-01
22	62	0.4160E+00	0.1230E+01	-0.1685E+00	0.1623E-01	0.2558E-01
22	63	0.4160E+00	0.1250E+01	-0.1357E+00	0.1509E-01	0.2509E-01
22	64	0.4160E+00	0.1270E+01	-0.7164E-01	0.1481E-01	0.2269E-01
22	65	0.4160E+00	0.1290E+01	-0.3048E-01	0.1391E-01	0.2117E-01
22	66	0.4160E+00	0.1310E+01	-0.1052E-01	0.1375E-01	0.2007E-01
22	67	0.4160E+00	0.1330E+01	0.1142E-01	0.1252E-01	0.1919E-01
22	68	0.4160E+00	0.1350E+01	0.4385E-01	0.1233E-01	0.1871E-01
22	69	0.4160E+00	0.1370E+01	0.5366E-01	0.1150E-01	0.1834E-01
22	70	0.4160E+00	0.1390E+01	0.5830E-01	0.1170E-01	0.1822E-01
22	71	0.4160E+00	0.1410E+01	0.5660E-01	0.1241E-01	0.1819E-01
22	72	0.4160E+00	0.1430E+01	0.9919E-01	0.1355E-01	0.1937E-01
22	73	0.4160E+00	0.1450E+01	0.9208E-01	0.1472E-01	0.2006E-01
22	74	0.4160E+00	0.1470E+01	0.1622E+00	0.1626E-01	0.2209E-01
22	75	0.4160E+00	0.1490E+01	0.2356E+00	0.1920E-01	0.2525E-01
22	76	0.4160E+00	0.1510E+01	0.2914E+00	0.2051E-01	0.2677E-01
22	77	0.4160E+00	0.1530E+01	0.2867E+00	0.1940E-01	0.2437E-01
22	78	0.4160E+00	0.1550E+01	0.1905E+00	0.1843E-01	0.2424E-01
22	79	0.4160E+00	0.1570E+01	0.1857E+00	0.1823E-01	0.2379E-01
22	80	0.4160E+00	0.1590E+01	0.1346E+00	0.1959E-01	0.2690E-01

continued on next page

Q^2_{bin}	W_{bin}	Q^2	W	g_1^p	Δg_1^p	$\Delta_s g_1^p$
22	81	0.4160E+00	0.1610E+01	0.1422E+00	0.2247E-01	0.1947E-01
22	82	0.4160E+00	0.1630E+01	0.1419E+00	0.2355E-01	0.1907E-01
22	83	0.4160E+00	0.1650E+01	0.1374E+00	0.2835E-01	0.1923E-01
22	84	0.4160E+00	0.1670E+01	0.1138E+00	0.3666E-01	0.2115E-01
22	85	0.4160E+00	0.1690E+01	0.7724E-01	0.5960E-01	0.2379E-01
22	86	0.4160E+00	0.1710E+01	0.4815E-01	0.9230E-01	0.2280E-01
22	87	0.4160E+00	0.1730E+01	0.2822E-02	0.2867E+00	0.2170E-01
23	55	0.4960E+00	0.1090E+01	-0.5702E-02	0.7493E-02	0.2666E-02
23	56	0.4960E+00	0.1110E+01	-0.1827E-02	0.7158E-02	0.4156E-02
23	57	0.4960E+00	0.1130E+01	-0.9619E-02	0.7864E-02	0.6705E-02
23	58	0.4960E+00	0.1150E+01	-0.2407E-01	0.8350E-02	0.1022E-01
23	59	0.4960E+00	0.1170E+01	-0.5865E-01	0.9395E-02	0.1264E-01
23	60	0.4960E+00	0.1190E+01	-0.1085E+00	0.1141E-01	0.1604E-01
23	61	0.4960E+00	0.1210E+01	-0.1280E+00	0.1273E-01	0.1991E-01
23	62	0.4960E+00	0.1230E+01	-0.1586E+00	0.1345E-01	0.2238E-01
23	63	0.4960E+00	0.1250E+01	-0.7464E-01	0.1253E-01	0.2040E-01
23	64	0.4960E+00	0.1270E+01	-0.5886E-01	0.1207E-01	0.1968E-01
23	65	0.4960E+00	0.1290E+01	-0.3562E-01	0.1160E-01	0.1877E-01
23	66	0.4960E+00	0.1310E+01	0.5159E-02	0.1107E-01	0.1806E-01
23	67	0.4960E+00	0.1330E+01	-0.7744E-03	0.1140E-01	0.1749E-01
23	68	0.4960E+00	0.1350E+01	0.5760E-01	0.1193E-01	0.1737E-01
23	69	0.4960E+00	0.1370E+01	0.3577E-01	0.1209E-01	0.1689E-01
23	70	0.4960E+00	0.1390E+01	0.7557E-01	0.1267E-01	0.2325E-01
23	71	0.4960E+00	0.1410E+01	0.8267E-01	0.1337E-01	0.1716E-01
23	72	0.4960E+00	0.1430E+01	0.7506E-01	0.1514E-01	0.1722E-01
23	73	0.4960E+00	0.1450E+01	0.1288E+00	0.1626E-01	0.1816E-01
23	74	0.4960E+00	0.1470E+01	0.1848E+00	0.1825E-01	0.1958E-01
23	75	0.4960E+00	0.1490E+01	0.2453E+00	0.1982E-01	0.2358E-01
23	76	0.4960E+00	0.1510E+01	0.2987E+00	0.2176E-01	0.2623E-01
23	77	0.4960E+00	0.1530E+01	0.2681E+00	0.1953E-01	0.2407E-01
23	78	0.4960E+00	0.1550E+01	0.2147E+00	0.1958E-01	0.2305E-01
23	79	0.4960E+00	0.1570E+01	0.1786E+00	0.2049E-01	0.2149E-01
23	80	0.4960E+00	0.1590E+01	0.1972E+00	0.2372E-01	0.2068E-01
23	81	0.4960E+00	0.1610E+01	0.1037E+00	0.3237E-01	0.1926E-01
23	82	0.4960E+00	0.1630E+01	0.1722E+00	0.5354E-01	0.1950E-01
23	83	0.4960E+00	0.1650E+01	0.2120E+00	0.1215E+00	0.2028E-01
23	84	0.4960E+00	0.1670E+01	0.1424E+00	0.2667E+00	0.2308E-01
23	85	0.4960E+00	0.1690E+01	-0.3504E+00	0.2616E+00	0.2510E-01

continued on next page

Q^2_{bin}	W_{bin}	Q^2	W	g_1^p	Δg_1^p	$\Delta_s g_1^p$
24	55	0.5920E+00	0.1090E+01	-0.1975E-01	0.6247E-02	0.7277E-02
24	56	0.5920E+00	0.1110E+01	-0.2131E-01	0.6058E-02	0.7426E-02
24	57	0.5920E+00	0.1130E+01	-0.1408E-01	0.6903E-02	0.6784E-02
24	58	0.5920E+00	0.1150E+01	-0.2220E-01	0.8118E-02	0.9219E-02
24	59	0.5920E+00	0.1170E+01	-0.3474E-01	0.9193E-02	0.1064E-01
24	60	0.5920E+00	0.1190E+01	-0.9063E-01	0.1131E-01	0.1381E-01
24	61	0.5920E+00	0.1210E+01	-0.1335E+00	0.1275E-01	0.1826E-01
24	62	0.5920E+00	0.1230E+01	-0.1038E+00	0.1326E-01	0.1829E-01
24	63	0.5920E+00	0.1250E+01	-0.8725E-01	0.1304E-01	0.1817E-01
24	64	0.5920E+00	0.1270E+01	-0.3643E-01	0.1198E-01	0.1706E-01
24	65	0.5920E+00	0.1290E+01	-0.3243E-01	0.1185E-01	0.1665E-01
24	66	0.5920E+00	0.1310E+01	0.1906E-01	0.1225E-01	0.1633E-01
24	67	0.5920E+00	0.1330E+01	0.1422E-01	0.1310E-01	0.1606E-01
24	68	0.5920E+00	0.1350E+01	0.6722E-01	0.1268E-01	0.1604E-01
24	69	0.5920E+00	0.1370E+01	0.5341E-01	0.1238E-01	0.1578E-01
24	70	0.5920E+00	0.1390E+01	0.6311E-01	0.1186E-01	0.1570E-01
24	71	0.5920E+00	0.1410E+01	0.7037E-01	0.1320E-01	0.1580E-01
24	72	0.5920E+00	0.1430E+01	0.8566E-01	0.1469E-01	0.1618E-01
24	73	0.5920E+00	0.1450E+01	0.1327E+00	0.1738E-01	0.1710E-01
24	74	0.5920E+00	0.1470E+01	0.1810E+00	0.2074E-01	0.1885E-01
24	75	0.5920E+00	0.1490E+01	0.2270E+00	0.2675E-01	0.2351E-01
24	76	0.5920E+00	0.1510E+01	0.2565E+00	0.3518E-01	0.2624E-01
24	77	0.5920E+00	0.1530E+01	0.1748E+00	0.4773E-01	0.2367E-01
24	78	0.5920E+00	0.1550E+01	0.3128E+00	0.8213E-01	0.2285E-01
24	79	0.5920E+00	0.1570E+01	-0.5147E-01	0.1495E+00	0.2140E-01
24	80	0.5920E+00	0.1590E+01	-0.1077E+00	0.1537E+00	0.2043E-01
24	81	0.5920E+00	0.1610E+01	-0.7205E-01	0.1532E+00	0.1999E-01
25	55	0.7070E+00	0.1090E+01	0.6963E-02	0.8216E-02	0.3224E-02
25	56	0.7070E+00	0.1110E+01	0.1102E-02	0.7913E-02	0.3901E-02
25	57	0.7070E+00	0.1130E+01	-0.5149E-02	0.8295E-02	0.5728E-02
25	58	0.7070E+00	0.1150E+01	-0.5635E-02	0.8595E-02	0.7263E-02
25	59	0.7070E+00	0.1170E+01	-0.4106E-01	0.1012E-01	0.9078E-02
25	60	0.7070E+00	0.1190E+01	-0.5027E-01	0.1208E-01	0.1131E-01
25	61	0.7070E+00	0.1210E+01	-0.9117E-01	0.1345E-01	0.1492E-01
25	62	0.7070E+00	0.1230E+01	-0.8501E-01	0.1376E-01	0.1562E-01
25	63	0.7070E+00	0.1250E+01	-0.6507E-01	0.1272E-01	0.1528E-01
25	64	0.7070E+00	0.1270E+01	-0.1911E-01	0.1126E-01	0.1473E-01
25	65	0.7070E+00	0.1290E+01	-0.1155E-01	0.1106E-01	0.1466E-01

continued on next page

Q^2_{bin}	W_{bin}	Q^2	W	g_1^p	Δg_1^p	$\Delta_s g_1^p$
25	66	0.7070E+00	0.1310E+01	0.1558E-01	0.1136E-01	0.1463E-01
25	67	0.7070E+00	0.1330E+01	0.5017E-01	0.1286E-01	0.1465E-01
25	68	0.7070E+00	0.1350E+01	0.6499E-01	0.1365E-01	0.1471E-01
25	69	0.7070E+00	0.1370E+01	0.3789E-01	0.1675E-01	0.1457E-01
25	70	0.7070E+00	0.1390E+01	0.2474E-01	0.2160E-01	0.1463E-01
25	71	0.7070E+00	0.1410E+01	0.1047E+00	0.2944E-01	0.1520E-01
25	72	0.7070E+00	0.1430E+01	0.1811E+00	0.6409E-01	0.1589E-01
25	73	0.7070E+00	0.1450E+01	0.2298E+00	0.1204E+00	0.1690E-01
25	74	0.7070E+00	0.1470E+01	-0.3852E-01	0.2473E+00	0.1865E-01
25	75	0.7070E+00	0.1490E+01	-0.6395E-02	0.1367E+00	0.2132E-01
26	55	0.8400E+00	0.1090E+01	-0.1273E-01	0.5732E-02	0.5089E-02
26	56	0.8400E+00	0.1110E+01	-0.7308E-02	0.6249E-02	0.3898E-02
26	57	0.8400E+00	0.1130E+01	-0.4367E-02	0.7236E-02	0.4786E-02
26	58	0.8400E+00	0.1150E+01	-0.2225E-01	0.9301E-02	0.7084E-02
26	59	0.8400E+00	0.1170E+01	-0.2030E-01	0.1255E-01	0.7853E-02
26	60	0.8400E+00	0.1190E+01	-0.1499E-01	0.1596E-01	0.9998E-02
26	61	0.8400E+00	0.1210E+01	-0.1146E+00	0.2169E-01	0.1514E-01
26	62	0.8400E+00	0.1230E+01	-0.3826E-01	0.2411E-01	0.1347E-01
26	63	0.8400E+00	0.1250E+01	-0.7587E-01	0.2664E-01	0.1393E-01
26	64	0.8400E+00	0.1270E+01	-0.5579E-01	0.3341E-01	0.1337E-01
26	65	0.8400E+00	0.1290E+01	0.1269E-01	0.4397E-01	0.1305E-01
26	66	0.8400E+00	0.1310E+01	0.1279E+00	0.8054E-01	0.1363E-01
26	67	0.8400E+00	0.1330E+01	0.1679E+00	-0.1947E+00	0.1504E-01
26	68	0.8400E+00	0.1350E+01	-0.6423E+01	0.4308E+01	0.2434E+00
26	69	0.8400E+00	0.1370E+01	-0.1994E+00	0.1943E+00	0.1544E-01
27	55	0.1000E+01	0.1090E+01	-0.2988E-01	0.1387E-01	0.1109E-01
27	56	0.1000E+01	0.1110E+01	-0.2544E-02	0.7183E-01	0.2668E-02
27	59	0.1000E+01	0.1170E+01	-0.5399E-01	0.1478E+00	0.6430E-02

Appendix F

Data Table for $\Gamma_1^p(Q^2)$, E=1.6 GeV

Q^2 Bin	Q^2	Γ_{exp}	Γ_{dis}	Γ_{sum}	R	$\Delta\Gamma$	$\Delta_s\Gamma$
10	0.0496	-0.0121	0.0001	-0.0120	0.9332	0.0043	0.0025
11	0.0592	-0.0132	0.0001	-0.0130	0.9135	0.0024	0.0020
12	0.0707	-0.0200	0.0002	-0.0198	0.9380	0.0026	0.0027
13	0.0844	-0.0222	0.0003	-0.0219	0.9390	0.0027	0.0025
14	0.1010	-0.0161	0.0005	-0.0156	0.9296	0.0026	0.0030
15	0.1200	-0.0157	0.0010	-0.0147	0.9342	0.0027	0.0035
16	0.1440	-0.0174	0.0019	-0.0154	0.9159	0.0027	0.0038
17	0.1710	-0.0179	0.0032	-0.0146	0.9021	0.0025	0.0043
18	0.2050	-0.0156	0.0054	-0.0102	0.8557	0.0018	0.0046
19	0.2440	-0.0135	0.0086	-0.0049	0.7974	0.0014	0.0047
20	0.2920	-0.0097	0.0126	0.0029	0.7219	0.0012	0.0047
21	0.3480	-0.0051	0.0181	0.0130	0.6452	0.0011	0.0047
22	0.4160	-0.0004	0.0252	0.0247	0.5665	0.0011	0.0046
23	0.4960	0.0029	0.0345	0.0375	0.4644	0.0010	0.0044
24	0.5920	0.0038	0.0434	0.0472	0.3994	0.0013	0.0047
25	0.7070	0.0008	0.0548	0.0555	0.2361	0.0035	0.0052
26	0.8400	-0.0026	0.0728	0.0702	0.1419	0.0034	0.0062
27	1.0000	-0.0051	0.0814	0.0763	0.0591	0.0036	0.0067

Appendix G

Data Table for $\Gamma_1^p(Q^2)$, E=5.6 GeV

Q^2 Bin	Q^2	Γ_{exp}	Γ_{dis}	Γ_{sum}	R	$\Delta\Gamma$	$\Delta_s\Gamma$
24	0.5920	0.0542	0.0122	0.0664	0.8516	0.0062	0.0052
25	0.7070	0.0491	0.0159	0.0650	0.8082	0.0037	0.0048
26	0.8440	0.0479	0.0208	0.0687	0.7728	0.0030	0.0048
27	1.0100	0.0589	0.0261	0.0850	0.7320	0.0028	0.0051
28	1.2000	0.0620	0.0329	0.0949	0.6926	0.0025	0.0052
29	1.4400	0.0607	0.0413	0.1021	0.6059	0.0019	0.0051
30	1.7100	0.0570	0.0506	0.1076	0.5427	0.0015	0.0050
31	2.0500	0.0526	0.0615	0.1141	0.4676	0.0012	0.0046
32	2.4400	0.0423	0.0729	0.1151	0.3749	0.0010	0.0040
33	2.9200	0.0344	0.0867	0.1211	0.2901	0.0009	0.0036
34	3.4800	0.0245	0.1000	0.1245	0.1994	0.0009	0.0032
35	4.1600	0.0178	0.1135	0.1312	0.1363	0.0009	0.0027

References

[1] W. Greiner and A. Schafer, *Quantum Chromodynamics*, (Springer) (1994).

[2] P. Renton, *Electroweak Interactions*, (Cambridge University Press) (1990).

[3] B. Lampe and B. Reya, *hep-ph/9810270* (1998).

[4] J. Ashman et al., *Phys.Lett.B* **206**, 364, (1988).

[5] E. Leader and E. Predazzi, *An introduction to gauge theories and the 'new physics'*, (Cambridge University Press) (1982).

[6] A. Thomas and W. Weise, *The Structure of the Nucleon*, (WILEY-VCH) (2000).

[7] S. Kuhn, *Nucleon Structure Functions*, lectures given at HUGS (1997).

[8] X. Ji and P. Unrau, *Phys. Rev. D*,52 (1995)

[9] G. Ricco et al., *Nuclear Physics* **B**, 555 (1999).

[10] X. Ji, *hep-ph/9502288v1* (1995).

[11] B. W. Fillipone and Xiangdong Ji, *Adv.Nucl.Phys*, **26**,1 (2001)

[12] B. Frois, *The spin structure of the nucleon*, International School of Nucleon Structure, Erice, Italy, (World Scientific Publishing), 384 (1997).

[13] S. A. Larin, *Phys. Lett. B.* **334**, 192 (1994).

[14] M. Anselmino, A. Efremov, E. Leader, CERN Reports TH/7216/94 (1994).

[15] S. Adler and W. Bardeen, *Phys. Rev.* **182**, 1517 (1969).

[16] Yu-Bing Dong, *Z.Phys.* **A 359**, 453 (2000).

[17] S. D. Drell and A. C. Hearn, *Phys. Rev. Lett* **16**, 908 (1966).

[18] J. Edelmann et al., *Nuclear Physics A* **665**, 125 (2000).

[19] S. B. Gerasimov, *Sov. J. Nucl. Phys.* **2**, 430 (1966).

[20] D. Drechsel, S. S. Kamalov, L. Tiator, *hep-ph/0008306* (2000).

[21] V. D. Burkert and B. L. Ioffe, *Phys. Lett. B* **296**, 223 (1992).

[22] J. Soffer and O. V. Teryaev, *Phys. Rev. D* **51**, 25 (1994).

[23] H. A. Grunder, *The Continuous Electron Beam Accelerator Facility* **CEBAF-PR-87-017** (1987).

[24] W. Diamond, *The Injector For the CEBAF CW Superconducting LINAC*, TJNAF report **CEBAF-PR-87-011** (1987)

[25] I. Kominis, *Measurement of the Neutron (^{3}He) Spin Structure at Low Q2 and the Extended Gerasimov-Drell-Hearn Sum Rule*, PhD thesis, Princeton University, 2001.

[26] M. Poelker et al., *Polarized Source Performance and Developments at Jefferson Lab*, 14th International Spin Physics Symposium, AIP Conference Proceedings, 943 (2000).

[27] J. Grames, *Unique Electron Polarimeter Comparison and Spin-Based Energy Measurement*, TJNAF Report **JLAB-ACC-01-12** (2001).

[28] M. Steigerwald, *MeV Mott Polarimetry at Jefferson Lab*, 14th International Spin Physics Symposium, AIP Conference Proceedings, 945 (2000).

[29] C. K. Sinclair, *Electron Beam Polarimetry*, TJNAF Report **JLAB-ACC-98-04** (1998).

[30] St. Goertz, W. Meyer, G. Reicherz, *Prog.Part.Nucl.Phys.* **49**, 403-489 (2002).

[31] A. Abragam, *Principles of Nuclear Magnetism*, (Oxford Science Publications) (1989).

[32] M. Borghini, *Proton spin orientation*, CERN Yellow Report, 68-32 (1968).

[33] D. G. Crabb and W. Meyer, *Ann.Rev.Nucl.Part.Sci* **47**, 67-109 (1997).

[34] C. D. Keith et al., *Nucl.Instr.Meth* **A 501** 327-339 (2003).

[35] B. A. Mecking et al., *Nucl.Instr.Meth* **503/3**, 513 (2003).

[36] R. C. Fernow, *Introduction To Experimental Particle Physics*, (Cambridge University Press) (1986).

[37] R. De Vita, *Measurement of the double spin asymmetry in* π^+ *electroproduction with CLAS*, PhD Thesis, University of Genova, 2000.

[38] E. S. Smith et al., *Nucl.Instr.Meth.* **A 432**, 265-298 (1999).

[39] A. Biselli, *Private Communication*

[40] P. Bosted et al., *Raster Corrections for EG1b*, CLAS-Note-2003-008 (2003)

[41] V. Burkert, *Private Communication*

[42] A. Klimenko and S. Kuhn, *Momentum Corrections for E6*, CLAS-Note-2003-005, (2003)

[43] S. Kuhn, *Data Analysis for EG1*, Analysis note, (2003).

[44] M. Anghinolfi et al., *Measure of the target per beam polarization in EG1 data*, CLAS-Note-2000-001, (2000).

[45] T. W. Donnelly and A. S. Raskin, *Annals of Physics* **169**, 247-351 (1986).

[46] P. Bosted et al., P_bP_T *from ep coincidence for EG1b*, EG1b-Note-PB1, (2003)

[47] Gregory S. Mitchell, *A precision measurement of the spin structure function* $g_1(x, Q^2)$ *for the proton and deuteron*, PhD Thesis, University of Wisconsin, 2000.

[48] O. A. Rondon, *Phys.Rev.* **C60**, 035201 (1999).

[49] P. Bosted, *Pair Symmetric Contributions to EG1*, analysis Note, unpublished (2001).

[50] T. V. Kuchto and N. M. Shumeiko, *Nucl.Phys.* **B219**, 412-436 (1983).

[51] K. Abe, *Phys.Rev.* **D58**, 112003 (1998).

[52] L. W. Mo and Y. S. Tsai, *Rev.Mod.Phys.* **41**, 1 (1969).

[53] S. Kuhn, *EG1 Analysis: Models for inclusive cross sections and asymmetries*, Analysis note, (2001).

[54] F. E. Close and W. Melnitchouk, *hep-ph/0302013* (2003).

[55] N.Isgur, *Phys.Rev.D* **59**, 034013 (1999).

[56] E. Bloom and F. Gilman, *Phys. Rev. D* **4**, 2901 (1971).

[57] H. Georgi and H. D. Politzer, *Phys. Rev. D* **14**, 1829 (1976).

[58] P. Bosted, *Pair Symmetric and Pion Background for EG1b*, CLAS-NOTE, unpublished (2004).

[59] S. Kuhn, *Private Communication*

[60] T. Muta, *Foundations of Quantum Chromodynamics*, (World Scientific Publishing), 1998.